THE SHADES OF ENVIRONMENT

Pioneering Environmental Research: Faculty Perspectives from DRIEMS University

Vol.2(2025)

MR. PARTHA SARATHI SATAPATHY

OrangeBooks Publication

1stFloor,RajhansArcade,MallRoad,Kohka,Bhilai,Chhattisgarh490020

Website: **www.Orangebooks.in**

Second Edition,2025

ISBN:978-93-6554-870-9

PrintedinIndia

THE SHADES OF ENVIRONMENT

Pioneering Environmental Research: Faculty Perspectives from DRIEMS University

MR. PARTHA SARATHI SATAPATHY

OrangeBooks Publication
www.orangebooks.in

" Dedicated To DRIEMS University, With Gratitude ForFosteringKnowledgeAndInspiringExcellence."

Preface

In an era where environmental concerns transcend borders and generations, our relationship with the natural world has never been more critical—or more complex. The environment remains our greatest sustainer, yet it faces unprecedented challenges from the pace and pressures of modern human activity. As we confront climate change, biodiversity loss, resource depletion, and the intricate interplay of ecological systems, the urgency to understand, protect, and restore our planet has reached a defining moment.

The Shades of Environment, Vol. 2 (2025) emerges from this moment of both crisis and opportunity. Conceived within the vibrant academic and research culture of **DRIEMS University**, this volume stands as a testament to our faculty's unwavering commitment to advancing environmental knowledge. It is the result of rigorous inquiry, collaborative effort, and an enduring belief that science must guide the path toward sustainability.

Within these pages lies a tapestry of diverse studies—ranging from the conservation of fragile ecosystems and the exploration of sustainable resource management practices, to the analysis of human impacts on environmental health. Each contribution is unique in its scope and methodology, yet all are united by a common vision: to illuminate the many "shades" of environmental science and inspire action toward preserving the delicate balance that sustains life.

At **DRIEMS University**, research is not merely an academic pursuit; it is a responsibility to society and the planet. This book embodies that responsibility, showcasing innovative approaches, scientific rigor, and a deep sense of stewardship. It aims to serve not only as a repository of knowledge but as a catalyst for dialogue, policy innovation, and future research—bridging the gap between academia and real-world environmental challenges.We express our profound gratitude to the faculty members whose dedication and expertise breathe life into this volume, and to the institutional support that makes such scholarly endeavors possible. Without their passion for discovery and their drive to make a difference, this work would not exist.

As you explore *The Shades of Environment, Vol. 2*, we invite you to see beyond the statistics and scientific models—to witness the interconnectedness of all life and the shared responsibility we bear. May this volume inspire you, as it has inspired us, to envision a future where progress and preservation walk hand in hand, ensuring that the Earth's diverse shades remain vibrant for generations to come.

Acknowledgement

We extend our deepest gratitude to the esteemed leadership of **DRIEMS University** whose vision, guidance, and steadfast support have been the cornerstone of bringing *The Shades of Environment, Vol. 2 (2025)* to fruition. This compilation, representing the scholarly contributions of our distinguished faculty across diverse departments, reflects our shared commitment to advancing environmental knowledge and fostering sustainable solutions for the future.

Our heartfelt thanks to:
Dr. Pramod Chandra Rath – Founder Chairman, DRIEMS University
Er. Durga Prasad Rath – Vice-Chairman, DRIEMS University
Dr. P.K. Hota – Vice-Chancellor, DRIEMS University
Sj. BalaramKar – Director Administration, DRIEMS University
Smt. ChinmayeeRath – Director Coordination, DRIEMS University
Dr. BhaktaCharanPradhan – Registrar, DRIEMS University
Prof. (Dr.) Susant Kumar Das – Advisor, DRIEMS University

Your visionary leadership and unwavering encouragement have created a fertile ground for academic innovation and meaningful research. The support you have extended has empowered our faculty to explore critical environmental issues, present diverse perspectives, and contribute to the global discourse on sustainability.This book is not merely a collection of research papers; it is a testament to the collaborative spirit, academic excellence, and research-driven culture that define DRIEMS University. We are profoundly grateful for your commitment to nurturing an environment where ideas flourish, research thrives, and knowledge transforms into action.

.

Index

Integrating Environmental Sciences and Medical Rehabilitation Sciences for Sustainable Health Outcomes

Author: Dr. Durga Prasad Mishra, Dean, School of Occupational and Physiotherapy, DRIEMS UNIVERSITY

Dr. Durga Prasad Mishra is a distinguished academician, clinician, and administrator with over 11 years of experience in healthcare and education. Currently serving as the Dean of the School of Occupational and Physiotherapy at DRIEMS University, he brings a multidisciplinary background with degrees in Occupational Therapy (BOT & MOT), Applied Clinical Psychology (MAPC), Nutrition & Dietetics (PGDND), and currently pursuing PhD in Physiology. He is also a Fellow in Advanced Occupational Therapy with specialization in Neurodevelopmental Disorders.

Dr. Mishra has made significant contributions to research and clinical practice in autism, cerebral palsy, and developmental delays. His research has been published in Scopus-indexed and peer-reviewed journals, and he has authored several chapter published in SPRIGER NATURE(Rehabilitation Approach in Autism) and in the Government of India's Handbook on Early Intervention Centers. As an educator and mentor, he is known for his dynamic teaching style and his commitment to evidence-based, holistic care.

Beyond academia, Dr. Mishra is a strong advocate for disability rights and inclusive healthcare. He is a recognized speaker at national and international conferences, a resource person in CME and CRE programs, and a regular contributor to public health awareness via newspapers, TV channels, All India Radio, and web portals. He also authored an Odia-language booklet on Autism for SVNIRTAR.

Dr. Mishra works closely with university leadership and compliance bodies to uphold academic integrity and institutional accountability, ensuring excellence in education, research, and community outreach.

Abstract

Environmental sciences and medical rehabilitation sciences are often considered distinct disciplines. However, the intersection between human health, recovery, and the environment is becoming increasingly critical in the 21st century. This review explores the interrelationship between environmental factors (including pollution, climate change, green space access, and built environment) and rehabilitation outcomes, while also addressing the role of eco-sustainable practices in rehabilitation services. It underscores the necessity for an interdisciplinary approach to improve patient recovery, enhance public health, and foster a sustainable healthcare model.

Keywords

Rehabilitation, environmental health, climate change, eco-therapy, sustainable healthcare, occupational therapy, physiotherapy, pollution, green space, neuroplasticity.

1. Introduction

The growing awareness of environmental degradation and its impact on health has necessitated a cross-disciplinary approach to healthcare, particularly in the field of medical rehabilitation. Medical rehabilitation aims to restore function and quality of life following injury, surgery, or

chronic disease. However, recovery outcomes are often influenced by external environmental factors, including air and noise pollution, urban density, climate conditions, and access to nature.

Concurrently, healthcare practices themselves can exert significant environmental burdens due to resource use, waste generation, and carbon emissions. Thus, incorporating environmental considerations into rehabilitation sciences can lead to improved patient outcomes and a more sustainable healthcare model.

2. Environmental Determinants of Rehabilitation Outcomes

2.1 Air Pollution and Neurological Recovery

Exposure to fine particulate matter (PM2.5) and nitrogen dioxide (NO2) is linked to poor cognitive outcomes and neuroinflammation, both of which can impair recovery in stroke or traumatic brain injury patients. Chronic exposure may worsen symptoms in neurodegenerative diseases, such as Parkinson's and Alzheimer's, thus delaying or reversing rehabilitation gains.

2.4 Water Quality and Rehabilitation Settings

Water contamination, particularly with heavy metals like lead and arsenic, has been associated with cognitive deficits and developmental delays, particularly in pediatric populations. In rehabilitation settings, clean and safe water is vital not only for hydration but also for hydrotherapy interventions. Facilities in regions with poor water infrastructure face challenges that compromise both hygiene and therapy quality.

2.5 Indoor Environmental Quality (IEQ)

IEQ encompasses air quality, thermal comfort, lighting, and acoustics within indoor environments. Studies reveal that rehabilitation centers with optimized IEQ report better patient satisfaction, fewer therapy dropouts, and quicker recovery timelines. Integrating biophilic design—use of natural materials and plant elements—can reduce stress and improve engagement, particularly in patients undergoing neurorehabilitation.

2.2 Urban Noise and Stress Response

Environmental noise contributes to stress, disrupted sleep, and elevated cortisol levels, which impair neuroplasticity and wound healing. In patients undergoing cognitive or physical rehabilitation, these factors can critically affect engagement and progress.

2.3 Green Spaces and Mental Health

Numerous studies have confirmed that access to green spaces enhances mental well-being, promotes physical activity, and reduces symptoms of anxiety and depression. For individuals with post-stroke depression, spinal cord injuries, or chronic pain syndromes, green therapy (or eco-therapy) significantly augments conventional rehabilitation protocols.

3. Climate Change and Rehabilitation Services

3.1 Impact on Rehabilitation Access

Climate change has led to more frequent extreme weather events, which disrupt health services and hinder access to rehabilitation centers. Populations with mobility impairments or chronic illnesses are disproportionately affected during climate emergencies.

3.2 Heat Stress and Physical Therapy

Rising temperatures pose specific risks for physiotherapy patients, particularly during aerobic or gait training. Heat-related illness, dehydration, and fatigue can impede session quality and outcomes. Adaptive cooling technologies and indoor climate control are thus vital.

4. The Built Environment and Functional Recovery

4.1 Accessibility and Design

Environmental design profoundly influences functional outcomes. Barrier-free architecture, smart homes, and adaptive technologies support autonomy and reinforce therapy goals post-discharge.

4.2 Sensory Modulation in Therapy Spaces

The use of natural lighting, calming colors, soundproofing, and air purification in rehabilitation spaces creates environments conducive to neuroplasticity, motivation, and psychological resilience.

5. Eco-Friendly Rehabilitation Practices

5.1 Reducing Carbon Footprint of Rehabilitation Services

Rehabilitation centers consume substantial energy, produce waste (plastics, single-use devices), and rely on transportation. Strategies to minimize the ecological impact include:

- Tele-rehabilitation to reduce travel
- Green building certification (LEED)
- Renewable energy sources
- Biodegradable equipment and eco-friendly materials

5.2 Sustainable Prosthetics and Assistive Devices

Innovations in bioplastics, 3D printing, and recyclable materials have led to the production of eco-friendly assistive devices. For example, bamboo-fiber wheelchairs and modular prosthetics can be both sustainable and cost-effective.

6. Integration Models and Case Studies

6.1 Green Rehabilitation Model

An integrated “Green Rehab” approach incorporates green infrastructure (e.g., therapeutic gardens), sustainable architecture, and environmentally informed therapy. Pilot programs in Scandinavian countries have shown improved patient satisfaction and lower hospital energy usage.

6.1.1 Case Study: Singapore’s Khoo Teck Puat Hospital

A regional leader in sustainable healthcare, this hospital incorporates lush gardens visible from patient rooms, natural ventilation, and solar power. Rehabilitation outcomes improved due to reduced patient anxiety and higher staff satisfaction. The hospital serves as a model for eco-integrated medical care in tropical urban contexts.

6.1.2 Case Study: Rural India and Traditional Eco-Rehabilitation

In parts of India, traditional medicine systems like Ayurveda incorporate nature-based therapies using local herbs, forest walks, and water treatments. Community rehabilitation centers integrate

these modalities with modern physiotherapy, leveraging natural surroundings for low-cost, culturally resonant interventions.

6.1.3 European Perspective: Nordic Green-Care Models

Finland and Norway have pioneered “Green Care” practices, integrating nature activities into long-term psychiatric and physical rehabilitation. Patients engage in animal-assisted therapy, forest walks, and horticulture, which support motor recovery, emotional regulation, and social integration.

6.2 Nature-Based Interventions (NBI)

Programs such as “Green Gym” and “Walk-and-Talk Therapy” provide structured physical and occupational therapy in natural settings. These have shown significant results in patients with depression, stroke, and chronic pain.

7. Recommendations for Future Integration

- Policy: Environmental impact should be considered in health policy, with incentives for green infrastructure in rehabilitation.

- Curriculum: Introduce environmental health in the curriculum of medical rehabilitation professionals.

- Research: More longitudinal studies to explore the direct influence of environmental variables on therapy outcomes.

- Technology: Encourage development of sustainable rehabilitation technology and smart environmental monitoring.

- Regional Customization: Environmental rehab integration should be tailored to local climate, culture, and resource availability. What works in Scandinavia may need adaptation in tropical or arid regions.

- Intersectoral Collaboration: Health departments must collaborate with urban planners, environmental scientists, and ecologists to design environments conducive to healing and rehabilitation.

- Capacity Building: Training programs for rehabilitation professionals must include modules on environmental health, climate adaptation, and eco-design principles.

8. Conclusion

The synergy between environmental sciences and rehabilitation sciences represents a promising frontier in healthcare. A patient’s environment — both physical and ecological — plays a pivotal role in recovery, while rehabilitation itself can either exacerbate or alleviate environmental harm. By adopting sustainable practices and optimizing environmental exposures, the healthcare system can advance toward a model that promotes both human and planetary well-being.

References

1. Calderón-Garcidueñas, L., et al. (2020). Neuroinflammation, Alzheimer’s-like pathology, and health effects in children exposed to air pollution. Environmental Research, 183, 109226.

2. Basner, M., et al. (2014). Auditory and non-auditory effects of noise on health. Lancet, 383(9925), 1325–1332.

3. Twohig-Bennett, C., & Jones, A. (2018). The health benefits of the great outdoors: A systematic review. Environmental Research, 166, 628–637.

4. Watts, N., et al. (2023). The 2023 report of the Lancet Countdown on health and climate change. Lancet, 402(10412), 1786–1835.

5. Steinfeld, E., & Maisel, J. (2012). Universal Design: Creating Inclusive Environments. John Wiley & Sons.

6. Islam, M. T., et al. (2022). Sustainable and low-cost assistive technology: A review. Journal of Rehabilitation and Assistive Technologies Engineering, 9, 1–14.

7. Sundquist, K., et al. (2017). Effect of green-space intervention on mental health in rehabilitation. IJERPH, 14(10), 1156.

Environmental Science in the Digital Age: Recent Breakthroughs and Emerging Challenges

Dr. Alok Ranjan Biswal, Director (IQAC), DRIEMS University
Dr. Deepak Ranjan Biswal, HoD (ME), SOET, DRIEMS University

Environmental science stands at a critical juncture where traditional ecological challenges intersect with cutting-edge technological solutions. The past two years have witnessed unprecedented developments in how we monitor, understand, and address environmental problems. From artificial intelligence revolutionizing pollution detection to breakthrough carbon capture technologies, the field is experiencing a transformation that promises both innovative solutions and new complexities. This comprehensive analysis explores the most significant recent developments in environmental science, examining how emerging technologies are reshaping our approach to planetary stewardship while creating novel challenges that demand immediate attention.

The Integration of Artificial Intelligence in Environmental Monitoring

The application of artificial intelligence in environmental science has emerged as one of the most transformative developments of recent years. The application of Artificial Intelligence (AI) in environmental monitoring offers accurate disaster forecasts, pollution source detection, and comprehensive environmental assessment capabilities that were previously impossible with traditional monitoring methods.AI-driven environmental monitoring systems are revolutionizing how scientists collect, analyze, and interpret environmental data. These systems can process vast amounts of information from multiple sources simultaneously, including satellite imagery, sensor networks, weather stations, and biological monitoring equipment. The integration of machine learning algorithms enables these systems to identify patterns, predict environmental changes, and detect anomalies that might indicate emerging environmental threats.

One of the most significant applications of AI in environmental monitoring is in air quality management. AI-driven models predict pollution levels by integrating data from various monitoring stations and meteorological inputs. These models help cities implement timely interventions to reduce pollution and protect public health. This capability is particularly crucial in urban environments where air pollution poses immediate health risks to millions of people.The precision and speed of AI-powered monitoring systems enable real-time responses to environmental threats. Traditional monitoring methods often required days or weeks to process data and identify problems, by which time significant environmental damage might have already occurred. AI systems can detect changes within minutes or hours, allowing for immediate intervention and damage mitigation.This paradox highlights the need for sustainable AI development that minimizes its own environmental footprint while maximizing its environmental benefits.

The Micro plastics Crisis and Technological Solutions

Micro plastic pollution has emerged as one of the most pervasive environmental challenges of our time, requiring innovative technological solutions for detection, monitoring, and remediation. Recent research has revealed the complex relationships between micro plastics and climate change, creating new urgency around addressing this pollution source.Micro plastics are polymer-based materials with carbon as their main framework. During degradation, they release greenhouse gases such as carbon dioxide and methane. This discovery has fundamentally changed how scientists understand the role of plastic pollution in climate change, revealing that micro plastics are not just a separate environmental problem but are directly contributing to global warming.

The interconnected nature of micro plastic pollution and climate change creates complex feedback loops that amplify both problems. The production, dispersal, and accumulation of micro plastics are interconnected with climate change. Plastic production, which involves fossil resources like oil, generates greenhouse gas emissions during extraction and processing, contributing to global warming. Simultaneously, climate change influences the dispersion, fragmentation, and accumulation of MPs; extreme weather events facilitate plastic transport to the sea and natural environments.Addressing the micro plastics challenge requires sophisticated detection and monitoring systems that can operate in diverse environmental conditions. The project addresses a critical environmental challenge: the vast amounts of plastic waste entering our oceans from rivers and coastlines. Traditional waste collectors often struggle to differentiate between plastic and natural debris, leading to inefficiencies and increased maintenance costs.

Recent advances in machine learning have enabled the development of automated systems for micro plastic detection and characterization. Micro plastics are increasingly recognized as a pervasive pollutant in both aquatic and terrestrial environments, raising pressing concerns about their ecological impacts, and AI-powered detection systems offer the precision and scale necessary to monitor these widespread pollutants effectively.The development of AI-driven micro plastic monitoring systems represents a significant breakthrough in environmental technology. These systems can distinguish between different types of plastic materials, track their movement through ecosystems, and predict their accumulation patterns. This capability is essential for developing targeted remediation strategies and preventing further micro plastic pollution.

Carbon Capture Technology and Climate Mitigation

Carbon capture technology has experienced remarkable advances in recent years, driven by the urgent need to reduce atmospheric carbon dioxide concentrations and mitigate climate change. The integration of artificial intelligence into carbon capture systems represents a significant leap forward in efficiency and effectiveness.Artificial intelligence and environmental points are equally important components within the response to local weather change. Therefore, based on the efforts of reducing carbon emissions, AI-enhanced carbon capture systems are becoming increasingly sophisticated in their ability to optimize capture processes, predict optimal operating conditions, and integrate with renewable energy systems.The latest carbon capture technologies extend beyond traditional

industrial applications to include direct air capture systems, enhanced natural carbon sequestration methods, and innovative material science approaches. These technologies are becoming more energy-efficient and cost-effective, making large-scale implementation increasingly feasible.

Recent developments in carbon capture include the use of novel materials such as metal-organic frameworks (MOFs) and advanced sorbents that can selectively capture carbon dioxide from various sources. These materials can be precisely engineered at the molecular level to optimize their carbon capture properties while minimizing energy requirements for regeneration.The integration of AI in carbon capture systems enables dynamic optimization of capture processes based on real-time environmental conditions, energy availability, and carbon dioxide concentrations. This adaptive capability significantly improves the efficiency and economic viability of carbon capture technologies.

Renewable Energy Integration and Environmental Impact

The rapid expansion of renewable energy systems has created new opportunities and challenges for environmental science. Recent developments in renewable energy technology have focused on minimizing environmental impacts while maximizing energy production efficiency.Efforts in environmental technologies focus on developing innovative solutions to mitigate environmental degradation. These include renewable energy systems, waste management innovations, water purification technologies, carbon capture and sustainable agricultural practices. This integrated approach recognizes that environmental solutions must address multiple challenges simultaneously to be truly effective.Wind energy technology has advanced significantly in recent years, with larger, more efficient turbines and improved materials that reduce environmental impacts throughout their lifecycle. Solar photovoltaic technology has achieved remarkable efficiency improvements while reducing manufacturing costs and environmental footprints.

Energy storage technologies have emerged as critical components of renewable energy systems, enabling better integration with electrical grids and reducing the environmental impacts associated with energy intermittency. Advanced battery technologies, pumped hydro storage, and emerging storage methods like compressed air energy storage are all contributing to more sustainable energy systems.The environmental assessment of renewable energy systems has become increasingly sophisticated, incorporating lifecycle analysis, ecosystem impact assessments, and cumulative environmental effects. This comprehensive approach ensures that renewable energy deployment truly contributes to environmental sustainability rather than simply shifting environmental impacts to different sectors.

Water Purification and Resource Management

Water purification technology has experienced significant advances driven by increasing water scarcity, pollution challenges, and the need for energy-efficient treatment methods. Recent innovations in membrane technology, advanced oxidation processes, and biological treatment systems are transforming how we approach water treatment and resource management. Advanced membrane technologies now incorporate nanotechnology, biomimetic designs, and smart materials that can adapt to changing water quality conditions. These innovations enable more selective pollutant removal, reduced energy consumption, and extended membrane lifespans. The integration of AI and machine learning in water treatment systems enables predictive maintenance, optimal process control, and real-time adaptation to changing water quality conditions. These smart water treatment systems can automatically adjust treatment parameters to maintain optimal performance while minimizing energy consumption and chemical usage.

Biological water treatment systems have been enhanced through genetic engineering, synthetic biology, and advanced bioreactor designs. These systems can now target specific pollutants, operate under extreme conditions, and integrate with other treatment technologies to provide comprehensive water purification solutions.The development of decentralized water treatment systems has gained momentum as communities seek resilient, locally controlled water supplies. These systems incorporate advanced treatment technologies in compact, modular designs that can be deployed at various scales from individual buildings to entire neighbourhoods.

Biodiversity Monitoring and Conservation Technology

Recent advances in biodiversity monitoring technology have revolutionized how scientists track species populations, ecosystem health, and conservation effectiveness. Environmental DNA (e-DNA) analysis, remote sensing, acoustic monitoring, and AI-powered species identification are transforming biodiversity science. Environmental DNA analysis allows scientists to detect species presence from water, soil, or air samples by identifying genetic material shed by organisms. This technique enables non-invasive monitoring of elusive or rare species and can detect species presence even when direct observation is impossible. Remote sensing technology, including satellite imagery, drone-based sensors, and ground-based monitoring stations, provides comprehensive ecosystem monitoring capabilities. Advanced image analysis algorithms can automatically identify species, track vegetation changes, and monitor habitat modifications across vast spatial scales.

Acoustic monitoring systems equipped with AI-powered sound recognition can continuously monitor wildlife populations through their vocalizations. These systems can identify individual species, track population trends, and detect changes in ecosystem soundscapes that indicate environmental stress or recovery.Citizen science platforms enhanced with AI capabilities enable widespread participation in biodiversity monitoring while maintaining scientific rigor. Mobile applications can identify species from photographs,

record observations, and contribute to global biodiversity databases, dramatically expanding the scale and scope of biodiversity monitoring efforts.

Climate Modelling and Prediction Advances

Climate modelling has experienced significant advances through the integration of machine learning, improved computational capabilities, and enhanced observational data integration. These developments have improved the accuracy of climate predictions and enabled more detailed analysis of climate system interactions. Advanced climate models now incorporate machine learning algorithms that can identify complex patterns in climate data and improve prediction accuracy. These hybrid models combine traditional physics-based approaches with data-driven machine learning techniques to capture climate system behaviours that were previously difficult to model. High-resolution climate modelling capabilities have improved dramatically, enabling scientists to analyze climate impacts at local and regional scales with unprecedented detail. These detailed models are essential for climate adaptation planning and impact assessment in specific geographic areas.

The integration of real-time observational data from satellites, weather stations, ocean buoys, and other monitoring systems enables continuous model updating and improvement. This dynamic approach to climate modelling provides more accurate and timely climate information for decision-making. Ensemble modelling approaches that run multiple climate scenarios simultaneously provide better estimates of uncertainty and enable probabilistic climate predictions. This uncertainty quantification is crucial for risk assessment and adaptation planning in the face of climate change.

Sustainable Agriculture and Food Security

Recent developments in sustainable agriculture technology address the dual challenges of feeding a growing global population while minimizing environmental impacts. Precision agriculture, vertical farming, alternative protein production, and sustainable intensification strategies are all contributing to more environmentally friendly food systems.Precision agriculture technologies use GPS, sensors, AI, and robotics to optimize crop production while minimizing inputs such as water, fertilizers, and pesticides. These systems can apply treatments only where needed, reducing environmental impacts while maintaining or improving crop yields.

Vertical farming and controlled environment agriculture technologies enable food production in urban areas with minimal land use, water consumption, and chemical inputs. These systems can produce fresh produce year-round regardless of climate conditions and eliminate agricultural runoff pollution. Alternative protein production, including plant-based proteins, cultured meat, and insect farming, offers potential solutions to the environmental impacts of conventional animal agriculture. These technologies can significantly reduce greenhouse gas emissions, land use, and water consumption associated with protein production. Sustainable intensification strategies focus on increasing agricultural productivity while reducing environmental impacts through improved crop varieties,

integrated pest management, regenerative agriculture practices, and ecosystem service enhancement.

Environmental Remediation and Restoration

Environmental remediation technology has advanced significantly in recent years, with new approaches for cleaning up contaminated sites, restoring degraded ecosystems, and preventing further environmental damage. Bioremediation, phytoremediation, nanotechnology applications, and ecosystem restoration techniques are all evolving rapidly. Bioremediation techniques now incorporate genetically engineered microorganisms, enhanced bioavailability methods, and optimized environmental conditions to accelerate the breakdown of pollutants. These biological approaches can address a wide range of contaminants while avoiding the environmental impacts of traditional remediation methods. Phytoremediation uses plants to remove, transfer, stabilize, or destroy contaminants in soil, water, or air. Recent advances include the development of hyper accumulator plants, genetic modifications to enhance pollutant uptake, and integrated systems that combine multiple plant species for comprehensive remediation.

Nanotechnology applications in environmental remediation include nanoparticles that can target specific contaminants, Nano membranes for selective pollutant removal, and Nano catalysts for pollutant degradation. These technologies offer unprecedented precision in environmental clean-up while minimizing collateral environmental impacts.Ecosystem restoration techniques have become more sophisticated through better understanding of ecological processes, improved restoration materials, and long-term monitoring capabilities. Large-scale restoration projects now incorporate landscape-level planning, species reintroduction programs, and adaptive management approaches.

Environmental Policy and Regulatory Frameworks

The regulatory landscape for environmental protection has evolved significantly in response to emerging technologies, new scientific understanding, and global environmental challenges. Recent policy developments focus on integrated approaches that address multiple environmental issues simultaneously while promoting technological innovation.CDP has fully aligned its 2024 corporate questionnaire with the IFRS S2 (ISSB) climate standard, and on November 12, 2024, it announced extensive interoperability with ESRS (E1), meaning CDP-disclosing companies will be well prepared for climate disclosures required by the CSRD. This alignment of environmental reporting standards represents a significant step toward comprehensive corporate environmental accountability.

Environmental justice considerations have become increasingly prominent in policy development, ensuring that environmental benefits and burdens are distributed equitably across communities. New policies explicitly address the disproportionate environmental impacts on vulnerable populations and require meaningful community participation in environmental decision-making. International cooperation on environmental issues has intensified through multilateral agreements, technology transfer programs, and coordinated research initiatives. These collaborative approaches recognize that environmental

challenges transcend national boundaries and require coordinated global responses.The integration of economic incentives in environmental policy has expanded through carbon pricing mechanisms, payments for ecosystem services, and green financing initiatives. These market-based approaches harness economic forces to drive environmental improvements while supporting sustainable development.

Emerging Contaminants and New Challenges

The identification and characterization of emerging contaminants represents a rapidly evolving area of environmental science. Pharmaceuticals in water systems, per- and polyfluoroalkyl substances (PFAS), nanomaterials, and endocrine-disrupting chemicals are all receiving increased scientific attention and regulatory scrutiny.Pharmaceutical contamination of water systems has emerged as a significant environmental concern as advanced analytical techniques reveal widespread presence of medications in surface waters, groundwater, and even drinking water supplies. These compounds can have subtle but significant effects on aquatic ecosystems and potentially human health.PFAS contamination has been recognized as a major environmental challenge due to the persistence, bioaccumulation, and toxicity of these "forever chemicals." Recent scientific advances in PFAS detection, treatment, and disposal are driving new regulatory approaches and remediation strategies.

Nanomaterial pollution represents a new category of environmental contaminants with unique properties and potential impacts. The small size and engineered properties of nanomaterials create novel exposure pathways and biological interactions that require new assessment methods and regulatory frameworks.Endocrine-disrupting chemicals continue to pose challenges due to their subtle effects at low concentrations and complex interactions with biological systems. Recent research has revealed new sources of exposure and mechanisms of action that are informing updated risk assessment approaches.

Future Directions and Research Priorities

The future of environmental science will be shaped by continued technological advancement, increasing environmental challenges, and the need for integrated solutions that address multiple problems simultaneously. Several key areas are emerging as priority research directions for the coming years. Integrated Earth system science approaches that combine atmospheric, terrestrial, and aquatic research will become increasingly important as scientists seek to understand complex environmental interactions and feedback mechanisms. These holistic approaches require interdisciplinary collaboration and advanced modelling capabilities.

The development of nature-based solutions that harness natural processes to address environmental challenges represents a promising research direction. These solutions can provide cost-effective environmental benefits while supporting biodiversity and ecosystem services. Environmental justice and equity considerations will become increasingly integrated into environmental science research, ensuring that scientific advances contribute to fair and equitable environmental outcomes for all communities.The

circular economy concept will drive research into waste reduction, material recycling, and resource efficiency across all sectors of the economy. This systems approach requires new technologies, policies, and business models that minimize environmental impacts throughout product lifecycles.

Conclusion

Environmental science in 2024 and 2025 represents a field in rapid transformation, where traditional ecological principles intersect with cutting-edge technologies to address unprecedented environmental challenges. The integration of artificial intelligence, advanced materials science, biotechnology, and systems thinking approaches is creating new possibilities for environmental monitoring, pollution prevention, and ecosystem restoration. The challenges facing environmental science are complex and interconnected, requiring integrated solutions that address multiple problems simultaneously. Climate change, pollution, biodiversity loss, and resource depletion cannot be solved in isolation but must be addressed through comprehensive approaches that recognize the fundamental interconnectedness of environmental systems. Recent technological advances offer hope for addressing environmental challenges at the scale and speed required by current environmental crises. However, these technologies also create new challenges and ethical considerations that must be carefully managed to ensure that technological solutions truly contribute to environmental sustainability. The next generation of environmental scientists will inherit both unprecedented challenges and powerful tools for addressing them. Their success will determine whether humanity can achieve a sustainable relationship with the natural world and ensure a healthy planet for future generations. The foundations being laid today through advances in environmental science, technology, and policy will be critical for meeting this ultimate test of human ingenuity and environmental stewardship.

References

[1]. Anderson, M. K., & Chen, L. (2024).*Digital twins for ecosystem management: Applications in forest conservation and biodiversity monitoring.* Environmental Modelling & Software, 156, 105-118.

[2]. Bharti, R., Singh, P., & Kumar, A. (2023).*Machine learning approaches for air quality prediction: A comprehensive review of IoT-enabled monitoring systems.* Journal of Environmental Management, 342, 118-134.

[3]. Chen, X., Williams, J. R., & Thompson, S. E. (2024).*Artificial intelligence in climate change mitigation: From carbon footprint analysis to smart grid optimization.* Nature Climate Change, 14(3), 245-258.

[4]. Davis, E. M., & Rodriguez, C. (2023).*Remote sensing and big data analytics for deforestation monitoring in the Amazon: Challenges and opportunities.* Remote Sensing of Environment, 298, 113-127.

[5]. Foster, K. L., Park, H. J., & Miller, D. A. (2024).*Blockchain technology for environmental compliance and carbon credit verification: A systematic review.* Environmental Science & Policy, 152, 78-92.

[6]. Garcia, A., Liu, Y., & Patel, N. (2023).*Internet of Things (IoT) sensors for real-time water quality monitoring: Technological advances and field applications.* Water Research, 245, 120-135.

[7]. Hassan, M. R., & O'Brien, K. (2024).*Digital environmental governance: How smart cities are reshaping urban sustainability practices.* Cities, 143, 104-119.

[8]. Johnson, T. P., & Lee, S. (2023).*Satellite-based monitoring of plastic pollution in marine environments: Recent technological developments.* Marine Pollution Bulletin, 196, 115-128.

[9]. Kumar, S., Brown, M., & Zhang, W. (2024).*Precision agriculture and environmental sustainability: The role of drone technology and AI-driven crop monitoring.* Computers and Electronics in Agriculture, 218, 108-122.

[10]. Martinez, L. C., & Taylor, R. J. (2023).*Virtual reality applications in environmental education and conservation awareness: A meta-analysis of effectiveness.* Environmental Education Research, 29(8), 1156-1174.

[11]. Nielsen, P. K., & Yamamoto, H. (2024).*Digital carbon footprinting: Assessing the environmental impact of data centres and cloud computing infrastructure.* Journal of Cleaner Production, 432, 139-154.

[12]. Okonkwo, C. E., & Singh, R. (2023).*Edge computing for environmental monitoring: Reducing latency in real-time pollution detection systems.* Environmental Monitoring and Assessment, 195(11), 1287-1302

[13]. Peterson, A. M., & Green, L. (2024).*Quantum computing applications in climate modelling: Potential breakthroughs and current limitations.* Science of the Total Environment, 912, 169-183.

[14]. Roberts, J., & Kumar, V. (2023).*Augmented reality for environmental field research: Enhancing data collection and visualization in ecological studies.* Ecological Informatics, 78, 102-115.

[15]. Wilson, D. R., Campbell, S., & Zhou, M. (2024). *The digital divide in environmental justice: Examining inequities in access to environmental monitoring technologies.* Environmental Research Letters, 19(4), 044028.

Challenges of Biofilm Associated UTIs: A Clinical Update

Susmita Chakrabarty
School of Paramedical and Allied Sciences, DRIEMS University, Odisha, 754022, India

Abstract:

Urinary tract infections (UTIs) are still one of the most common infectious diseases worldwide, with a large percentage becoming chronic or recurrent because of biofilm formation. Biofilms are organized microbial communities embedded in a self-secreted polymeric matrix, commonly found on urinary catheters and uroepithelial surfaces. These biofilm-related infections are particularly problematic in clinical practice, such as being more resistant to antibiotics, resistant to host immunity, and refractory to eradication and diagnosis. This is a clinical update that focuses on the pathogenesis of biofilm-related UTIs, the prime microbial perpetrators (most notably Escherichia coli, Proteus mirabilis, and Klebsiella pneumoniae), and the mechanisms of persistence. It also discusses the constraints of existing antimicrobial therapies, the function of indwelling medical devices, and nascent approaches in prevention and treatment—such as Conventional Antibiotic Combination Therapies, Nanotechnology, Vaccine production, medical devices or indwelling catheter Coating formation, Surface Modification, Irrigation and Debridement to Physically Remove Biofilms. It is paramount that the variability of biofilm-related UTIs be understood in order to enhance patient outcomes and direct future therapeutic innovation.

Introduction:

The Infectious Disease Society of America (ISDA) and the European Society of Clinical Microbiology and Infectious Diseases classified UTIs as uncomplicated and complicated in 1992 to harmonize participants in clinical trials. Urinary tract infection (UTI) is among the most common infections in the outpatient and various healthcare settings. It manifests a wide clinical spectrum, from benign with little symptom to lethal conditions [1].These infections are usually classified based on clinical presentation, laboratory findings, and microbiological data. UTIs are divided into cystitis (bladder or lower urinary tract infection), pyelonephritis (kidney or upper urinary tract infection), and prostatitis (prostate inflammation) [2]. More recently, however, UTIs have been clinically divided into groups based on clinical factors and their impact on morbidity and treatment [3].Classifications involve acute uncomplicated cystitis in young women, recurrent cystitis in young women, acute uncomplicated pyelonephritis in young women, complicated urinary tract infection, catheter-associated infections, urinary tract infections in men, and asymptomatic bacteriuria [4].

Thus, UTIs have been divided into uncomplicated or complicated. While urinary tract infections (UTIs) are one of the most common forms of infection globally, the wide variety of symptoms and severity of illness may render management complicated. The definition of uncomplicated UTIs (uUTIs) is generally taken to refer to UTIs of healthy, non-pregnant women, with all others being considered as complicated. There is, however, a lack of a consensus definition of complicated UTIs (cUTIs) that has led to worldwide variations in treatment. In addition, complicated UTI patients usually have other comorbidities that need to be treated sooner. UTIs, particularly those associated with biofilm-forming pathogens, represent a growing concern in clinical microbiology

and infectious disease management.One of the biggest challenges in treating cUTIs is the growing issue of antimicrobial resistance (AMR) [4].

Relationship between Biofilm and AMR:

Antibiotics are impressive discoveries for use against microbes. Over the past many years, different types of antibiotics have been used to treat patients in hospitals and societies all over the world. Unfortunately, bacteria have developed resistance against widely used antibiotic [5]. The development of antibiotic-resistant bacteria is a significant global health threat, and among the most concerning are the ESKAPE pathogens: *Enterococcus faecium, Staphylococcus aureus, Klebsiella pneumoniae, Acinetobacter baumannii, Pseudomonas aeruginosa,* and *Enterobacter spp.* To fight infections caused by these multidrug-resistant pathogens, the World Health Organization has reserved a set of last-resort antibiotics [6].

It is assumed that more than 80% of microbial infections are associated with biofilms. Biofilms produced by bacteria are responsible for causing infections in the urinary tract and leading to recurrences and relapses. Biofilms are aggregates of microorganisms that attach to a biological or non-biological surface and are covered by a self-produced extracellular matrix [7].Biofilm cells have inherent characteristics that are different from planktonic cells. Antimicrobial resistance of biofilms has gained increasing interest. It is now generally acknowledged that biofilms associated with medical devices and tissues could mainly be responsible for the failure of antibiotic treatments and may cause many chronic infections. It is very difficult to eradicate biofilms. Several scientists are currently looking into eliminating infections that involve biofilms, with several creative measures having been engineered and accepted as effective and promising [8].In biofilm populations, bacteria exhibit an increased rate of horizontal gene transfer and exchange of resistance and virulence genes. Additionally, bacterial interactions in the biofilm allow them to synchronize the expression of virulence genes, which further enhances the infestation and increases the invasiveness of the infection. These facts highlight the need to constantly update our information and awareness of the causes, progression, and eradication measures of this growing public health problem [9].

The mode of growth of the biofilm renders it protection from many biocides and antibiotics; hence, controlling and completely eradicating biofilms is difficult. It has been indicated that microorganisms resuspended from biofilms were much more resistant compared to planktonic cells, while cells in biofilms were more resistant than those resuspended from biofilms. Biofilm cells have resistance to antibacterial agents that is at least hundreds of times more than planktonic cells, with enhancements up to 1,000-fold. Biofilms protect cells from dehydration, chemical perturbations, assaults by other bacteria, and removal by immune cells by acting as protective refuges or physical barriers [10].

Common Infection causing Pathogens

E. coli is the leading causative pathogen in uncomplicated and complicated urinary tract infection. After *E. Coli,* the usual causative organisms for uncomplicated UTI by frequency are *Klebsiella pneumoniae (K. pneumoniae), Staphylococcus saprophyticus, Enterococcus faecalis, group B Streptococcus (GBS), Proteus mirabilis, Pseudomonas aeruginosa (P. aeruginosa), Staphylococcus aureus (S. aureus), and Candida spp.* In complicated UTI, the order of frequency of causative organisms after *E. Coli* is *Enterococcus spp., K. pneumoniae, Candida spp., S. aureus, P. mirabilis, P. aeruginosa*, and GBS. Another study of hospitalized patients with cUTI found the most common occurring pathogens to be *E. coli, K. pneumoniae, P. aeruginosa, P. mirabilis, Enterococcus spp,* and *Enterobacter* in order of occurrence. One further complication,

though, is that these patients also can carry more than one causative pathogen, thus making the treatment of these infections even more complicated. [11,12].

Biofilm Formation Steps:

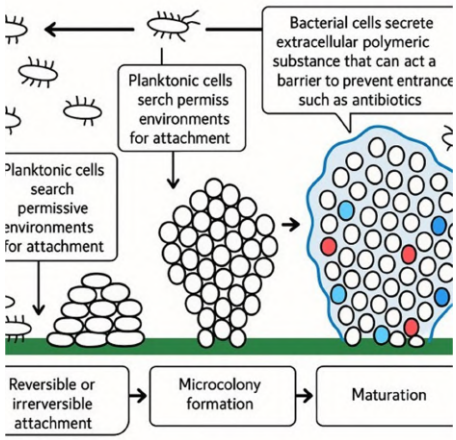

Biofilm formation [27]

Challenges Associated with Diagnosing and Treating UTIs

Challenges in making proper diagnoses of UTIs include the lack of obvious signs and symptoms, no proper diagnostic criteria that are conclusive, a high prevalence of ASB, misuse of antibiotics without proper prescription, contamination of samples, and usually inadequate justification for ordering urine cultures. Encouraging strategies include education and feedback, defining ordering culture requirements, and reflex culture policies limiting urine cultures [13].

New preventive strategies like catheter materials and coatings, vaccinations, and bacterial interference are under investigation and development. The antibiotic pipeline is poor, and novel strategies for finding new classes of antibiotics and the rational design of small molecule inhibitors are being pursued for the therapy of major recurrent UTIs [14].

Promising Therapeutic Strategies Against Microbial Biofilm Related UTI Challenges

Urinary tract infections (UTIs), particularly those caused by biofilm-producing uropathogens, have a high global health burden as a result of their chronicity, recurrence, and resistance to standard treatment. Biofilms serve as a physical and biochemical barrier that shields bacterial communities against host immunity as well as antibiotics. Biofilm-related UTIs need an integrative strategy fusing conventional as well as novel therapeutic modalities. Recent studies present a number of promising approaches, such as combination antibiotic treatments, nanotechnology-delivered drug treatment, antibiofilm drugs, vaccine targeting, catheter surface coating innovations, surface modification, and mechanical destruction through irrigation and debridement [15].

- Traditional Antibiotic Combination Treatments:Resistance to antibiotics among biofilm-forming uropathogens reduces the effectiveness of monotherapies. As a result, combination antibiotic therapies have emerged in popularity. The combinations take advantage of synergistic interactions between the drugs to promote bacterial killing in biofilms. For example, studies have shown that use of fosfomycin with fluoroquinolones or beta-lactams enhances the penetration and compromises biofilm matrix integrity in drug-resistant Escherichia coli and Klebsiella pneumoniae infections [16]. Furthermore, carbapenem-containing combinations have been specifically effective against carbapenemase-producing

organisms, frequently involved in complicated UTIs. However, judicious stewardship and susceptibility testing are essential to avoid further resistance development.

- Nanotechnology:Nanoparticles provide novel solutions to drug delivery in biofilm-coated UTIs through increased penetration and local residence. Metal nanoparticles, including silver, zinc oxide, and gold nanoparticles, possess inherent antimicrobial and antibiofilm activities. For instance, silver nanoparticles (AgNPs) interfere with microbial membranes and increase antibiotic efficacy against Pseudomonas aeruginosa and Proteus mirabilis biofilms on catheter surfaces [17]. Improved polymeric nanoparticles and liposomes enable targeted antibiotic delivery, lowering systemic toxicity and enhancing drug concentration at sites of infection. In addition, bioresponsive drug nanocarriers that release according to pH or enzymes in the biofilm environment provide precision and efficiency [17, 18].
- Antibiofilm Agents:Direct antibiofilm agents are created to disrupt biofilm formation, quorum sensing, or extracellular polymeric substance (EPS) integrity. Enzymes like DNase I, dispersin B, and proteases break down EPS, allowing for antibiotic penetration. Natural products like curcumin, quercetin, and cinnamaldehyde have shown antibiofilm activity by inhibiting microbial adhesion and communication processes. Additionally, synthetic compounds that target quorum sensing mechanisms in E. coli and K. pneumoniae inhibit biofilm maturation and improve immune clearance. Scientists are also investigating phage-derived lysins and peptides as new antibiofilm agents with high specificity and low risk of resistance [19].
- Vaccine Production:Preventive measures, especially vaccines, are promising in preventing recurrent UTIs, especially in high-risk groups like women, catheterized individuals, and the elderly. A number of vaccine candidates against uropathogenic E. coli (UPEC) adhesins, iron acquisition proteins, and outer membrane components have demonstrated preclinical efficacy. FimH adhesin, an important mediator of UPEC binding, is an overexpressed antigen in many vaccine candidates such as protein subunit and mRNA-based vaccines [20]. A multivalent vaccine regimen could be used to overcome antigenic heterogeneity of uropathogens and their biofilm-associated phenotypes.
- Medical Devices and Indwelling Catheter Coatings:Indwelling urinary catheters are a source of biofilm-based UTIs. Anti-adhesive and antimicrobial coatings are essential in preventing biofilm colonization. Silver, chlorhexidine, and nitrofurazone-based coatings have proven useful in inhibiting microbial adhesion. Some of the latest advances involve hydrophilic polymer coatings that lower friction and attachment of bacteria, as well as drug-eluting coatings that release antibiotics or antiseptics for extended durations [21]. Certain devices now utilize more than one mechanism—surface topography, chemical agents, and controlled release systems—to offer better protection against biofilms.
- Surface Modification Techniques:In addition to coatings, surface modification of urinary catheters and stents by plasma treatment, nanopatterning, and biofunctionalization provides advanced resistance to biofilm formation. Surface roughness and hydrophobicity are significant factors affecting microbial adhesion. Altering these parameters can stop initial colonization. For example, superhydrophobic or microtextured surfaces have been found to significantly decrease bacterial load in model systems [22]. Certain surfaces are made to dynamically respond to environmental stimuli, inhibiting microbial growth through pH- or temperature-induced alterations.
- Irrigation and Debridement:Physical debridement of biofilms by bladder irrigation and mechanical debridement continues to be a supportive but integral part of catheter-associated UTI (CAUTI) management. Although not therapeutic, irrigation with antimicrobial or surfactant solutions (such as povidone-iodine, acetic acid, or EDTA-based solutions) can decrease biofilm biomass and bacterial load. More recent strategies include catheter systems that allow continuous irrigation, reducing biofilm formation on device surfaces [23]. Used with systemic antibiotics or localized nanoparticle therapy, these techniques improve infection control and discourage complications like encrustation or obstruction[24].

Finally, the treatment of microbial biofilm-associated UTIs requires a multidisciplinary approach that integrates established standards with novel technologies. Traditional antibiotics need to be optimized through synergy-based combinations, and advancements in nanotechnology and antibiofilm agents increase penetration and efficacy. Prophylactic vaccines are imminent, and the design of anti-biofilm surfaces on urinary devices provides long-term protection. Physical measures such as irrigation further enhance biofilm control. Blending these strategies, informed by precision diagnostics and patient-specific considerations, is the key to successfully tackling this ongoing clinical problem [25].

Conclusion:

Microorganisms with biofilm-forming capabilities are a challenge in the health care sector. Biofilm-forming bacteria have a matrix that enables them to resists antibiotics and evade the immune system of the host. In addition to having structural barriers, biofilm-forming bacteria can undergo physiological changes, such as a lower growth rate and the production of tolerant cells. In such instances, antibiotics cannot prevent, eliminate, or eradicate these slow-growing and persistent cells found within the biofilm matrix. Consequently, chronic infection due to biofilms is usually difficult to treat successfully, in part because biofilms are resistant to antimicrobial treatments [10].

A number of various strategies are under investigation for inhibiting the formation of biofilm, and some encouraging results have been found. Nevertheless, a perfect strategy has yet to be created. Future studies must strive to determine effective mechanisms for biofilm growth inhibition and to create antimicrobial drugs that are effective against bacteria in biofilms [26].

References:

1. Marantidis J, Sussman RD. Unmet needs in complicated urinary tract infections: challenges, recommendations, and emerging treatment pathways. Infection and drug resistance. 2023 Dec 31:1391-405.
2. Grabe M, Bjerklund-Johansen TE, Botto H, Çek M, Naber KG, Tenke P, Wagenlehner F. Guidelines on urological infections. European association of urology. 2015 Mar;182:237-57.
3. Stamm WE, Hooton TM. Management of urinary tract infections in adults. New England journal of medicine. 1993 Oct 28;329(18):1328-34.
4. Soto SM. Importance of biofilms in urinary tract infections: new therapeutic approaches. Advances in biology. 2014;2014(1):543974.
5. MKK F, Rashid SS, MHM N, Baharudin R, Ramli AN. A clinical update on Antibiotic Resistance Gram-negative bacteria in Malaysia-a review. arXiv preprint arXiv:1903.03486. 2019 Feb 13.
6. Bereanu AS, Bereanu R, Mohor C, Vintilă BI, Codru IR, Olteanu C, Sava M. Prevalence of Infections and Antimicrobial Resistance of ESKAPE Group Bacteria Isolated from Patients Admitted to the Intensive Care Unit of a County Emergency Hospital in Romania. Antibiotics (Basel). 2024 Apr 27;13(5):400. doi: 10.3390/antibiotics13050400. PMID: 38786129; PMCID: PMC11117271.
7. Chakrabarty S, Mishra MP, Bhattacharyay D. Targeting microbial bio-film: an update on MDR gram-negative bio-film producers causing catheter-associated urinary tract infections. Applied Biochemistry and Biotechnology. 2022 Jun;194(6):2796-830.
8. Zhang K, Li X, Yu C, Wang Y. Promising therapeutic strategies against microbial biofilm challenges. Frontiers in Cellular and Infection Microbiology. 2020 Jul 28;10:359.

9. Lila ASA, Rajab AAH, Abdallah MH, Rizvi SMD, Moin A, Khafagy ES, Tabrez S, Hegazy WAH. Biofilm Lifestyle in Recurrent Urinary Tract Infections. Life (Basel). 2023 Jan 4;13(1):148. doi: 10.3390/life13010148. PMID: 36676100; PMCID: PMC9865985.
10. Abebe GM. The Role of Bacterial Biofilm in Antibiotic Resistance and Food Contamination. Int J Microbiol. 2020 Aug 25;2020:1705814. doi: 10.1155/2020/1705814. PMID: 32908520; PMCID: PMC7468660.
11. Zilberberg MD, Nathanson BH, Sulham K, Fan W, Shorr AF. Development and validation of a bedside instrument to predict carbapenem resistance among gram-negative pathogens in complicated urinary tract infections. Infection Control & Hospital Epidemiology. 2018 Sep;39(9):1112-4.
12. Flores-Mireles AL, Walker JN, Caparon M, Hultgren SJ. Urinary tract infections: epidemiology, mechanisms of infection and treatment options. Nature reviews microbiology. 2015 May;13(5):269-84.
13. Claeys KC, Blanco N, Morgan DJ, Leekha S, Sullivan KV. Advances and challenges in the diagnosis and treatment of urinary tract infections: the need for diagnostic stewardship. Current infectious disease reports. 2019 Apr;21:1-9.
14. Werneburg GT. Catheter-associated urinary tract infections: current challenges and future prospects. Research and reports in urology. 2022 Apr 4:109-33.
15. Klein RD, Hultgren SJ. Urinary tract infections: microbial pathogenesis, host-pathogen interactions and new treatment strategies. Nat Rev Microbiol. 2020 Apr;18(4):211-226. doi: 10.1038/s41579-020-0324-0. Epub 2020 Feb 18. PMID: 32071440; PMCID: PMC7942789.
16. Bari AK, Belalekar TS, Poojary A, Rohra S. Combination drug strategies for biofilm eradication using synthetic and natural agents in KAPE pathogens. Front Cell Infect Microbiol. 2023 Apr 17;13:1155699. doi: 10.3389/fcimb.2023.1155699. PMID: 37139491; PMCID: PMC10149696.
17. Mohanta YK, Chakrabartty I, Mishra AK, Chopra H, Mahanta S, Avula SK, Patowary K, Ahmed R, Mishra B, Mohanta TK, Saravanan M, Sharma N. Nanotechnology in combating biofilm: A smart and promising therapeutic strategy. Front Microbiol. 2023 Mar 3;13:1028086. doi: 10.3389/fmicb.2022.1028086. PMID: 36938129; PMCID: PMC10020670.
18. Sánchez SV, Navarro N, Catalán-Figueroa J, Morales JO. Nanoparticles as Potential Novel Therapies for Urinary Tract Infections. Front Cell Infect Microbiol. 2021 Apr 19;11:656496. doi: 10.3389/fcimb.2021.656496. PMID: 33954121; PMCID: PMC8089393.
19. Asma ST, Imre K, Morar A, Herman V, Acaroz U, Mukhtar H, Arslan-Acaroz D, Shah SRA, Gerlach R. An Overview of Biofilm Formation-Combating Strategies and Mechanisms of Action of Antibiofilm Agents. Life (Basel). 2022 Jul 23;12(8):1110. doi: 10.3390/life12081110. PMID: 35892912; PMCID: PMC9394423.
20. O'Brien VP, Hannan TJ, Nielsen HV, Hultgren SJ. Drug and Vaccine Development for the Treatment and Prevention of Urinary Tract Infections. MicrobiolSpectr. 2016 Feb;4(1):10.1128/microbiolspec.UTI-0013-2012. doi: 10.1128/microbiolspec.UTI-0013-2012. PMID: 26999391; PMCID: PMC4887100.
21. Kanti SPY, Csóka I, Jójárt-Laczkovich O, Adalbert L. Recent Advances in Antimicrobial Coatings and Material Modification Strategies for Preventing Urinary Catheter-Associated Complications. Biomedicines. 2022 Oct 14;10(10):2580. doi: 10.3390/biomedicines10102580. PMID: 36289841; PMCID: PMC9599887.
22. Taheran L, Zarrini G, Khorram S, Zakerhamidi MS. Plasma surface modification as a new approach to protect urinary catheter against *Escherichia coli* biofilm formation. Iran J Microbiol. 2016 Aug;8(4):257-262. PMID: 28210465; PMCID: PMC5296940.

23. Trautner BW, Darouiche RO. Role of biofilm in catheter-associated urinary tract infection. Am J Infect Control. 2004 May;32(3):177-83. doi: 10.1016/j.ajic.2003.08.005. PMID: 15153930; PMCID: PMC2963581.
24. González-Alonso M, Guerra-González A, Villar-Suárez V, Fernández-Castilla B, Sánchez-Lázaro JA. Efficacy of Different Irrigation Solutions on Bacterial Biofilm in Periprosthetic Joint Infections: A Systematic Review and Network Meta-Analysis. Life. 2025 Apr 1;15(4):568.
25. Mancuso G, Trinchera M, Midiri A, Zummo S, Vitale G, Biondo C. Novel Antimicrobial Approaches to Combat Bacterial Biofilms Associated with Urinary Tract Infections. Antibiotics (Basel). 2024 Feb 4;13(2):154. doi: 10.3390/antibiotics13020154. PMID: 38391540; PMCID: PMC10886225.
26. Tenke P, Köves B, Nagy K, Hultgren SJ, Mendling W, Wullt B, Grabe M, Wagenlehner FM, Cek M, Pickard R, Botto H. Update on biofilm infections in the urinary tract. World journal of urology. 2012 Feb;30:51-7.
27. Rather MA, Gupta K, Mandal M. Microbial biofilm: formation, architecture, antibiotic resistance, and control strategies. Braz J Microbiol. 2021 Dec;52(4):1701-1718. doi: 10.1007/s42770-021-00624-x. Epub 2021 Sep 23. PMID: 34558029; PMCID: PMC8578483.

Role of Stearic Acid toward the Gelation of Cocoa Butter and Wheat Germ Oil-Based Oleogels: Preparation, Physical Properties, and Application in Topical Mupirocin Delivery

Sindhu I Sanakal, Anubhab Das, Lavanya Jujjuri, Abirami R, Dwaipayan Pal, Raja Shunmugam,* Debmalya Banerjee, Biswaranjan Mohanty,* Kunal Pal,* and Samarendra Maji*

ABSTRACT: Oleogel (OG) is one of the popular sources of unsaturated fatty acids that replace hazardous saturated fatty acids, synthesized by structuring edible oils using gelators. In our present investigation, we prepared OGs by varying the ratios of cocoa butter (CB), wheat germ oil (WGO), and a fixed amount of stearic acid (SA) for topical drug delivery application. The critical gelation concen- tration of CB in WGO was found to be 3% (w/w) in the presence of 7.75% (w/w) SA. Various characterization techniques were employed for the developed OGs, including bright-field and polarized light microscopy, crystallization kinetics, X-ray diffraction (XRD), and rheology. Micrographs captured by using polarized light and bright- field microscopes illustrated the crystalline structure of the OGs. OGs displayed a network of needle-shaped arrangements due to the presence of SA and CB. XRD results demonstrated the formation of a β' polymorph structure inside the OG and rheological data proves that the OG formulation with 20% (w/w) CB (OG 20) forms the strongest OG among all formulations. Moreover, the crystallization kinetics was studied to observe the development of solid fat crystals in OGs. The in vitro release of mupirocin from the OGs was best described by the Korsmeyer–Peppas and Peppas–Sahlin models, indicating that drug diffusion occurred via Fickian mechanism. Additionally, OGs were investigated and explored for potential topical drug delivery applications through ex vivo permeation studies.

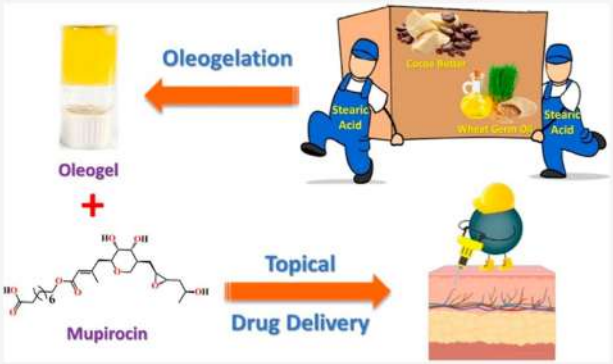

1. INTRODUCTION

Oleogels (OGs) are semisolid arrangements of edible oils such as wheat germ oil (WGO), sunflower oil, olive oil, flaxseed oil, sesame oil, grape seed oil, algal oil, soybean oil, salmon oil, and palm oil.[1] In the gel-based network, a solid component (lower in concentration) is used for gelation of the liquid oil (higher in concentration). The solid component is called a gelator.[2] They tend to arrest the movement of edible oil components, forming OGs.[3] Although the ratio of the solid fraction is lower than the liquid fraction, the formulation indicates a solid-like characteristic. A permanent macrostructure is formed because of the ability of OGs to exhibit a homogeneous microstructural organization.[2] The process of providing solid properties to oils with the assistance of an oleogelator is defined as oleogelation or oil structuring. Critical gelation concentration (CGC) is the least concentration of gelator molecules required to entrap the oil into forming the three-dimensional (3D) network through van der Waals forces, hydrogen bonding, ionic interactions, and $\pi-\pi$ stacking between the gelator and oil molecules. Instantly, there exist two distinct sets of structurants/gelators, viz., low-molecular weight oleogelators and high-molecular weight oleogelators, which are mostly used to form organized OG systems.[4] Frequently handled gelators are high-melting triacylglycerides (TAGs), hydrophilic and hydrophobic proteins, fatty acids, fatty alcohols, diglycerides or monoglycerides, ethyl cellulose or native phytosterols, and edible waxes.[5] The lipophilic nature of OGs promotes the penetration of drug molecules into biological tissues.[6] OGs offer cost-effectiveness, biocompatibility, shielding against microbial contamination, and longer stability than traditional drug delivery systems.[7] Currently, OGs have become a progressive method for nasal,[8] parenteral,[9] ocular,[10] topical,[11] and periodontal[6] drug delivery applications.

WGO is a byproduct of the wheat-milling process. Also, it has a significant medicinal component that has anti-inflammatory and antioxidant properties. WGO functions as

Received: August 5, 2024
Revised: September 25, 2024
Accepted: September 25, 2024

a reservoir of polyunsaturated fatty acids such as omega-6 (44–65%) and omega-3 (4–11%) fatty acids. In addition, WGO also contains the maximum amount of α tocopherol (vitamin E) in comparison with additional edible oils.[12] Due to the aforementioned properties, WGO is highly advantageous for healthiness. It decreases plasma and liver cholesterol in animals, delays aging impacts, and significantly enhances physical persistence.[13]

Cocoa butter (CB) is a key component in chocolates and is characterized based on three main triacylglycerols: glycerol-1,3-dipalmitate-2-oleate (POP; P palmitic, O oleic; 13.6–15.5%), glycerol-1-palmitate-2-oleate-3-stearate (POSt; St stearic; 33.7–40.5%), and glycerol-1,3-distearate-2-oleate (StOSt, 23.8–31.2%) corresponding to three major fatty acids, namely, palmitic (C16:0, 24.4%), stearic (C18:0, 33.6%), and oleic acids (C18:1, 37.0%).[14] CB obtained from the beans of the cocoa tree (Theobroma cocoa) is a natural fat.[15] It mostly consists of a mixture of TAGs,[16] which differ with the source of the plant, the period of bean accumulation, the kind of the tree, and how it is handled during the extraction process.[17] CB has diverse crystallization properties and is an important product in many confectionery items, including chocolate fillings. This is the very primary reason why CB is utilized in various industries like pharmaceuticals (as topical and suppository bases), food (in chocolate formulations), and cosmetics (as moisturizers, lipsticks, perfumes, soaps, etc.).[18]

Along with the base oil (WGO) and gelator (CB), stearic acid (SA) was employed as an activator molecule. SA is a long-chain fatty acid that can be represented as octadecanoic acid [($CH_3(CH_2)_{16}COOH$)] or as 18:0, as it is constituted of 18 carbons and no double bonds (Figure S1).[19] This activator molecule is inherently nontoxic and biocompatible.[20] SA and its derivatives have been studied for medicinal, cosmetic, and food applications.[21] It also has various health benefits when applied to the skin and consumed orally. The properties of CB-based OGs have been improved using an activator.[22,23]

Topical semisolid products make up a significant class of drug delivery systems. Due to the impenetrable nature of the skin, dermal drugs are not easy to apply. The presence of a microbial infection is a critical concern for burn wounds. Mupirocin (MUP), a topical antibiotic agent, is used to treat primary and secondary skin infections.[24] MUP is produced by the bacterium *Pseudomonas fluorescens*. It is highly active against Gram-positive bacteria such as *Staphylococcus aureus*. MUP formulations are available as an ointment and a cream. 2% MUP ointment with polyethylene glycol must be applied three times daily, directed to deprived patient acquiescence. The controlled release of a topical distribution of MUP increases its effectiveness and reduces the frequency of usage to once daily.[25,26] Gel is a semisolid dosage form made up of a 3D framework of natural or synthetic polymers filled with an immobilized liquid. The network structure, biocompatibility, and molecular stability of the bioactive agents within the gels make them an appropriate carrier. These formulations have greater stability and better application qualities than creams and ointments. They can ensure sustained release of the bioactive agents with improved patient compliance in contrast to ointments and creams.[27,28] Bujubarah et al. have synthesized nanoemulgels using nanoemulsions by incorporating a gel base for topical drug delivery application of MUP.[29] Similarly, Alhasso et al. have reported the synthesis of nanoemulgels by incorporating an optimized MUP-loaded nanoemulsion into an appropriate gel.[30] This article has focused on an alternate approach of topical MUP delivery via OGs that can solve some of the issues associated with the controlled topical release of MUP.

In this study, we employed WGO as the basic oil phase and CB as the gelator with the accompaniment of SA as an activator to prepare OGs, which have been explored as topical delivery systems to deliver MUP. Additionally, none has investigated the method of producing OG from WGO, CB, and SA until now. We have emphasized obtaining the least concentration of the gelator molecule essential to trigger gelation, i.e., CGC, with the help of SA as an activator. The samples prepared ranged from 3% to 40% (w/w) CB in concentration after determining the CGC. Different characterization techniques, viz., X-ray diffraction (XRD), Fourier transform infrared (FTIR) spectroscopy, and bright-field and polarized light microscopy, were used to investigate the molecular interactions and microstructure. The properties and stability of synthesized OGs were examined by colorimetry, crystallization kinetics, mechanical and thermal analyses. Along with that, topical MUP delivery was investigated using an eggshell membrane as the biological tissue. The release phenomena were analyzed with the help of Korsmeyer–Peppas (KP) and Peppas–Sahlin (PS) drug release kinetic models. These models are commonly used to describe and analyze drug release kinetics. Additionally, the observation of Fickian diffusion-mediated drug delivery suggests that these results of OGs could be a promising approach in case of potential application for the topical delivery of MUP.

2. EXPERIMENTAL SECTION

2.1. Materials. CB (melting point 40 °C) was purchased from Minimal Confection, Gujarat, India. WGO was obtained from AOS Products Private Limited, Ghaziabad, India. SA, extrapure, 99% was bought from SRL Private Limited in Mumbai, India. MUP was received from Bills Biotech Private Limited as a gift sample.

2.2. Preparation of OGs. A sequence of different types of OGs was prepared in clean vials made of glass to determine the CGC of SA by varying the amount of SA with fixed CB. Initially, the concentration of CB 3% (w/w) was kept constant and SA was altered at five different concentrations, viz., 5.75, 6.75, 7.75, 9.75, and 11.75% (w/w). Later, these samples were heated to 70 °C in a water bath to dissolve CB and SA within the WGO. A magnetic stirrer was used to homogenize the melted solutions for 10 min at the temperature mentioned above. Later, these homogeneous mixtures were kept for cooling at room temperature (~28 °C) for 24 h to promote the crystallization of gelator molecules. By approving CGC based on SA, a series of OGs were prepared in glass vials using the same procedure where the concentration of SA (7.75% w/w) was kept constant, and CB concentration was varied, viz., 1, 2, 3, 5, and 7% (w/w). Finally, after the CGC concerning SA (7.75% (w/w)) and CB (3% (w/w)), the impact of gelator molecules on the features of OGs was evaluated. A series of OGs was synthesized with fixed SA concentration (7.75% (w/w)) and varying CB content between 3, 7, 15, 20, 25, 30, 35, and 40% (w/w). These OGs were prepared by following a similar method. The samples were named OG 3, OG 7, OG 15, OG 20, OG 25, OG 30, OG 35, and OG 40, respectively (Table 1).

2.3. Characterizations of OGs. *2.3.1. Colorimetric Study.* The colorimetric studies of developed OGs were carried out using an in-house colorimeter device. This design consisted of a Picam color camera and a light-emitting diode for illumination. In the beginning, the device was calibrated with standard black and white placards. The gel was incubated at 25 °C. Later, L^*, a^*, and b^* values were verified by analyzing the photograph which represents colors. The photographs of the samples were then examined to identify colors

Table 1. Composition of WGO, CB, and SA in OGs

sample name	amount of CB (g)	amount of SA (g)	amount of WGO (g)
OG 3	0.15	0.3875	4.4625
OG 7	0.35	0.3875	4.2625
OG 15	0.75	0.3875	3.8625
OG 20	1.00	0.3875	3.6125
OG 25	1.25	0.3875	3.3625
OG 30	1.50	0.3875	3.1125
OG 35	1.75	0.3875	2.8625
OG 40	2.00	0.3875	2.6125

comprising L^* (lightness), a^* ("positive" redness and "negative" greenness), and b^* ("positive" yellowness and "negative" blueness), among others. The values, as mentioned earlier, of the color parameters were used to calculate the whiteness index (WI) (eq 1), the yellowness index (YI) (eq 2), and the complete color variation (ΔE) (eq 3). A standard white calibration plate was used as the control test with the subsequent parameters: L_p^* = 97.83, a_p^* = −0.45, and b_p^* = 1.88. The x tag was swapped for the mathematical standards for a particular OG sample. The equations formed by using all of those parameters are given below.

$$WI = 100 - \sqrt{(100 - L^*)^2 + (a^*)^2 + (b^*)^2} \quad (1)$$

$$YI = \frac{142.86 b^*}{L^*} \quad (2)$$

$$\Delta E = \sqrt{(L_p^* - L_x^*)^2 + (a_p^* - a_x^*)^2 + (b_p^* - b_x^*)^2} \quad (3)$$

2.3.2. Crystallization Study. The gelation kinetics experiment was operated by using a colorimeter (CL223 Colorimeter, Elico Ltd., Hyderabad, India). The OG was warmed to 70 °C and placed in the testing container of the colorimeter. The optical density (OD) and the temperature were documented during the cooling process at 25 °C. The time and OD readings were noted simultaneously. Subsequently, a graph of OD versus time and OD versus temperature was generated.

2.3.3. Microscopic Study. A bright-field microscope (model: DM750; Leica Microsystems, Germany) was used for the optical microscopy examination of the prepared OGs. The LEICA SAPO Stereo zoom optical microscope was utilized for further analyses of OGs. The analysis was carried out using a metallurgical microscope (AmScope, ME580TA, Irvine, CA, USA). After the solid sample was loaded on a 35 mm glass Petri plate, the upper layer was examined under a microscope.

2.3.4. FTIR Spectroscopy. FTIR (Model: Alpha-e; Bruker, Germany) was utilized to examine the bands of the OG samples in attenuated total reflection mode in the wavenumber range of 4000–500 cm^{-1} with 25 scans at a spectral resolution of 4 cm^{-1}.

2.3.5. X-ray Diffraction. Wide-angle X-ray diffractograms were obtained using a diffractometer Bruker's "DAVINCI design", the D8 ADVANCE system. A copper target was utilized as the generator of the X-rays (Cu K radiation, which has a wavelength of 1.5406 Å). Scanning was measured in the range of 5–80° 2θ with a scanning rate of 5° 2θ/min at a temperature of 35 °C.

Bragg's law (eq 4) was employed to determine the d spacing of the XRD parameter, whereas the Debye–Scherrer equation (eq 5) was used to calculate the crystallite size (D).

$$2d\sin\theta = n\lambda \quad (4)$$

$$D = \frac{\lambda k}{\beta \cdot \cos\theta} \quad (5)$$

where λ refers to the wavelength of the X-ray (1.5406 Å), θ refers to the diffraction angle, and n indicates an integer. Eqs 6 and 7 are utilized for calculating lattice strain (ε) and dislocation density (δ) (lines/m^2), where the full width at half-maximum (fwhm) at a scattering angle of 2θ is represented by the radian β and k corresponds to the Scherrer constant.

$$\varepsilon = \frac{\beta}{4 \cdot \tan\theta} \quad (6)$$

$$\delta = \frac{1}{D^2} \quad (7)$$

2.3.6. Study of Oil-Binding Capacity. The foremost aim of the oil-released study was to ascertain the oil-binding capacity (OBC) of OGs. Initially, a 2.0 mL blank Eppendorf tube (weight "a") was measured, and 1.0 mL of the molten OG was poured into the Eppendorf tube. Then, the sample was kept at room temperature to convert into an OG, and the weight of the Eppendorf tube (weight "b") was taken again. The samples were then placed at 4 °C for 24 h, followed by a 15 min centrifugation at 10,000 rpm using a Remi C-24 BL chilled centrifuge. Then, the Eppendorf was inverted, and the spare oil was extracted from the upper layer of OGs using tissue paper. Thereafter, the weight of the Eppendorf tube was taken (weight "c"). The below-mentioned eqs 8 and 9 were utilized to calculate the OBC and the % of oil released.

$$\%\ \text{oil released} = \frac{(b - a) - (c - a)}{(b - a)} \quad (8)$$

$$OBC = 100 - \%\ \text{oil released} \quad (9)$$

2.3.7. Rheology. We conducted rheological studies using an Anton Paar MCR 92 rheometer. The samples were tested using a cone and plate probe with a diameter of 25 mm. We monitored the strain sweep by altering the strain at a constant frequency of 1.5 Hz while maintaining a temperature of 25 °C. Gel samples were analyzed for storage and loss modulus by varying the strain from 0.001 to 100%.

2.3.8. Drug Release Study. Drug release from formulations (basket-type) was assessed using dissolution equipment (DS-8000, Lab India). A dialysis membrane tube (HiMedia, with a molecular weight cutoff of 12000–14000 Da) was filled with 1.0 g of OGs. The diffusion process was conducted in 200 mL of PBS (phosphate buffer solution, pH 6.8) at 37 °C for 3 h. The OG-loaded dialysis bags were inserted into the basket, which was then rotated at 100 rpm. 5 mL of the aliquot was removed at each interval and refilled with PBS. MUP concentration was measured at 221 nm using a UV–visible spectrometer (UV-1900i, Shimadzu, Japan).

$$F = K \times t^n \quad (10)$$

here, F indicates the fraction of solute released, K refers to the released rate constant, t indicates the time, and n is the diffusion exponent.

$$\frac{Mt}{M_\infty} = k_d t^m + k_r t^{2m} \quad (11)$$

here, M_t/M_∞ is the fraction of the drug incorporated in the solution, k_d and k_r are the diffusion and kinetic relaxation constants, and m is the slope.

2.3.9. Ex Vivo Permeation Studies. The permeation properties of MUP from OGs were evaluated by using a chicken eggshell membrane. The membrane was prepared by immersing a whole egg in vinegar for 24 h, draining the contents, and washing the membrane with double distilled water. After cleaning, the membrane was stored overnight in PBS. For the permeation study, a modified Franz's diffusion cell (permeation area: 0.64 cm^2) was employed. The eggshell membrane was positioned between the receptor and the donor compartments. 1.0 g of OG was placed in the donor compartment directly in contact with the egg membrane. The compartments were securely clamped. The receptor compartment was filled with 12 mL of freshly prepared phosphate buffer solution (PBS, pH 6.8). The opening of the donor compartment was sealed with a coverslip, and the receptor compartment was maintained at 37 °C with constant stirring using a Teflon-coated magnetic stir bead. The permeation study was conducted over 180 min, with samples

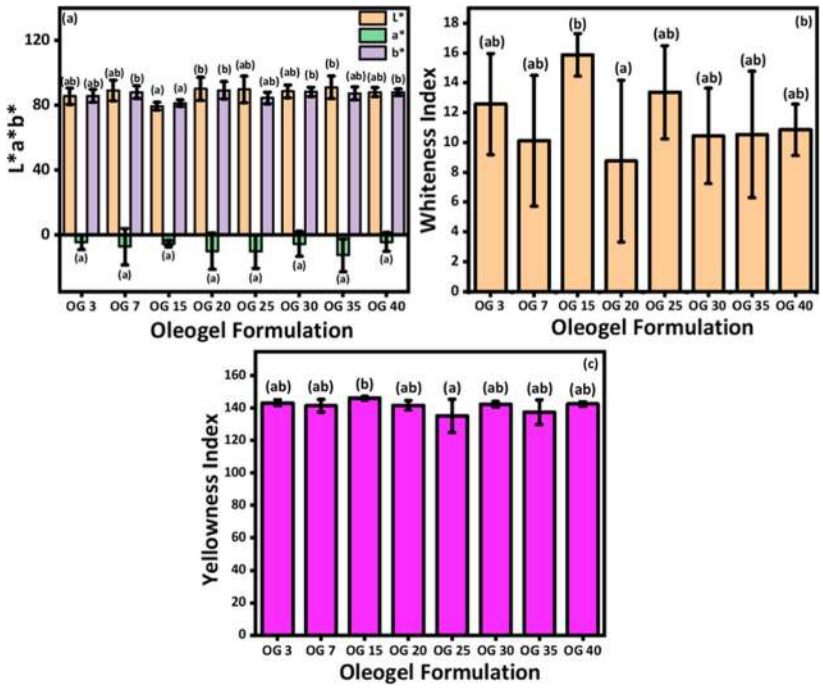

Figure 1. Colorimetric analysis of different OGs: (a) L^*, a^*, and b^*; (b) WI; (c) YI.

withdrawn from the receptor compartment at 5, 15, 30, 45, 60, 90, 120, and 180 min. Each withdrawn sample was immediately replaced with an equal volume of PBS. The samples were analyzed to determine the MUP content using a spectrophotometer at 221 nm. The results were expressed as the cumulative percentage drug permeation (CPDP).

2.3.10. Statistical Analysis. The experiments were conducted at least in triplicates, and the data were depicted as mean ± standard deviation. Statistical analysis was performed by using one-way analysis of variance, followed by the posthoc Tukey test, with the help of IBM SPSS Statistics 20 (Inc. Chicago, USA). The significance level of the data sets was set to be $p < 0.05$.

3. RESULTS AND DISCUSSION

3.1. Preparation of OGs. Initially, we tried to prepare the control according to Table S1 with only WGO and CB, CW 5 (w/w) –CW 55 (w/w), but there was no formation of OGs as shown in Figure S2. Later, a series of CB, SA, and WGO-based OG formulations were prepared to identify the CGC. The lowest gelator concentration at which OGs are formed is regarded as CGC.[31] Initially, we optimized the condition of OGs by varying SA and WGO where CB (3% w/w) concentration was kept constant (Table S2) and is shown in Figure S3. Later, we investigated the CGC of CB in WGO where the SA amount was kept constant according to Table S3 and is depicted in Figure S4. The OG formulation formed at the CGC was then used to prepare OGs. After confirming the CGC, a series of OGs were designed by changing the concentration of CB in WGO from OG 3 (w/w) to OG 40 (w/w), where the SA amount was kept constant (7.75% w/w). The composition of the added CB to WGO is given in Table 1. We added CB and SA to WGO (Figure S5a), where CB and SA were insoluble and settled down. This was then heated to 70 °C in a water bath with continuous stirring by using a magnetic stirrer. This resulted in a homogenized light yellow-colored clear solution (Figure S5b). Then, the samples were allowed to cool at room temperature. Initially, as the temperature was lowered, a cloudy mixture was formed, and as time progressed, the viscosity of the mixture increased, and it finally turned to semisolid stable OGs (Figure S5c). This process is called oleogelation. The formation of a cloudy mixture confirms the nucleation of CB. Inverting the vial helped to verify the formation of stable OGs (Figure S5d). It was observed that the inversion of the tube did not induce the downward flow movement of the formulations up to OG 35. This indicates that the WGO was immobilized entirely within the fat network of CB and therefore formed a gelled structure. In contrast, OG 40 remained in the liquid form without gelation due to the higher loading of CB.

3.2. Colorimetric Analysis. Colorimetry is a technique that offers information on the color characteristics of a test sample, such as lightness, saturation, hue, and so on.[32] Moreover, color study gives information about visual appearance of food samples, which helps to predict the smell and taste. Color characterization was done based on the Commission internationale de l'éclairage (CIE) system, which segregates the color based on luminance and two-color parameters (Figure 1).[33] The color parameter was assessed by using a CIE lab standard scale that measures the psychometric index of lightness (L^*) ranging from 0 (black) to 100 (white). The two-color parameters are a^* and b^*, where a^* ranges from green (negative) to red (positive) and b^* ranges from blue (negative) to yellow (positive). The L^* average values for all OGs were in the range of 79–91 (Table S4). Having greater L* values in formulations is beneficial since it helps enhance color perception.[34] The L^* value for OG 3 was around 85.66 ± 5.07. As the amount of CB increased in OG 7 (89.20 ± 6.42), OG 20 (90.16 ± 7.18), and OG 35 (91.10 ± 7.023), there is a gradual increase in the corresponding L^* value except OG 15 (79.51 ± 2.3). A significant reduction in the L^* value is due to the formation of larger crystals or crystal aggregation on the surface of OG 15.[35] The size of the crystals formed was confirmed by the XRD result, which is reported later. A similar L^* value was demonstrated in the case of OG 25 (89.8 ± 8.28), OG 30

https://doi.org/10.1021/acs.cgd.4c01095

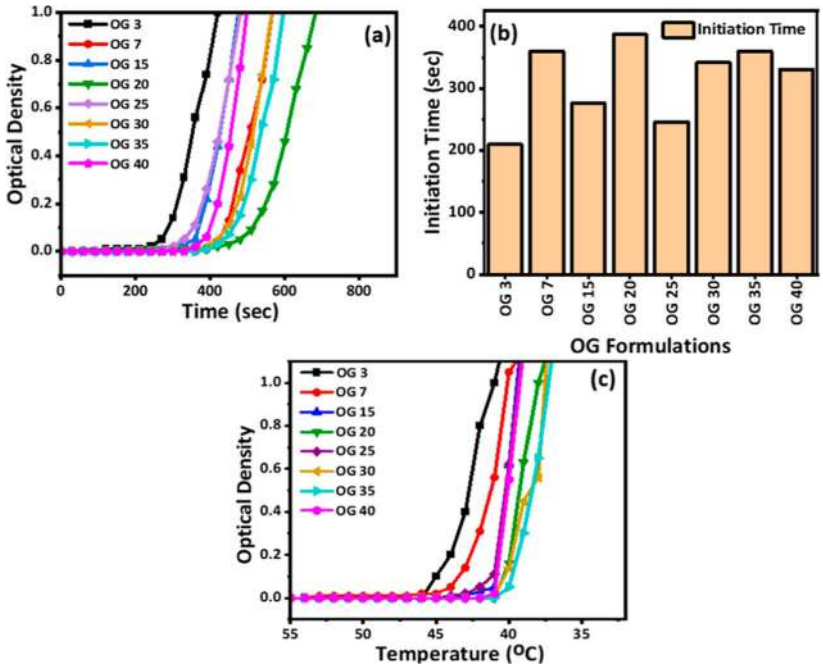

Figure 2. Crystallization kinetics profile of the OGs: (a) OD vs time, (b) initiation time vs OG formulations, and (c) OD vs temperature.

(88.61 ± 3.95), and OG 40 (88.20 ± 2.90). The L^* value of OG 3 was similar to that of OG7, OG 25, OG 30, and OG 40 ($p > 0.05$) while that of OG 15 was statistically significant compared to OG 20 and OG 35 ($p < 0.05$). The L^* value of OG 35 was the highest and insignificant ($p > 0.05$) with all other combinations except OG 15.

All the OGs exhibited negative a^* values, which refer to the green tones of prepared OGs (Table S4). The a^* value of OG 3 is −4.64 ± 4.58. As the concentration of CB increases, the a^* value also increases except OG 15, OG 30, and OG 40. At the highest content of the CB (for OG 40), the lowest value of a^* (4.401 ± 5.86) was observed. The a^* value of OG 3 was similarly valued with all the compositions ($p > 0.05$). Further, the positive value of b^* specifies the yellowness of the OG formulations. A significant variation in the b^* value was seen when the composition was altered by increasing the CB amount. Initially, the b^* value of OG 3 was demonstrated as 85.87 ± 4.02. The b^* value keeps increasing with the increase of CB content in OGs except OG 15 (81.35 ± 2.05) and OG 25 (84.54 ± 3.62). The b^* values in case of OG 3, OG 25, and OG 35 are insignificant ($p > 0.05$) but those of OG 15 when compared with OG 7, OG 20, OG 30, and OG 40 are statistically different ($p < 0.05$), while OG 20 exhibited the highest b^* value (89.34 ± 5.33) and was similar ($p > 0.05$) to every formulation without OG 15.

The white index (WI) and yellow index (YI) of the OG samples were calculated by using eqs 1 and 2, respectively, with L^*, a^*, and b^*. WI was measured to check the degree of perfect whiteness which refers to the amount of visible light a given sample reflects.[36] WI can be correlated to the quality and consumers' acceptance of food products.[37] The WI values of prepared OGs are in the range of 8−16 (Table S4), which indicates the relative lightness of the samples. First, sample OG 3 exhibited a WI value of 12.57 ± 3.39 and with further addition of CB does not alter the WI value much except for OG 15 (Table S4). The result demonstrated that most of the sample does not lose substantial whiteness after increasing the CB amount. The OG 15 showed the highest WI (15.88 ± 1.43) among all other OGs and was similar to every combination without OG 20 ($p > 0.05$). To assess the level of yellowness present in our samples, we calculated the YI. An increase or decrease in the YI value emphasizes the white-to-yellow gradient.[38] The YI values for the OG samples were between 135 and 146 (Table S4). The YI value of OG 3 is 143.31 ± 1.80. However, incorporating more CB reduces the YI value except for OG 15 (146.18 ± 0.98) and the values of OG 3 were similar to OG 7, OG 25, OG 30, OG 35, and OG 40 ($p > 0.05$). The highest YI value was observed in the case of OG 15 and the value was significant compared to OG 25 ($p < 0.05$). The high YI values suggested that the OGs were predominantly yellowish. At last, the absolute color difference (ΔE) was calculated by using eq 3 regarding a particular standard. Every OG sample demonstrated an ΔE value above 3, which indicates that the color difference could be observed with the naked eye (Table S4).

3.3. Crystallization Kinetics. Crystallization is the process of crystal formation from a molten state and is first-order kinetics.[39] Generally, it contains three steps: nucleation, crystal growth, and maturation.[33,40] The crystallization is mainly based on the nucleation process, which is the initial stage in forming crystals. A rapid rate of crystallization results in the formation of a diffuse crystalline phase associated with low-energy polymorphs. However, the growing crystals are arranged into a consistent 3D lattice under a slow crystallization rate.[41] The nature of the crystallization process in the prepared OGs can be determined by monitoring it as a function of time and temperature, with respect to OD. The process was started by taking melted OGs at room temperature. The OD versus time plots (Figure 2a) revealed that initially with the increase in time, the OD value remained the same, although after a certain time, a steep increase in OD was observed which indicated the crystal formation. The curve was used to calculate the period needed by the OG compositions for observable crystal growth to occur. OG with the lowest CB concentration (OG 3) starts the gelation at 210 s after keeping the prepared formulation at room temperature. The period of crystallization increased with

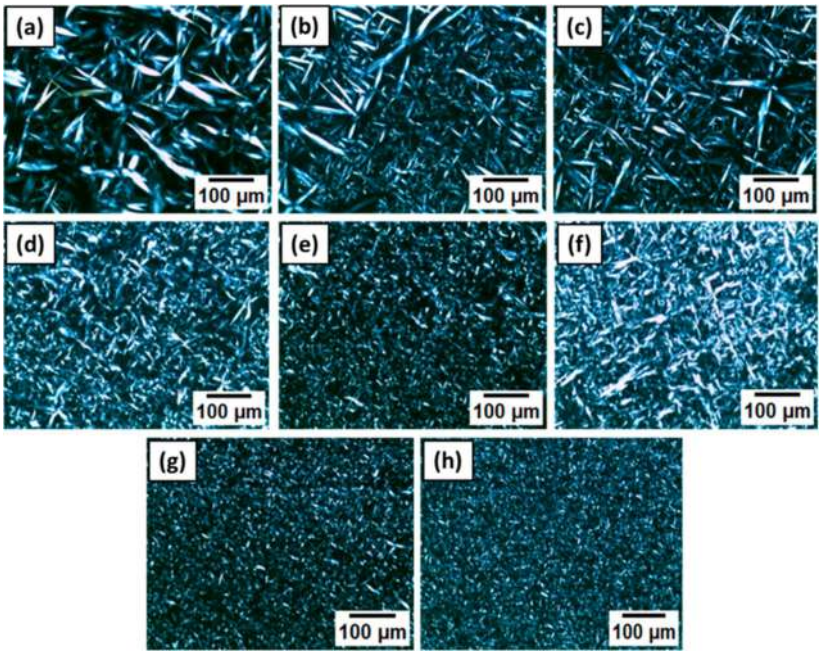

Figure 3. Polarized light microscopy of the prepared OGs: (a) OG 3, (b) OG 7, (c) OG 15, (d) OG 20, (e) OG 25, (f) OG 30, (g) OG 35, and (h) OG 40.

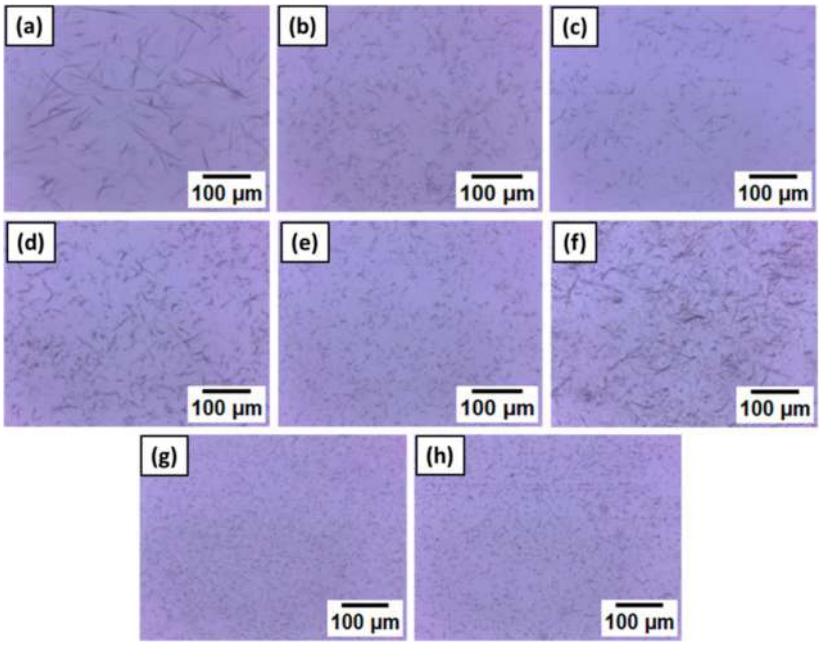

Figure 4. Bright-field micrograph of synthesized OGs: (a) OG 3, (b) OG 7, (c) OG 15, (d) OG 20, (e) OG 25, (f) OG 30, (g) OG 35, and (h) OG 40.

an increment in the CB of OG formulations. CB concentration was found to be a factor in the formulations during the initiation of crystallization. After the increase in the amount of SA in OG, gelation time was enhanced, and the order of time required to start gelation was OG 20 > OG 35 ≈ OG 7 > OG 30 > OG 40 > OG 15 > OG 25 > OG 3 (Figure 2b). The higher gelation time of OG 20, OG 35, and OG 30 might be attributed to the formation of larger crystals which was proven by XRD data.[38] The activator's amount, composition, and mechanism of action could affect the nucleation or/and growth. The addition of SA shortened the onset time in all of the formulations. The use of SA may have accelerated the early crystallization phase through heterogeneous nucleation with CB molecules.[42] This would eventually affect the crystallization kinetics and polymorphic transition in the formulated OGs.[43] On the other hand, the OD versus temperature graph is another important factor in examining the crystalline nature of the various OG compositions (Figure 2c). In the OD vs temperature plot, a decrease in OD was observed with the increase in temperature, which is a sign that solid fat crystals are developing with the reduction of temperature.[44] The crystal formation for OG 3 began at 46 °C, which was the maximum temperature. The order of the temperature required for forming the crystals was OG3 > OG 7 > OG 25 > OG 15 >

OG 20 ≈ OG 30 ≈ OG 35 ≈ OG 40. This order demonstrated that the OG 3 sample possessed the highest degree of crystallization among the others as crystals started to grow at higher temperatures and exhibited the change of OD. Further increase of the CB amount within OGs reduced the crystallization temperature. OG 20 to OG 40 samples exhibited lower crystallization temperature at 41 °C due to a less crystalline nature.

3.4. Microscopic Analysis. Optical microscopy was employed to assess the fat network and crystal morphology in OGs generated with CB, WGO, and SA.[45] The samples were observed with bright-field and polarized light microscopes and a Stereo zoom microscope to analyze the internal structure of the OGs. The physical properties of OGs can be determined by monitoring their polymorphism and morphology. CB-based OGs entrap the oil phase by forming crystals. The polarized light microscopic images can be used to observe micro-structural changes (Figure 3).[46] The properties of OGs differ based on crystal size, habit, and crystal–crystal interactions. Crystallite size is frequently associated with significant functional characteristics, including the OG texture.[47] OGs displayed a network of needle-shaped arrangements due to the presence of SA and CB. However, the Maltese cross, a sign of a lamellar structure, was visible in OGs.[48] The CB and SA were dissolved in WGO; both gelators were assembled into an independent structure. They retained their crystalline shape in the OG, indicating independent self-organization.[49] There is a possibility of the existence β' crystals similar to fats assumed due to the needle-like arrangement of OGs.[50] The large surface area of this needle/fiber-type morphology allowed for extensive interaction between the oil and microstructures.[51] In OG 3, there was a long needle-like shape. However, there is a reduction in the particle size of OGs upon increasing the CB content. The results suggest that the CB may be acting as a nucleation point, which may help to alter the growth of the fat crystals. These increased nucleation points helped in the uniform crystallization of solid fats and can explain the formation of increasingly smaller fat crystals.

A similar type of result was exhibited by observing a bright-field microscope image (Figure 4). The OG 3 sample demonstrated a fibrous system of SA by molecular self-assembly due to noncovalent interactions.[52,53] With the increase of the CB in the next sample, OG 7, the fibrous network is broken into smaller parts. Further increase of CB in OG reduces the crystalline size. However, the density of the crystals increases gradually. From Figure S6, we can see breakage of the crystal structure with the increase of CB amount, which we have also observed earlier. Due to the overconcentration of CB, OG 35 and OG 40 showed the development of tiny crystals. The Stereo zoom images of CB and WGO (Figure S7) exhibited the formation of no crystals.

3.5. FTIR Analysis. The FTIR characterization was conducted to demonstrate the existence of functional groups in the samples.[54] We examined the FTIR data of prepared OGs in the current investigation. Figure S8a represents the FTIR spectra of WGO, CB, and SA. The FTIR spectrum of WGO exhibits peaks at 2926 and 2846 cm^{-1} because of the asymmetrical and symmetrical stretching vibration of methylene (–CH_2) groups. The strong absorption band of the ester carbonyl functional group (-C□O) was observed around 1741 cm^{-1}.[13] A spectral peak at 1450 cm^{-1} demonstrated the C–H bending vibration.[3] The stretching vibration of –C–O ether groups appeared at 1158 cm^{-1}.[55] Furthermore, a new vibration representing the methylene group was detected at 710 cm^{-1}. The FTIR spectrum of CB shows the absorption of a dual peak at 2914 and 2846 cm^{-1} because of asymmetrical and symmetrical stretching of the –CH_2 groups, respectively.[56] The strong peak at 1735 cm^{-1} relates to the stretching vibrations of the carbonyl groups (C□O) of triglyceride esters.[18] The spectral band at 1473 cm^{-1} represents the bending vibration of –CH_2 and –CH_3 aliphatic groups. The small peak at 1385 cm^{-1} is due to the symmetrical bending vibration of –CH_3. The peaks at 1251 and 1168 cm^{-1} indicate the stretching of the –CO groups of the esters. Lastly, the peaks at 711 cm^{-1} correspond to the oscillation of the –CH_2 groups and olefins. The FTIR spectrum of SA exhibits its characteristic bands at 1700 and 930 cm^{-1} which are assigned to the stretching vibration of the carboxylic group and bending vibrations of hydrogen bonds containing carboxylic acid, respectively.[57] The FTIR spectra of all OGs (Figure S8b) demonstrated the distinctive peaks of the individual WGO, CB, and SA. The absorption bands found in OG 3–OG 40 at 2923 cm^{-1}, 2850 cm^{-1}, 1742 cm^{-1}, 1455 cm^{-1}, 1156 cm^{-1}, and 718 cm^{-1} are in good agreement with the aforementioned functional groups.

3.6. XRD Study. XRD is often used to investigate polymorphism and crystallite size in fat arrangements. The XRD spectra of the OGs are depicted in Figure 5. The peak intensity decreased as the immobilization of CB increased. The diffractogram displayed a broadband near 20.5° because of the amorphous region and the diffraction spectra of the OG were deconvoluted using a nonlinear peak fitting method by OriginPro 2024b software. The XRD data was deconvoluted

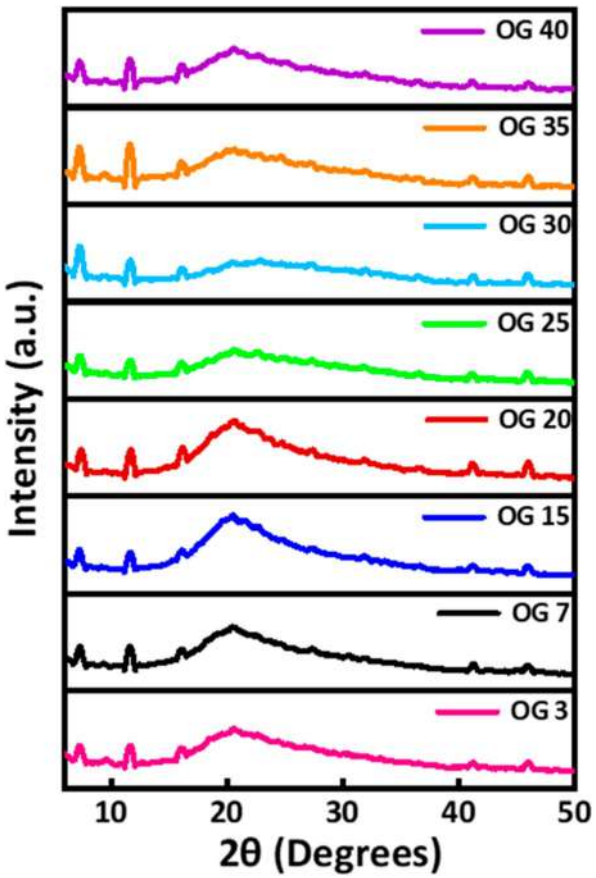

Figure 5. XRD patterns of the prepared OGs.

with the Gaussian function, and the parameters like crystallite size, peak position, full width at half-maximum (fwhm), lattice strain, and dislocation density are analyzed and listed in Table S5.

The addition of CB within the OGs decreased the intensity and crystalline size except for OG 15 and OG 20. The alterations in the fwhm of the diffraction peaks may be associated with the crystalline quality of the OGs. The lowest average fwhm of OG 15 indicates a more crystalline nature of the formulations compared to the remaining OGs. Bragg's equation (eq 4) was used to compute the interplanar spacing (d spacing) within the lattice structure of the developed OGs.[58] The parameter d spacing offers statistics about lattice firmness.[59] The average d-spacing data of OG 3 was 0.4267 nm. As the amount of CB amplified, there was a gradual increase in the d-spacing data, except for that of OG 20. Among all the OGs, OG 20 showed the lowest average d-spacing value (0.4233 nm), possibly because of the formation of a compacted lattice structure of the crystalline fields.[60] The addition of SA may have changed the firmness of the CB fat crystals' assembly by influencing the CB's crystallization. The triglycerides present in the fat are aligned in crystalline forms known as polymorphs.[61] According to the American Oil Chemists' Society (AOCS), a sample's polymorphic form is α if it has a peak at 0.42 nm, β' if it has peaks at 0.38 and 0.42 nm, and β if it has a peak at 0.46 nm.[62] All OGs had d-spacing values around 0.47, 0.43, and 0.39 nm, indicating the presence of two crystal polymorphs: metastable β' form and the most stable β form. The XRD spectra of CB (Figure S9) exhibited sharp peaks at 11.6, 13.04, and 17.1°. Other peaks were demonstrated at 21.32, 23.14, and 24.54°, respectively. The d-spacing standards were measured as 0.76, 0.68, 0.52, 0.42, 0.38, and 0.36 nm. The d-spacing data at 0.42 and 0.38 demonstrated the formation of β' polymorph.

Next, the crystalline size was measured using the Debye–Scherrer equation (eq 5), Table S5. We surveyed that there is a decrease in average crystalline size, except OG 15 and OG 20. The average size of the crystallites was greatest in OG 15, showing the presence of exceptionally compact and crystalline CB crystals. Interestingly, this observation does not follow the order of microscopic images, where OG 3 showed the highest crystalline size and demonstrated a lack of a compact network structure. Additionally, the average lattice strain of the fat crystallite domains was assessed (eq 6, Table S5). According to Risan et al., nanoparticles can influence nucleation and particle assembly. This can be a reason for the change in the anisotropy and lattice strain of crystals.[59] The insertion of CB decreased the lattice strain of OGs except OG 25 (0.063) and OG 40 (0.0627), which might be due to the irregularities in its crystal lattice.[63] The higher the lattice strain measurement, the lower the crystallinity of these OGs. The lattice strain is inversely connected to crystal perfection. Hence, less average lattice strain values in the situations of OG 15 and OG 20 (0.047) indicated that the fat crystal network was highly ordered.[64] Dislocation density (δ) refers to the number of dislocation lines per unit volume in a crystal and is calculated by using eq 7. Dislocation sites have higher free energy and are relatively unstable. The dislocation density was observed to be less for more stable OG 7 and OG 15.

3.7. Oil-Binding Capacity. The OBC of OGs is one of the most important physical characteristics. OBC measures the capacity of OGs by computing their capacity to grip liquid oil within the 3D network formed by gelator molecules. This study shows that all OGs showed a decent OBC, more than 99%, with tougher mechanical strength (Figure 6). With the alteration of component ratio in the OG, the amounts of oil loss can vary drastically. This could indicate that a particular proportion of fatty acids in the WGO is linked to low OBC. With the exception of OG 35 and OG 40, all the OGs showed about 100% OBC, indicating that each OG has a 3D network structure that holds the WGO. The OBC of OGs could be connected with the mechanical strength of OGs, based on the amount of oil lost.[65] It has been discovered that emulsions with superior mechanical strength are likely to produce OGs with stronger gel strength and better OBC. With the addition of CB, there is a decrease in the OBC of other formulations, but there is no significant difference in OG 7, OG 20, OG 25, and OG 30 ($p > 0.05$). OG 3 and OG 15 which have higher OBC are significantly different valued with OG 40 ($p < 0.05$). However, the OBC value of OG 35 is significantly different from OG 40 ($p < 0.05$).

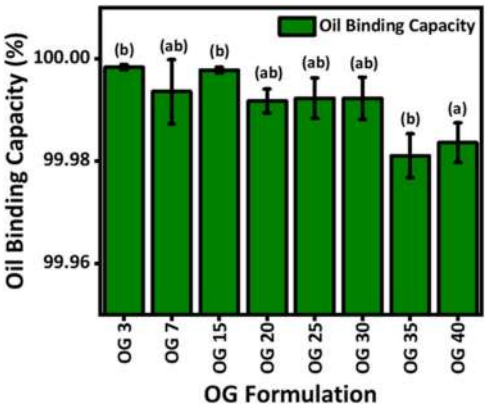

Figure 6. OBC plot of synthesized OGs.

3.8. Rheological Data. Rheological experiments were carried out to describe deformation phenomena in the nondestructive range. This range refers to the linear viscoelastic region and is defined as the region with an upper value of storage modulus (G') in comparison with loss modulus (G''). The plot (Figure 7) demonstrated an upper value of G' than G'', which indicates the gel/semisolid

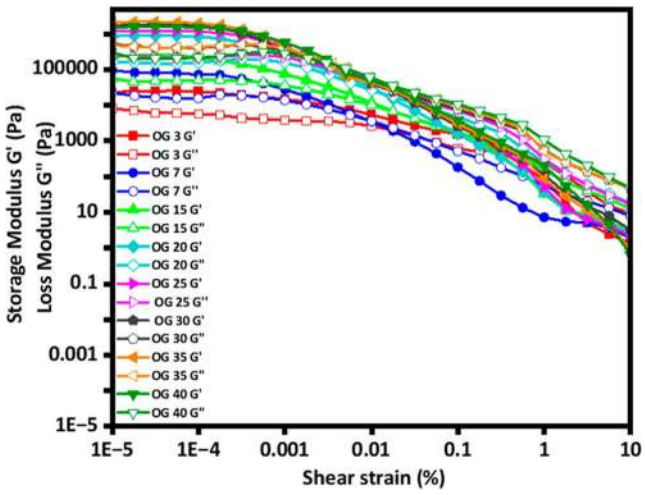

Figure 7. Rheological data of the OGs.

behavior of the OGs. However, higher G' values correspond to a stronger 3D network produced through aggregation. The breakpoint of the OG at a particular strain corresponds to the critical strain value (γ_c).[35] The OGs prepared in the present work showed a mainly elastic nature in the range of 0.00001–0.1% strain. After that, they began to flow similarly to liquid materials.

The sample OG 3 displayed the lowest rate of G', which indicates the feeblest among all OG formulations (Figure 7). The G' value is enhanced with the increase in the amount of CB in the OGs, which is associated with a stronger 3D network formed by aggregation. A sudden increase in the G' value was observed in the case of OG 20, which represents the strongest OG in comparison to other OGs. A specific amount of CB promotes a higher level of structural organization, resulting in supramolecular contacts and self-assembly of colloidal structures, as shown in OG 20. OG 35 showed the highest storage modulus (G') value among all of the OG formulations. With the further increase of CB in OG 40, CB crystal aggregates, and the result was reflected by reduction of G'.

3.9. Drug Release Studies. The drug release study of MUP (0.5%w/w)-loaded OGs was done up to 180 min. The cumulative percentage drug release (CPDR) value demonstrated the drug release potential of the OGs. It was observed that OG 7 showed the highest CPDR (18.17 ± 0.63%) for 180 min among all OG formulations. The increment in CB concentration reduced the CPDR. However, OG 30 showed a higher CPDR in comparison to OG 3 and OG 15. This could be due to denser crystal growth than OG 3 and OG 15. Although from the microscope data, OG 3 shows the largest crystal size, they demonstrated a lack of network structure that could provide the strength to hold the drug on its 3D structure. From the XRD result, OG 15 exhibits the highest crystal size, but it shows the lowest CPDR value due to the trapping of the drug into it, whereas OG 7 shows an appropriate combination of crystal size and network structure which made a strong network structure among all the OG formulations and is reflected by its highest CPDR value. The CPDR was used to fit with KP and PS mathematical models to understand the drug release mechanism from the OGs. The parameters of both KP and PS models were determined using eq 10 and eq 11, respectively.[66] The results of the kinetic parameters are shown in Figure 8 and Table 2. The release constant (K) represents the diffusion of the drug molecules through the OG samples. The K value was the highest in OG 7. The diffusion exponent (n) explains the mechanism of drug release. If the "n" value is ≤ 0.45, the release is primarily facilitated by Fickian diffusion. If the "n" value is in the range of 0.5 and 0.89, then it is non-Fickian transport. If the "n" value is ≥ 0.89, then the polymer swelling-mediated diffusion process occurs.[1] The observed value of "n" for all OG formulations is less than 0.45, except for OG 35. Thus, Fickian diffusion-mediated drug release was identified in all of the OG formulations except for OG 35. Therefore, for OG 35, the diffusion occurs through non-Fickian diffusion ($n > 0.45$).[66] Considering the PS model in mind, the drug release process was further validated. Following the model parameters, diffusion, because of both k_r and k_d, played a vital role in the drug release procedure. The nonzero k_r value explained the drug delivery via non-Fickian diffusion.[67]

3.10. Ex Vivo Permeation Studies. The penetration profile of the drug molecules through the egg membrane is illustrated in Figure 9. OG 7, which exhibited the highest CPDR, was selected for the permeability study. After 180 min,

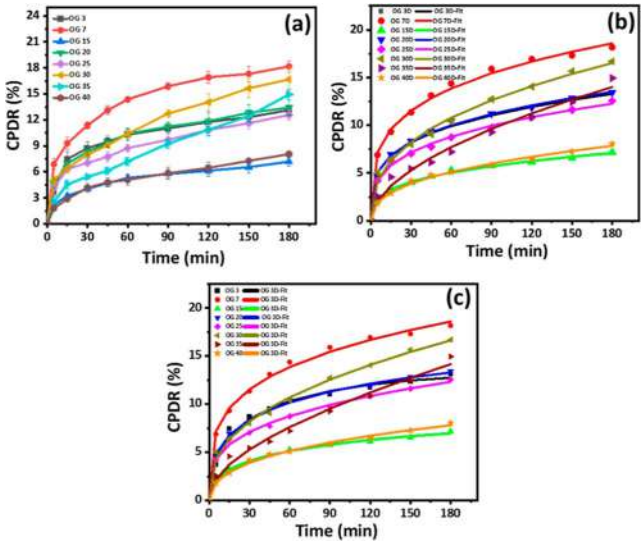

Figure 8. Diffusion profile of OG, (a) CPDR, (b) KP model, and (c) PS model.

the ex vivo egg shell membrane CPDP of MUP was found to be 3.008 ± 0.045% per cm^2. The mechanism of drug permeation was analyzed by fitting the CPDP data to the KP and PS mathematical models, with the permeation parameters summarized in Table 3. The diffusion exponent (n) value from the KP model was less than 0.45, indicating that drug permeation follows the Fickian process. An R^2 value greater than 0.98 demonstrated an excellent fit for both the KP and PS models. Additionally, the PS model parameters clarified the permeation mechanism, confirming that drug permeation occurs through diffusion rather than fat-network relaxation.[18]

4. CONCLUSIONS

In this work, we prepared OGs from CB, SA, and WGO for MUP topical drug delivery. Many formulations with varied concentrations of CB were produced. Initially, we found the CGC of OGs by varying the concentration of CB and SA. OG 3% (w/w) was found to be the CGC of the OG formulations. Afterward, OBC, color analysis, rheological study, and thermal analysis were used to examine the OG's different physical characteristics. FTIR spectroscopy and bright-field, polarized light, and Stereo zoom microscopy were used to investigate the molecular interactions and microstructure. Colorimetric data suggested that the OGs were predominantly yellowish in appearance. Microscopic studies reveal that OGs displayed a network of needle-shaped arrangements due to the presence of SA and CB. The crystallization kinetics data showed that as the concentration of CB increases, a longer time is required for the CB to reach saturation crystallization. The FTIR spectra of the OGs revealed distinctive SA and WGO vibrational signatures. XRD research revealed that varying CB concentrations affected the firmness of OG fat crystals, resulting in the development of β and β' polymorphs. Except for OG 35, drug release through the semipermeable membrane from all OG formulations followed the Fickian diffusion process, and OG 7 demonstrated the highest CPDR (18.17 ± 0.63%) for 180 min among all OG formulations. Similarly, drug permeation through the eggshell membrane also followed the Fickian process. The drug release and permeation mechanism was attributed to diffusion rather than fat-network relaxation. Therefore, MUP-loaded OG formulations could be suitable for topical applications.

Table 2. Model Parameters Obtained from the KP and PS Models

formulation	KP			PS			
	k	n	R^2	k_r	k_d	m	R^2
OG 3	3.315 ± 0.501	0.269 ± 0.022	0.979 ± 0.011	2.562 ± 0.473	−0.127 ± 0.045	0.419 ± 0.038	0.988 ± 0.006
OG 7	4.701 ± 0.703	0.266 ± 0.038	0.995 ± 0.003	4.027 ± 0.856	−0.205 ± 0.077	0.375 ± 0.055	0.998 ± 0.001
OG 15	1.442 ± 0.256	0.309 ± 0.054	0.992 ± 0.005	1.194 ± 0.338	0.078 ± 0.204	0.366 ± 0.163	0.995 ± 0.005
OG 20	3.267 ± 0.308	0.274 ± 0.022	0.996 ± 0.002	2.944 ± 0.479	−0.129 ± 0.021	0.356 ± 0.046	0.998 ± 0.001
OG 25	2.251 ± 0.396	0.301 ± 0.007	0.995 ± 0.003	2.310 ± 0.171	0.442 ± 0.025	0.229 ± 0.005	0.995 ± 0.003
OG 30	2.251 ± 0.396	0.385 ± 0.050	0.993 ± 0.004	2.119 ± 0.277	0.402 ± 0.090	0.229 ± 0.005	0.995 ± 0.003
OG 35	0.845 ± 0.127	0.542 ± 0.028	0.982 ± 0.005	0.960 ± 0.118	0.097 ± 0.019	0.404 ± 0.020	0.986 ± 0.004
OG 40	1.036 ± 0.231	0.393 ± 0.030	0.965 ± 0.016	0.950 ± 0.105	0.023 ± 0.073	0.401 ± 0.073	0.993 ± 0.003

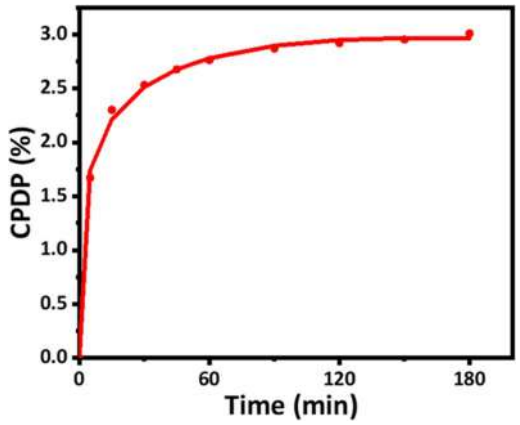

Figure 9. Ex vivo egg shell membrane permeation profile of the MUP (OG 7).

Table 3. CPDR of OG 7 from an In Vitro Analysis Fitted to Different Mathematical Models

	KP			PS			
Parameters	k	n	R^2	k_r	K_d	m	R^2
	1.53	0.14	0.99	1.32	−0.15	0.30	0.99

■ ASSOCIATED CONTENT

* Supporting Information

The Supporting Information is available free of charge at https://pubs.acs.org/doi/10.1021/acs.cgd.4c01095.

Schematic representation of OG formulations, colorimetric data, microscope images, and FTIR and XRD data (PDF)

■ AUTHOR INFORMATION

Corresponding Authors

Raja Shunmugam − *Polymer Research Centre, Department of Chemical Sciences, Indian Institute of Science Education and Research−Kolkata, Kolkata, West Bengal 741246, India;* orcid.org/0000-0002-0221-127X; Email: polyraja@gmail.com

Biswaranjan Mohanty − *School of Pharmacy, DRiEMS University, Odisha 754022, India*; Email: biswaranjanm5@gmail.com

Kunal Pal − *Department of Biotechnology and Medical Engineering, National Institute of Technology Rourkela, Rourkela, Odisha 769008, India;* orcid.org/0000-0002-4618-8809; Email: kpal.nitrkl@gmail.com

Samarendra Maji − *Department of Chemistry, Faculty of Engineering and Technology, SRM Institute of Science and Technology (SRMIST), Kattankulathur, Tamil Nadu 603203, India;* orcid.org/0000-0002-9153-2031; Email: samarenr@srmist.edu.in

Authors

Sindhu I Sanakal − *Department of Chemistry, Faculty of Engineering and Technology, SRM Institute of Science and Technology (SRMIST), Kattankulathur, Tamil Nadu 603203, India*

Anubhab Das − *Department of Chemistry, Faculty of Engineering and Technology, SRM Institute of Science and Technology (SRMIST), Kattankulathur, Tamil Nadu 603203, India*

Lavanya Jujjuri − *Department of Chemistry, Faculty of Engineering and Technology, SRM Institute of Science and Technology (SRMIST), Kattankulathur, Tamil Nadu 603203, India*

Abirami R − *Department of Chemistry, Faculty of Engineering and Technology, SRM Institute of Science and Technology (SRMIST), Kattankulathur, Tamil Nadu 603203, India*

Dwaipayan Pal − *Polymer Research Centre, Department of Chemical Sciences, Indian Institute of Science Education and Research−Kolkata, Kolkata, West Bengal 741246, India*

Debmalya Banerjee − *Department of Biotechnology and Medical Engineering, National Institute of Technology Rourkela, Rourkela, Odisha 769008, India*

Complete contact information is available at: https://pubs.acs.org/10.1021/acs.cgd.4c01095

Author Contributions

The manuscript was written through the contributions of all authors. All authors have approved the final version of the manuscript.

Funding

Science and Engineering Research Board (SERB), India, core research grant (CRG/2021/004203).

Notes

The authors declare no competing financial interest.

■ ACKNOWLEDGMENTS

S.S. thanks the Science and Engineering Research Board (SERB), India, for providing fellowship to support the Ph.D. program. S.M. acknowledges SRMIST for providing SRMIST seed grant and SERB, India, for a core research grant (CRG/2021/004203). We thank Dr. Titash Mondal and Prama Adhya from the Indian Institute of Technology, Kharagpur, West Bengal, India, for conducting the Rheology of the OG samples.

https://doi.org/10.1021/acs.cgd.4c01095

REFERENCES

(1) Qureshi, D.; Nadikoppula, A.; Mohanty, B.; Anis, A.; Cerqueira, M.; Varshney, M.; Pal, K. Effect of Carboxylated Carbon Nanotubes on Physicochemical and Drug Release Properties of Oleogels. *Colloids Surfaces A Physicochem. Eng. Asp.* 2021, *610*, 125695.

(2) Mohanty, B.; Pal, K.; Quereshi, D.; Nayak, S. K.; Rathnam, V. S. S.; Banerjee, I.; Anis, A.; Barik, C. S.; Sarkar, P.; Rout, S. K. Oleogels Based on Palmitic Acid and Saffiower Oil: Novel Formulations for Ocular Drug Delivery of Voriconazole. *Eur. J. Lipid Sci. Technol.* 2020, *122* (4)..

(3) Babu, A.; Sivakumar, G.; Das, A.; Bharti, D.; Qureshi, D.; Habibullah, S.; Satheesan, A.; Mohanty, B.; Pal, K.; Maji, S. Preparation and Characterization of Novel Oleogels Using Jasmine Floral Wax and Wheat Germ Oil for Oral Delivery of Curcumin. *ACS Omega* 2022, *7* (34), 30125.

(4) Davidovich-Pinhas, M. Oil Structuring Using Polysaccharides. *Curr. Opin. Food Sci.* 2019, *27*, 29–35.

(5) Pehlivano; lu, H.; Demirci, M.; Toker, O. S.; Konar, N.; Karasu, S.; Sagdic, O. Oleogels, a Promising Structured Oil for Decreasing Saturated Fatty Acid Concentrations: Production and Food-Based Applications. *Crit. Rev. Food Sci. Nutr.* 2018, *58* (8), 1330–1341.

(6) Hamed, R.; AbuRezeq, A.; Tarawneh, O. Development of Hydrogels, Oleogels, and Bigels as Local Drug Delivery Systems for Periodontitis. *Drug Dev. Ind. Pharm.* 2018, *44* (9), 1488.

(7) Macoon, R.; Robey, M.; Chauhan, A. In Vitro Release of Hydrophobic Drugs by Oleogel Rods with Biocompatible Gelators. *Eur. J. Pharm. Sci.* 2020, *152*, 105413.

(8) Fréchou, M.; Zhang, S.; Liere, P.; Delespierre, B.; Soyed, N.; Pianos, A.; Schumacher, M.; Mattern, C.; Guennoun, R. Intranasal Delivery of Progesterone after Transient Ischemic Stroke Decreases Mortality and Provides Neuroprotection. *Neuropharmacology* 2015, *97*, 394–403.

(9) Wang, D.; Zhao, J.; Liu, X.; Sun, F.; Zhou, Y.; Teng, L.; Li, Y. Parenteral Thermo-Sensitive Organogel for Schizophrenia Therapy, in Vitro and in Vivo Evaluation. *Eur. J. Pharm. Sci.* 2014, *60*, 40–48.

(10) Macoon, R.; Guerriero, T.; Chauhan, A. Extended Release of Dexamethasone from Oleogel Based Rods. *J. Colloid Interface Sci.* 2019, *555*, 331–341.

(11) Ash, D.; Majee, S. B.; Biswas, G. R. Oleogels of Olive Oil And Soybean Oil For Topical Drug Delivery: A Comparative Analysis. *Int. J. Pharm. Pharm. Sci.* 2019, 4–10.

(12) Ghafoor, K.; Özcan, M. M.; AL-Juhaımı, F.; Babıker, E. E.; Sarker, Z. I.; Ahmed, I. A. M.; Ahmed, M. A. Nutritional Composition, Extraction, and Utilization of Wheat Germ Oil: A Review. *Eur. J. Lipid Sci. Technol.* 2017, *119*(7)..

(13) Niu, L.-Y.; Jiang, S.-T.; Pan, L.-J.; Pang, M. Characterization of Wheat Germ Oil in Terms of Volatile Compounds, Lipid Composition, Thermal Behavior, and Structure. *Int. J. Food Prop.* 2013, *16* (8), 1740.

(14) Biswas, N.; Cheow, Y. L.; Tan, C. P.; Siow, L. F. Physicochemical Properties of Enzymatically Produced Palm-Oil-Based Cocoa Butter Substitute (CBS) With Cocoa Butter Mixture. *Eur. J. Lipid Sci. Technol.* 2018, *120* (3)..

(15) Kongor, J. E.; Hinneh, M.; de Walle, D. Van; Afoakwa, E. O.; Boeckx, P.; Dewettinck, K. Factors Influencing Quality Variation in Cocoa (Theobroma Cacao) Bean Flavour Profile — A Review. *Food Res. Int.* 2016, *82*, 44.

(16) Oracz, J.; Zyzelewicz, D.; Nebesny, E. The Content of Polyphenolic Compounds in Cocoa Beans (Theobroma Cacao L.), Depending on Variety, Growing Region, and Processing Operations: A Review. *Crit. Rev. Food Sci. Nutr.* 2015, *55* (9), 1176–1192.

(17) Buscato, M. H. M.; Grimaldi, R.; Kieckbusch, T. G. Cocoa Butter Symmetrical Monounsaturated Triacylglycerols: Separation by Solvent Fractionation and Application as Crystallization Modifier. *J. Food Sci. Technol.* 2017, *54* (10), 3260–3267.

(18) Qureshi, D.; Choudhary, B.; Mohanty, B.; Sarkar, P.; Anis, A.; Cerqueira, M. A.; Banerjee, I.; Maji, S.; Pal, K. Graphene Oxide Increases Corneal Permeation of Ciprofloxacin Hydrochloride from Oleogels: A Study with Cocoa Butter-Based Oleogels. *Gels* 2020, *6* (4), 43.

(19) Ye, S.; Noda, H.; Morita, S.; Uosaki, K.; Osawa, M. Surface Molecular Structures of Langmuir-Blodgett Films of Stearic Acid on Solid Substrates Studied by Sum Frequency Generation Spectroscopy. *Langmuir* 2003, *19* (6), 2238–2242.

(20) Ng, W. F.; Wong, M. H.; Cheng, F. T. Stearic Acid Coating on Magnesium for Enhancing Corrosion Resistance in Hanks' Solution. *Surf. Coat. Technol.* 2010, *204* (11), 1823–1830.

(21) Jiang, Z.; Lu, X.; Geng, S.; Ma, H.; Liu, B. Structuring of Sunflower Oil by Stearic Acid Derivatives: Experimental and Molecular Modelling Studies. *Food Chem.* 2020, *324*, 126801.

(22) Bharti, D.; Kim, D.; Cerqueira, M. A.; Mohanty, B.; Habibullah, S.; Banerjee, I.; Pal, K. Effect of Biodegradable Hydrophilic and Hydrophobic Emulsifiers on the Oleogels Containing Sunflower Wax and Sunflower Oil. *Gels* 2021, *7* (3), 133.

(23) Pérez-Martínez, J.; Sánchez-Becerril, M.; Marangoni, A. G.; Toro-Vazquez, J. F.; Ornelas-Paz, J. J.; Ibarra-Junquera, V. Structuration, Elastic Properties Scaling, and Mechanical Reversibility of Candelilla Wax Oleogels with and without Emulsifiers. *Food Res. Int.* 2019, *122*, 471–478.

(24) Pappa, K. A. The Clinical Development of Mupirocin. *J. Am. Acad. Dermatol.* 1990, *22* (5), 873–879.

(25) Amrutiya, N.; Bajaj, A.; Madan, M. Development of Microsponges for Topical Delivery of Mupirocin. *AAPS PharmSciTech* 2009, *10* (2), 402–409.

(26) Goldmann, O.; Cern, A.; Müsken, M.; Rohde, M.; Weiss, W.; Barenholz, Y.; Medina, E. Liposomal Mupirocin Holds Promise for Systemic Treatment of Invasive Staphylococcus Aureus Infections. *J. Controlled Release* 2019, *316*, 292–301.

(27) Singh, A. P.; Kumar Gaur, P.; Kumar Sharma, S.; Gupta, D. K. Formulation and Characterization of Mupirocin Gel and Evaluation of in Vitro Antimicrobial Activity Against Staphylococcus Aureus. *Eur. J. Mol. Clin. Med.* 2021, *7* (11), 7491–7501.

(28) Verma, A.; Singh, S.; Kaur, R.; Jain, U. K. Topical Gels as Drug Delivery Systems: A Review. *Int. J. Pharm. Sci. Rev. Res.* 2013, *23* (2), 374–382.

(29) Bujubarah, M. M.; Elsewedy, H. S.; Shehata, T. M.; Soliman, W. E. Formulation by Design of an Innovative Tea Tree Oil Nanoemulgel Incorporating Mupirocin for Enhanced Wound Healing Activity. *Appl. Sci.* 2023, *13* (24), 13244.

(30) Alhasso, B.; Ghori, M.; Rout, S.; Conway, B. Development of a Nanoemulgel for the Topical Application of Mupirocin. *Pharmaceutics* 2023, *15* (10), 2387.

(31) Flöter, E.; Wettlaufer, T.; Conty, V.; Scharfe, M. Oleogels—Their Applicability and Methods of Characterization. *Molecules* 2021, *26* (6), 1673.

(32) Monogarova, O. V.; Oskolok, K. V.; Apyari, V. V. Colorimetry in Chemical Analysis. *J. Anal. Chem.* 2018, *73* (11), 1076–1084.

(33) Bharti, D.; Kim, D.; Banerjee, I.; Rousseau, D.; Pal, K. Effects of Sorbitan Monostearate and Stearyl Alcohol on the Physicochemical Parameters of Sunflower-Wax-Based Oleogels. *Gels* 2022, *8* (8), 520.

(34) Sena, B.; Dhal, S.; Sahu, D.; Sarkar, P.; Mohanty, B.; Jarz; Wieruszewski, M.; Behera, H.; Pal, K.; Pal, K. Variations in Microstructural and Physicochemical Properties of Soy Wax/Soybean Oil-Derived Oleogels Using Soy Lecithin. *Polymers* 2022, *14* (19), 3928.

(35) Das, A.; Sanakal, S. I.; Sahu, D.; Sahoo, S.; Adhya, P.; Ravi, S.; Chakraborty, S.; Mohanty, B.; Pal, K.; Maji, S. Effect of Cholesterol on Oral Delivery of Curcumin Using Oleogels Containing Wheat Germ Oil and Rose Floral Wax. *Cryst. Growth Des.* 2023, *23* (12), 9025.

(36) Pathare, P. B.; Opara, U. L.; Al-Said, F. A.-J. Colour Measurement and Analysis in Fresh and Processed Foods: A Review. *Food Bioprocess Technol.* 2013, *6* (1), 36–60.

(37) Ürkek, B. Effect of Using Chia Seed Powder on Physicochemical, Rheological, Thermal, and Texture Properties of Ice Cream. *J. Food Process. Preserv.* 2021, *45* (5)..

https://doi.org/10.1021/acs.cgd.4c01095

(38) Dhal, S.; Alhamidi, A.; Al-Zahrani, S. M.; Anis, A.; Pal, K. The Influence of Emulsifiers on the Physiochemical Behavior of Soy Wax/Rice Bran Oil-Based Oleogels and Their Application in Nutraceutical Delivery. *Gels* 2023, *9* (1), 47.
(39) Pang, M.; Cao, L.; Kang, S.; Jiang, S.; Cao, L. Controlled Release of Flavor Substances from Sesame-Oil-Based Oleogels Prepared Using Biological Waxes or Monoglycerides. *Foods* 2021, *10* (8), 1828.
(40) Das, P.; Qureshi, D.; Paul, S.; Mohanty, B.; Anis, A.; Verma, S.; Wilczyński, S.; Pal, K. Effect of Sorbitan Monopalmitate on the Polymorphic Transitions and Physicochemical Properties of Mango Butter. *Food Chem.* 2021, *347*, 128987.
(41) Douaire, M.; di Bari, V.; Norton, J. E.; Sullo, A.; Lillford, P.; Norton, I. T. Fat Crystallisation at Oil-Water Interfaces. *Adv. Colloid Interface Sci.* 2014, *203*, 1–10.
(42) Sonwai, S.; Podchong, P.; Rousseau, D. Crystallization Kinetics of Cocoa Butter in the Presence of Sorbitan Esters. *Food Chem.* 2017, *214*, 497–506.
(43) Liu, C.; Zheng, Z.; Meng, Z.; Chai, X.; Cao, C.; Liu, Y. Beeswax and Carnauba Wax Modulate the Crystallization Behavior of Palm Kernel Stearin. *LWT* 2019, *115*, 108446.
(44) Zampouni, K.; Soniadis, A.; Moschakis, T.; Biliaderis, C. G.; Lazaridou, A.; Katsanidis, E. Crystalline Microstructure and Physicochemical Properties of Olive Oil Oleogels Formulated with Monoglycerides and Phytosterols. *LWT* 2022, *154*, 112815.
(45) Kupiec, M.; Zbikowska, A.; Marciniak-Lukasiak, K.; Kowalska, M. Rapeseed Oil in New Application: Assessment of Structure of Oleogels Based on Their Physicochemical Properties and Microscopic Observations. *Agriculture* 2020, *10* (6), 211.
(46) Attama, A.; Schicke, B.; Müllergoymann, C. Further characterization of theobroma oil–beeswax admixtures as lipid matrices for improved drug delivery systems. *Biopharm.* 2006, *64* (3), 294–306.
(47) Manzoor, S.; Masoodi, F. A.; Naqash, F.; Rashid, R. Oleogels: Promising Alternatives to Solid Fats for Food Applications. *Food Hydrocoll. Heal.* 2022, *2*, 100058.
(48) Galvão, J. G.; Trindade, G. G. G.; Santos, A. J.; Santos, R. L.; Chaves Filho, A. B.; Lira, A. A. M.; Miyamoto, S.; Nunes, R. S. Effect of Ouratea Sp. Butter in the Crystallinity of Solid Lipids Used in Nanostructured Lipid Carriers (NLCs). *J. Therm. Anal. Calorim.* 2016, *123* (2), 941–948.
(49) Patel, A. R. A Colloidal Gel Perspective for Understanding Oleogelation. *Curr. Opin. Food Sci.* 2017, *15*, 1–7.
(50) Visser, J.; Smits, P. Number 2 Article 10 1985 Part of the Food Science Commons Recommended Citation Recommended Citation Heertje. *I. Food Struct.* 1985, *4* (2), 267–277.
(51) Blake, A. I.; Co, E. D.; Marangoni, A. G. Structure and Physical Properties of Plant Wax Crystal Networks and Their Relationship to Oil Binding Capacity. *J. Am. Oil Chem. Soc.* 2014, *91* (6), 885–903.
(52) Daniel, J.; Rajasekharan, R. Organogelation of Plant Oils and Hydrocarbons by Long-chain Saturated FA, Fatty Alcohols, Wax Esters, and Dicarboxylic Acids. *J. Am. Oil Chem. Soc.* 2003, *80* (5), 417–421.
(53) Sagiri, S. S.; Behera, B.; Rafanan, R. R.; Bhattacharya, C.; Pal, K.; Banerjee, I.; Rousseau, D. Organogels as Matrices for Controlled Drug Delivery: A Review on the Current State. *Soft Mater.* 2014, *12* (1), 47–72.
(54) La Russa, M. F.; Ruffolo, S. A.; Barone, G.; Crisci, G. M.; Mazzoleni, P.; Pezzino, A. The Use of FTIR and Micro-FTIR Spectroscopy: An Example of Application to Cultural Heritage. *Int. J. Spectrosc.* 2009, *2009*, 1–5.
(55) Vlachos, N.; Skopelitis, Y.; Psaroudaki, M.; Konstantinidou, V.; Chatzilazarou, A.; Tegou, E. Applications of Fourier Transform-Infrared Spectroscopy to Edible Oils. *Anal. Chim. Acta* 2006, *573–574*, 459–465.
(56) Satapathy, M.; Quereshi, D.; Hanh Nguyen, T. T.; Pani, D.; Mohanty, B.; Anis, A.; Maji, S.; Kim, D.; Sarkar, P.; Pal, K. Preparation and Characterization of Cocoa Butter and Whey Protein Isolate Based Emulgels for Pharmaceutical and Probiotics Delivery Applications. *J. Dispers. Sci. Technol.* 2020, *41* (3), 426–440.
(57) Xiong, G.; Zhi, Z. L.; Yang, X.; Lu, L.; Wang, X. Characterization of Perovskite-Type LaCoO3 Nanocrystals Prepared by a Stearic Acid Sol-Gel Process. *J. Mater. Sci. Lett.* 1997, *16* (13), 1064–1068.
(58) Rakhshaei, R.; Namazi, H. A Potential Bioactive Wound Dressing Based on Carboxymethyl Cellulose/ZnO Impregnated MCM-41 Nanocomposite Hydrogel. *Mater. Sci. Eng., C* 2017, *73*, 456–464.
(59) Risan, J.; Jain, G.; Pendola, M.; Evans, J. S. Intracrystalline Incorporation of Nacre Protein Hydrogels Modifies the Mechanical Properties of Calcite Crystals: A Microcompression Study. *J. Mater. Chem. B* 2018, *6* (25), 4191–4196.
(60) Mimouni, R.; Kamoun, O.; Yumak, A.; Mhamdi, A.; Boubaker, K.; Petkova, P.; Amlouk, M. Effect of Mn Content on Structural, Optical, Opto-Thermal and Electrical Properties of ZnO:Mn Sprayed Thin Films Compounds. *J. Alloys Compd.* 2015, *645*, 100–111.
(61) Merchán Sandoval, J.; Carelli, A.; Palla, C.; Baümler, E. Preparation and Characterization of Oleogel Emulsions: A Comparative Study between the Use of Recovered and Commercial Sunflower Waxes as Structuring Agent. *J. Food Sci.* 2020, *85* (9), 2866–2878.
(62) Yilmaz, E.; Keskin Uslu, E.; Öz, C. Oleogels of Some Plant Waxes: Characterization and Comparison with Sunflower Wax Oleogel. *J. Am. Oil Chem. Soc.* 2021, *98* (6), 643–655.
(63) Bin Sintang, M. D.; Danthine, S.; Brown, A.; Van de Walle, D.; Patel, A. R.; Tavernier, I.; Rimaux, T.; Dewettinck, K. Phytosterols-Induced Viscoelasticity of Oleogels Prepared by Using Monoglycerides. *Food Res. Int.* 2017, *100*, 832–840.
(64) Galbraith, S. C.; Flood, A. E.; Rugmai, S.; Chirawatkul, P. Relationship between Surface Roughness, Internal Crystal Perfection, and Crystal Growth Rate. *Chem. Eng. Technol.* 2016, *39* (2), 199–207.
(65) Meng, Z.; Qi, K.; Guo, Y.; Wang, Y.; Liu, Y. Effects of Thickening Agents on the Formation and Properties of Edible Oleogels Based on Hydroxypropyl Methyl Cellulose. *Food Chem.* 2018, *246*, 137–149.
(66) Sivakumar, G.; Babu, A.; Das, A.; Bharti, D.; Sahu, D.; Pal, A.; Patel, S.; Mohanty, B.; Pal, K.; Maji, S. Structuring of Wheat Germ Oil into Oleogels Using Rose Floral Wax via Entanglement of Needle-Like Crystal Networks: Preparation, Characterizations, and Application. *Cryst. Growth Des.* 2023, *23* (2), 769–781.
(67) Dhal, S.; Mohanty, A.; Yadav, I.; Uvanesh, K.; Kulanthaivel, S.; Banerjee, I.; Pal, K.; Giri, S. Magnetic Nanoparticle Incorporated Oleogel as Iontophoretic Drug Delivery System. *Colloids Surf., B* 2017, *157*, 118–129.

https://doi.org/10.1021/acs.cgd.4c01095

Silk fibroin: An innovative protein macromolecule-based hydrogel/ scaffold revolutionizing breast cancer treatment and diagnosis – Mechanisms, advancements, and targeting capabilities

Shubhrajit Mantry [a,*], Kotaiah Silakabattini [b], Prabhat Kumar Das [c], Jonna Sankaraiah [d], Chandra Shekhar Barik [e], Satyajit Panda [f,*], Shadma Wahab [g], Mohammad Khalid [h]

[a] *Department of Pharmacy, Sarala Birla University, Birla Knowledge City, P.O.- Mahilong, Purulia Road, Ranchi 835103, Jharkhand, India*
[b] *Department of Pharmacognosy, Chebrolu Hanumaiah Institute of Pharmaceutical Sciences, Chandramoulipuram, Chowdavaram, Guntur 522019, Andhra Pradesh, India*
[c] *Department of Pharmacology, GRY Institute of Pharmacy, Borawan, Khargone, Madhya Pradesh 451228, India*
[d] *Department of Process Development, Medytox Inc., 102, Osongsaengmyeong 4-ro, Osong-eup, Heugdeok-gu, Cheongju-si, Chungcheongbuk-do, Republic of Korea*
[e] *Department of Pharmacology, School of Pharmacy, DRIEMS University, Kotasahi, Kairapari, Tangi, Cuttack, Odisha Pin-754022, India*
[f] *Department of Pharmaceutics, Institute of Pharmacy and Technology, Salipur, Cuttack, Odisha 754202, India.*
[g] *Department of Pharmacognosy, College of Pharmacy, King Khalid University, Abha 62529, Saudi Arabia*
[h] *Department of Pharmacognosy, College of Pharmacy, Prince Sattam Bin Abdulaziz University Alkharj, Saudi Arabia*

ARTICLE INFO

Keywords:
Breast cancer
Protein
Silk fibroin
Biological macromolecules
Hydrogel
Scaffolds

ABSTRACT

Breast cancer (BC) is recognized as the most typical cancer diagnosed in women globally, posing significant public health challenges. Several protein-based biological macromolecules have been investigated for drug delivery in BC treatment due to biological and tunable mechanical properties. Silk fibroin (SF)-based hydrogel/ scaffold is gaining attraction in BC therapy. The functionalization of SF with folic acid or antibodies enables targeted delivery to BC cells that overexpress folate receptors. In this context, this perspective article explored the potential biological activity, targeting capacity, functionalization, and drug carrier abilities of SF-based hydrogel for BC therapy. In addition, the article exclusively delves into the potential molecular pathways of SF-based hydrogel/ scaffolds for targeted therapy in BC. The article also summarizes the perspectives on the diagnosis abilities of SF-based hydrogel/ scaffolds in BC treatment, making it the first instance of such perspective literature. This insightful literature presents practical guidance for researchers, clinicians, and scientists eager to investigate the innovative biological applications and targeting potential of SF-based hydrogels and scaffolds in advancing breast cancer treatments.

1. Introduction

Breast cancer (BC) is recognized as the most typical cancer diagnosed in women around the world and posses a significant public health issue due to the elevated rates of occurrence and disease complications. The pathology originates in the mammary glandular tissue and has the potential for metastasis to distant sites if not identified and managed promptly [1]. In 2022, India reported approximately 192,020 new BC cases, with an ASR of 26.6 per 100,000 women [2,3]. In the same year, United State also reported 2,74,375 new BC cases with an ASR of 95.9 per 1,00,000 women. The number of deaths was 42,900, and survival rate exceeds 90 % within five years, reflecting advanced healthcare infrastructure and widespread screening programs [4–6]. Moreover, China also reported 3,57,161 new cases in 2022, with an ASR of 33.0 per 100,000 women and 74,986 deaths, resulting in a mortality ASR of 6.1 per 100,000 women [7]. The relatively lower mortality rate compared to incidence may be due to recent improvements in healthcare services. While high-income countries have seen stabilization or declines in BC mortality due to early detection and improved or new pharmacological interventions, many low- and middle-income countries, including India, continue to experience rising incidence and mortality rates [8–10].

BC arises from a complex interaction of genetic (i.e., BRCA1, TP53, PTEN, CHEK2, and BRCA2 mutations), hormonal, environmental, and lifestyle factors. The genes are essential for DNA repair, and their

* Corresponding authors.
E-mail addresses: shubhrajit.mantry@sbu.ac.in (S. Mantry), satya.jcp@gmail.com (S. Panda).

https://doi.org/10.1016/j.ijbiomac.2025.142870
Received 24 January 2025; Received in revised form 30 March 2025; Accepted 3 April 2025
Available online 5 April 2025

dysfunction may increase susceptibility to the disease [11,12]. Moreover, the extended exposure towards estrogen and progesterone, may occur as a cause of early menarche, delayed menopause, or hormone replacement treatment, which might further correlate with an elevated risk [13,14]. In addition, the life-style associated reasons, i.e., obesity, alcohol consumption, radiation exposure, etc., further contribute to an elevated risk of developing/ progression of BC [1]. At initial context, the disease arises in the epithelial cells of the breast ducts or lobules, further translate through distinct stages, influenced by genetic and epigenetic changes that impair normal cellular functions, culminating in malignant transformation, enhanced cell proliferation, invasion, and metastasis [15]. The tumor microenvironment (TME) is shaped by fibroblasts, immune cells, and adipocytes in breast tissue, which supply critical growth factors (GFs) and inflammatory cytokines that facilitate tumor progression. The tumor facilitates angiogenesis via vascular endothelial growth factor (VEGF), securing a sufficient supply of nutrients and oxygen for its proliferation [16].

In medical science, several pharmacological and non-pharmacological interventions for BC, such as surgical technique, chemotherapy, hormonal therapy, and targeted therapy, have markedly enhanced patient prognoses [17,18]. Nonetheless, traditional therapeutic approaches contribute to the development of acquired resistance, particularly in hormonal therapy (e.g., tamoxifen) and targeted therapies [e.g., HER2 inhibitors] [18,19]. Chemotherapy and radiation therapy frequently induce significant side effects, including fatigue, nausea, alopecia, neuropathy, and cardiotoxicity [18]. Additionally, long-term complications such as secondary malignancies and chronic lymphedema may adversely impact quality of life [17,18]. In general context, the triple-negative BC (TNBC) further characterized by the non-availability of hormonal receptors and HER2 expression, rendering it resistant to hormone and HER2-targeted treatments [20,21]. BC demonstrates considerable genetic and molecular heterogeneity both within and among tumors, complicating the selection of treatment [22,23]. The intratumoral heterogeneity may result in disparate responses to the same therapies. The advancement in medical science, such as targeted therapies and immunotherapy, are costly and frequently unattainable in low- and middle-income nations. Treatment modalities for metastatic BC are predominantly palliative, emphasizing symptom alleviation rather than curative intent [24]. The failure to eliminate micrometastases leads to recurrence and decreased survival in advanced stages. Despite progress in standard BC therapy, issues including resistance, adverse effects, and accessibility underscore the necessity for enhanced diagnostic instruments, innovative treatments, and tailored therapeutic interventions to improve patient outcomes and well-being [25].

Recently, biomaterials-based advanced therapeutic and targeted strategies for the treatment and diagnosis of BC have emerged in clinical science. Various biological macromolecules, including proteins, nucleic acids, monoclonal antibodies, and carbohydrates, have transformed BC treatment by facilitating targeted therapy that reduces side or toxic effects to healthy tissues [26–28]. In this context, silk fibroin (SF), a naturally found protein sourced from the silkworm, i.e., *Bombyx mori*, has attracted interest in BC therapy owing towards its biocompatibility, biodegradability, mechanical strength, and potential for functionalization [29]. SF can be engineered into nanoparticles, hydrogels, or films for the targeted delivery of chemotherapeutics such as doxorubicin (DOX) and paclitaxel (PTX) to BC cells [30–33]. The sustained release profile via SF reduces systemic toxicity and improves drug efficacy. The functionalization of SF with ligands, including folic acid or antibodies, facilitates targeted delivery to BC cells that overexpress specific receptors, such as folate receptors or HER2 [34–36]. The systems based on SF are capable of co-delivering various drugs, such as chemotherapeutics and siRNA, to produce synergistic anti-cancer effects. SF nanoparticles can be conjugated with photothermal agents such as gold or graphene, or photosensitizers, to facilitate tumor ablation through the application of near-infrared radiation (NIR). These scaffolds replicate the ECM, facilitating cell adhesion, proliferation, and differentiation. SF exhibits non-immunogenic and biodegradable properties, diminishing the likelihood of adverse reactions compared to synthetic polymers [37–40].

Thus, this perspective article further aligned to explore the potential biological activity, targeting capacity, and drug carrier abilities of SF-based hydrogel/ scaffolds for the various types of BC therapy. The article initially delves into the source, isolation strategies, and physicochemical and biological properties of SF, followed by the modifications or functionalization of SF-based delivery approaches for BC therapy, a new avenue in the existing literature. In addition, the article exclusively delves into the potential mechanisms or molecular pathways involved in SF-based hydrogel/ scaffolds based on the existing investigations. The later segment of the article further categorized the SF as a delivery carrier for various GFs, genes, cells, and therapeutics, as well as the advancement of targeted therapy by SF-based hydrogel/ scaffolds. The authors further tried to summarize the perspectives on the diagnosis abilities of SF-based hydrogel/ scaffolds in various types of BC treatment and also outline the potential challenges and overcome strategies of the existing investigations, as overviewed in Fig. 1. This exclusively “single-platted” perspective literature will further help researchers, clinicians, and scientists investigate the potential biological applications and targeting capacity of SF-based hydrogel/ scaffolds in BC treatment.

2. SF: Source, and chemistry

A naturally occurring protein, SF originates mainly from the silkworm cocoons, or *Bombyx mori*. The raw silk comprises two parallel SF fibers bonded by sericin on their outside [41]. The degumming of raw silk, which involves the removal of sericin, produces SF, a natural green protein compound that demonstrates mechanical properties, biocompatibility, and adjustable biodegradability [42,43]. Typically, SF exists in various polymorphic structures, specifically Silk I, Silk II, and Silk III. Silk I is a hydrophilic protein that possesses a significant proportion of α-helix domain and coils. Silk II predominantly exhibits a β-sheet structure exhibited stable and water-insoluble, whereas, Silk III is primarily prevalent at the air-water interface [44,45]. Silkworm cocoons are comprised of distinct layers that possess distinct structures and characteristics. The outer layer of the cocoon contains silk fibers with a larger diameter than those in the interior layer [46,47]. The sericin content elevates from the inner layer towards the outer layer, and the mechanical characteristics of the resultant material are contingent upon the specific layer of the silkworm cocoon [48,49]. Each silkworm cocoon layer has distinct biological properties due to its varying structural traits and content. The intermediate layer exhibits the optimal performance for bone regeneration [50]. Silk fibre is composed mostly of two unique protein substances, i.e., SF filaments, which constitute 75 % of the entire silk fibre, and sericin coating, accounting for 25 % of the total silk fibre [48]. Fibroin and sericin proteins consist of the similar 18 amino acids. SF exhibits a highly repetitive β-sheet crystalline or semicrystalline form, facilitating superior distinctive features of silk [51]. The crystalline structures consist of heavy and light chain polypeptides, primarily comprising of amino acids, i.e., Gly and Ala, hydrogen bonds promote the β-sheet anti-parallel configuration by connecting the adjoining chains [52]. The H-L complex is non-covalently associated with glycoprotein (P25) of ~25 kDa in a 6:6:1 ratio to produce micellar units [53]. Fig. 2 further summarized the silk proteins extraction process, composition, and structure to develop various delivery systems for biomedical and tissue engineering applications.

Silk proteins are substantial proteins and have similarities to linear copolymers, comprising non-repetitive N- and C-terminals alongside numerous repeated segments characterized by either hydrophobic or hydrophilic properties [54,55]. The SF heavy chain and MaSp1 are predominantly influenced by hydrophobic motifs, which includes AAAAAA and GAGAGS. The polypeptide chains produce micelle-alike

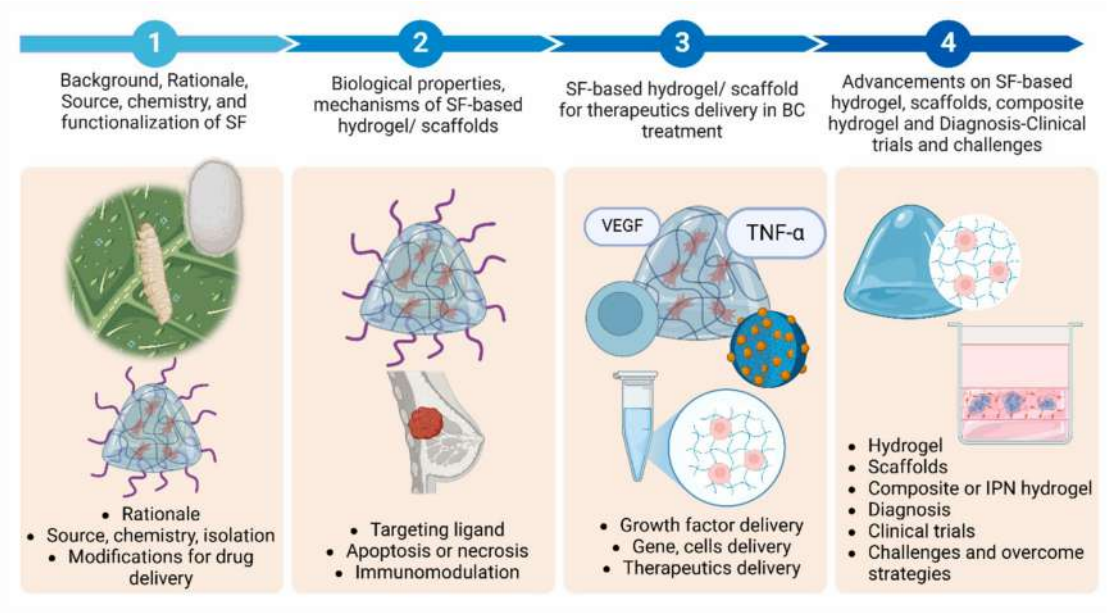

Fig. 1. Summarize the overview on SF-based hydrogel/ scaffolds for BC treatment and diagnosis.

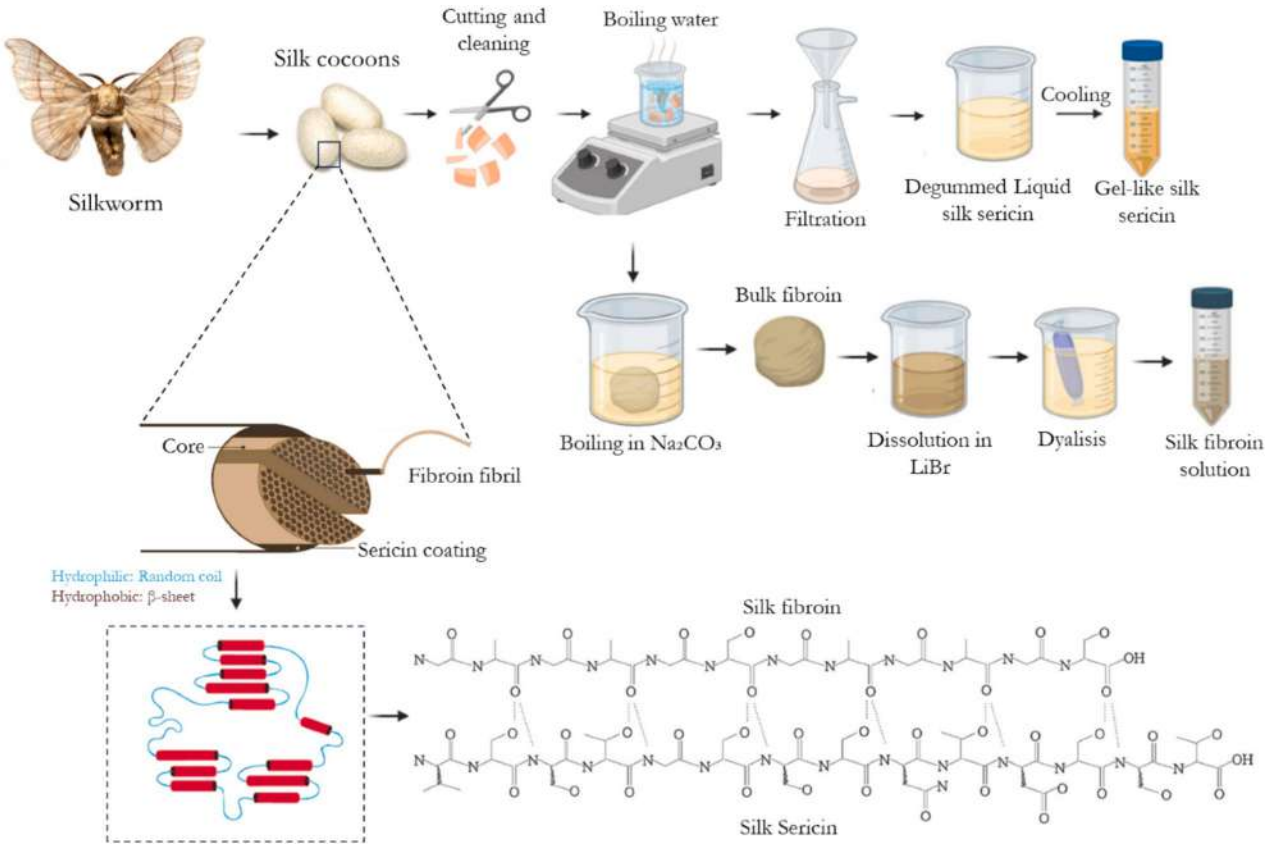

Fig. 2. Summarized the silk protein extraction process, composition, and chemical structure for the development of hydrogel/ scaffolds in biomedical applications, reproduced with permission from Ref. [69], under CC BY 4.0 license.

structures and liquid crystals. The alignment of crystalline sheets in SF-based coatings typically influences substrate stiffness, degradation kinetics, and biocompatibility [56]. In respond to external influences, i.e., pH, the resulting secondary structure and configuration of SF could be adaptively adjusted. The decreased pH level leads to inter-chain accumulation because of the involvement of significant hydrophilic groups, while high pH resulted in an elongated conformation due to the repellent nature of charged carboxyl groups. SF chains possessed a negative charge owing to acidic aspartate and glutamate residues, which constrains their pH responsiveness [57]. Fibroin derived from *B. mori* comprises an equimolar light chain (approximately 26 kDa) and a heavy chain (around 325 kDa) connected by a disulfide bond [58]. The

copolymeric structure encompasses extensive hydrophobic segments embedded with shorter hydrophilic segments. The heavy and light chains exhibited variations in their amino acid sequences, with heavy chain characterized by a higher proportion of Gly and Ala, resulting in its hydrophobic nature [59,60]. SF is a naturally acquired protein and an emerging biomaterial, extensively utilized in tissue engineering because of its biodegradability, biocompatibility, accessibility, high tensile strength, diverse mechanical properties, immunogenicity, and potential to be addressed into various forms with exceptional mechanical features [61,62]. SF is also utilized for numerous novel biomedical applications, such as wound dressing, due to the outstanding biological and mechanical characteristics. The mechanical rigidity, adaptability, water vapor permeability, and moderate antibacterial capabilities enable SF as a potential biomaterial for wound dressing [63].

Moreover, SF possesses or mimic the properties of ECM, facilitating the controlled release of therapeutic agents and thereby enhancing their efficacy in medical applications [64]. To enhance the properties of SF, several methods can be employed, including crosslinking, blending with other materials, or conjugating it with various moieties or polymers [65–67]. These approaches aim to improve critical aspects such as cell attachment and mechanical strength, which are often limitations in the natural form of SF. By implementing these strategies, researchers can create more effective biomaterials suitable for wide range of applications in tissue engineering and biomedical applications. In addition, physical crosslinking techniques have been developed to mitigate the toxicity associated with chemical crosslinking [68].

3. Modifications or functionalization of SF for drug delivery

SF fibers exhibit a distinctive combination of remarkable properties that exceed those of numerous other natural and synthetic fibers. Nevertheless, natural SF has certain limitations. The insertion of additional characteristics into SF fibers enhances their potential use while retaining their desirable distinctive characteristics. The functional alteration of SF fibers with modified aspects may provide them with novel characteristics and activities, hence expanding their applicability in the delivery of drugs [70–72]. The diverse functional alterations on SF have been recently documented, including polymeric coatings, i.e., pH-responsive polymethacrylate copolymers, serve the purpose of protecting therapeutics for oral usage against the acidic gastric condition enabling the administration of drugs instantly to the intestine. In this context, Navamajiti N et al. designed a copolymer that covered SF and polymethacrylate for dosage forms for oral use. The studies revealed that capsules covered with SF composition facilitated pancreatin-dependent release of drug. This innovative formulation and its enhancements may further lead to more efficient and personalized drug delivery methods for those at risk, including individuals with compromised and extremely diverse gut physiology [73]. In addition, the hydrogels loaded with GFs have also been investigated as potential components for repair of bone defects; nevertheless, it is still difficult to develop smarter hydrogels with preferable gelation or mechanical characteristics, together with a regulated release of GFs [74]. In addition, Lv Z et al. reported the insertion of bone morphogenetic protein 2 (BMP-2)-modified MgFe-LDH nanosheets into CS/SF hydrogels embedded with PDGF-BB to generate an effective injectable form of thermo-responsive hydrogel, capable of facilitating the rapid release of PDGF-BB and a prolonged release of BMP-2, thus, enhance the bone regeneration capacity. The inclusion of MgFe-LDH into CS hydrogel lowers gelation time and sol-gel transition temperature, simultaneously improving the mechanical characteristics of hydrogel. The consecutive release of dual GFs and the prolonged action of bioactive Mg^{2+} and Fe^{3+} ions demonstrated that the hydrogel CSP-LB possessed enhanced angiogenic and osteogenic characteristics in contrast to the CS hydrogel. This investigation demonstrated that the CSP-LB hydrogel considerably enhanced the regeneration of bone, demonstrating greater bone capacity and mineral density compared to the CS hydrogel. This innovative thermo-sensitive hydrogel CSP-LB exhibited enhanced gelation ability along with angiogenic and osteogenic characteristics, hence offering the potential medication technique for bone defects [75].

The distinctive structure and preventive mechanism of the ocular physiology, results in reduced bioavailability of ocular medications. In this context, a mucoadhesive compound is an efficient approach to enhance the therapeutic efficacy of ophthalmic drugs. Therefore, Dong Y et al. developed a liposomal preparation surrounded with a novel adhesive additive, SF, for topical ocular delivery of drug. The regenerative SFs with differing dissolution times were added to the ibuprofen-loaded liposomes. The shape, drug encapsulation efficacy, *in vitro* release of drug, and *in vitro* corneal penetration of SLs were studied in contrast to conventional method of liposomes. The cell adhesion and cytotoxicity studies of SF and SLs were conducted using HCEC. SLs demonstrated prolonged drug release and *in vitro* corneal permeability of ibuprofen in comparison to the drug solution and conventional liposomes. The cell fluorescence emerged after 7 mins of being exposed to SF, and its brightness progressively increased for up to 12 h., without any observable cytotoxicity. A significant increase in fluorescent intensity of Nile red in SLs was detected during a brief duration of 15 mins, indicating a faster absorption rate. These advantageous characteristics render SF-coated liposomes a promising ocular medication delivery method [76]. Diabetic wounds are challenging to cure due to its chronic inflammation and decreased angiogenesis. The plant derived extracellular vesicles (PDEVs) are abundant in both cytokines and GFs that facilitate cell proliferation and angiogenesis. Regardless, monotherapy exhibits restricted effectiveness along with delivery efficiency. Henceforth, bioengineering can enhance the constrained efficacy of individual medications by integrating drugs and materials to create complementary or synergistic bioengineered therapeutics. Hence, Zhu W et al. synthesized gelatin methacrylate (GelMA)/ SF methacrylate (SFMA) composite hydrogels with GelMA and SFMA, achieving appropriate swelling ratio, mechanical characteristics, and biodegradability. The hydrogel composite served as a wound dressing for prolonged release of drug. RES incorporated into MSNs forming MSN-RES, thereby improving the release kinetics. Subsequently, PDEVs and MSN-RES were integrated with hydrogels composite to produce GelMA/SFMA/MSN-RES/PDEVs hydrogels. The hydrogels exhibited low cytotoxicity and favorable biocompatibility, suppressing the macrophage inducible nitric oxide synthase (iNOS) expression, and enhanced the development of tubes by Human umbilical vein endothelial cells (HUVECs). Furthermore, the hydrogels diminished the pro-inflammatory factors, i.e., tumor necrosis factor-alpha (TNF-α) and iNOS, elevated Transforming growth factor beta 1 (TGF-β1) and arginase-1 (Arg-1) factors, facilitated angiogenesis, and improved diabetic wound healing. The hydrogels enhanced the proliferation of the extracellular purinergic signaling pathway-CD73 and adenosine 2A receptor. Hence, hydrogels may serve as wound dressing for regulating angiogenesis and inflammation in diabetic wounds, thereby accelerating the process of healing [77].

4. Characteristics of SF-based hydrogel/ scaffolds for BC management

SF hydrogels present several significant advantages in the field of biomedicine. These hydrogels are known for their biocompatibility, multifunctionality, exceptional mechanical properties, biodegradability, and cytocompatibility. They exhibit characteristics such as injectability, self-healing capabilities, environmental responsiveness, and antibacterial properties, further established as significant biomaterials for various applications, including drug delivery and tissue engineering [64,78,79]. The reconstitution process, which eliminates the sericin coating, enhances biocompatibility and facilitates the customization of mechanical properties and structural characteristics for biomedical applications. SF hydrogels can optimize implant structures and release behaviors by enabling the controlled release of therapeutics, due to their pH-responsive nature and tunable properties [64,80,81].

The molecular weight and pore size of SF significantly impact the release profile, allowing for sustained drug delivery [31,82]. Additionally, blending SF with other polymers can improve swelling properties and mechanical strength, thereby enhancing the overall performance of the hydrogel in tissue engineering applications [67,83,84].

4.1. Drug delivery carrier

SF has been extensively investigated as a carrier for drug delivery due to various inherent biological and physicochemical characteristics. The β-sheet crystalline structure in SF allows for the extended release of encapsulated drugs, enhanced therapeutic efficiency followed by minimizing systemic side effects [31,85]. In the context of BC, SF can effectively deliver chemotherapeutic agents such as DOX, PTX, and tamoxifen, allowing for improved targeting and sustained action. By encapsulating these anti-cancer agents within SF nanoparticles or hydrogels, the drugs are protected from premature degradation [64,86]. Additionally, covalent attachment of the drugs to the SF chains can facilitate sustained release through hydrolysis [86]. Upon administration, the drug-loaded SF matrix degrades slowly, ensuring a controlled release of the drug and maintaining prolonged therapeutic levels at the tumor site [82]. The gradual breakdown of the polymer is aided by enzymatic degradation from proteases such as chymotrypsin and protease XIV [87,88]. Furthermore, the degradation rate can be modulated by adjusting the β-sheet content during processing, which can be accomplished through methanol or water vapor treatment [84].

4.2. Targeting ligand

SF can be modified by incorporating specific ligands, peptides, or antibodies that selectively interact with receptors overexpressed on BC cells, including HER2 and estrogen receptors [32,89]. This modification improves the precise delivery of therapies to tumors, minimizing the impact on normal tissues. SF nanoparticles modified with folic acid preferentially target BC cells that overexpress folate receptors, resulting in enhanced cellular uptake of therapeutic agents [90]. Hyaluronic acid (HA) also interacts with CD44 receptors, frequently overexpressed in BC and cancer stem cells (CSCs) [91,92]. Certain peptides, including Arginylglycylaspartic acid (RGD) peptides, interact with integrins such as αvβ3 on BC cells, facilitating increased cellular uptake [93,94]. SF can be conjugated with antibodies such as trastuzumab, specifically targeting the HER2 receptor, enabling targeted delivery to HER2-positive BC cells [29,95]. Drugs or ligands are connected via acid-sensitive bonds, including hydrazone or imine bonds, which decompose under acidic conditions, facilitating the targeted drug release at the tumor site. The *co*-functionalization of SF with pH-sensitive polymers, such as poly (β-amino esters), enhances drug release in acidic environments [79]. In general, breast tumors frequently overexpress particular enzymes, including matrix metalloproteinases (MMPs). The integration of MMP-cleavable linkers in SF facilitates drug release through activation by enzymes present in the TME [89,96,97]. Additionally, the efficacy of BC therapy may be enhanced by administering genetic material. SF can be modified using cationic polymers, such as polyethyleneimine (PEI), or peptides to effectively bind and safeguard nucleic acids, including siRNA, mRNA, and DNA, from degradation [86].

4.3. Apoptosis or necrosis mechanism

SF exhibits distinctive properties that may inhibit the proliferation of cancer cells [29]. Recent investigations suggest that SF scaffolds modulate cellular signaling pathways associated with tumor growth and metastasis, potentially increasing the efficacy of complementary therapeutic agents [98,99]. SF contains significant levels of antioxidant amino acids, such as tyrosine and serine, which can effectively scavenge reactive oxygen species (ROS) [100]. SF-based nanoparticles and scaffolds can modulate oxidative stress and impact key signaling pathways (i.e., Mitogen-activated protein kinase or MAPK/ AKT/ mammalian target of rapamycin or mTOR/ phosphoinositide 3-kinase or PI3K pathways), which are vital for BC cells [29]. SF scaffolds, by replicating the ECM, can affect cell adhesion, migration, and differentiation, which in turn mitigates oxidative stress and stabilizes cellular functions to enhance redox balance. Additionally, SF nanoparticles modified with small interfering RNA (siRNA) or microRNA (miRNA) can inhibit the overexpression of elements in the PI3K/AKT/mTOR pathway, resulting in decreased proliferation and survival of cancer cells [101]. An excessive ROS can activate the PI3K/AKT/mTOR signaling pathway. However, scaffolds made from SF that are loaded with antioxidants can reduce ROS levels, thereby indirectly inhibiting the hyperactivation of the pathway. The minimization of oxidative stress allows SF scaffolds to stabilize upstream regulatory molecules, including PTEN, a tumor suppressor that is sensitive to ROS. Furthermore, SF scaffolds can reduce ROS-mediated activation of MAPK signaling components, specifically JNK and p38, which are influenced by oxidative stress [102–104]. This regulation in cancer cells can induce apoptosis or inhibit cell proliferation by maintaining redox homeostasis. Additionally, SF nanoparticles can encapsulate and deliver inhibitors that target specific components of the MAPK pathway, including MEK inhibitors such as trametinib, thereby improving tumor specificity [102–104].

4.4. 3D tumor model

BC is the primary reason of mortality among women due to recurrence and metastasis. The 3D breast cancer models are regarded as effective techniques for drug screening and elucidating cancer-driving processes, owing to their capacity to replicate tumor heterogeneity. In this context, Pierantoni L et al. designed a 3D model utilizing enzymatic crosslinked SF (eSF)-based hydrogels. The study reported eSF-based hydrogels loaded with MCF-7 cells with or without the presence of human mammary fibroblasts. The mechanical characterization of the hydrogels further demonstrated conformational transition (from random coil to β-sheet), higher stiffness, etc. Additionally, the mechanical properties assessments further revealed that the cells can modify the stiffness of the hydrogels, mimicking the *in vivo* microenvironment's stiffening. The co-cultured fibroblast-mediated 3D cancer cells further demonstrated overexpression of genes associated with ECM remodeling and fibroblast activation for up to 14 days. To establish an anti-cancer screening model, the authors further reported doxorubicin and paclitaxel treatment in 3D culture. The results suggest that co-culturing MCF-7 cells with fibroblasts in eSF hydrogels creates a more accurate *in vitro* environment for studying cancer progression. This approach opens up new research opportunities to explore innovative molecular targets for cancer treatment [105]. An integrated approach that allows for administration of anti-cancer agents and GFs via a minimally invasive method is sought for the effective treatment of TNBC following lumpectomy. Therefore, Jaiswal C et al. developed a novel 3D *in vitro* SF-based hydrogel lumpectomy model with MDA-MB-231 cells for TNBC treatment via DOX delivery in eliminating residual breast cancer post-lumpectomy. The study end point reported the assessment of adipose tissue regeneration in the lumpectomy site via DOX-loaded BMSF/AASF blended hydrogels. The authors reported significant viscoelasticity and syringeability of BMSF/AASF blended hydrogels for invasive administration in TNBC treatment. The cytotoxicity against MDA-MB-231 cells reported due to prolonged release of DOX in blended hydrogels at localized site. Moreover, dextran-loaded hydrogel facilitated the adipogenic development of adipose tissue-derived stem cells (ADSCs), while the released factors were identified to promote vascularization and macrophage polarization. This was validated via *in vitro* angiogenic tube formation test and macrophage polarization analysis, respectively. This results further supported the prospective use of the injectable blended hydrogels for localized anti-cancer therapy and facilitates breast tissue formation in lumpectomy [106].

4.5. Immunomodulatory effects

SF may act as an immunomodulatory agent, positively influencing the TME to enhance anti-cancer immunity. It may improve the immune system's ability to target BC by modulating immune cell activity and enhancing antigen presentation [29]. SF -based formulations effectively deliver anti-angiogenic drugs or siRNA molecules to inhibit VEGF pathways, thereby restricting tumor vascularization and angiogenesis [31,79,108].

4.6. Alignment with photothermal and photodynamic therapy

SF can serve as an effective carrier for photosensitizers or nanoparticles that convert light energy into heat [109,110]. When subjected to specific wavelengths of light, these systems generate localized heat or ROS, which selectively target and kill cancer cells. Additionally, several hydrophobic photosensitizer molecules, such as porphyrins and phthalocyanines, interact favorably with the hydrophobic domains of SF [97,111]. The covalent conjugation of photosensitizer molecules to SF chains ensures stable integration and customizable release profiles. This encapsulation method prevents self-quenching of the photosensitizers, thereby enhancing their photodynamic activity. Gold nanoparticles (AuNPs), carbon nanotubes, and other plasmonic nanomaterials can be incorporated into SF matrices through non-covalent interactions (such as electrostatic and hydrophobic forces) or through covalent bonding to the reactive groups on SF (like amine, carboxyl, or hydroxyl groups) [112–114]. Nanoparticles, such as AuNPs, effectively absorb NIR light and convert it into heat via surface plasmon resonance. These agents focus on oncogenes associated with the advancement of BC, offering a targeted treatment approach. Scientists have explored a variety of materials, such as metallic, inorganic, organic, and polymeric compounds, to enhance the characteristics of natural polymers like silk. Graphene oxide has been integrated into SF hydrogels to enhance their mechanical and structural properties [115,116]. AuNPs have been incorporated into chitosan and SF hydrogels to enhance the gelation time, demonstrating significant intermolecular interactions among the polymers [117–119]. The degradation products of SF are non-toxic, and its gradual degradation rate facilitates prolonged therapeutic effects while minimizing the risk of adverse reactions [31,64]. SF is an optimal material for prolonged cancer therapies. Research is being conducted on SF -based scaffolds for reconstructive applications post- BC surgery [120]. These scaffolds facilitate the development of tumor models for evaluating drug efficacy, thereby supporting precision medicine strategies. Challenges persist, including the restricted scalability of functionalized SF nanoparticles, the necessity for a more comprehensive understanding of SF's interaction with tumor biology, and the requirement for regulatory approval for clinical application, all of which are critical for the advancement of innovative and patient-centered BC therapies.

5. SF-based hydrogel as delivery system for BC treatment

5.1. Growth factor delivery

SF-based hydrogels have received considerable interest in treating BC, especially for the targeted delivery of GFs [29,106,121]. Several GFs such as fibroblast growth factor (FGF), VEGF, and TGF-β are vital in angiogenesis, proliferation, and immune modulation, essential for tumor development and tissue healing [122]. To fully utilize the therapeutic benefits of GFs, precise delivery methods are necessary to ensure localized and controlled release while minimizing systemic side effects—this makes SF -based hydrogels a highly suitable option [82]. GFs are naturally unstable and susceptible to degradation. SF hydrogels protect molecules from enzymatic breakdown and denaturation, maintaining their structural integrity and biological activity. These hydrogels demonstrate exceptional thermal and enzymatic stability, which helps safeguard GFs from environmental degradation. SF can spontaneously form hydrogels under mild conditions, such as changes in pH, temperature, or ionic strength [123,124]. This eliminates the need for harsh chemical cross-linkers, ensuring the preservation of the bioactivity of the GFs contained within the moiety. Following BC surgery, SF hydrogels can release GFs like FGF to enhance wound or tissue regeneration of breast tissues [64,125].

The development of 3D culture models proposes considerable potential for cancer research and identifying new anti-cancer therapeutics compared to complicated animal models. To develop such 3D matrix culture model, Shokri R et al. constructed methylcellulose/ HA/ SF-based temperature-sensitive hydrogel (MCHASF) which further mimics the ECM microenvironment. The study results further determined the stiffness of the hydrogel matrix similar to breast tumors, non-uniform surface, high porosity, and stability up to 6 weeks. In addition, the morphological assessment on MDA-MB-231 cell line further demonstrated the irregular cytoskeletal shapes and mimic the breast malignancy TME, as shown in Fig. 3 (**i**). Furthermore, the cells demonstrated an enhanced migration rate and elevated expression levels of VEGF, MMP2, and MMP9, along with augmented resistance to chemotherapy relative to 2D cultures. This study further suggested that the SF-based 3D environment enhances metastatic potential and presents significant insights into tumor cell behavior, encompassing metastasis and treatment responses [126]. In similar context, Arora D et al. also developed 3D scaffold culture system combining silk from *Bombyx mori* and arginine-Gly-aspartate (RGD)-enriched silk from *Antheraea assama* for MCF-7 tumoroids. The study reported the cellular mechanisms underlying the physiological adaptations of 3D constructs and their drug responses compared to traditional monolayer and multicellular spheroid cultures. In addition, the silk-based composite scaffolds exhibited enhance growth factor and metabolic activity via P450 reductase, CD44 receptor adhesion, aldehyde dehydrogenase-1, Vimentin, etc., further suggested that the bioactive macromolecule-based scaffold enhances the metastatic potential of the breast tumoroids. The study further concluded the expression of TGF-β, proliferation of cells in 3D microenvironment. Thus, this additional investigation further supports the utilization of SF-based scaffolds for anti-cancer drug screening, i.e., DOX and PTX, demonstrate considerable potential for developing robust and sustainable 3D tumoroids, positioning them as a valuable resource for high-throughput drug screening [127].

The post-surgical recurrence at the primary site and distant metastasis continues to pose challenges in the treatment of TNBC due to its unpredictable invasion into nearby tissues. While systemic chemotherapy is commonly used to reduce recurrence and metastasis, the extensive blood vessel supplying nutrients can accelerate the proliferation of tumor cells and support angiogenesis. To address the challenges, Wang H et al. introduced a strategy that deprives nutrients by effectively obstructing remaining blood vessels and inhibiting angiogenesis to enhance treatment outcomes for TNBC. The study developed an injectable hydrogel with light-responsive properties, created from a polydopamine crosslinked collagen/ SF composite, designed to deliver thrombin to block blood vessels and inhibit angiogenesis. When exposed to NIR light, the hydrogel releases thrombin into the blood vessels of surrounding tissues, promoting clot formation. Additionally, the photothermal effect reduces VEGF secretion, thereby hindering angiogenesis in nearby tissues. Thus, this study further indicated that the restriction of the nutrient supply by obstructing adjacent blood vessels and preventing angiogenesis presents a promising approach to mitigate recurrence and metastasis in TNBC [128].

The mimic the equivalent microenvironment of ECM in BC progression, several innovative biomaterials have been further investigated for various dynamic and temporal mechanical signals in 3D microenvironment. In this context, Major G et al. constructs SF-loaded adipose-derived decellularized ECM (AdECM)-based hydrogel via photopolymerization technique. The study reported increase in stiffness after crosslinking (25 kPa). The MCF-7 cells further incorporated and cultured in the hydrogel, forming 1000 μm^2 in area of spheroids. As the stiffness

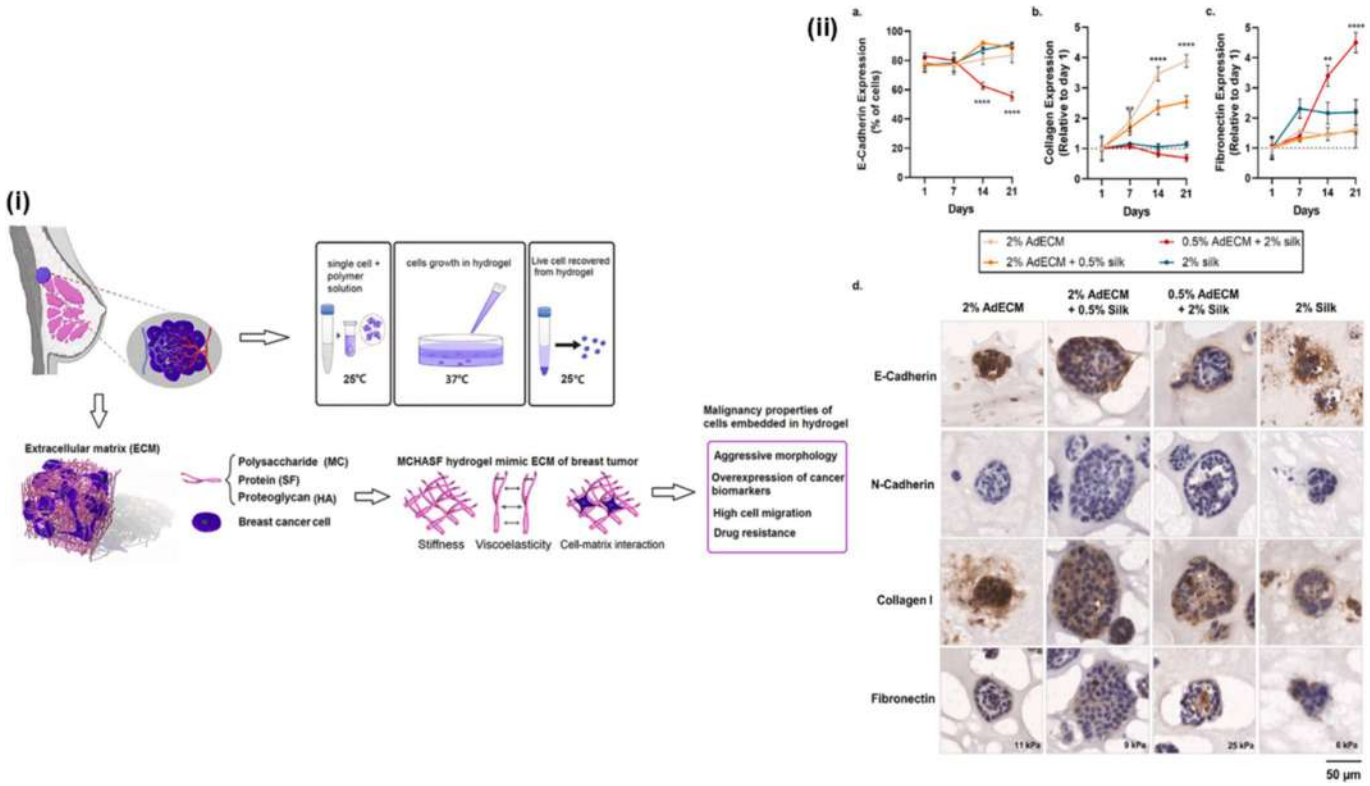

Fig. 3. (**i**) Summarized the stimuli-responsive composite MCHASF-based ECM-type hydrogel for BC, reproduced with permission from Ref. [126], Copyright 2022, Elsevier. (**ii**) Summarized the potential results of AdECM/SF hydrogels in MCF-7 cells estimated the expression of (**a**) E-cadherin, (**b**) collagen-I, (**c**) fibronectin for 21 days. (**d**) Graphical representation of immunohistochemistry of E-cadherin, N-cadherin, collagen-I, and fibronectin in various AdECM/SF hydrogels groups, reproduced with permission from Ref. [129], under CC BY 4.0 license.

escalated, the cells underwent growth cessation and displayed phenotypic alterations, resulting in intratumoral diversity. In contrast to conventional static mechanical models, this hydrogel with stiffening properties enabled the observation of gradual phenotypic changes and supported the formation of mature organoid-like spheroids that mirrored the organization and acinar structures of fully developed breast epithelium. The study further reported fibronectin overexpression and reduced E-cadherin levels, which further indicated cell proliferation, as summarized the results in Fig. 3 (**ii**). Therefore, the SF-based model created showcases an innovative approach to separate the biomechanical characteristics of ECM from the intricate cellular aspects of the disease microenvironment and retains considerable promise for broad utilization in other 3D *in vitro* disease models [129].

Moreover, the GFs are sensitive to environmental conditions, i.e., pH, temperature, and enzymatic degradation, leading to reduced bioactivity during encapsulation and release. Several investigations further suggested the modification of GFs via stabilizing agents (e.g., heparin) [130] or crosslinking approaches, encapsulation in SF micelles or nanoparticles to maintain growth factor structure and activity. In addition, the modification of SF structure (e.g., β-sheet contents), development of SF-based composite hydrogel, etc., further enhance or improve the degradation rate and release kinetics. While SF is generally biocompatible, variations in its processing and impurities can lead to local inflammation or immune responses. The optimization of SF purification and processing to minimize contaminants, functionalization with bioactive peptides or cell-adhesion molecules can enhance compatibility. Non-specific release of GFs may lead to off-target effects, promoting unwanted angiogenesis or supporting other proliferative diseases.

5.2. Gene, cells delivery

The development of large, implantable, and cost-effective bio prostheses, including breast implants, presents a substantial challenge in regenerative medicine. To simplify the current problems, Mehrabi A et al. developed composite hydrogel incorporated decellularized human placenta (dHplacenta)/ SF and further characterized via advanced analytical techniques. The study reported that the 3D microstructure exhibited porous structure, superior mechanical properties, and further confirmed the absence of cells in the dHplacenta. The authors further incubated the hydrogels with adipose-derived mesenchymal stem cells (ADSCs) acquired from patients via liposuction and subsequently characterized using flow cytometry and karyotyping. The findings revealed a reduction in CD34 and CD31 levels, accompanied by a rise in CD105 and CD90 levels in ADSCs, suggesting a phenotype similar to that of MSCs derived from human bone marrow, as shown in Fig. 4 (**i**). Additionally, after the re-cellularization of the hydrogel, live/dead assays and SEM analysis indicated that the highest levels of viability and cellular growth were observed in hydrogels with a greater proportion of dHplacenta (30/70) than in the other groups. Thus, the results indicate that the 30/70 dHplacenta/ SF hydrogel is a promising substrate for breast tissue engineering applications [131]. The utilization of phytopharmaceuticals in various treatment regimens have emerged in recent years. Several reported further suggested the combinatorial effect of phytocompounds along with cell-based therapy especially MScs in BC management. Therefore, to explore the potential of such combinatorial treatments, Ghaedamini S et al. investigated the combinatorial effect of ellagic acid (EA)/ adipose tissue stem cells (ADSCs-CM) via 3D- printed polycaprolactone (PCL)/agarose scaffold for BC treatment. The viability of MCF-7 cancer cell was assessed using the flow cytometry, MTT assay, cell cycle analysis, and quantitative real-time PCR inside a 3D cell culture setting. The results showed a decline in viability of cancerous cell in

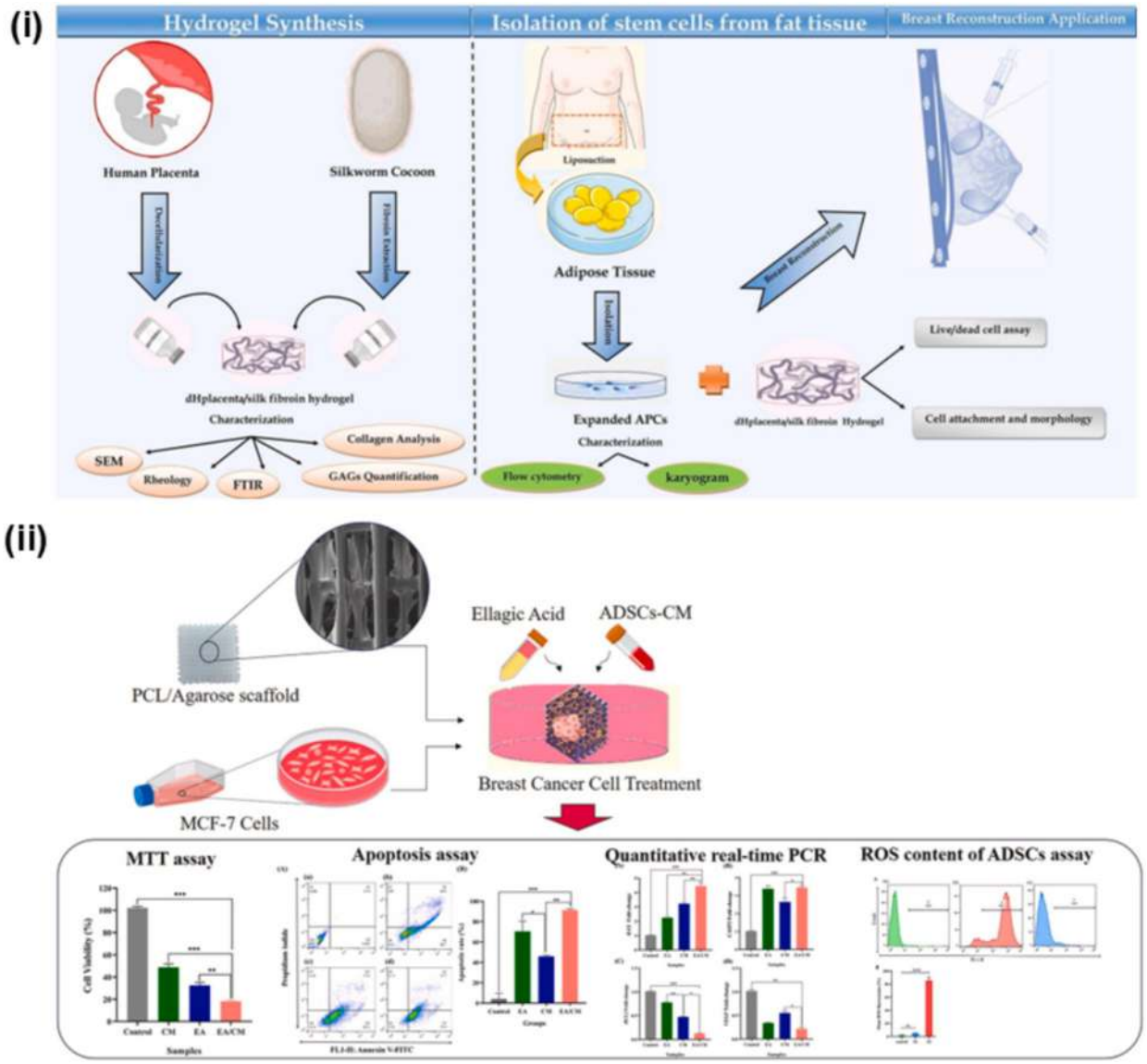

Fig. 4. (**i**) Graphical representation of hydrogel composed of SF/ placenta matrix for breast tissue reconstruction, reproduced with permission from Ref. [131], Copyright 2023, Elsevier. (**ii**) Summarized the potential outcomes of the anti-tumor effect of EA/ MSCs-laden 3D printed PCL/agarose scaffolds in BC treatment, reproduced with permission from Ref. [132], Copyright 2024, Elsevier.

all treatment groups compared to the control group. In addition, the authors reported that the combinatorial EA + CM further demonstrated significant increase in efficacy independently, detected decrease in cancer cells via annexin V/PI staining, and expression of BCL2, BAX, VEGF, and caspase-3 genes corresponded with apoptosis-related pathways. The combined anti-proliferative effects of EA alongside ADSCs-CM on MCF-7 cells further offer two significant implications for BC research by using PCL/agarose scaffold as a model for cancer and indicate potential new pathways for creating complementary anti-cancer treatment strategies [132], as indicated the results in Fig. 4 (**ii**).

Despite of the significant capacity of immune checkpoint blockade (ICB) therapy for treating tumors, the broad clinical implementation is presently hindered through inadequate therapeutic effects and off-target side effects. To further overcome the problems, Gou S et al. construct an injectable silk sericin (SS)/ SF recombinant hydrogel, referred to as SF-SS-SMC hydrogel, designed for the local delivery of the anti-CD47 antibody (α CD47). This hydrogel exhibits self-reinforcement in the elevated H2O2 concentrations found in the TME, as the SS/Fe2+ supramolecular nanocomplex (SS-SMC) within the hydrogel transforms H2O2 into ROS, which subsequently promotes additional crosslinking between the SF polymers. Consequently, the hydrogel SF-SS-SMC has a retention time *in vivo* that exceeds 21 days and serves as a reservoir for the prolonged and sustained release of α CD47. More significantly, the SF-SS-SMC hydrogel effectively alters the characteristics of a protumor immunosuppressive TME to an antitumoral TME by transitioning tumor-associated macrophages from an anti-inflammatory M2 phenotype to a proinflammatory M1 phenotype, all without requiring any additional drugs. Considering the dual impact of continuous α CD47 release and TME reprogramming, the hydrogel SF-SS-SMC demonstrates favorable immunotherapeutic outcomes for managing local, remitting, abscopal, and metastatic tumors. Additional benefits such as low production costs, straightforward fabrication, and user-friendly application further enhance its potential for large-scale commercial production [133].

Functionalize SF using protective agents such as PEI or cationic polymers to prevent genes from being degraded enzymatically. Modify SF by adding functional groups (like amine or thiol groups) to enhance gene binding and retention. Introduce stimuli-responsive elements (such as pH-sensitive or enzyme-sensitive linkers) that can release genes in reaction to signals from the TME. Conjugate SF with targeting ligands (including folate, peptides, or antibodies) to identify specific markers on

BC cells. Ensure that the hydrogel remains stable while also being injectable and adaptable to the contours of the tissue. Optimize the concentration of SF and the density of crosslinking to achieve a balance between mechanical strength and flexibility. Incorporate secondary reinforcing agents like nanocellulose or graphene oxide. Be aware of the risk of immune activation against the hydrogel or the genes being delivered. Rigorously purify SF to eliminate immunogenic sericin residues. Utilize gene-editing tools such as CRISPR that have minimal off-target effects and low immunogenicity.

5.3. Therapeutics delivery

A unified system is required to administer anti-cancer medications and GFs via a minimally invasive approach to effectively treat TNBC post-lumpectomy. Therefore, Jaiswal C et al. introduced a hydrogel composed of *Bombyx mori* SF (BMSF) and *Antheraea assamensis* SF (AASF) for characterization in 3D *in vitro* lumpectomy model. The study reported that the developed *in vitro* model used the MDA-MB-231 cell line to assess the DEX delivery via an injectable hydrogel system for TNBC treatment. The authors reported that the adipose tissue regeneration at the lumpectomy site was achieved by administering DEX via injectable hydrogels. The study further documented the blended BMSF/AASF hydrogels exhibited viscoelasticity and injectability, facilitating a release of DOX in a slow and sustained, demonstrating cytotoxic effects on MDA-MB-231 cells as evidenced by *in vitro* experiments, as shown in Fig. 5 (**i**). The hydrogel loaded with dexamethasone enabled the conversion of adipose tissue-derived stem cells (ADSCs) into adipocytes, whereas the factors released contributed to vascular development and the polarization of macrophages. This was validated through *in vitro* experiments on angiogenic tube formation and investigations into macrophage polarization. The results suggest the potential use of these injectable hydrogels for the precise delivery of anti-cancer medications and for enhancing breast reconstruction after lumpectomy [106].

Anastrozole (ANS) serves as an effective oral hormonal therapy for estrogen-positive (ER+) BC. Nonetheless, numerous side effects and pharmacokinetic limitations have restricted the application of ANS in BC treatment. This research developed an injectable in situ gelling system containing SF (SF)-ANS nanoparticles, offering sustained drug release and improved pharmacokinetic properties at the targeted site relative to conventional oral formulations. An optimized in situ gel (ISG) incorporating SF-ANS-NPs was developed, and pharmacokinetic parameters were assessed following subcutaneous administration in NMU-induced Wistar albino rats, as shown in Fig. 5 (**ii**). The results demonstrated that SF-ANS-NP-ISG exhibited significantly elevated C_{max}, T_{max}, and AUC values compared to pure ANS suspension. Furthermore, tumor multiplicity (1.40 ± 0.66), tumor latency (75 ± 9.2 days), and incidence rate (90 ± 2.1 %) were recorded, with post-treatment analysis indicating a significant decrease in tumor volume and weight relative to the positive control over 90 days following a single dose. Histopathological evaluation of the SF-ANS-NP-ISG treated group indicated low-grade carcinoma, diminished epithelial hyperplasia, and reduced hemorrhage in mammary tumor tissues relative to the positive control. The SF-ANS-NPs-ISG investigated effectively addressed the pharmacokinetic limitations of ANS, while also exhibiting targeted delivery and enhanced bioavailability compared to conventional dosage forms [134].

Artemisinin (ART), a natural extract with diverse pharmacological effects, faces limitations because of its poor solubility, hepatic metabolism, and short half-life. Therefore, Bao Y et al. developed SF/ gelatin (G)-based composite hydrogel to deliver ART in BC treatment. The SF-G-ART hydrogel, crosslinked with genipin, exhibited notable flexibility

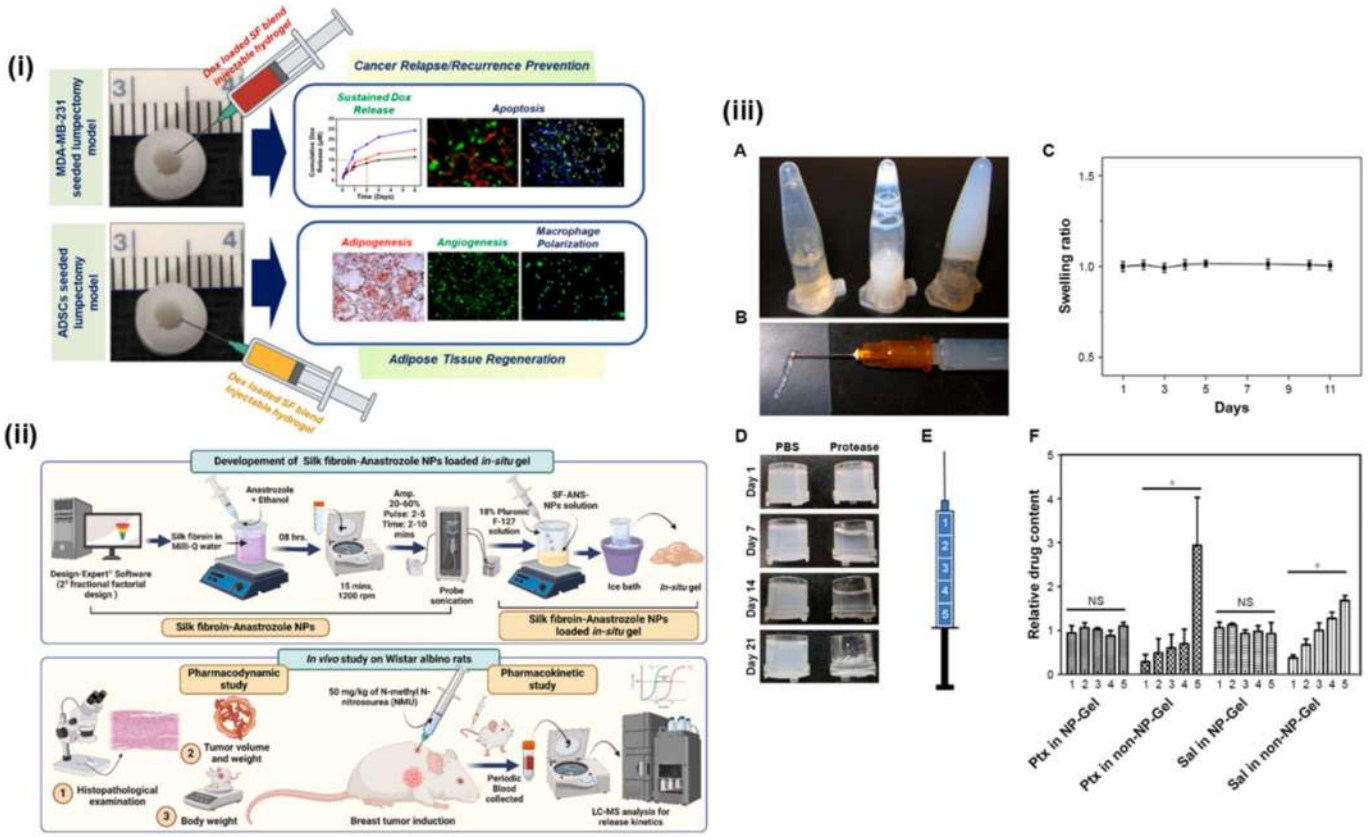

Fig. 5. (**i**) Graphical representation of SF-based hydrogel loaded DOX for TNBC treatment, reproduced with permission from Ref. [106], Copyright 2023, Elsevier. (**ii**) Schematic representation of SF-based in situ gel loaded ANS-SF nanoparticles for estrogen-positive BC therapy, reproduced with permission from Ref. [134], Copyright 2025, Taylor & Francis. (**iii**) Graphical overview of the development and characterization of Sal- PTX -NP-Gel via 26G syringe needle, swelling ratio, *in vitro* degradation study, and drug loading homogeneity, reproduced with permission from Ref. [137], under CC BY 4.0 license.

and ductility, characterized by tensile strength (1.42 MPa) and elevated elongation (124.99 %), and cumulative drug release up to 81.74 % at 120 h., based on the pH variations in media. The study further reported the hydrogel's significant anti-inflammatory and anti-cancer properties, significantly inhibiting tumor growth and improving wound healing and anti-angiogenesis of tumor cells. Thus, SF-based composite hydrogel is again documented as a potential therapeutic delivery system in BC therapy [135]. In another instance, to facilitate the delivery of anti-cancer molecules, Laomeephol C et al. developed dimyristoyl glycerophosphorylglycerol (DMPG)-based liposome conjugated SF system for Curcumin delivery in BC treatment. The encapsulation of curcumin in the liposomal system further improves the stability. In addition, the authors reported that the gelatin time of the liposome-based hydrogels improved from 3 mins to 6 h., due to the concentration changes in SF. The biological effectiveness of liposome-SF hydrogels was assessed using L929 fibroblasts and MDA-MB-231 BCE cells. The study further reported that curcumin could obstruct the cancer cells growth via a reduction in survival rates, which were linked to poor cell attachment and the toxic effects of curcumin. Thus, this study further confirms the SF-based hydrogel system's effectiveness in curcumin delivery or therapeutic in BC treatment [136].

A multi-drug delivery system is crucial because of the intra-tumoral heterogeneity of cancer, leading to differing drug susceptibilities. CSCs, a small fraction of tumor cells that are responsible for tumor initiation and regrowth, exhibited resistance to chemotherapeutic treatment and demonstrated a more favorable response to salinomycin (Sal) compared to PTX. Thus, Wu P and colleagues presented an innovative SF hydrogel incorporating Sal and PTX through drug-loaded SF-NPs to target both CSCs and non-CSCs effectively. The ultrasound-treated SF solution incorporated drug-loaded SF-NPs before the gelation process. The SF hydrogel (Sal- PTX -NP-Gel) maintained its injectable characteristics, exhibited biodegradability, and showed a more consistent drug distribution than hydrogels without NP incorporation, as shown in Fig. 5 (**iii**). In a murine hepatic carcinoma H22 subcutaneous tumor model, Sal- PTX -NP-Gel exhibited better tumor growth inhibition than both the single drug-loaded hydrogel and the systemic dual drug treatment. In addition, the study further reported that Sal- PTX -NP-Gel significantly reduced the presence of $CD44^+$ and $CD133^+$ tumor cells and demonstrated the lowest tumor growth in the tumor seeding experiment. These findings suggest that the SF-NPs integrated into SF hydrogel constitute a promising drug delivery system, with Sal- PTX -NP-Gel potentially serving as a novel and effective locoregional tumor treatment strategy [137].

The injectable SF-based hydrogel has emerged as an effective platform for localized cancer therapy. To explore the further potential, Gou S et al. investigated hydrophilic SF (HSF)-based DOX/Cy7-loaded hydrogel (DOX/Cy7-hydrogel) combined with NIR irradiation for significant viscoelasticity, thixotropic properties, and self-healing capabilities. The proposed system further enhances the most effective antitumor response compared to all other treatment groups, demonstrating the notable synergistic effects of chemotherapy, photothermal therapy, and photodynamic therapy. In addition, the DOX/Cy7-hydrogel successfully eradicated almost all tumor masses and greatly extended the survival of mice with tumors to over 60 days, without any noticeable negative side effects. These results indicate that the injectable DOX/Cy7-hydrogel, given its thixotropic properties and responsiveness to multiple stimuli, could serve as an effective platform for targeted and combined cancer treatment [138].

6. SF-based hydrogel/ scaffolds delivery systems for BC treatment

6.1. Hydrogel

BC is one of the common prevalent malignancies in women, and although therapies exist, their efficacy differs within people. The two-dimensional models are frequently employed to create novel therapies. Several macromolecules derived from marine and terrestrial sources can generate biopolymers (i.e., polysaccharides including chitosan, HA, alginate, and cellulose) and bioactive constituents (i.e., gelatin, collagen, and SF) in hydrogels possessing suitable physical characteristics pertaining to porosity, rheology, and mechanical strength [139].

The invasive cancerous cells modify the migratory phenotype in accordance to mechanical and metabolic signals from the ECM. Mesenchymal migration is characterized through significant cell-matrix adhesions and extended morphological structure whereas amoeboid migration is identified through limited cell-matrix adhesions and a round structure. Therefore, elucidating the involvement of matrix mechanics and biochemistry remains problematic, as both are interdependent upon ECM protein concentration. Khoo AS et al. produced a composite hydrogel of SF and collagen I, wherein rigidity and microstructure could be systematically adjusted across a broad spectrum. They demonstrated the proliferation of metastatic BC cells indicates a biphasic relationship with SF concentration at a constant concentration of collagen I, at first it rises with increasing hydrogel firmness, and then experiences decline in the size of the pores of SF diminishes. Mesenchymal morphology demonstrated a biphasic dependency on SF concentration, but amoeboid morphologies are preferred under conditions of diminished cell-matrix adhesion efficacy. They employed exogenous biochemical therapy to induce enhanced contraction and a mesenchymal shape in cells, in addition to disrupting cytoskeletal activity to facilitate an amoeboid morphology. They anticipated that the adjustable biomaterial in a 96-well plate could be extensively utilized to evaluate the migration of cancer cell in response to various forms of engineered biomaterials and targeted inhibitors [140].

In general, the postoperative exposure to radiation is the conventional approach for preventing BC regrowth and metastasis [141]; however, radiation resistance and unavoidable skin radiation damage remains significant challenge in BC prognosis. Zhang Z et al., internally implanted biodegradable hydrogel and extracutaneous useful for antioxidant bioadhesive were developed to avoid post- surgery tumor development and radioactive injury of skin followed by simultaneous radiotherapy. The study involved a biodegradable SF/perfluorocarbon hydrogel encapsulating DOX, designed through subsequent ultrasonication-induced β-sheet cross-linking of amphiphilic SF/perfluorocarbon/DOX nanoemulsion, as shown in Fig. 6 (**i**). The hydrogel demonstrated a sustained release of oxygen in physiological environment to enhance hypoxia and radiation therapy sensitivity, alongside a simultaneous release of DOX to ultimately attain an efficient anti-cancer impact. A stretchy bioadhesive was synthesized by copolymerization of α-thioctic acid and N, N-diacryloyl-L-lysine, incorporating gold nanorods and gallic acid to provide mild photothermal therapy and antioxidant properties. The controlled release of gallic acid formed through NIR light, along with minimal photothermal therapy, effectively eradicated excessive free radicals produced by radiation and enhanced radioactive healing of wound. Animal study confirmed the effectiveness of our approach, demonstrating that the administration of hydrogel post tumor removal, alongside the usage of bioadhesive patch with an antioxidant property, significantly prevented tumor regrowth and restricted the growth of radiation skin injury [142]. BC is the common dominant malignancies among women globally, and adjuvant radiation therapy (RT) subsequent to tumor eradication is one of the most frequently used therapies for the disease. However, the significant chance of recurrence of the tumor and unavoidable radiation-induced skin damage post radiotherapy persist as major issues, significantly hampering the patient's recovery after surgery. In this context, Zhang Z et al. developed a multifunctional poly (lipoic acid)-based hydrogel by single step heating of a mixture which includes α-LA, Arg, and SF, without the incorporation of any synthetic components. Numerous synergistic relationships between LA, SF, and Arg not only improved the LA solubilization in aqueous environments but also stabilized poly (lipoic acid) via resistant salt bridge hydrogen bridges and ionic hydrogen bonds. The surfactant

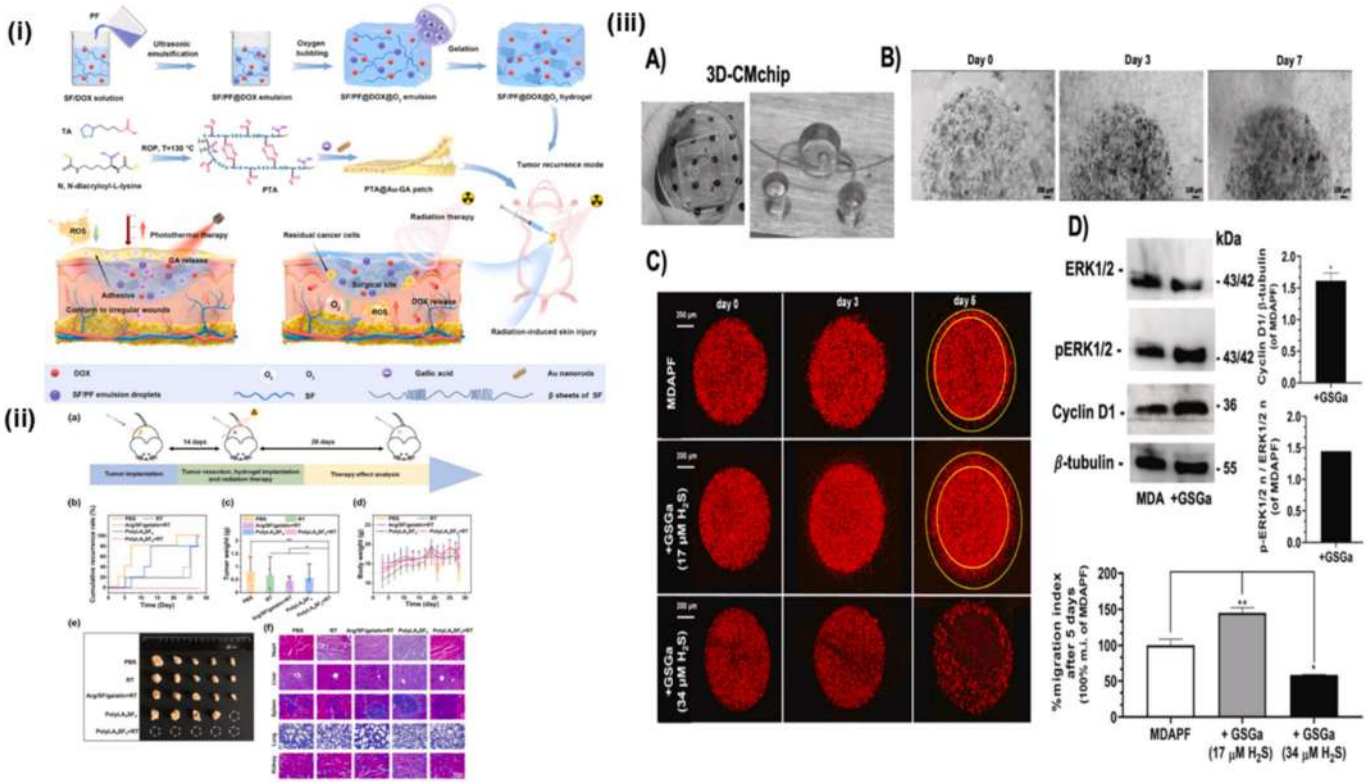

Fig. 6. (**i**) A diagrammatic representation of the creation of SF/PF@DOX hydrogel and PTA@Au-GA patch, along with their use in the management of BC recurrence and skin damage caused by radiation, reproduced with permission from Ref. [142], under CC BY-NC-ND 4.0. (**ii**) Summarization of treatment results of multi-functional poly (lipoic acid)-based hydrogel loaded α-LA/ Arg/ SF. The local suppression of breast cancer regrowth after surgery. (a) A diagram showing the setup and treatment approach for an *in vivo* 4T1 breast cancer recurrence model. (b) The cumulative recurrence rates of mice across various treatment groups. (c) Tumor weights of mice in different treatment groups. (d) Body weights of mice bearing 4 T1 tumors. (e) Photographs of representative tumors following various treatments on day 28. (f) H&*E*-stained microscopy images of the heart, liver, spleen, lungs, and kidneys after various treatments, reproduced with permission from Ref. [143], under CC BY-NC-ND 4.0. (**iii**) Various results of GSGa treatment effect on MDAPFs cell migration on (**A**) 3D culture chip (**B**) Micrographs of the MDAPFs (3 μl, 104 cells/μl) after 0, 3 and 7 days of cell growth (**C**) Invasion assay of MDAmCherryPFs in the 3DCM-chip monitored for 5 days (**D**) Estimation of ERK 1/2, p-ERK 1/2 and cyclin D1 expression in 3D culture cells, reproduced with permission from Ref. [144], under CC BY 4.0.

from LA induced β-sheet transformation of SF, which further influenced the bulk strength of the hydrogel. Modulating the concentration of LA in hydrogels facilitated effective management of hydrogel bioactivity and permitted the transition of hydrogels from intravenous to sticky patches. In spite of numerous biological properties and shapes, hydrogels could be implanted both internally or applied externally to the mice skin, effectively preventing tumor recurrence after surgery while aiding the management of radiation-induced skin damage following radiotherapy [143], as summarized in Fig. 6 (**ii**).

In addition, the 3D cell cultivation techniques offer more physiologically appropriate data, accurately reflecting the true environment in which cells exist within tissues. However, the variations between TCP and 3D culture systems related to tumor cell development, proliferation, migration, differentiation, and response to therapy remains inadequately defined. Buonvino S et al. designed tumoroid microspheres harboring the BC cell line MDA-MB 231, utilizing either the adjustable PFs or tunable PSFs hydrogels, designated as MDAPFs and MDAPSFs, respectively. The cancerous cells within the tumoroids exhibited alterations in both globular shape and protein expression levels. A reduction in Histone H3 acetylation and cyclin D1 expression was observed in all three-dimensional systems, comparative to the two-dimensional cell culture, corresponding with alterations in matrix rigidity. The impact of GSGa, a mild H2S-releasing donor, was examined across both tumoroid systems. A pro-apoptotic effect of GSGa on tumor cell development in two-dimensional culture was noted, in contrast to proliferative effect observed in both MDAPFs and MDAPSFs. A specialized ad hoc three-dimensional cell migration chip was developed and refined for the investigation of tumor cell invasion in a gel-in-gel arrangement. The GSGa exhibited an anti-cell-invasion impact in two-dimensional cell culture, considering a pro-migratory effect was noted in both MDAPFs and MDAPSFs during the three-dimensional cell migration chip assay. An elevation in expression of cyclin D1 following GSGa therapy was noted, correlating an increase in the cell invasion index. Their findings indicated that the "dimensionality" and rigidity of the three-dimensional cell culture environment can alter the way cells react to the gaso-transmitter H2S and DOX, attributable to variations in H2S diffusion and modifications in protein expression. Furthermore, they identified a direct correlation between expression of cyclin D1 and the rigidity of the three-dimensional cell culture environment, indicating the possible causal role of cyclin D1 as a biomarker for tumor cell sensitivity to matrix stiffness. Consequently, the hydrogel-based tumoroids serve as a viable and adjustable model for examining the induced physical trans-differentiation of cancer cells [as depicted the outcomes in Fig. 6 (**iii**)], as well as a more dependable and predictable platform for assessing the impact of anti-tumor medications [144].

The reconstructive surgery is a multifaceted and challenging inter-disciplinary subject due to the manufacturing of large, implantable, cost-effective bio-prostheses, which include breast implants. The study by Mehrabi A et al. addressed the fabrication of porous hybrid hydrogels by combinatorial technique utilizing dHplacenta and SF. Histology has been utilized to verify the cellularity of the dHplacenta. The physico-chemical parameters of the hydrogels were assessed using FTIR, SEM, and rheological analysis. The developed hydrogels displayed a consistent three-dimensional microstructure featuring an interrelated porosity

network, whereas the hybrid hydrogels with a ratio of 30:70 illustrated enhanced mechanical properties in comparison to the other hydrogels. The hybrid hydrogels were cultivated with ADSCs and liposuction was employed to extract adipose tissues from patients, which were later examined by flow cytometry and karyotyping. The findings indicated the decrease in CD34 and CD31, whereas CD105 and CD90 was found to be increased in ADSCs, suggesting a phenotype similar to that of MSCs derived from human bone marrow. Furthermore, following the re-cellularization of the hydrogel, the live/dead assays and SEM study demonstrated that the majority of viability and cellular proliferation in the hydrogels had greater percentage of dHplacenta than other two groups. All these data suggested that the 30:70 dHplacenta/SF hydrogel served as an exceptional platform for breast tissue engineering [131].

Several investigations, i.e., *Bombyx mori* SF (BMSF)/ *Antheraea assamensis* derived SF (AASF), XG hydrogel/SF/Fe_3O_4 [146], enzymatically-crosslinked SF (eSF)/ Human MCF7 BC cells [147], MSN/ SH/ SF/ O-CMC [148], $CaCO_3$ /4T1 cells-DCs fusion cells (FP) / SF [149], polydopamine crosslinked collagen/ SF /thrombin [128], acacia hydrogel/natural SF protein/polyvinyl alcohol/iron oxide nanoparticles [151], chitosan/ SF nanoparticles (SFNPs)/ DOX (DOXSFNPs)/ CuO/ TiO_2 nanoparticles (CTNPs) [152], AdECM/ SF [129], PEG/ SF [154], etc., further utilized the SF-based hydrogel systems for BC treatment.

6.2. Scaffold

A comprehensive examination for cancer biology has resulted in the creation of several 3D culture techniques that more accurately replicate *in vivo* environments. TME is influenced by immediate interactions between cancer-associated cells, cancer cells, and the ECM. Dondajewska E et al. designed a three-dimensional BC model, acknowledging the necessity to integrate tissue dimensionality and cellular heterogeneity. NIH3T3 fibroblasts and EMT6 BC cell lines were inoculated in diverse ratios onto a SF scaffold. The scaffold's porosity was adjusted to enhance the proliferation of cancerous cells. EMT6 and NIH3T3 cells were altered to express GFP and turboFP635, respectively, enabling direct examination of cell shape and scaffold colonization, as well as allowing the segregation of cells post co-culture. The application of 3D monoculture and 3D co-culture techniques led to alterations in cell morphology and a substantial enhancement in ECM synthesis. The culture techniques also prompted cellular alterations associated with EMT and CAF markers. The proposed model is a readily manufacturable, well-defined instrument for investigating processes within the TME [120].

The electrospun hybrid nanofibrous scaffolds have become more significant in tissue engineering and applications involving drug delivery due to their diverse characteristics. This study by Laiva AL et al. explored the capabilities of composite PCL/SF nanofibrous scaffolds as a possible scaffold for cell development as well as a drug-eluting mat to regulate the MCF-7 cells. Titanocene dichloride was selected as the model compound to investigate its anti-cancer activity on cell-lines of MCF-7. Intriguing characteristics of the crystallization of SF and drug binding have also been examined for the regulated drug release. The residues of amino acid in SF significantly influenced cell-scaffold interactions, drug binding properties, and release features that regulate cell proliferation. Research on the material features of hybrid nanofibrous scaffolds revealed interconnected variations in fibre diameter and mechanical properties for the nanofibers with drug loaded. A notable reduction in fibre diameters and a significant rise in tensile strength were reported for drug-loaded scaffolds compared to PCL fibers. A study on cell viability and morphology was conducted to evaluate the impact of varying doses of titanocene dichloride incorporated into PCL/SF nanofibrous scaffolds. The maximum percentage of cell viability inhibition decreased, compared to 0.01 % on day 3. The results demonstrated that the hybrid mat with drug-loaded effectively regulated the development of MCF-7 cells at various time intervals and functions as a role model for cancer treatment [155].

A comprehensive strategy employing a combination of anti-cancer nanotherapeutics and natural biomaterials, specifically SF and CS blended scaffolds, were examined for the medical treatment of tissue defects following tumor surgery. This approach aimed to facilitate localized therapeutic release and to fill the area of defect with regenerative bio-scaffolds. Gupta V et al. developed and analyzed scaffold-emodin nanoparticle composites for drug entrapment, drug release, mechanical strength, and effectiveness against GILM2 BC cells in rat model. Emodin NPs were incorporated into SF and SFCS scaffolds, with an extent of emodin entrapment depending upon the scaffold composition and emodin loaded concentration. A rapid release of emodin occurred from scaffolds within an initial of 2 days, which was also later detected after 24 days. An elevated level in concentration of emodin within the scaffolds resulted in a reduction of both elastic modulus and the final tensile strength of the scaffolds. Subsequently in a 6-week *in vivo* implantation, the cell density and percentage of degradation found no emodin SFCS scaffold were considerably increased than those in the emodin-loaded SFCS scaffolds; however, no substantial variation in collagen deposition was found among the renewed SFCS scaffold. The existence and disappearance of emodin from the SFCS scaffolds hindered the integration of SFCS into the surrounding tumor by creating an interfacial barrier of connective tissue, which was absent in emodin-free SFCS scaffolds, as summarized the potential outcomes in Fig. 7 (**i**). No significant variance in tumor size was noted among the *in vivo* tested groups; however, tumors treated with emodin-loaded SFCS scaffolds exhibited reduced appearance and size, including comparable regrowth of new tissue when contrasted with non-emodin SFCS scaffolds [156].

The epithelial-stromal interaction is essential in healthy embryonic growth and breast carcinogenesis in humans, however the mechanisms behind these processes are inadequately recognized. In order to address this problem, Wang X et al. developed a 3D physiologically relevant culture model of intricate human breast tissue, incorporating a tri-culture system consisting of human fibroblasts, MCF10A, and adipocytes— the two primary breast stromal cell types—within a Matrigel™/collagen composite on porous silk protein scaffolds. The stromal cells increased alveolar and ductal morphogenesis, decreased MCF10A cell growth, and elevated casein expression. Despite the immature polarity produced by co-cultures with fibroblasts or adipocytes, the alveolar structures produced by tri-cultures demonstrated appropriate polarity like that found *in vivo* breast tissue. The alveolar structures only exhibiting reversed polarity were identified in MCF10A monocultures. In accordance with the phenotypic characteristics, enhanced functional differentiation of epithelial cells was noted in the tri-cultures, where casein α- and β mRNA expression was markedly elevated. The *in vitro* tri-culture breast tissue system supported by SF scaffold more effectively simulated a physiologically relevant 3D environment for mammary epithelial and stromal cells compared to co-cultures or monocultures, as shown in Fig. 7 (**ii**). This experimental model represented a significant initial advancement in the development of a human breast tissue system, facilitating the investigation of normal breast morphogenesis and neoplastic transformation [157].

In general, cell cultures or xenografts are insufficient methods for elucidating the intricate biology of cancer. The 3D tumor models have drawn the attention because of their superior capability to replicate the dynamic processes that lead to cancer; yet, a definitive model that accurately simulates solid tumors remains unknown. Brancato V et al. produced a 3D BC model developed from freeze-dried SF scaffolds. MCF-7 and MDA-MB231the BC cell lines were inoculated with normal breast fibroblasts onto SF scaffolds. Proliferation of cells is assessed using the Alamar Blue test and the morphology of 3D BC models is examined using confocal microscopy. The modification of gene expression related to ECM indicators was assessed. Additionally, three-dimensional bio-engineered BC models were treated with DOX. SF scaffolds facilitated the development of cancer cells and fibroblasts. The proliferation of cells improved when cancerous cells and fibroblasts were co-cultured. Histological staining revealed three-dimensional cell structure. The expression of MMP-1, MMP-2, MMP-3, Col-1, and Fibronectin increased

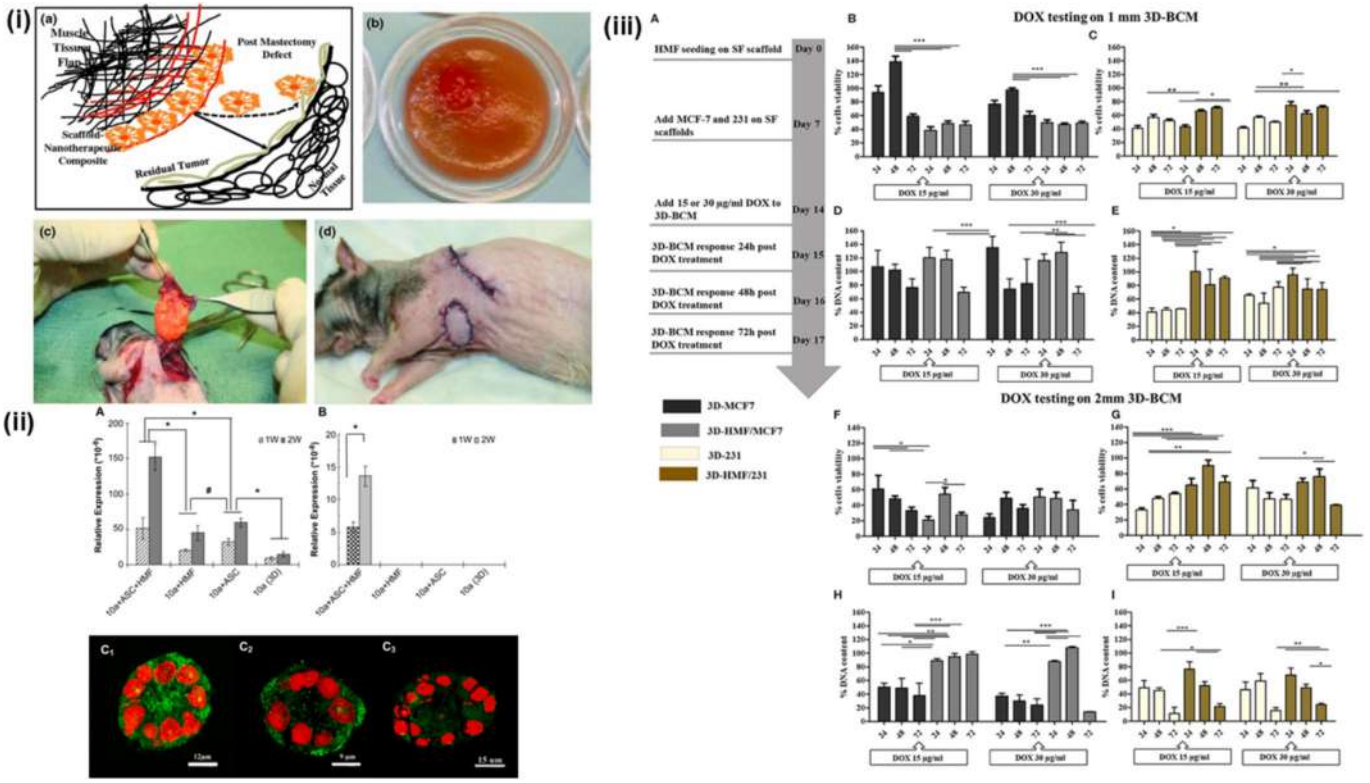

Fig. 7. (**i**) (**a**) Depicted the mechanism of development of SFCS/ emodin nanoparticle- latissimus dorsi muscle (LDM) flap composite scaffold in breast tissue reconstruction. (**b**) Depicted emodin+ SFCS scaffold in petri dish culture. (**c**) During the treatment of breast tissue area, the scaffold loaded with emodin was stitched to the underside of the latissimus dorsi muscle (LDM) flap. (**d**) Depicted the wound closure after implantation of SF-based scaffold at tumor site, reproduced with permission from Ref. [156], under CC BY-NC 2.0. (**ii**) Estimation of (**A**) α-casein, and (**B**) β-casein via RT-PCR of the treatment via human fibroblasts, MCF10A, and adipocyte within a Matrigel™/collagen composite on porous silk protein scaffolds, reproduced with permission from Ref. [157], under CC BY 4.0. (**iii**) DOX treatment on 3D BC model involved evaluating drug activity at 24, 48, and 72 h., starting on Day 14 of culture. The anti-proliferative effects of DOX on 3D-MCF7 and 3D-HMF/MCF7 (**B, F**) and 3D-231 and 3D-HMF/231 (**C, G**) were assessed using Alamar blue assay in 1 mm and 2 mm SF scaffolds. The dsDNA levels in these models were measured after 24, 48, and 72 h., of treatment (**D, E**) for 1 mm and (**H, I**) for 2 mm SF scaffolds, reproduced with permission from Ref. [158], under CC BY 4.0.

in co-culture conditions, as summarized in comprehensive Fig. 7 (**iii**). Post-DOX treatment, a more pronounced decrease in cellular activity was noted in the SF scaffold of 2 mm relative to the 1 mm scaffold. The three-dimensional BC model designed could be readily expanded and adapted for preclinical evaluation of innovative chemotherapeutics [158]. In addition, several investigations, i.e., SF / HFIP [159], 3D porous SF / PTX /Celecoxib/ZD6474 [160], SF /poly (ethylene oxide) (PEO) [161], granular NaCl particles/ SF solution [162], silk-fibroin (SF) scaffold/ GelMA hydrogel [163], etc., further shown promising advantages of SF-based scaffolds for BC treatment.

6.3. Others

In regard to recent advancements in cancer therapy, the exploration of alternative approaches has arisen because of the increase cost of current chemotherapy treatments, its adverse reactions, and the prolonged process required for regulatory approval of novel cancer therapies. In this regard, the utilization of carcino-preventive therapies, specifically plant polyphenols, presented a novel alternative to handle and resolve these problems. Radinekiyan F et al. designed a novel magnetic nanobiocomposite through the synthesis of cross-linking of Alg hydrogel utilizing $CaCl_2$ as a cross-linking agent, and its alteration by flaxseed mucilage hydrogel, and SF biopolymer extraction, alongside the in-situ synthesis of Fe_3O_4 MNPs within this biopolymeric matrix, as shown in Fig. 8 (**i**). The analytical studies of XRD, FT-IR, VSM, FE-SEM, EDX, and TG elucidated the physicochemical characteristics of the magnetic cross-linked Alg/flaxseed mucilage hydrogel/SF nanobiocomposite. The subsequent structural analysis of this magnetic natural-origin composition, toxicity and hemolysis assays were conducted at various concentrations that revealed significant biological results, as shown in Fig. 8 (**ii**). Survival rates for normal HEK293T cells and BT549 BC cells after 48 and 72 h., confirmed the biocompatibility and anti-cancer efficacy of this novel nanobiocomposite. Furthermore, fewer than 5 % of the hemolytic effect demonstrated its hemocompatibility. Moreover, a specific rate of absorption was produced by the magnetic nanobiocomposite. It may be concluded that the magnet responsive cross-linked Alg/flaxseed mucilage hydrogel/SF nanobiocomposite was capable of effectively functioning in magnetic hyperthermia therapy [164].

7. SF-based hydrogel/ scaffolds for diagnosis (bio-imaging, biosensor) of BC

SF-based hydrogels are emerging as promising biomaterials for biomedical applications, including cancer diagnosis and treatment. Their unique properties, such as biocompatibility, biodegradability, mechanical robustness, and tunable physicochemical characteristics, make them highly suitable for developing diagnostic platforms, especially for BC. The gelation technique can be regulated to achieve precise stiffness, porosity, and degradation rates, which are critical for biosensing and tissue interchange. The chemical structure of SF allows for straightforward conjugation with biomolecules such as antibodies, peptides, and enzymes, thus improving its diagnostic potential [165–167]. SF hydrogels can serve as substrates for microfluidic sys- tems, enabling the capture and analysis of circulating tumor cells, exosomes, or biomarkers. SF hydrogels can be engineered with

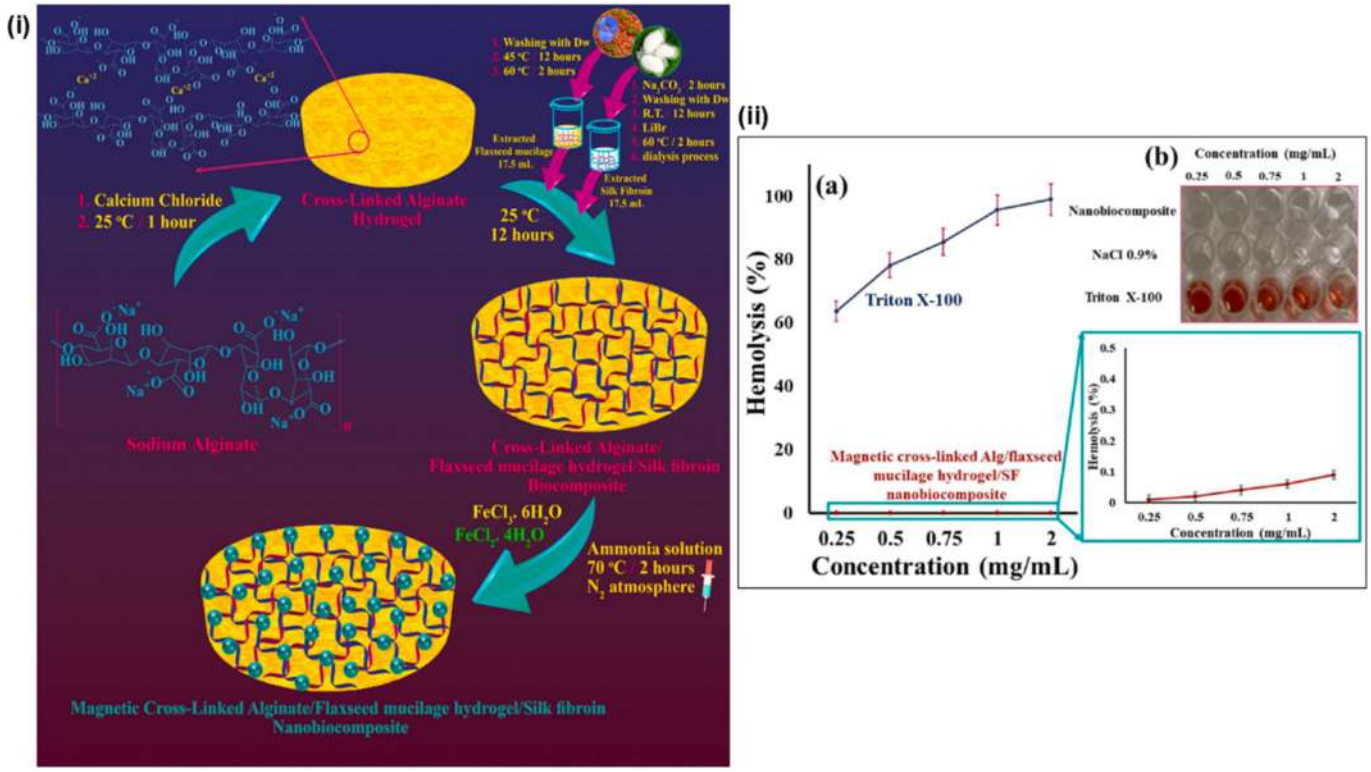

Fig. 8. (**i**) Summarized the graphical representation of the development of magnetic cross-linked Alg/flaxseed mucilage hydrogel/SF nanobiocomposite. (**ii**) Depicted (**a**) hemolysis percentage graph, and (**b**) hemolysis plate images at different concentrations of magnetic cross-linked Alg/flaxseed mucilage hydrogel/SF nanobiocomposite, 0.9 % sterile sodium chloride solution as negative control, and Triton X-100 as positive control, reproduced with permission from Ref. [164], under CC BY-NC 4.0.

functionalized probes for specific BC markers like HER2, CA153, or estrogen/progesterone receptors, allowing sensitive detection. When integrated with conductive materials, SF hydrogels can facilitate real-time monitoring of BC biomarkers [168–171]. SF hydrogels mimic the ECM of breast tissue, making them excellent scaffolds for developing 3D tumor models. These models allow for studying tumor biology and drug response. SF hydrogels can capture circulating DNA, RNA, or proteins from body fluids (e.g., blood or saliva), enabling non-invasive BC diagnosis. Functionalized SF hydrogels with ligands or antibodies can enable tumor-specific imaging, improving the detection of early-stage BC.

The three-dimensional cell culture systems offered enhanced physiologically relevant data by better mimicking the tissue microenvironment [172]. However, the differences in tumor cell growth, proliferation, migration, differentiation, and treatment responses between tissue culture plates (TCP) and 3D cultures are still not well defined. To overcome the current challenges, Buonvino S et al. developed MDA-MB-231 BC cells-laden tunable PEG-fibrinogen (PFs) or tunable PEG- SF (PSFs) hydrogels. The study documented that the tumor cells in tumoroids exhibited decrease in expression of Histone H3 acetylation and cyclin D1 in all 3D systems compared to 2D cell culture, coinciding with alterations in stiffness of the matrix. The effects of glutathionylated garlic extract (GSGa), a slow H2S-releasing donor, were studied in two tumoroid systems. GSGa exhibited a pro-apoptotic effect on tumor cell growth in two-dimensional culture, while promoting proliferation of both MDAPFs and MDAPSFs. A specialized 3D cell migration chip was developed to study tumor cell invasion in a gel-in-gel setup. GSGa showed an anti-cell-invasion effect in 2D cultures, but a pro-migratory effect in 3D assays. Increased expression of cyclin D1 after GSGa treatment correlated with higher cell invasion rates. The study found that the stiffness of the 3D environment influences responses to H2S and DOX, impacting diffusion and protein expression. Cyclin D1 was identified as a potential biomarker for tumor cell sensitivity to matrix stiffness. Thus, these hydrogel-based tumoroids offer a reliable model for examining the physically induced trans-differentiation of cancer cells and testing anti-tumor therapies [144].

The epithelial-stromal interactions are crucial for embryonic development and breast carcinogenesis, yet their mechanisms are poorly understood. Therefore, to understand the mechanisms, Wang X et al. constructed a 3D culture model using a tri-culture system of human mammary epithelial cells (MCF10A), fibroblasts, and adipocytes within Matrigel™ and collagen on silk protein scaffolds. The stromal cells reduced MCF10A proliferation, enhanced alveolar and ductal morphogenesis, and increased casein expression. The tri-culture produced alveolar structures with appropriate polarity, unlike monocultures, which showed inverted polarity. This cutting-edge model furnishes a more specific 3D microenvironment for analyzing mammary cells, representing a significant advancement in the bioengineering of human BC [157].

An imbalance in redox homeostasis can lead to oxidative damage to cellular components, which may hinder the proliferation of cancer cells and result in tumor regression. This study presents the development of a nanosystem utilizing a metal-organic framework (NMOF) created through the coordination of Fe (III) and 4,4,4,4-(porphine-5,10,15,20-tetrayl) tetrakis (benzoic acid) (TCPP) via a one-pot synthesis method. After surface capping with SF (SF), nanoparticles (NMOF@SF) for an effective nanocarrier for tirapazamine (TPZ) delivery, which is activated under hypoxic conditions. The NS@TPZ (NST) nanoparticles demonstrated inactivity in normal tissues but showed significant efficacy upon uptake by tumor cells, where glutathione (GSH) mediates the reduction of Fe (III) to Fe (II), thus facilitating Fe (II)-dependent chemodynamic therapy (CDT). Optical laser irradiation in TCPP-driven photodynamic therapy (PDT) combined with CDT increases intracellular oxidative stress, causing ROS accumulation and GSH depletion, leading to redox

imbalance. Local deoxygenation induced by PDT enhances the cytotoxicity of released TPZ, significantly improving overall therapeutic effectiveness through the combined disruption of redox balance and bioreductive chemotherapy, as shown in Fig. 9. The combination of these treatment approaches, together with the presence of SF, can trigger immunogenic cell death, which may facilitate tumor elimination *in vivo*. This strategy offers a means to tackle tumor-specific redox imbalance through chemotherapy driven by deoxygenation, potentially improving antitumor effectiveness and minimizing side effects [175]. Although SF hydrogels have significant potential, numerous challenges must be overcome to maximize their use in BC diagnostics, such as achieving large-scale production of SF hydrogels with uniform quality. Furthermore, comprehensive preclinical and clinical evaluations are necessary, and integrating SF hydrogels with artificial intelligence (AI) and the Internet of Things (IoT) can potentially revolutionize early detection strategies.

8. Recent innovations on SF-based delivery approaches for BC therapy

Several recent innovations on SF-based delivery approaches for BC have been reported or documented in various patent database. To streamline the search strategies, this article further focused on the some of the approved or granted patent applications on SF-based delivery approaches for BC from Lens.org platform. In addition, the search strategy further includes the different geographical locations, earliest priority date, approved date, application number, etc. Table 1 further summarizes the recent innovations approved for SF-based delivery approaches in BC therapy.

9. Conclusion

Protein-based biomaterials are essential for drug delivery, providing flexible and biocompatible platforms for therapeutic applications. Materials sourced from natural or modified proteins have gained considerable attention because of their degradability, low immunogenic response, and the ability to be customized for specific biomedical uses. Protein engineering enables the precise design of structural and functional properties based on their amino acid sequences, which can be modified to incorporate chemical groups for drug attachment or responsive elements. In addition, protein-based systems can be designed to respond to external stimuli such as pH, temperature, and enzymatic activity, enabling targeted and controlled drug release. In this context, SF, a natural protein has attracted interest in BC therapy owing to its biocompatibility, biodegradability, tunable mechanical strength, and potential for functionalization [29]. SF can be engineered into nanoparticles, hydrogels, or films for the targeted delivery of chemotherapeutics such as DOX and PTX to BC cells [30–32]. The functionalization of SF with ligands, including folic acid or antibodies, facilitates targeted delivery to BC cells that overexpress specific receptors, such as folate receptors or HER2 [34–36].

Nonetheless, several issues must be resolved before viewing SF as a viable biomaterial for developing hydrogels or scaffolds in BC treatment. The main challenges in the production of raw SF include its poor aqueous solubility, brittleness, susceptibility to degradation from degumming and dissolving agents, temperature and duration factors, and the risk of bacterial growth. These issues must be thoroughly addressed before considering SF as a viable biomaterial for drug delivery applications. Natural silk protein has inherent limitations, and without the incorporation of functional composite factors such as functional nanomaterials or functional polymer materials, the pure silk protein-based hydrogels will face constraints in their practical applications [190–192]. The mechanical properties, such as strength and elasticity, of hydrogels made from SF can vary greatly based on the methods used for fabrication, the cross-linking agents chosen, and the processing conditions applied [83,84]. A balance between mechanical stability and degradability to ensure compatibility with the TME is quite challenging. SF hydrogels necessitate careful control over pore dimensions and connectivity to enable effective drug diffusion and penetration into tumors, which can be technically difficult to reproduce consistently [193,194]. Although SF hydrogels can encapsulate a range of drugs, creating a controlled and targeted release profile specifically for BC cells remains difficult due to issues with premature or burst release, potentially diminishing therapeutic effectiveness and increasing systemic toxicity [86,195]. Administering multiple agents (such as chemotherapy drugs, immunotherapy agents, or vectors for gene therapy) simultaneously within a single hydrogel often results in compatibility problems that disrupt their release rates [196–198].

In addition, BC tumors exhibit high heterogeneity in vascularization, pH, enzyme activity, and hypoxia, which can influence hydrogel degradation and drug release [199]. The adoption of SF hydrogels to such diverse microenvironments remains a major challenge. While SF hydrogels are biodegradable, their enzymatic degradation *in vivo* can vary between patients and tumor types, leading to unpredictable drug release patterns [31,64]. Despite being biocompatible, improperly purified SF or residual sericin contamination can provoke immune responses or inflammation, particularly in sensitive breast tissue [200–202]. Uncontrolled breakdown or release of encapsulated medi- cations can cause unintended effects on healthy tissues adjacent to the breast tumor. Additionally, conventional sterilization techniques like autoclaving or gamma irradiation might change the structure and performance of SF hydrogels [84,203,204]. SF hydrogels rely on the

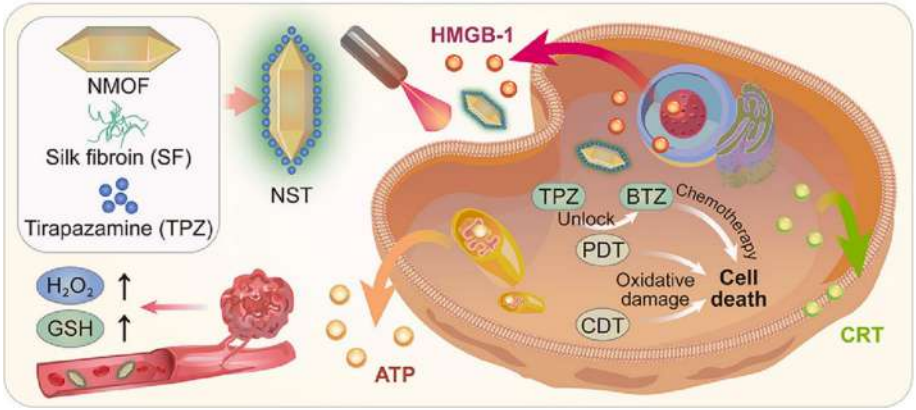

Fig. 9. A metal-organic framework capped with SF has been developed for the treatment of tumor-specific redox imbalances, enhanced by chemotherapy that is driven by deoxygenation, reproduced with permission from Ref. [175], Copyright 2022, Elsevier.

Table 1
Recent granted innovations on various SF -based delivery approaches for BC management.

Title of the innovation	Publication date	Publication year	Application number	Earliest priority date	Applicants	References
Silk fibroin hydrogels and uses thereof	06-10-2015	2015	US 201313787707 A	20-04-2009	Allergan Inc	[176]
Silk fibroin hydrogels and uses thereof	14-04-2015	2015	US 201213420334 A	20-04-2009	Altman Gregory H; Horan Rebecca L; Collette Adam L; Chen Jingsong; Allergan Inc	[177]
Compositions and soft tissue replacement methods	06-01-2015	2015	US 201213398667 A	19-08-2010	Van Epps Dennis E; Jiang Guang-Liang; Collette Adam L; Horan Rebecca L; Chen Jingsong; Altman Gregory H; Allergan Inc	[178]
Injectable silk fibroin foams and uses thereof	15-11-2016	2016	US 201214357420 A	09-11-2011	Tufts College	[179]
Compositions and improved soft tissue replacement methods	02-11-2016	2016	EP 13706876 A	16-02-2012	Allergan Inc	[180]
Active silk muco-adhesives, silk electro gelation process, and devices	01-03-2017	2017	EP 13175299 A	26-09-2008	Tufts College	[181]
Injectable silk fibroin foams and uses thereof	12-01-2017	2017	US 201615273327 A	09-11-2011	Tufts College	[179]
pH induced silk gels and uses thereof	04-07-2017	2017	US 201313933611 A	26-09-2008	Tufts College	[182]
Co-crosslinked hyaluronic acid-silk fibroin hydrogels for improving tissue graft viability and for soft tissue augmentation	01-03-2018	2018	US 201715686036 A	24-08-2016	Allergan Inc	[183]
Injectable silk fibroin particles and uses thereof	03-04-2018	2018	US 201214357443 A	09-11-2011	Tufts College; Univ of Pittsburgh—Of the Commonwealth System of Higher Education; Univ Wake Forest Health Sciences; Univ Pittsburgh Commonwealth Sys Higher Education	[184]
Functionalization of biomaterials to control regeneration and inflammation responses	10-07-2019	2019	EP 12862472 A	29-12-2011	Tufts College	[185]
Methods and compositions for preparing a silk microsphere	02-01-2019	2019	EP 13775182 A	13-04-2012	Tufts College	[186]
Preparation method of doxorubicin-loaded methyl cellulose/silk fibroin composite hydrogel	24-03-2020	2020	CN 201911300215 A	16-12-2019	Univ Anhui	[188]
Injectable silk fibroin foams and uses thereof	01-04-2020	2020	EP 12846855 A	09-11-2011	Tufts College	[179]
Innervated artificial skin	12-04-2022	2022	US 201716314169 A	01-07-2016	Tufts College	[189]
Injectable silk fibroin foams and uses thereof	18-07-2023	2023	US 201615273327 A	09-11-2011	Tufts College	[179]
Injectable silk fibroin particles and uses thereof	24-05-2023	2023	EP 12846915 A	09-11-2011	Tufts College; Univ Pittsburgh Commonwealth Sys Higher Education; Wake Forest Univ Health Services	[184]

enhanced permeability and retention (EPR) effect for passive tumor targeting. However, EPR efficacy is highly variable in BC due to differences in tumor vasculature and interstitial pressure [97,205,206]. The long-term biocompatibility, degradation behavior, and potential toxicological effects of SF hydrogels in BC patients are not yet fully understood. SF hydrogels face significant regulatory challenges in gaining approval for clinical use, including proving consistent safety, efficacy, and manufacturing reproducibility.

SF -based hydrogels have considerable promise for treating BC; however, their use in clinical settings is obstructed by various structural, functional, and translational obstacles. To overcome these challenges, it is essential to engage a multidisciplinary approach that includes material science, biomedical engineering, and oncology in order to create advanced silk-based hydrogels designed for efficient and targeted therapy for BC.

List of abbreviations

BC Breast cancer
ASR Age-standardized incidence rate
VEGF Vascular endothelial growth factor
TNBC Triple-negative breast cancer
HER2 Human epidermal growth factor receptor 2
SF Silk fibroin
NIR Near-infrared radiation
Gly Glycine
Ala Alanine
GFs Growth factors
BMP-2 Bone morphogenetic protein 2
RES Resveratrol
PDEVs Plant derived extracellular vesicles
GelMA Gelatin methacrylate
SFMA Silk fibroin methacrylate
HUVECs Human umbilical vein endothelial cells
TNF-α Tumor necrosis factor-alpha
iNOS Inducible nitric oxide synthase
Arg-1 Arginase-1
TGF-β1 Transforming growth factor beta 1

HA	Hyaluronic acid
RGD	Arginylglycylaspartic acid
MMPs	Matrix metalloproteinases
PEI	Polyethyleneimine
ROS	Reactive oxygen species
ECM	Extracellular matrix
PI3K	Phosphoinositide 3-kinase
MAPK	Mitogen-activated protein kinase
mTOR	Mammalian target of rapamycin
JNK	c-Jun N-terminal kinase
AuNPs	Gold nanoparticles
FGF	Fibroblast growth factor
AdECM	Adipose-derived decellularized ECM
GB	Glioblastoma
dHplacenta	Decellularized human placenta
EA	Ellagic acid
TME	Tumor microenvironment
ER+	Estrogen-positive
CSCs	Cancer stem cells
PTX	Paclitaxel
DOX	Doxorubicin
RT	Radiation therapy
CDT	Chemodynamic therapy

CRediT authorship contribution statement

Shubhrajit Mantry: Writing – review & editing, Writing – original draft, Visualization, Supervision, Resources, Formal analysis, Data curation, Conceptualization. **Kotaiah Silakabattini:** Writing – review & editing, Writing – original draft, Resources, Formal analysis, Data curation. **Prabhat Kumar Das:** Writing – review & editing, Writing – original draft, Formal analysis. **Jonna Sankaraiah:** Writing – review & editing, Writing – original draft, Supervision, Formal analysis. **Chandra Shekhar Barik:** Writing – review & editing, Writing – original draft. **Satyajit Panda:** Writing – review & editing, Writing – original draft, Formal analysis, Data curation, Conceptualization. **Shadma Wahab:** Writing – review & editing, Writing – original draft, Visualization, Resources, Formal analysis. **Mohammad Khalid:** Writing – review & editing, Writing – original draft, Visualization, Formal analysis.

Informed consent statement

Not applicable.

Funding source

The authors extend their appreciation to the Deanship of Research and Graduate Studies at King Khalid University for funding this work through Small Research Project under grant number RGP.1/30/45.

Declaration of competing interest

The authors declare that they have no known competing financial interests or personal relationships that could have appeared to influence the work reported in this paper.

Acknowledgements

The authors would like to acknowledge to their parent organizations/ institutes for providing the support to conduct various literature of review. The Graphical abstract and Fig. 1 were drawn via Biorender.com.

Data availability

No data was used for the research described in the article.

References

[1] S. Nag, O. Mitra, G. Tripathi, I. Adur, S. Mohanto, M. Nama, S. Samanta, B.H. J. Gowda, V. Subramaniyan, V. Sundararajan, V. Kumarasamy, Nanomaterials-assisted photothermal therapy for breast cancer: state-of-the-art advances and future perspectives, Photodiagn. Photodyn. Ther. 45 (2024) 103959, https://doi.org/10.1016/j.pdpdt.2023.103959.

[2] K. Sathishkumar, M. Chaturvedi, P. Das, S. Stephen, P. Mathur, Cancer incidence estimates for 2022 & projection for 2025: Result from National Cancer Registry Programme, India, Indian J. Med. Res. 156 (2022) 598–607, https://doi.org/10.4103/ijmr.ijmr_1821_22.

[3] V. Kulothungan, T. Ramamoorthy, K. Sathishkumar, R. Mohan, N. Tomy, G. J. Miller, P. Mathur, Burden of female breast cancer in India: estimates of YLDs, YLLs, and DALYs at national and subnational levels based on the national cancer registry programme, Breast Cancer Res. Treat. 205 (2024) 323–332, https://doi.org/10.1007/s10549-024-07264-3.

[4] A.N. Giaquinto, H. Sung, K.D. Miller, J.L. Kramer, L.A. Newman, A. Minihan, A. Jemal, R.L. Siegel, Breast cancer statistics, CA Cancer J. Clin. 72 (2022) (2022) 524–541, https://doi.org/10.3322/caac.21754.

[5] World Cancer Research Fund, Breast cancer Statistics. https://www.wcrf.org/preventing-cancer/cancer-statistics/breast-cancer-statistics/, 2024. (Accessed 24 November 2024).

[6] National Cancer Institute, Cancer Stat Facts: Female Breast Cancer. https://seer.cancer.gov/statfacts/html/breast.html, 2024.

[7] B. Han, R. Zheng, H. Zeng, S. Wang, K. Sun, R. Chen, L. Li, W. Wei, J. He, Cancer incidence and mortality in China, Journal of the National Cancer Center 4 (2024) (2022) 47–53, https://doi.org/10.1016/j.jncc.2024.01.006.

[8] F.Z. Francies, R. Hull, R. Khanyile, Z. Dlamini, Breast cancer in low-middle income countries: abnormality in splicing and lack of targeted treatment options, Am. J. Cancer Res. 10 (2020) 1568–1591.

[9] O. Ginsburg, F. Bray, M.P. Coleman, V. Vanderpuye, A. Eniu, S.R. Kotha, M. Sarker, T.T. Huong, C. Allemani, A. Dvaladze, J. Gralow, K. Yeates, C. Taylor, N. Oomman, S. Krishnan, R. Sullivan, D. Kombe, M.M. Blas, G. Parham, N. Kassami, L. Conteh, The global burden of women's cancers: a grand challenge in global health, Lancet 389 (2017) 847–860, https://doi.org/10.1016/S0140-6736(16)31392-7.

[10] H. Sung, J. Ferlay, R.L. Siegel, M. Laversanne, I. Soerjomataram, A. Jemal, F. Bray, Global Cancer Statistics, GLOBOCAN estimates of incidence and mortality worldwide for 36 cancers in 185 countries, CA Cancer J. Clin. 71 (2021) (2020) 209–249, https://doi.org/10.3322/caac.21660.

[11] S. Shiovitz, L.A. Korde, Genetics of breast cancer: a topic in evolution, Ann. Oncol. 26 (2015) 1291–1299, https://doi.org/10.1093/annonc/mdv022.

[12] M. Mahdavi, M. Nassiri, M.M. Kooshyar, M. Vakili-Azghandi, A. Avan, R. Sandry, S. Pillai, A.K.-Y. Lam, V. Gopalan, Hereditary breast cancer; genetic penetrance and current status with BRCA, J. Cell. Physiol. 234 (2019) 5741–5750, https://doi.org/10.1002/jcp.27464.

[13] G.V. Dall, K.L. Britt, Estrogen effects on the mammary gland in early and late life and breast cancer risk, Front. Oncol. 7 (2017) 110, https://doi.org/10.3389/fonc.2017.00110.

[14] P. Tagde, A. Najda, K. Nagpal, G.T. Kulkarni, M. Shah, O. Ullah, S. Balant, Md. H. Rahman, Nanomedicine-based delivery strategies for breast cancer treatment and management, Int. J. Mol. Sci. 23 (2022), https://doi.org/10.3390/ijms23052856.

[15] K. Brennan, G. Offiah, E.A. McSherry, A.M. Hopkins, Tight junctions: a barrier to the initiation and progression of breast cancer? J. Biomed. Biotechnol. 2010 (2010) 460607 https://doi.org/10.1155/2010/460607.

[16] K.E. de Visser, J.A. Joyce, The evolving tumor microenvironment: from cancer initiation to metastatic outgrowth, Cancer Cell 41 (2023) 374–403, https://doi.org/10.1016/j.ccell.2023.02.016.

[17] M.I. Nounou, F. ElAmrawy, N. Ahmed, K. Abdelraouf, S. Goda, H. Syed-Sha-Qhattal, Breast cancer: conventional diagnosis and treatment modalities and recent patents and technologies, Breast Cancer (Auckl.) 9 (2015) 17–34, https://doi.org/10.4137/BCBCR.S29420.

[18] B. Liu, H. Zhou, L. Tan, K.T.H. Siu, X.-Y. Guan, Exploring treatment options in cancer: tumor treatment strategies, Signal Transduct. Target. Ther. 9 (2024) 175, https://doi.org/10.1038/s41392-024-01856-7.

[19] M. Will, J. Liang, C. Metcalfe, S. Chandarlapaty, Therapeutic resistance to anti-oestrogen therapy in breast cancer, Nat. Rev. Cancer 23 (2023) 673–685, https://doi.org/10.1038/s41568-023-00604-3.

[20] H. Yao, G. He, S. Yan, C. Chen, L. Song, T.J. Rosol, X. Deng, Triple-negative breast cancer: is there a treatment on the horizon? Oncotarget 8 (2017) 1913–1924, https://doi.org/10.18632/oncotarget.12284.

[21] L. Yin, J.-J. Duan, X.-W. Bian, S. Yu, Triple-negative breast cancer molecular subtyping and treatment progress, Breast Cancer Res. 22 (2020) 61, https://doi.org/10.1186/s13058-020-01296-5.

[22] F. Lüo¨nd, S. Tiede, G. Christofori, Breast cancer as an example of tumour heterogeneity and tumour cell plasticity during malignant progression, Br. J. Cancer 125 (2021) 164–175, https://doi.org/10.1038/s41416-021-01328-7.

[23] R.E. Ellsworth, H.L. Blackburn, C.D. Shriver, P. Soon-Shiong, D.L. Ellsworth, Molecular heterogeneity in breast cancer: state of the science and implications for patient care, Semin. Cell Dev. Biol. 64 (2017) 65–72, https://doi.org/10.1016/j.semcdb.2016.08.025.

[24] S. Al Sukhun, S. Temin, C.H. Barrios, N.Z. Antone, Y.C. Guerra, M. Chavez-MacGregor, R. Chopra, M.A. Danso, H.L. Gomez, N.M. Homian, A. Kandil, B. Kithaka, B. Koczwara, B. Moy, G. Nakigudde, F.E. Petracci, H.S. Rugo, N.S. El Saghir, B.K. Arun, Systemic treatment of patients with metastatic breast cancer:

ASCO resource–stratified guideline, JCO Glob Oncol (2024) e2300285, https://doi.org/10.1200/GO.23.00285.
[25] A. Rai, S.G. Deshpande, A. Vaidya, R.K. Shinde, Advancements in immunotherapy for breast cancer: mechanisms, efficacy, and future directions, Cureus 16 (2024) e68351, https://doi.org/10.7759/cureus.68351.
[26] H.-J. Wu, P.-Y. Chu, Recent discoveries of macromolecule- and cell-based biomarkers and therapeutic implications in breast cancer, Int. J. Mol. Sci. 22 (2021), https://doi.org/10.3390/ijms22020636.
[27] M. Chehelgerdi, M. Chehelgerdi, O.Q.B. Allela, R.D.C. Pecho, N. Jayasankar, D. P. Rao, T. Thamaraikani, M. Vasanthan, P. Viktor, N. Lakshmaiya, M.J. Saadh, A. Amajd, M.A. Abo-Zaid, R.Y. Castillo-Acobo, A.H. Ismail, A.H. Amin, R. Akhavan-Sigari, Progressing nanotechnology to improve targeted cancer treatment: overcoming hurdles in its clinical implementation, Mol. Cancer 22 (2023) 169, https://doi.org/10.1186/s12943-023-01865-0.
[28] M.J. Ansari, R.R. Rajendran, S. Mohanto, U. Agarwal, K. Panda, K. Dhotre, R. Manne, A. Deepak, A. Zafar, M. Yasir, S. Pramanik, Poly(N-isopropylacrylamide)-based hydrogels for biomedical applications: a review of the state-of-the-art, Gels 8 (2022), https://doi.org/10.3390/gels8070454.
[29] B. Yu, Y. Li, Y. Lin, Y. Zhu, T. Hao, Y. Wu, Z. Sun, X. Yang, H. Xu, Research progress of natural silk fibroin and the application for drug delivery in chemotherapies, Front. Pharmacol. 13 (2022) 1071868, https://doi.org/10.3389/fphar.2022.1071868.
[30] A. Rakhshani, S. Maghsoudian, H. Motasadizadeh, Y. Fatahi, A. Malek-Khatabi, M.H. Ghahremani, F. Atyabi, R. Dinarvand, Synergistic effects of doxorubicin PLGA nanoparticles and simvastatin loaded in silk films for local treatment of breast cancer, J Drug Deliv Sci Technol 104 (2025) 106431, https://doi.org/10.1016/j.jddst.2024.106431.
[31] B Kundu, R Rajkhowa, SC Kundu, X Wang, Silk fibroin biomaterials for tissue regenerations, Adv Drug Deliv Rev 65 (4) (2013) 457–470, https://doi.org/10.1016/j.addr.2012.09.043.
[32] P Tulay, N Galam, T Adali, The Wonders of Silk Fibroin Biomaterials in the Treatment of Breast Cancer, Crit Rev Eukaryot Gene Expr 28 (2) (2018) 129–134, https://doi.org/10.1615/CritRevEukaryotGeneExpr.2018021331.
[33] R. Harishchandra Yadav, M. Kenchegowda, M. Angolkar, M. TS, R. Ali M. Osmani, S. Palaksha, H. Veerabhadrappa Gangadharappa, A review of silk fibroin-based drug delivery systems and their applications, Eur. Polym. J. 216 (2024) 113286, https://doi.org/10.1016/j.eurpolymj.2024.113286.
[34] A. Angelopoulou, A. Kolokithas-Ntoukas, C. Fytas, K. Avgoustakis, Folic acid-functionalized, condensed magnetic nanoparticles for targeted delivery of doxorubicin to tumor cancer cells overexpressing the folate receptor, ACS Omega 4 (2019) 22214–22227, https://doi.org/10.1021/acsomega.9b03594.
[35] A. Prajapati, S. Rangra, R. Patil, N. Desai, V.G.S.S. Jyothi, S. Salave, P. Amate, D. Benival, N. Kommineni, Receptor-targeted nanomedicine for cancer therapy, Receptors 3 (2024) 323–361, https://doi.org/10.3390/receptors3030016.
[36] E. Bellotti, M.G. Cascone, N. Barbani, D. Rossin, R. Rastaldo, C. Giachino, C. Cristallini, Targeting cancer cells overexpressing folate receptors with new terpolymer-based nanocapsules: toward a novel targeted DNA delivery system for cancer therapy, Biomedicines 9 (2021), https://doi.org/10.3390/biomedicines9091275.
[37] L. Karthikeyan, R. Vivek, Synergistic anti-cancer effects of NIR-light responsive nanotherapeutics for chemo-photothermal therapy and photothermal immunotherapy: a combined therapeutic approach, Advances in Cancer Biology - Metastasis 4 (2022) 100044, https://doi.org/10.1016/j.adcanc.2022.100044.
[38] P.P.P. Kumar, D.-K. Lim, Photothermal effect of gold nanoparticles as a nanomedicine for diagnosis and therapeutics, Pharmaceutics 15 (2023), https://doi.org/10.3390/pharmaceutics15092349.
[39] J. Li, S. Wang, F. Fontana, C. Tapeinos, M.-A. Shahbazi, H. Han, H.A. Santos, Nanoparticles-based phototherapy systems for cancer treatment: current status and clinical potential, Bioact Mater 23 (2023) 471–507, https://doi.org/10.1016/j.bioactmat.2022.11.013.
[40] J. Wang, N. Jin, Z. Xie, Q. Cheng, B. Jiang, Y. Shuai, Z. Xu, Q. Wan, Y. Chen, C. Mao, M. Yang, Gold nanorods coated by self-assembled silk fibroin for improving their biocompatibility and facilitating targeted photothermal-photodynamic cancer therapy, Nanoscale (2025), https://doi.org/10.1039/D4NR03641G.
[41] Y. Qi, H. Wang, K. Wei, Y. Yang, R.-Y. Zheng, I.S. Kim, K.-Q. Zhang, A review of structure construction of silk fibroin biomaterials from single structures to multi-level structures, Int. J. Mol. Sci. 18 (2017), https://doi.org/10.3390/ijms18030237.
[42] F. Wang, T.-T. Cao, Y.-Q. Zhang, Effect of silk protein surfactant on silk degumming and its properties, Mater. Sci. Eng. C 55 (2015) 131–136, https://doi.org/10.1016/j.msec.2015.05.041.
[43] A.S. Silva, E.C. Costa, S. Reis, C. Spencer, R.C. Calhelha, S.P. Miguel, M.P. Ribeiro, L. Barros, J.A. Vaz, P. Coutinho, Silk sericin: a promising sustainable biomaterial for, Biomedical and Pharmaceutical Applications., Polymers (Basel) 14 (2022), https://doi.org/10.3390/polym14224931.
[44] S.U.D. Wani, M.I. Zargar, M.H. Masoodi, S. Alshehri, P. Alam, M.M. Ghoneim, A. Alshlowi, H.G. Shivakumar, M. Ali, F. Shakeel, Silk fibroin as an efficient biomaterial for drug delivery, gene therapy, and wound healing, Int. J. Mol. Sci. 23 (2022), https://doi.org/10.3390/ijms232214421.
[45] Wei He, Po Li, Yue Zhu, Mingming Liu, Xiaonan Huang, An injectable silk fibroin nanofiber hydrogel hybrid system for tumor upconversion luminescence imaging and photothermal therapy, New J. Chem. 43 (2019) 2213–2219, https://doi.org/10.1039/C8NJ05766D.
[46] B. Zhou, H. Wang, Structure and functions of cocoons constructed by Eri silkworm, Polymers (Basel) 12 (2020), https://doi.org/10.3390/polym12112701.
[47] F. Chen, D. Porter, F. Vollrath, Silk cocoon (Bombyx mori): multi-layer structure and mechanical properties, Acta Biomater. 8 (2012) 2620–2627, https://doi.org/10.1016/j.actbio.2012.03.043.
[48] Y.Y. Choi, M.J. Jang, B.-D. Park, I.C. Um, Fabrication, structure, and properties of nonwoven silk fabrics prepared with different cocoon layers, Int. J. Mol. Sci. 24 (2023), https://doi.org/10.3390/ijms241411485.
[49] R. Aad, I. Dragojlov, S. Vesentini, Sericin protein: structure, properties, and applications, J Funct Biomater 15 (2024), https://doi.org/10.3390/jfb15110322.
[50] Leng-Duei Koh, Cheng Yuan, Teng Choon-Peng, Khin Yin-Win, Xian-Jun Loh, Si-Yin Tee, Michelle Low, Ye Enyi, Hai-Dong Yu, Yong-Wei Zhang, Ming-Yong Han. Structures, mechanical properties and applications of silk fibroin materials, Prog. Polym. Sci. 46 (2015) 86–110, https://doi.org/10.1016/j.progpolymsci.2015.02.001.
[51] J. and M.C, M.A. Yang Yuejiao, Chen, Natural fibrous protein for advanced tissue engineering applications: focusing on silk fibroin and keratin, in: R.L. and M.A, K. G. Chun Heung Jae, Reis (Eds.), Bioinspired Biomaterials: Advances in Tissue Engineering and Regenerative Medicine, Springer Singapore, Singapore, 2020, pp. 39–49, https://doi.org/10.1007/978-981-15-3258-0_3.
[52] M. Pollini, F. Paladini, Bioinspired materials for wound healing application: the potential of silk fibroin, Materials 13 (2020), https://doi.org/10.3390/ma13153361.
[53] S. and O.J.M, R.R.L. Ribeiro Viviana, P. Pina, Silk fibroin-based hydrogels and scaffolds for osteochondral repair and regeneration, in: S. and R.R.L. and S.R.J, Oliveira J. Miguel, Pina (Eds.), Osteochondral Tissue Engineering: Nanotechnology, Scaffolding-Related Developments and Translation, Springer International Publishing, Cham, 2018, pp. 305–325, https://doi.org/10.1007/978-3-319-76711-6_14.
[54] O. Hakimi, D.P. Knight, F. Vollrath, P. Vadgama, Spider and mulberry silkworm silks as compatible biomaterials, Compos B Eng 38 (2007) 324–337, https://doi.org/10.1016/j.compositesb.2006.06.012.
[55] D.H. De Oliveira, M. Biler, C. Mim, L. Enstedt, M. Kvick, P. Norman, M. Linares, M. Hedhammar, Silk assembly against hydrophobic surfaces—modeling and imaging of formation of nanofibrils, ACS Appl. Bio Mater. 6 (2023) 1011–1018, https://doi.org/10.1021/acsabm.2c00878.
[56] X. Li, N. Li, Q. Fan, K. Yan, Q. Zhang, D. Wang, R. You, Silk fibroin scaffolds with stable silk I crystal and tunable properties, Int. J. Biol. Macromol. 248 (2023) 125910, https://doi.org/10.1016/j.ijbiomac.2023.125910.
[57] Ung-Jin Kim, Jaehyung Park, Chunmei Li, Hyoung-Joon Jin, Regina Valluzzi, David L. Kaplan, Structure and properties of silk hydrogels, Biomacromolecules 5 (3) (2004) 786–792, https://doi.org/10.1021/bm0345460.
[58] M. Ashtikar, M.G. Wacker, Nanopharmaceuticals for wound healing – lost in translation? Adv. Drug Deliv. Rev. 129 (2018) 194–218, https://doi.org/10.1016/j.addr.2018.03.005.
[59] M.K. DeBari, R.D. Abbott, Microscopic considerations for optimizing silk biomaterials, WIREs Nanomedicine and Nanobiotechnology 11 (2019) e1534, https://doi.org/10.1002/wnan.1534.
[60] L. Huang, J. Shi, W. Zhou, Q. Zhang, Advances in preparation and properties of regenerated silk fibroin, Int. J. Mol. Sci. 24 (2023), https://doi.org/10.3390/ijms241713153.
[61] Z. Mao, X. Bi, F. Ye, P. Du, X. Shu, L. Sun, J. Guan, X. Li, S. Wu, The relationship between crosslinking structure and silk fibroin scaffold performance for soft tissue engineering, Int. J. Biol. Macromol. 182 (2021) 1268–1277, https://doi.org/10.1016/j.ijbiomac.2021.05.058.
[62] S. Zou, X. Yao, H. Shao, R.L. Reis, S.C. Kundu, Y. Zhang, Nonmulberry silk fibroin-based biomaterials: impact on cell behavior regulation and tissue regeneration, Acta Biomater. 153 (2022) 68–84, https://doi.org/10.1016/j.actbio.2022.09.021.
[63] P.P. Patil, M.R. Reagan, R.A. Bohara, Silk fibroin and silk-based biomaterial derivatives for ideal wound dressings, Int. J. Biol. Macromol. 164 (2020) 4613–4627, https://doi.org/10.1016/j.ijbiomac.2020.08.041.
[64] A.P. Madappura, S. Madduri, A comprehensive review of silk-fibroin hydrogels for cell and drug delivery applications in tissue engineering and regenerative medicine, Comput Struct, Biotechnol. J. 21 (2023) 4868–4886, https://doi.org/10.1016/J.CSBJ.2023.10.012.
[65] Q. Lu, Y. Han, Y. Ma, S. Lv, Design of silk fibroin-based supramolecular hydrogels through host-guest interactions: influence of the crosslinking type, Colloids Surf. A Physicochem. Eng. Asp. 652 (2022) 129898, https://doi.org/10.1016/j.colsurfa.2022.129898.
[66] P.K. Byram, K.C. Sunka, A. Barik, M. Kaushal, S. Dhara, N. Chakravorty, Biomimetic silk fibroin and xanthan gum blended hydrogels for connective tissue regeneration, Int. J. Biol. Macromol. 165 (2020) 874–882, https://doi.org/10.1016/j.ijbiomac.2020.09.231.
[67] S. Grabska-Zielin´ska, A. Sionkowska, How to improve physico-chemical properties of silk fibroin materials for biomedical applications?—blending and cross-linking of silk fibroin—a review, Materials 14 (2021) 1510, https://doi.org/10.3390/ma14061510.
[68] P. Bhattacharjee, M. Ahearne, Significance of crosslinking approaches in the development of next generation hydrogels for corneal tissue engineering, Pharmaceutics 13 (2021), https://doi.org/10.3390/pharmaceutics13030319.
[69] B.G. Bernardes, A. Veiga, J. Barros, C.A. García-Gonz´alez, A.L. Oliveira, Sustainable silk-based particulate systems for the controlled release of pharmaceuticals and bioactive agents in wound healing and skin regeneration, Int. J. Mol. Sci. 25 (2024), https://doi.org/10.3390/ijms25063133.

[70] H.-Y. Wang, Y. Zhang, M. Zhang, Y.-Q. Zhang, Functional modification of silk fibroin from silkworms and its application to medical biomaterials: a review, Int. J. Biol. Macromol. 259 (2024) 129099, https://doi.org/10.1016/j.ijbiomac.2023.129099.

[71] C. Lujerdean, G.-M. Baci, A.-A. Cucu, D.S. Dezmirean, The contribution of silk fibroin in biomedical engineering, Insects 13 (2022), https://doi.org/10.3390/insects13030286.

[72] P.K.M. Rajendra, B.S.S. Nidamanuri, A.P. Balan, S. Venkatachalam, N. Jawahar, A review on structure, preparation and applications of silk fibroin-based nano-drug delivery systems, J. Nanopart. Res. 24 (2022) 141, https://doi.org/10.1007/s11051-022-05526-z.

[73] N. Navamajiti, A. Gardner, R. Cao, Y. Sugimoto, J.W. Yang, A. Lopes, N.V. Phan, J. Collins, T. Hua, S. Damrongsakkul, S. Kanokpanont, C. Steiger, D. Reker, R. Langer, G. Traverso, Silk fibroin-based coatings for pancreatin-dependent drug delivery, J. Pharm. Sci. 113 (2024) 718–724, https://doi.org/10.1016/j.xphs.2023.09.001.

[74] S. Mohanto, S. Narayana, K.P. Merai, J.A. Kumar, A. Bhunia, U. Hani, A. Al Fatease, B.H.J. Gowda, S. Nag, M.G. Ahmed, K. Paul, L.K. Vora, Advancements in gelatin-based hydrogel systems for biomedical applications: a state-of-the-art review, Int. J. Biol. Macromol. 253 (2023) 127143, https://doi.org/10.1016/j.ijbiomac.2023.127143.

[75] Z. Lv, T. Hu, Y. Bian, G. Wang, Z. Wu, H. Li, X. Liu, S. Yang, C. Tan, R. Liang, X. Weng, A MgFe-LDH nanosheet-incorporated smart thermo-responsive hydrogel with controllable growth factor releasing capability for bone regeneration, Adv. Mater. 35 (2023) 2206545, https://doi.org/10.1002/adma.202206545.

[76] Y. Dong, P. Dong, D. Huang, L. Mei, Y. Xia, Z. Wang, X. Pan, G. Li, C. Wu, Fabrication and characterization of silk fibroin-coated liposomes for ocular drug delivery, Eur. J. Pharm. Biopharm. 91 (2015) 82–90, https://doi.org/10.1016/j.ejpb.2015.01.018.

[77] W. Zhu, Y. Dong, P. Xu, Q. Pan, K. Jia, P. Jin, M. Zhou, Y. Xu, R. Guo, B. Cheng, A composite hydrogel containing resveratrol-laden nanoparticles and platelet-derived extracellular vesicles promotes wound healing in diabetic mice, Acta Biomater. 154 (2022) 212–230, https://doi.org/10.1016/j.actbio.2022.10.038.

[78] H. Zhang, D. Xu, Y. Zhang, M. Li, R. Chai, Silk fibroin hydrogels for biomedical applications, Smart Med. 1 (2022) e20220011, https://doi.org/10.1002/SMMD.20220011.

[79] H. Zheng, B. Zuo, Functional silk fibroin hydrogels: preparation{,} properties and applications, J. Mater. Chem. B 9 (2021) 1238–1258, https://doi.org/10.1039/D0TB02099K.

[80] V. Singh, D.K. Tripathi, V.K. Sharma, D. Srivastava, U. Kumar, K.M. Poluri, B. N. Singh, D. Kumar, V.K. R, Silk fibroin hydrogel: a novel biopolymer for sustained release of vancomycin drug for diabetic wound healing, J. Mol. Struct. 1286 (2023) 135548, https://doi.org/10.1016/j.molstruc.2023.135548.

[81] P. Lu, D. Ruan, M. Huang, M. Tian, K. Zhu, Z. Gan, Z. Xiao, Harnessing the potential of hydrogels for advanced therapeutic applications: current achievements and future directions, Signal Transduct. Target. Ther. 9 (2024) 166, https://doi.org/10.1038/s41392-024-01852-x.

[82] T. Yucel, M.L. Lovett, R. Giangregorio, E. Coonahan, D.L. Kaplan, Silk fibroin rods for sustained delivery of breast cancer therapeutics, Biomaterials 35 (2014) 8613–8620, https://doi.org/10.1016/j.biomaterials.2014.06.030.

[83] Y. Zhao, Z.S. Zhu, J. Guan, S.J. Wu, Processing, mechanical properties and bio-applications of silk fibroin-based high-strength hydrogels, Acta Biomater. 125 (2021) 57–71, https://doi.org/10.1016/j.actbio.2021.02.018.

[84] N. Johari, L. Moroni, A. Samadikuchaksaraei, Tuning the conformation and mechanical properties of silk fibroin hydrogels, Eur. Polym. J. 134 (2020) 109842, https://doi.org/10.1016/j.eurpolymj.2020.109842.

[85] K.A. Karve, E.S. Gil, S.P. McCarthy, D.L. Kaplan, Effect of β-sheet crystalline content on mass transfer in silk films, J. Membr. Sci. 383 (2011) 44–49, https://doi.org/10.1016/j.memsci.2011.08.032.

[86] M.A. Tomeh, R. Hadianamrei, X. Zhao, Silk fibroin as a functional biomaterial for drug and gene delivery, Pharmaceutics 11 (2019), https://doi.org/10.3390/pharmaceutics11100494.

[87] J. Brown, C.-L. Lu, J. Coburn, D.L. Kaplan, Impact of silk biomaterial structure on proteolysis, Acta Biomater. 11 (2015) 212–221, https://doi.org/10.1016/j.actbio.2014.09.013.

[88] K. Numata, P. Cebe, D. Kaplan, Mechanism of enzymatic degradation of beta-sheet crystals, Biomaterials 31 (2010) 2926–2933, https://doi.org/10.1016/j.biomaterials.2009.12.026.

[89] A. Florczak, T. Deptuch, K. Kucharczyk, H. Dams-Kozlowska, Systemic and local silk-based drug delivery systems for cancer therapy, Cancers (Basel) 13 (2021), https://doi.org/10.3390/cancers13215389.

[90] M.G. Fuster, M.G. Montalba´n, I. Moulefera, G. Víllora, D.L. Kaplan, Folic acid-modified Ibrutinib-loaded silk fibroin nanoparticles for cancer cell therapy with over-expressed folate receptor, Pharmaceutics 15 (2023), https://doi.org/10.3390/pharmaceutics15041186.

[91] L.Y.W. Bourguignon, M. Shiina, J.-J. Li, Hyaluronan-CD44 interaction promotes oncogenic signaling, microRNA functions, chemoresistance, and radiation resistance in cancer stem cells leading to tumor progression, Adv. Cancer Res. 123 (2014) 255–275, https://doi.org/10.1016/B978-0-12-800092-2.00010-1.

[92] S. Tan, A. Yamashita, S.J. Gao, M. Kurisawa, Hyaluronic acid hydrogels with defined crosslink density for the efficient enrichment of breast cancer stem cells, Acta Biomater. 94 (2019) 320–329, https://doi.org/10.1016/j.actbio.2019.05.040.

[93] H. Javid, M.A. Oryani, N. Rezagholinejad, A. Esparham, M. Tajaldini, M. Karimi-Shahri, RGD peptide in cancer targeting: benefits, challenges, solutions, and possible integrin-RGD interactions, Cancer Med. 13 (2024) e6800, https://doi.org/10.1002/cam4.6800.

[94] P. Kesharwani, J. Chandra, S. Karim, G. Gupta, R. Karwasra, A. Sharma, αvβ3 integrin targeting RGD peptide-based nanoparticles as an effective strategy for selective drug delivery to tumor microenvironment, J Drug Deliv Sci Technol 96 (2024) 105663, https://doi.org/10.1016/j.jddst.2024.105663.

[95] J.P. Santerre, Y. Yang, Z. Du, W. Wang, X. Zhang, Biomaterials' enhancement of immunotherapy for breast cancer by targeting functional cells in the tumor micro-environment, Front. Immunol. 15 (2024) 1492323, https://doi.org/10.3389/fimmu.2024.1492323.

[96] X. Lin, L. Cai, X. Cao, Y. Zhao, Stimuli-responsive silk fibroin for on-demand drug delivery, Smart Med. 2 (2023) e20220019, https://doi.org/10.1002/SMMD.20220019.

[97] A. Florczak, I. Grzechowiak, T. Deptuch, K. Kucharczyk, A. Kaminska, H. Dams-Kozlowska, Silk particles as carriers of therapeutic molecules for cancer treatment, Materials 13 (2020), https://doi.org/10.3390/ma13214946.

[98] L. Bin, Y. Yang, F. Wang, R. Wang, H. Fei, S. Duan, L. Huang, N. Liao, S. Zhao, X. Ma, Biodegradable silk fibroin nanocarriers to modulate hypoxia tumor microenvironment favoring enhanced chemotherapy, Front Bioeng Biotechnol 10 (2022) 960501, https://doi.org/10.3389/fbioe.2022.960501.

[99] K.S. Mistretta, J.M. Coburn, Three-dimensional silk fibroin scaffolded co-culture of human neuroblastoma and innate immune cells, Exp. Cell Res. 443 (2024) 114289, https://doi.org/10.1016/j.yexcr.2024.114289.

[100] J. Liu, X. Han, T. Zhang, K. Tian, Z. Li, F. Luo, Reactive oxygen species (ROS) scavenging biomaterials for anti-inflammatory diseases: from mechanism to therapy, J. Hematol. Oncol. 16 (2023) 116, https://doi.org/10.1186/s13045-023-01512-7.

[101] H. Liu, X. Zhu, Y. Wei, C. Song, Y. Wang, Recent advances in targeted gene silencing and cancer therapy by nanoparticle-based delivery systems, Biomed. Pharmacother. 157 (2023) 114065, https://doi.org/10.1016/j.biopha.2022.114065.

[102] M.E. Bahar, H.J. Kim, D.R. Kim, Targeting the RAS/RAF/MAPK pathway for cancer therapy: from mechanism to clinical studies, Signal Transduct. Target. Ther. 8 (2023) 455, https://doi.org/10.1038/s41392-023-01705-z.

[103] M.I. Ashraf, M. Ebner, C. Wallner, M. Haller, S. Khalid, H. Schwelberger, K. Koziel, M. Enthammer, M. Hermann, S. Sickinger, A. Soleiman, C. Steger, S. Vallant, R. Sucher, G. Brandacher, P. Santer, D. Dragun, J. Troppmair, A p38MAPK/MK2 signaling pathway leading to redox stress, cell death and ischemia/reperfusion injury, Cell Communication and Signaling 12 (2014) 6, https://doi.org/10.1186/1478-811X-12-6.

[104] X. Huang, D. He, Z. Pan, G. Luo, J. Deng, Reactive-oxygen-species-scavenging nanomaterials for resolving inflammation, Mater Today Bio 11 (2021) 100124, https://doi.org/10.1016/j.mtbio.2021.100124.

[105] Vinay Kumar, Gopinath Packirisamy. 3D porous sodium alginate-silk fibroin composite bead based in vitro tumor model for screening of anti-cancer drug and induction of magneto-apoptosis. International Journal of Biological Macromolecules Volume 242, Part 3, 1 July 2023, 124827. doi: https://doi.org/10.1016/j.ijbiomac.2023.124827.

[106] C. Jaiswal, T. Gupta, P.K. Jadi, J.C. Moses, B.B. Mandal, Injectable anti-cancer drug loaded silk-based hydrogel for the prevention of cancer recurrence and post-lumpectomy tissue regeneration aiding triple-negative breast cancer therapy, Biomaterials Advances 145 (2023) 213224, https://doi.org/10.1016/J.BIOADV.2022.213224.

[108] Y. Lyu, Y. Liu, H. He, H. Wang, Application of silk-fibroin-based hydrogels in tissue engineering, Gels 9 (2023), https://doi.org/10.3390/gels9050431.

[109] Z. Zhao, Y. Li, M. Bin Xie, Silk fibroin-based nanoparticles for drug delivery, Int. J. Mol. Sci. 16 (2015) 4880–4903, https://doi.org/10.3390/ijms16034880.

[110] K. Quan, Y. Lu, Z. Mao, S. Wang, X. Ren, C. Yu, T. Zhang, J.-J. Nie, Y. Cheng, D. Chen, Y. Zheng, D. Xia, Functionalized-nanoparticles/silk fibroin coating with anti-adhesive and photothermal capabilities to prevent implant-associated infections, Chem. Eng. J. 486 (2024) 150147, https://doi.org/10.1016/j.cej.2024.150147.

[111] J.E. Ulloa Rojas, B. Gerbelli, A. Ribeiro, I. Lourenço Nantes, F. Giuntini, W. Alves, Silk fibroin hydrogels for potential applications in photodynamic therapy, Biopolymers 110 (2018), https://doi.org/10.1002/bip.23245.

[112] T. Cohen-Karni, K.J. Jeong, J.H. Tsui, G. Reznor, M. Mustata, M. Wanunu, A. Graham, C. Marks, D.C. Bell, R. Langer, D.S. Kohane, Nanocomposite gold-silk nanofibers, Nano Lett. 12 (2012) 5403–5406, https://doi.org/10.1021/nl302810c.

[113] M. Arumugam, B. Murugesan, D. Kumar Chinnalagu, S. Mahalingam, Dual therapeutic approach: biodegradable nanofiber scaffolds of silk fibroin and collagen combined with silver and gold nanoparticles for enhanced bacterial infections treatment and accelerated wound healing, J Drug Deliv Sci Technol 95 (2024) 105620, https://doi.org/10.1016/j.jddst.2024.105620.

[114] O. Akturk, K. Kismet, A.C. Yasti, S. Kuru, M.E. Duymus, F. Kaya, M. Caydere, S. Hucumenoglu, D. Keskin, Wet electrospun silk fibroin/gold nanoparticle 3D matrices for wound healing applications, RSC Adv. 6 (2016) 13234–13250, https://doi.org/10.1039/C5RA24225H.

[115] L. Wang, R. Lu, J. Hou, X. Nan, Y. Xia, Y. Guo, K. Meng, C. Xu, X. Wang, B. Zhao, Application of injectable silk fibroin/graphene oxide hydrogel combined with bone marrow mesenchymal stem cells in bone tissue engineering, Colloids Surf. A Physicochem. Eng. Asp. 604 (2020) 125318, https://doi.org/10.1016/j.colsurfa.2020.125318.

[116] R. Eivazzadeh-Keihan, Z. Pajoum, H. Aghamirza Moghim Aliabadi, F. Ganjali, A. Kashtiaray, M. Salimi Bani, F. Lalebeigi, E. Ziaei Ziabari, A. Maleki, M. M. Heravi, M. Mahdavi, Magnetic chitosan-silk fibroin hydrogel/graphene oxide

nanobiocomposite for biological and hyperthermia applications, Carbohydr. Polym. 300 (2023) 120246, https://doi.org/10.1016/j.carbpol.2022.120246.
[117] H. Horo, S. Bhattacharyya, B. Mandal, L.M. Kundu, Synthesis of functionalized silk-coated chitosan-gold nanoparticles and microparticles for target-directed delivery of antitumor agents, Carbohydr. Polym. 258 (2021) 117659, https://doi.org/10.1016/j.carbpol.2021.117659.
[118] C. You, C. Wang, Z. Ma, Q. Yu, S. Liu, Review on application of silk fibroin hydrogels in the management of wound healing, Int. J. Biol. Macromol. (2025) 140082, https://doi.org/10.1016/j.ijbiomac.2025.140082.
[119] Z. Wu, W. Li, S. Cheng, J. Liu, S. Wang, Novel fabrication of bioengineered injectable chitosan hydrogel loaded with conductive nanoparticles to improve therapeutic potential of mesenchymal stem cells in functional recovery after ischemic myocardial infarction, Nanomedicine 47 (2023) 102616, https://doi.org/10.1016/j.nano.2022.102616.
[120] E. Dondajewska, W. Juzwa, A. Mackiewicz, H. Dams-Kozlowska, Heterotypic breast cancer model based on a silk fibroin scaffold to study the tumor microenvironment, Oncotarget 9 (2018) 4935–4950, https://doi.org/10.18632/oncotarget.23574.
[121] K. Jastrzebska, K. Kucharczyk, A. Florczak, E. Dondajewska, A. Mackiewicz, H. Dams-Kozlowska, Silk as an innovative biomaterial for cancer therapy, Reports of Practical Oncology & Radiotherapy 20 (2015) 87–98, https://doi.org/10.1016/j.rpor.2014.11.010.
[122] Z.-L. Liu, H.-H. Chen, L.-L. Zheng, L.-P. Sun, L. Shi, Angiogenic signaling pathways and anti-angiogenic therapy for cancer, Signal Transduct. Target. Ther. 8 (2023) 198, https://doi.org/10.1038/s41392-023-01460-1.
[123] H.A. Tran, T.T. Hoang, A. Maraldo, T.N. Do, D.L. Kaplan, K.S. Lim, J. Rnjak-Kovacina, Emerging silk fibroin materials and their applications: new functionality arising from innovations in silk crosslinking, Mater. Today 65 (2023) 244–259, https://doi.org/10.1016/j.mattod.2023.03.027.
[124] C. Yang, S. Li, X. Huang, X. Chen, H. Shan, X. Chen, L. Tao, M. Zhang, Silk fibroin hydrogels could be therapeutic biomaterials for neurological diseases, Oxidative Med. Cell. Longev. 2022 (2022) 2076680, https://doi.org/10.1155/2022/2076680.
[125] S. He, D. Shi, Z. Han, Z. Dong, Y. Xie, F. Zhang, W. Zeng, Q. Yi, Heparinized silk fibroin hydrogels loading FGF1 promote the wound healing in rats with full-thickness skin excision, Biomed. Eng. Online 18 (2019) 97, https://doi.org/10.1186/s12938-019-0716-4.
[126] R. Shokri, M. Fuentes-Chandía, J. Ai, M. Habibi Roudkenar, A. Reza Mahboubian, M. Rad Malekshahi, S. Nasser Ostad, A thermo-sensitive hydrogel composed of methylcellulose/hyaluronic acid/silk fibrin as a biomimetic extracellular matrix to simulate breast cancer malignancy, Eur. Polym. J. 176 (2022) 111421, https://doi.org/10.1016/j.eurpolymj.2022.111421.
[127] D. Arora, B.K. Bhunia, G. Janani, B.B. Mandal, Bioactive three-dimensional silk composite in vitro tumoroid model for high throughput screening of anticancer drugs, J. Colloid Interface Sci. 589 (2021) 438–452, https://doi.org/10.1016/j.jcis.2021.01.010.
[128] H. Wang, Y. Jin, Y. Tan, H. Zhu, W. Huo, P. Niu, Z. Li, J. Zhang, X. Liang, X. Yang, Photo-responsive hydrogel facilitates nutrition deprivation by an ambidextrous approach for preventing cancer recurrence and metastasis, Biomaterials 275 (2021) 120992, https://doi.org/10.1016/j.biomaterials.2021.120992.
[129] G. Major, M. Ahn, W.-W. Cho, M. Santos, J. Wise, E. Phillips, S.G. Wise, J. Jang, J. Rnjak-Kovacina, T. Woodfield, K.S. Lim, Programming temporal stiffness cues within extracellular matrix hydrogels for modelling cancer niches, Mater Today Bio 25 (2024) 101004, https://doi.org/10.1016/j.mtbio.2024.101004.
[130] N. Beheshtizadeh, M. Mohammadzadeh, M. Mostafavi, A.A. Seraji, F. Esmaeili Ranjbar, S.Z. Tabatabaei, R. Ghafelehbashi, M. Afzali, F. Lolasi, Improving hemocompatibility in tissue-engineered products employing heparin-loaded nanoplatforms, Pharmacol. Res. 206 (2024) 107260, https://doi.org/10.1016/j.phrs.2024.107260.
[131] A. Mehrabi, S. Mousazadeh, A. Mollafilabi, N. Nafissi, P.B. Milan, Synthesis and characterization of a silk fibroin/placenta matrix hydrogel for breast reconstruction, Life Sci. 334 (2023) 122236, https://doi.org/10.1016/j.lfs.2023.122236.
[132] S. Ghaedamini, M. Kazemi, A. Rabiei, A. Honarvar, M. Aliakbari, S. Karbasi, Anti-tumor effects of ellagic acid and mesenchymal stem cell-conditioned medium on breast cancer cells on the 3D printed PCL/agarose scaffolds, J Drug Deliv Sci Technol 101 (2024) 106315, https://doi.org/10.1016/j.jddst.2024.106315.
[133] S. Gou, W. Meng, A.C. Panayi, R. Wang, R. Zhang, P. Gao, T. He, W. Geng, S. Hu, Y. Yu, Q. Feng, K. Cai, Bioresponsive self-reinforcing sericin/silk fibroin hydrogel for relieving the immune-related adverse events in tumor immunotherapy, Adv. Funct. Mater. 33 (2023) 2213867, https://doi.org/10.1002/adfm.202213867.
[134] A. Nasrine, S. Mohanto, S. Narayana, M.G. Ahmed, Enhanced pharmacokinetic approach for anastrozole via macromolecule-based silk fibroin nanoparticles incorporated in situ injectables for oestrogen-positive breast cancer therapy, J. Drug Target. (2025) 1–11, https://doi.org/10.1080/1061186X.2024.2449486.
[135] Y. Bao, H. Zhang, L. Chen, H.-H. Cai, Z.-L. Liu, Y. Peng, Z. Li, F.-Y. Dai, Artemisinin-loaded silk fibroin/gelatin composite hydrogel for wound healing and tumor therapy, Arab. J. Chem. 16 (2023) 104782, https://doi.org/10.1016/j.arabjc.2023.104782.
[136] C. Laomeephol, H. Ferreira, S. Kanokpanont, N.M. Neves, H. Kobayashi, S. Damrongsakkul, Dual-functional liposomes for curcumin delivery and accelerating silk fibroin hydrogel formation, Int. J. Pharm. 589 (2020) 119844, https://doi.org/10.1016/j.ijpharm.2020.119844.
[137] P. Wu, Q. Liu, Q. Wang, H. Qian, L. Yu, B. Liu, R. Li, Novel silk fibroin nanoparticles incorporated silk fibroin hydrogel for inhibition of cancer stem cells and tumor growth, Int. J. Nanomedicine 13 (2018) 5405–5418, https://doi.org/10.2147/IJN.S166104.
[138] S. Gou, D. Xie, Y. Ma, Y. Huang, F. Dai, C. Wang, B. Xiao, Injectable, thixotropic, and multiresponsive silk fibroin hydrogel for localized and synergistic tumor therapy, ACS Biomater Sci Eng 6 (2020) 1052–1063, https://doi.org/10.1021/acsbiomaterials.9b01676.
[139] E. Pasquier, J. Rosendahl, A. Solberg, A. Ståhlberg, J. Håkansson, G. Chinga-Carrasco, Polysaccharides and structural proteins as components in three-dimensional scaffolds for breast cancer tissue models: a review, Bioengineering 10 (2023), https://doi.org/10.3390/bioengineering10060682.
[140] A.S. Khoo, T.M. Valentin, S.E. Leggett, D. Bhaskar, E.M. Bye, S. Benmelech, B. C. Ip, I.Y. Wong, Breast cancer cells transition from mesenchymal to amoeboid migration in tunable three-dimensional silk–collagen hydrogels, ACS Biomater Sci. Eng. 5 (2019) 4341–4354, https://doi.org/10.1021/acsbiomaterials.9b00519.
[141] S. Nag, S. Kar, S. Mishra, B. Stany, A. Seelan, S. Mohanto, S. Haryini, C. Kamaraj, V. Subramaniyan, Unveiling green synthesis and biomedical theranostic paradigms of selenium nanoparticles (SeNPs) - a state-of-the-art comprehensive update, Int. J. Pharm. 662 (2024) 124535, https://doi.org/10.1016/j.ijpharm.2024.124535.
[142] Z. Zhang, Q. Cao, Y. Xia, C. Cui, Y. Qi, Q. Zhang, Y. Wu, J. Liu, W. Liu, Combination of biodegradable hydrogel and antioxidant bioadhesive for treatment of breast cancer recurrence and radiation skin injury, Bioact Mater 31 (2024) 408–421, https://doi.org/10.1016/j.bioactmat.2023.08.021.
[143] Z. Zhang, Y. Xia, X. Li, Q. Zhang, Y. Wu, C. Cui, J. Liu, W. Liu, Arginine-solubilized lipoic acid-induced β-sheets of silk fibroin-strengthened hydrogel for postoperative rehabilitation of breast cancer, Bioact Mater 40 (2024) 667–682, https://doi.org/10.1016/j.bioactmat.2024.08.014.
[144] S. Buonvino, I. Arciero, E. Martinelli, D. Seliktar, S. Melino, Modelling the disease: H2S-sensitivity and drug-resistance of triple negative breast cancer cells can be modulated by embedding in isotropic micro-environment, Mater Today Bio 23 (2023) 100862, https://doi.org/10.1016/j.mtbio.2023.100862.
[146] H.A.M. Aliabadi, M. Forouzandeh-Malati, F. Hassanzadeh-Afruzi, E.B. Noruzi, F. Ganjali, A. Kashtiaray, M.S. Bani, R.B. Eftekhari, R. Eivazzadeh-Keihan, A. Maleki, Magnetic xanthan gum-silk fibroin hydrogel: a nanocomposite for biological and hyperthermia applications, Int. J. Biol. Macromol. 253 (2023) 127005, https://doi.org/10.1016/j.ijbiomac.2023.127005.
[147] L. Pierantoni, V. Brancato, J.B. Costa, S.C. Kundu, R.L. Reis, J. Silva-Correia, J. M. Oliveira, Synergistic effect of co-culturing breast cancer cells and fibroblasts in the formation of Tumoroid clusters and design of in Vitro 3D models for the testing of anticancer agents, Adv Biol 7 (2023) 2200141, https://doi.org/10.1002/adbi.202200141.
[148] L. Zhu, S. Wang, A convergent fabrication of pH and redox dual-responsive hybrids of mesoporous silica nanoparticles for the treatment of breast cancer, J. Biomater. Sci. Polym. Ed. 34 (2023) 147–165, https://doi.org/10.1080/09205063.2022.2112303.
[149] W. Huo, X. Yang, B. Wang, L. Cao, Z. Fang, Z. Li, H. Liu, X. Liang, J. Zhang, Y. Jin, Biomineralized hydrogel DC vaccine for cancer immunotherapy: a boosting strategy via improving immunogenicity and reversing immune-inhibitory microenvironment, Biomaterials 288 (2022) 121722, https://doi.org/10.1016/j.biomaterials.2022.121722.
[151] Z. Pajoum, H.A.M. Aliabadi, A. Mohammadi, Z. Sadat, A. Kashtiaray, M.S. Bani, M. Shahiri, M. Mahdavi, R. Eivazzadeh-Keihan, A. Maleki, M.M. Heravi, Hyperthermia and biological investigation of a novel magnetic nanobiocomposite based on acacia gum-silk fibroin hydrogel embedded with poly vinyl alcohol, Heliyon 10 (2024) e39073, https://doi.org/10.1016/j.heliyon.2024.e39073.
[152] S. Maghsoudian, M.P. Yektakasmaei, A. Shaabani, S. Perseh, Y. Fatahi, Z. Nouri, M. Gholami, N. Sayyari, H.A. Hoseinzadeh, H. Motasadizadeh, R. Dinarvand, Synergistic effects of doxorubicin loaded silk fibroin nanoparticles and Cu-TiO2 nanoparticles for local chemo-sonodynamic therapy against breast cancer, Int. J. Biol. Macromol. 289 (2025) 138910, https://doi.org/10.1016/j.ijbiomac.2024.138910.
[154] I. Arciero, S. Buonvino, V. Palumbo, M. Scimeca, S. Melino, A 3D-printable cell array for in vitro breast cancer modeling, Int. J. Mol. Sci. 25 (2024), https://doi.org/10.3390/ijms252313068.
[155] A.L. Laiva, J.R. Venugopal, P. Karuppuswamy, B. Navaneethan, A. Gora, S. Ramakrishna, Controlled release of titanocene into the hybrid nanofibrous scaffolds to prevent the proliferation of breast cancer cells, Int. J. Pharm. 483 (2015) 115–123, https://doi.org/10.1016/j.ijpharm.2015.02.025.
[156] V. Gupta, G.-H. Mun, B. Choi, A. Aseh, L. Mildred, A. Patel, Q. Zhang, J.E. Price, D. Chang, G. Robb, A.B. Mathur, Repair and reconstruction of a resected tumor defect using a composite of tissue flap–nanotherapeutic–silk fibroin and chitosan scaffold, Ann. Biomed. Eng. 39 (2011) 2374–2387, https://doi.org/10.1007/s10439-011-0335-0.
[157] X. Wang, L. Sun, M.V. Maffini, A. Soto, C. Sonnenschein, D.L. Kaplan, A complex 3D human tissue culture system based on mammary stromal cells and silk scaffolds for modeling breast morphogenesis and function, Biomaterials 31 (2010) 3920–3929, https://doi.org/10.1016/j.biomaterials.2010.01.118.
[158] V. Brancato, B. Kundu, J.M. Oliveira, V.M. Correlo, R.L. Reis, S.C. Kundu, Tumor-stroma interactions alter the sensitivity of drug in breast cancer, Front Mater 7 (2020), https://doi.org/10.3389/fmats.2020.00116.
[159] Y. Maghdouri-White, L.W. Elmore, G.L. Bowlin, D. Dre´au, Breast epithelial cell infiltration in enhanced electrospun silk scaffolds, J. Tissue Eng. Regen. Med. 10 (2016) E121–E131, https://doi.org/10.1002/term.1778.

[160] S. Talukdar, S.C. Kundu, A non-mulberry silk fibroin protein based 3D in vitro tumor model for evaluation of anticancer drug activity, Adv. Funct. Mater. 22 (2012) 4778–4788, https://doi.org/10.1002/adfm.201200375.
[161] G. Carrasco-Torres, M.A. Valde´s-Madrigal, V.R. V´asquez-Garzo´n, R. Balti´errez-Hoyos, E. la Cruz-Burelo, R. Roma´n-Doval, A.A. Valencia-Lazcano, Effect of silk fibroin on cell viability in electrospun scaffolds of polyethylene oxide, Polymers (Basel) 11 (2019), https://doi.org/10.3390/polym11030451.
[162] X. Wang, X. Zhang, L. Sun, B. Subramanian, M.V. Maffini, A. Soto, C. Sonnenschein, D.L. Kaplan, Preadipocytes stimulate ductal morphogenesis and functional differentiation of human mammary epithelial cells on 3D silk scaffolds, Tissue Eng. Part A 15 (2009) 3087–3098, https://doi.org/10.1089/ten.tea.2008.0670.
[163] C. Jaiswal, B.B. Mandal, A 3D in vitro triculture hybrid model recapitulating tumor stromal interaction of triple-negative breast cancer as a high throughput anticancer drug screening platform, Adv Ther (Weinh) 7 (2024) 2300450, https://doi.org/10.1002/adtp.202300450.
[164] F. Radinekiyan, M.R. Naimi-Jamal, R. Eivazzadeh-Keihan, H.A.M. Aliabadi, M. S. Bani, S. Shojaei, A. Maleki, A magnetic cross-linked alginate-biobased nanocomposite with anticancer and hyperthermia activities, Carbohydrate Polymer Technologies and Applications 7 (2024) 100481, https://doi.org/10.1016/j.carpta.2024.100481.
[165] A.B. Li, J.A. Kluge, N.A. Guziewicz, F.G. Omenetto, D.L. Kaplan, Silk-based stabilization of biomacromolecules, J. Control. Release 219 (2015) 416–430, https://doi.org/10.1016/j.jconrel.2015.09.037.
[166] F. Wang, Y.-Q. Zhang, Bioconjugation of silk fibroin nanoparticles with enzyme and peptide and their characterization, Adv. Protein Chem. Struct. Biol. 98 (2015) 263–291, https://doi.org/10.1016/bs.apcsb.2014.11.005.
[167] S. Nag, O. Mitra, G. Tripathi, I. Adur, S. Mohanto, M. Nama, S. Samanta, B.H. J. Gowda, V. Subramaniyan, V. Sundararajan, V. Kumarasamy, Nanomaterials-assisted photothermal therapy for breast cancer: state-of-the-art advances and future perspectives, Photodiagn. Photodyn. Ther. 45 (2024) 103959, https://doi.org/10.1016/j.pdpdt.2023.103959.
[168] M. Sharifi, M.R. Avadi, F. Attar, F. Dashtestani, H. Ghorchian, S.M. Rezayat, A. A. Saboury, M. Falahati, Cancer diagnosis using nanomaterials based electrochemical nanobiosensors, Biosens. Bioelectron. 126 (2019) 773–784, https://doi.org/10.1016/j.bios.2018.11.026.
[169] P. Tulay, N. Galam, T. Adali, The wonders of silk fibroin biomaterials in the treatment of breast cancer, Crit. Rev. Eukaryot. Gene Expr. 28 (2018) 129–134, https://doi.org/10.1615/CritRevEukaryotGeneExpr.2018021331.
[170] S. Das, R. Devireddy, M.R. Gartia, Surface plasmon resonance (SPR) sensor for cancer biomarker detection, Biosensors (Basel) 13 (2023), https://doi.org/10.3390/bios13030396.
[171] A.B. Chinen, C.M. Guan, J.R. Ferrer, S.N. Barnaby, T.J. Merkel, C.A. Mirkin, Nanoparticle probes for the detection of cancer biomarkers, cells, and tissues by fluorescence, Chem. Rev. 115 (2015) 10530–10574, https://doi.org/10.1021/acs.chemrev.5b00321.
[172] S. Ashique, N. Mishra, A. Garg, N. Kumar, Z. Khan, S. Mohanto, D.K. Chellappan, A. Farid, F. Taghizadeh-Hesary, A critical review on the role of probiotics in lung cancer biology and prognosis, Arch. Bronconeumol. 60 (2024) S46–S58, https://doi.org/10.1016/j.arbres.2024.04.030.
[175] H. Yu, Y. Li, Z. Zhang, J. Ren, L. Zhang, Z. Xu, Y. Kang, P. Xue, Silk fibroin-capped metal-organic framework for tumor-specific redox dyshomeostasis treatment synergized by deoxygenation-driven chemotherapy, Acta Biomater. 138 (2022) 545–560, https://doi.org/10.1016/j.actbio.2021.11.009.
[176] A.G. H, H.R. L, C.A. L, C.J. Song, V.A.N.E. Dennis, Silk Fibroin Hydrogels and Uses Thereof, (n.d.).
[177] A.G. H, H.R. L, C.A. L, C. Jingsong, Silk Fibroin Hydrogels and Uses Thereof, (n.d.).
[178] V.A.N.E.D. E, J. Guang-Liang, C.A. L, H.R. L, C. Jingsong, A.G. H, I.M.W.H.A. Bin, Compositions and Soft Tissue Replacement Methods, (n.d.).
[179] L.G. G, L.O.T.I.M. Jia-Ching, L.I. Lei, B. Evangelia, K.D. L, Injectable Silk Fibroin Foams and Uses Thereof, (n.d.).
[180] V.A.N.E.D. E, J. Guang-Liang, C.A. L, H.R. L, C.J. Song, A.G. H, I.M. Wha-Bin, Compositions and Improved Soft Tissue Replacement Methods, (n.d.).
[181] B.N. N, L.O.T.I.M. Jia-Ching, L.G. G, K.D. Lss, Active Silk Muco-adhesives, Silk Electrogelation Process, and Devices, (n.d.).
[182] K.D. L, Y. Tuna, L.O.T.I.M. Jia-Ching, L.G. G, pH Induced Silk Gels and Uses Thereof, (n.d.).
[183] Y.U. Xiaojie, M.D. J, P. Elizabeta, C.U.I. Cunqi, S.K. M, Co-crosslinked Hyaluronic Acid-Silk Fibroin Hydrogels For Improving Tissue Graft Viability and for Soft Tissue Augmentation, (n.d.).
[184] B. Evangelia, M. Kacey, R.J. Peter, K.D. L, Y.O.O.J. J, Injectable Silk Fibroin Particles and Uses Thereof, (n.d.).
[185] L.J. Gallego, K.D. L, P. Bruce, Functionalization of Biomaterials to Control Regeneration and Inflammation Responses, (n.d.).
[186] K.D. L, Y. Tuna, W. Xiaoqin, L. Michael, Methods and Compositions for Preparing a Silk Microsphere, (n.d.).
[188] N.I.E. Wangyan, J. Xingzi, Z. Yifeng, C. Pengpeng, X.U. Ying, Preparation Method of Doxorubicin-loaded Methyl Cellulose/Silk Fibroin Composite Hydrogel, (n.d.).
[189] K.D. L, V.S. Lightfoot, A. Rosalyn, Z. Siwei, C. Dana, O.F. G, Innervated Artificial Skin, (n.d.).
[190] J. Liu, X. Ge, L. Liu, W. Xu, R. Shao, Challenges and opportunities of silk protein hydrogels in biomedical applications, Mater. Adv. 3 (2022) 2291–2308, https://doi.org/10.1039/D1MA00960E.
[191] L. Bitar, B. Isella, F. Bertella, C. Bettker Vasconcelos, J. Harings, A. Kopp, Y. van der Meer, T.J. Vaughan, L. Bortesi, Sustainable Bombyx mori's silk fibroin for biomedical applications as a molecular biotechnology challenge: a review, Int. J. Biol. Macromol. 264 (2024) 130374, https://doi.org/10.1016/j.ijbiomac.2024.130374.
[192] S.U. Din Wani, G.H. Veerabhadrappa, Silk fibroin based drug delivery applications: promises and challenges, Curr. Drug Targets 19 (2018) 1177–1190, https://doi.org/10.2174/1389450119666171227205525.
[193] O.C. Onder, S.R. Batool, M.A. Nazeer, Self-assembled silk fibroin hydrogels: from preparation to biomedical applications, Mater. Adv. 3 (2022) 6920–6949, https://doi.org/10.1039/D2MA00568A.
[194] J. Kundu, L. Poole-Warren, P. Martens, S. Kundu, Silk fibroin/poly(vinyl alcohol) photocrosslinked hydrogels for delivery of macromolecular drugs, Acta Biomater. 8 (2012) 1720–1729, https://doi.org/10.1016/j.actbio.2012.01.004.
[195] D.T. Pham, W. Tiyaboonchai, Fibroin nanoparticles: a promising drug delivery system, Drug Deliv. 27 (2020) 431–448, https://doi.org/10.1080/10717544.2020.1736208.
[196] Y. Liu, Y. Geng, B. Yue, P.-C. Lo, J. Huang, H. Jin, Injectable hydrogel as a unique platform for antitumor therapy targeting immunosuppressive tumor microenvironment, Front. Immunol. 12 (2021) 832942, https://doi.org/10.3389/fimmu.2021.832942.
[197] X. Li, X. Xu, M. Xu, Z. Geng, P. Ji, Y. Liu, Hydrogel systems for targeted cancer therapy., front Bioeng, Biotechnol 11 (2023) 1140436, https://doi.org/10.3389/fbioe.2023.1140436.
[198] C. Pacheco, A. Bai˜ao, T. Ding, W. Cui, B. Sarmento, Recent advances in long-acting drug delivery systems for anticancer drug, Adv. Drug Deliv. Rev. 194 (2023) 114724, https://doi.org/10.1016/j.addr.2023.114724.
[199] K. Niveria, M. Yadav, K. Dangi, A.K. Verma, Overcoming challenges to enable targeting of metastatic breast cancer tumour microenvironment with nano-therapeutics: current status and future perspectives, OpenNano 8 (2022) 100083, https://doi.org/10.1016/j.onano.2022.100083.
[200] A.E. Thurber, F.G. Omenetto, D.L. Kaplan, In vivo bioresponses to silk proteins, Biomaterials 71 (2015) 145–157, https://doi.org/10.1016/j.biomaterials.2015.08.039.
[201] M. Yonesi, M. Garcia-Nieto, G.V. Guinea, F. Panetsos, J. P´erez-Rigueiro, D. Gonz´alez-Nieto, Silk fibroin: an ancient material for repairing the injured nervous system, Pharmaceutics 13 (2021), https://doi.org/10.3390/pharmaceutics13030429.
[202] B. Ode Boni, B. Bakadia, A. Osi, Z. Shi, H. Chen, M. Gauthier, G. Yang, Immune response to silk sericin-fibroin composites: potential immunogenic elements, and alternatives for immunomodulation, Macromol. Biosci. 22 (2021) e2100292, https://doi.org/10.1002/mabi.202100292.
[203] P. Thongnuek, S. Kanokpanont, P. Uttayarat, S. Damrongsakkul, Hydrogelation of regenerated silk fibroin via gamma irradiation, Polymers (Basel) 15 (2023), https://doi.org/10.3390/polym15183734.
[204] M.A. Asensio Ruiz, M.G. Fuster, T. Martínez Martínez, M.G. Montalb´an, J.L. Cenis, G. Víllora, A.A. Lozano-Pe´rez, The effect of sterilization on the characteristics of silk fibroin nanoparticles, Polymers (Basel) 14 (2022), https://doi.org/10.3390/polym14030498.
[205] J. Yuan, W. Sun, Z. Zhang, Y. Wang, D. Huang, D. Ren, H. Chen, X. Wang, G. Li, Z. Han, 5-fluorouracil/curcumin loaded silk fibroin hydrogel for the adjuvant therapy in colorectal cancer, Biomaterials Advances 168 (2025) 214108, https://doi.org/10.1016/j.bioadv.2024.214108.
[206] K. Greish, Enhanced permeability and retention (EPR) effect for anticancer nanomedicine drug targeting, Methods Mol. Biol. 624 (2010) 25–37, https://doi.org/10.1007/978-1-60761-609-2_3.

Evaluation of molecular inclusion of azole antifungals by β-cyclodextrin using computational molecular approach

Riya Shikha[1] · Sidhartha S. Kar[2]

Abstract

Fungal infection is an emerging global concern highlighting diseases like pneumonia, invasive candidiasis, chronic pulmonary aspergillosis, and meningitis. But major concern is development of antifungal drug resistance, necessitating novel pharmacological solutions. Azoles, particularly fluconazole and related compounds, are emphasized for their systemic efficacy via inhibition of CYP51, altering fungal cell membrane sterols. So, in this work we theoretically investigated the effect of complexation of azoles with β-cyclodextrin (β-CD), focusing on improving solubility and bioavailability. Using molecular docking, the interaction between azoles and β-CD is analyzed, predicting stability and binding energies. Docking studies elucidate specific binding modes and hydrogen bonding interactions, while PM3 calculations provide insights into electronic structures and properties such as HOMO–LUMO energy gaps, chemical potential, hardness, and electrophilicity. Our findings indicate that fluconazole-β-CD complexes, particularly FCZ-βCD2, exhibit stability and promising development potential due to low energy and favorable binding characteristics. The antifungal spectrum of all the inclusion complexes was predicted using the PASS web server which proved that that the complexes are more effective against fungal pathogens than bacterial pathogens. This preliminary theoretical study highlights β-CD's potential as a carrier to enhance the therapeutic efficacy of antifungal drugs, addressing key challenges in treating fungal infections through improved solubility and bioavailability.

Keywords Antifungal azoles · *β*-cyclodextrin · Inclusion complex · Molecular docking · PM3 calculations

Abbreviations

β-CD	*β*-Cyclodextrin
FLZ	Fluconazole
CTZ	Clotrimazole
MCZ	Miconazole
PCZ	Propioconazole
KTZ	Ketoconazole
DFT	Density functional theory
BPL	Bond path length
GLC	Glucosyl group
HB	Hydrogen bond
PM3	Parametric method3
HOMO	Highest occupied molecular orbita

LUMO Lowest unoccupied molecular orbital
RMSD Root mean square deviation

1 Introduction

Owing to their high rates of morbidity and mortality, fungal infections have a significant economic burden. *Pneumocystis jirovecii* pneumonia cases are estimated to be more than 10,000 per year, along with 700,000 cases of invasive candidiasis, 3,000,000 cases of chronic pulmonary aspergillosis, 3,223,100 cases of *Cryptococcal meningitis* complicated by HIV/AIDS, and 3,000,000 cases of chronic pulmonary aspergillosis. Fungal disease prevention, diagnosis, and treatment require increased attention. The emergence of drug resistance due to fungal activity presents a major risk to human health. The discovery of novel pharmacological entities is challenging due to the time-consuming, complex, and expensive nature of the process. Additional challenges in drug development include unknown pathophysiology, patient population variability, and regulatory procedures. Consequently, developing new therapeutic conjugates that combine antifungal activity with water solubility has become a major research focus in the field of antifungal medicine. One promising approach is the complexation of antifungals with soluble polymers and/or cyclodextrins [1–8].

Among the most effective antifungal medications available, azoles are used to treat both systemic and invasive fungal infections. Over an 8-year period, there has been a 2.9% increase in the use of azoles. The first-generation triazole, fluconazole, was derived from ketoconazole, an earlier imidazole molecule. It is mostly effective against primary fungal pathogens, such as yeasts, but is ineffective against infections caused by filamentous fungi. It inhibits CYP51, which catalyzes the conversion of lanosterol to ergosterol through a three-step process. Ergosterol is broken down and levels of methylated sterols, such as 4,14-dimethylzymosterol and 24-methylenedihydrolanesterol, increases when pathogenic fungal infections are treated with azoles. Fungal cell death or inhibition of fungal cell growth results from the accumulation of methyl sterols in the cell membranes. Only voriconazole and itraconazole are regarded as fungicidal azoles; while all other azoles are fungistatic. The skin and vaginal infections were treated with clotrimazole and miconazole. It works best against *Malazzesia furfur*, *Trichophyton* spp., *Microsporum* spp., and *Candida* spp. At very high doses, clotrimazole exhibits activity against *Trichomonas* species and some in vitro activity against several other gram-positive bacteria. Clotrimazole vaginal pills have demonstrated cure rates for vaginal candidiasis that are similar to those of traditional nystatin vaginal tablets. Oral administration of clotrimazole is generally well tolerated; however, in some cases, treatment must be discontinued due to local irritation. Additionally, the drug's efficacy in treating other significant fungal infections has not been adequately demonstrated [9–18].

The structure of ß-cyclodextrin (ß-CD) consists of seven glucopyranose units. Because of its exceptional ability to accommodate hydrophobic aromatic rings, which improves solubility and stability, and lowers the toxicity of medicinal molecules, it is widely used in pharmaceutical research. ß-CD fosters host–guest inclusion complexes with a wide range of solid, liquid, and gaseous substances. They can accommodate many types of guest molecules inside their cavities. The generation of inclusion complexes between ß-CDs and drug molecule significantly alters the physicochemical properties of the guest molecule, including its water solubility and hydrogen bonding capability, as well as the entire clathrate. Under specific conditions, ß-CD and hydrophobic molecules form inclusion complexes that can readily permeate body tissues and release physiologically active compounds [19–26]. For the conformational investigation of supramolecular systems, including ß-CD inclusion compounds, the PM3 approach is an effective tool. Nevertheless, little is now known about the geometrical aspects and interactions that maintain the molecular architecture of the ß-CD/azole inclusion complexes. Using PM3 semi-empirical quantum mechanical computations and molecular docking, this preliminary study theoretically investigates the interaction of azoles (Fluconazole, Ketoconazole, Miconazole, Clotrimazole, and Propiconazole) and ß-CD molecules. Furthermore, we examined which of the five azoles formed the most stable inclusion complex with ß-CD. The primary objective was to find the region of the molecular cavity most suited for complexation with the azole moiety. These data can be used to predict which cyclodextrin hydroxyl groups can be chemically tweaked to prevent shielding and enhance the pharmacokinetics and systemic bioavailability of the inclusion complexes. The HOMO–LUMO, chemical potential, electronegativity, and electrophilicity index of the azole-ß-CD complex are among the quantum parameters and experimental data investigated using Density Functional Theory (DFT). Frontier molecular orbitals (FMOs), which have the lowest unoccupied molecular orbital (LUMO) and highest occupied molecular orbital (HOMO), are used to evaluate the molecular properties [27–39].

2 Materials and methods

All investigational studies in this work were carried out on an Intel Core i3-based system with Windows 10. Structural preparation, modeling and analysis were performed using ChemDraw, BIOVIA Studio, and ChemSketch. PM3 semi-empirical caluculations were carried out using Argus Lab and IQmol software, whereas docking studies were carried out using Autodock Vina integrated Chimera 1.15 [40-44]. The Argus lab software was used to perform all the quantum chemistry calculations of the existing molecular structures. The 3D structures of *β*-cyclodextrin and azoles were retrieved from the Protein Data Bank (PDB ID: 3m3r) and PubChem. Chain I of the 3m3r protein was used as *β*-CD in this study. The structures were 'cleaned' w.r.t. geometries, atom types, and charges were computed using ANTICHAMBER (Gasteiger method) in the chimera.

2.1 Experimental

2.1.1 Molecular docking

To investigate the inclusion of antifungal azoles in ß-CD, we used molecular docking. To perform the molecular docking study, the three-dimensional structure of ß-CD obtained from protein data bank and structure of azoles were drawn in Chemdraw. ß-CD was imported into CHIMAERA (version 1.15) for docking analysis. Docking was performed to determine how azoles interacted with or docked with ß-CD as the ligand. The tertiary structure of ß-CD was prepared for docking (Gasteiger method) by adding polar hydrogen, charges, and computing charges using ANTICHAMBER (Gasteiger method) [45].

The tertiary structures of azoles were drawn in Chemdraw and minimized using the following parameters: Steepest descent steps: 1000 with a step size of 0.02 Å, Conjugate gradient steps: 10 with a step size of 0.02 Å.

Followed by addition of hydrogen atoms and charges (Amber ff99bsc0 for standard residues and Gasteiger for other residues). In the host molecule structure, a cubic box is formed to facilitate ligand binding [46, 47].

A theoretical study based on the most prevalent docking confirmation was conducted using geometrical optimization. The docking data were differentiated using root mean square deviation (RMSD) and binding energy. The stability of a complex can be investigated using the frequent cluster, lower binding energy, RMSD (lower bound and upper bound), and maximum number of hydrogen bonds for each structure box.

2.1.2 Quantum chemistry

The quantum mechanical technique of density functional theory (DFT) can be used to examine the electronic structure of organic molecules. DFT is the most frequently utilized approach for the quantum mechanical modeling of energy surfaces in molecules and other periodic systems. The first task carried out using the DFT method, which places no restrictions on molecular symmetry, was geometry optimization. Software programs such as Argus Lab and IQmol were used to conduct PM3 semiempirical calculations. Initially, the molecule was created and optimized to perform molecular modelling in the Argus Lab 4.0. Subsequently, the Hartree–Fock approximation of 200 interactions, geometry optimization, and single-point energy determination by semi-empirical computation (PM3) were performed. The frontier orbitals HOMO (Highest Occupied Molecular Orbital) and LUMOL (Lowest Unoccupied Molecular Orbital) were obtained and included in the output files together with the molecular electrostatic potential (MEP) [48-57].

2.1.2.1 Frontier orbital energies (E_{HOMO} and E_{LUMO}) The interactions of molecules with other species were studied using frontier molecular orbitals (E_{HOMO} and E_{LUMO}). Whereas the LUMO acts as an electron acceptor, the HOMO acts as an electron donor [58-62]. The amount of energy necessary to remove an electron from a single atom or molecule is known as the ionization potential (I). When a neutral atom acquires one electron to become a negative ion, the resulting energy change is known as electron affinity (EA). In the context of Koopmans' theorem, I and EA can be calculated using HOMO and LUMO energies:

$$= -EHOMO$$

$$EA = -ELUMO$$

Energy gap (E): Between the HOMO and LUMO levels, there is an energy difference, known as the energy gap (HOMO/LUMO gap). A larger energy gap increases the stability of the molecule. The molecular conductivities and solubility both increase when the energy gaps are narrow. Absolute hardness, half of the HOMO–LUMO gap in the Hartree–Fock or Hückel theory, is a good indicator of aromaticity, and a maximum hardness principle has been developed [53–57]. Generally, the energy gap depends on the electron-donating strength of the donor and the electron-withdrawing strength of the acceptor, and is given by

$$E = I - EA = E_{LUMO} - E_{HOMO}$$

The electronic chemical potential is linked to the feasibility of a system to exchange electron density with the ground-station environment. Hardness is a measure of the rate at which the chemical potential (μ) changes with electron density. In a hard system, the chemical potential is substantially changed by even small changes in the electron density. The hardness acts as a barrier to the change in electron density for a certain change in the chemical potential. As a result, the term "hardness," which denotes resistance to deforestation, originated. For the DFT to function, the hardness of the system does not have to be constant. Instead, it uses local values. Softness is an antithesis of hardness. Electronegativity, a negative value of the chemical potential, is a feature that remains constant within an atom or molecule and throughout orbitals, according to the Hohenberg–Kohn density functional theory [58, 59].

The following equations were used to analyze the reactivity of the investigated complexes, utilizing quantum mechanical descriptors such as the chemical potential (μ), global hardness (η), softness (S), and global electrophilicity index (ω):

- Electronic chemical potential (μ)

  $\mu = (E_{HOMO}+E_{LUMO})/2$

- Global hardness (η)

  $\eta = (E_{HOMO}-E_{LUMO})/2$

- Softness (S)

  $S = 1/\eta$

- Electrophilicity (ω)

  $\omega = \mu^2/2\eta$

2.1.3 PASS prediction

The antifungal activity spectrum of the inclusion complexes was assessed using the PASS online web application (http://www.way2drug.com/passonline/predict.php). The complexes resulting from docking were converted to SMILES format in Discovery studio for analysis with the PASS web tool. This tool predicts over 4000 types of antimicrobial functions, encompassing both drug and non-drug activities, with a claimed 90% accuracy rate. PASS provides results in terms of Pa (probability of active molecule) and Pi (probability of inactive molecule), each ranging from 0.00 to 1.00. Typically, $Pa + Pi \neq 1$, reflecting the probabilistic nature of the predictions. Biological activities where $Pa > Pi$ are considered plausible for the respective drug molecules. PASS outcomes guide decision-making based on thresholds such as $Pa > 0.7$ indicating high activity likelihood, $0.5 < Pa < 0.7$ suggesting lower activity likelihood, and $Pa < 0.5$ indicating minimal activity likelihood.

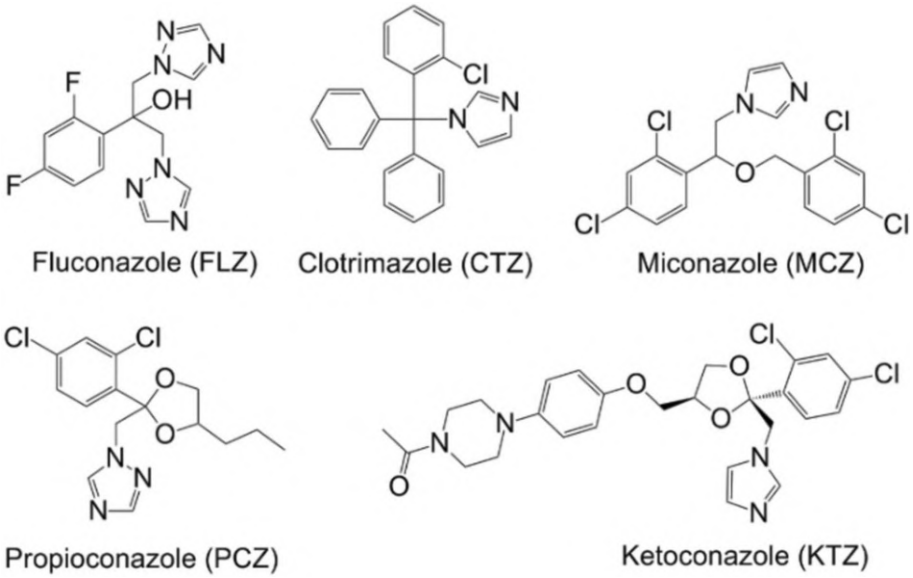

Fig. 1 Chemical structures of fluconazole (FCZ), clotrimazole (CTZ), miconazole (MCZ), propioconazole (PCZ) and ketoconazole (KTZ)

Table 1 Docking results of *β -CD*- Azoles inclusion complexes

Name of the inclusion complex	Docking energy (Kcal/mol)	RMSD l.b	RMSD u. b	No. of active torsions
FLZ-βCD1	− 5.6	0	0	6
FLZ-βCD2	− 5.5	2.966	4.352	6
CTZ-βCD1	− 5.5	0	0	4
CTZ-βCD2	− 5.2	2.351	5.01	4
MCZ-βCD1	− 5.4	0	0	6
MCZ-βCD2	− 5	2.865	5.405	6
PCZ-βCD1	− 5.2	0	0	5
PCZ-βCD2	− 5.1	3.066	4.357	5
KTZ-βCD1	− 5.1	0	0	5
KTZ-βCD2	− 4.8	3.101	5.202	5

3 Result and discussion

3.1 Molecular docking studies

The automated docking experiments were performed using the AutoDock Vina v1.5.6 integrated Chimera software. The ligands selected for the docking investigations were fuconazole (FLZ), clotrimazole (CTZ), miconazole (MCZ), propioconazole (PCZ), and ketoconazole (KTZ) (Fig. 1), with β-CD serving as the inclusion macromolecule [6, 63, 64]. This study investigated the interactions between azoles and two β-cyclodextrin (β-CD) models using molecular docking techniques. The docking process aimed to predict the primary binding mode between the azoles, acting as guest molecules, and β-CD, serving as the host molecule with a well-defined three-dimensional structure. Ten possible docking conformations of azoles within the β-CD cavity were generated. The docking energies for each complex, detailed in Table 1, identified the most favorable spatial conformations. Higher negative docking energy values indicate more stable interactions, while lower negative values suggest fewer stable interactions. Azoles with the lowest binding energies were selected for further study, as they exhibited the most advantageous spatial conformations compared to other azole-β-CD complexes [45, 65-71]. To enhance the accuracy of the docking process, the search space grid box was expanded, as shown in Table 2.

The hydrogen bonds in inclusion complexes and monomers were investigated using BIOVIA Discovery Studio and the Avogadro program (Table 3). Certain proton donors of β-CD were detected on the hydrophilic layer, whereas

Table 2 Inclusion complexes and their Grid box characteristics

Name of the inclusion complex	Grid box size	Gride box center	Energy_range	Num_modes
FLZ-ßCD	size_x = 25.48 size_y = 32.32 size_z = 34.07	center_x = 30.42 center_y = 32.35 center_z = 22.96	3	9
CTZ-ßCD	size_x = 39.43 size_y = 26.03 size_z = 33.00	center_x = 23.21 center_y = 30.01 center_z = 22.00	3	9
MCZ-ßCD	size_x = 15.93 size_y = 16.88 size_z = 14.95	center_x = 30.19 center_y = 32.72 center_z = 21.43	3	9
PCZ -ßCD	size_x = 21.26 size_y = 18.38 size_z = 18.81	center_x = 29.82 center_y = 31.97 center_z = 21.59	3	9
KTZ -ßCD	size_x = 18.72 size_y = 17.27 size_z = 16.08	center_x = 30.92 center_y = 32.22 center_z = 21.95	3	9

others were detected on the hydrophobic layer. There were two types of HBs: md HBs, which were identified inside the azole or ß-CD molecules, and intermolecular HBs, which were found to be HBS between the ß-CD and azole molecules. Of all the HBs present, the intermolecular HBs in each inclusion complex had the greatest influence on the stability of the inclusion complex. For convenience, in ß-CD, the 14 oxygen atoms act as acceptors of the intramolecular H-proton bond.

3.2 Intermolecular HBs in FCZ- β -CD

Four intermolecular HBs were observed in the FCZ-ßCD1 complex (Fig. 2a, b), whereas seven HBs were observed in the FCZ-ßCD2 complex (Fig. 2c, d). FCZ-ßCD1 contained three non-classical intermolecular HBs and one classical HB (FCZ1:H12-GLC: O4). Of the seven intermolecular HBs in FCZ-ßCD2, three were classical and four were non-classical. Given that FCZ-ßCD2 has more intramolecular HBs, it appears to be more stable.

3.3 Intermolecular HBs in CTZ-βCD

Three intermolecular HBs with bond lengths of 2.69 Å were found in the CTZ-*ß*CD1 (Fig. 3e, f) and CTZ-ßCD2 (Fig. 3g, h) inclusion complexes. However, in the case of CTZ-*ß*CD2, fewer intermolecular HBs are observed. CTZ-ßCD1 had more intermolecular HBs and one classical HB, indicating that CTZ-ßCD1 is more stable.

3.4 Intermolecular HBs in MCZ

Six intermolecular HBs were observed in the MCZ-*ß*CD1complex (Fig. 4i, j). The strongest bond among the tall bonds was observed in GLC: H5-MCZ1:Cl4 (2.35 Å), which has the shortest bond. The molecule is unstable because all intermolecular HBs are nonclassical. Although MCZ-*ß*CD2 (Fig. 4k, l) has one classical bond, GLC7:HO6-MCZ1:N2 (2.62 Å), it also has six intermolecular HBs. MCZ-*ß*CD2 has a single classical HB, making it more stable than MCZ-*ß*CD1, which contains equal amounts of intermolecular HBs.

3.5 Intermolecular HBS in PCZ: βCD

Owing to its five intermolecular HBs, one classical intermolecular HB, and one classical intermolecular HB, PCZ-ßCD1 (Fig. 5m, n) was more stable than PCZ-ßCD2 (Fig. 5o, p).

Table 3 Intermolecular hydrogen bonding (IHBs) in FCZ-*β*CDs, CTZ-*β*CDs, MCZ-*β*CDs, PCZ-*β*CDs and KTZ-*β*CDs

S. No.	Inclusion complex	IHBs	Distance (Å)
1	FCZ-*β*CD1	GLC_1:O_4-FCZ_1:H_{12}	2.7
		GLC_2:H_3-FCZ_1:O_1	2.71
		GLC_2:H_3-FCZ_1:N_6	2.73
		GLC_6:H_3-FCZ_1:F_2	2.36
		GLC_6:H_5-FCZ_1:F_2	2.81
2	FCZ-*β*CD2	GLC_6:O_4-FCZ_1:H_{12}	2.40
		GLC_3:HO_3-FCZ_1:F_1	2.91
		GLC7:HO_2-FCZ_1:N_6	2.93
		GLC_7:O_4-FCZ_1:C_8	3.36
		GLC_2:H_3-FCZ_1:F_2	2.37
		GLC_6:H_3-FCZ_1:N_6	2.98
		GLC_7-H_5-FCZ_1:N_3	2.76
3	CTZ-*β*CD1	GLC5:H3-CTZ_1:C_{l1}	2.27
		GLC_2:O_3-CTZ_1:C_{21}	3.39
		GLC_1:HO_3-CTZ_1:N_2	2.69
4	CTZ-*β*CD2	GLC_1:H_3-CTZ_1:C_{l1}	2.79
		GLC_4:HO_3-CTZ_1:N_2	2.84
5	MCZ-*β*CD1	GLC_5:O4.MCZ_1:C_7	3.622
		GLC_2:O_4-MCZ_1:C_{12}	3.511
		GLC_4:H_3-MCZ_1:Cl2	2.769
		GLC_4:H_3-MCZ_1:C_{l4}	2.35
		GLC_5:H_3-MCZ_1:C_{l2}	2.65
		GLC_5:H_5-MCZ_1:C_{l4}	2.75
6	MCZ-*β*CD2	GLC_7:HO_6-MCZ_1:N_2	2.62
		GLC_5:O_4-MCZ_1:C_7	3.464
		GLC_3:O_4-MCZ:C_9	3.73
		GLC_2:O_4-MCZ_1:C_{10}	3.78
		GLC_1:H_3-MCZ_1:C_{l4}	2.802
		GLC_2:H_3-MCZ_1C_{l4}	2.434
7	PCZ:*β*CD1	GLC_5:HO_3-PCZ_1:N_3	2.86
		GLC_4:O_4-PCZ_1:C_4	3.79
		GLC_4:O_4-PCZ_1:C_7	3.71
		GLC_4:O_4-PCZ_1:C_7	3.71
		GLC_6:H_3-PCZ_1:O_1	2.75
		GLC_6:H_3-PCZ_1:N_3	2.80
8	PCZ:*β*CD2	GLC_2:H_9-PCZ_1:N_3	2.75
		GLC_1:H_3-PCZ_1:Cl_2	2.95
		GLC_1:H_3-PCZ_1:N_3	2.96
9	KTZ-*β*CD1	GLC_4:O_4-KTZ:C_4	3.795
		GLC_4:O_4-KTZ_1:C_7	3.606
		GLC_4:H_3-KTZ_1:N_3	2.390
		GLC_4:H_3-KTZ_1:N_3	2.390
10	KTZ-*β*CD2	GLC_7:HO_6-KTZ_1:N_2	2.798
		GLC_7:O_4-KTZ:C_5	3.752
		GLC6:O4-KTZ_1:C_8	3.736
		GLC_5:H_3-KTZ_1:C_{l2}	2.611

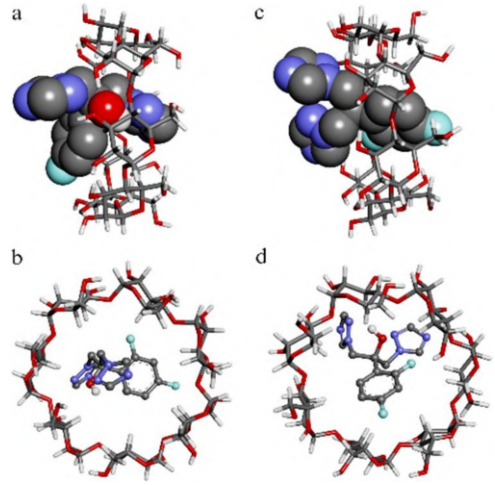

Fig. 2 Binding mode of Fluconazole (FCZ) within ßCD1 (FCZ: ßCD1, **a** and **b**) and ßCD2 (FCZ: ßCD2, **c** and **d**)

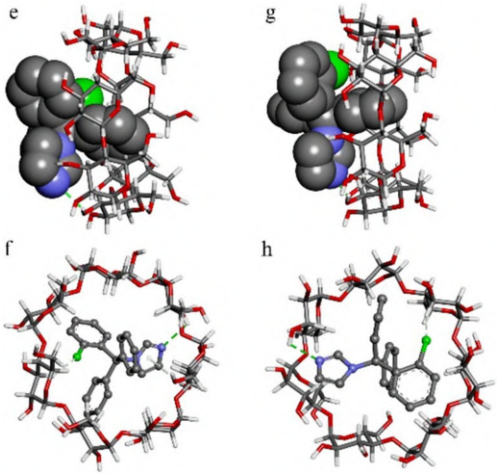

Fig. 3 Binding mode of clotrimazole with *ß*CD1 (CTZ: *ß*CD1, **e** and **f**) and *ß*CD2 (CTZ: *ß*CD2, **g** and **h**)

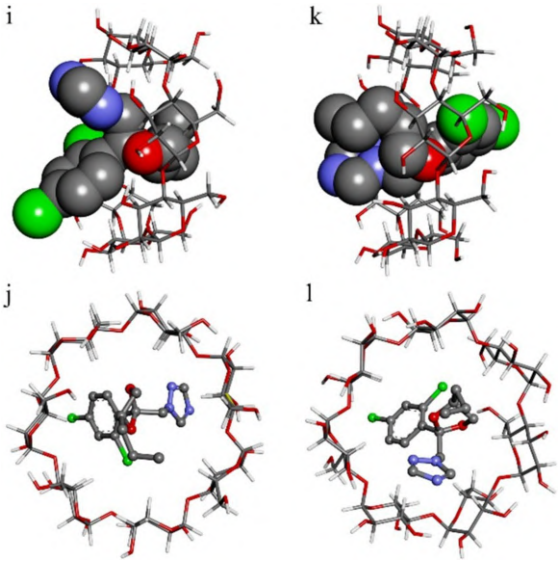

Fig. 4 Binding mode of miconazole with ßCD1 (MCZ: ßCD1, **i** and **j**) and ßCD2 (MCZ: ßCD2, **k** and **l**)

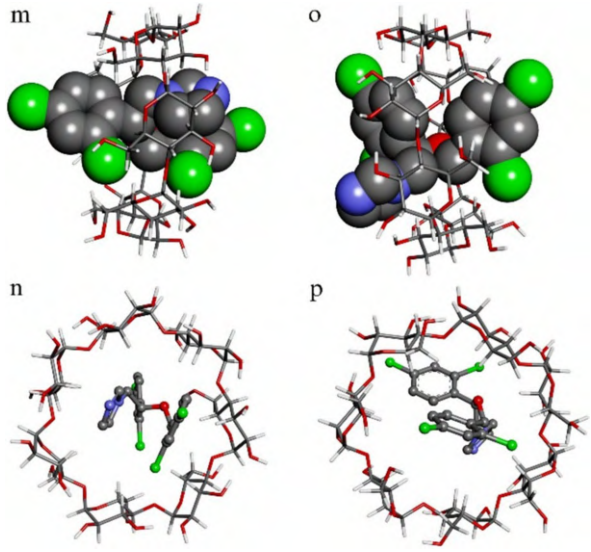

Fig. 5 Binding mode of propiconazole with *β*CD1 (PCZ: βCD1, **m** and **n**) and *β*CD2 (PCZ: *β*CD2, **o** and **p**)

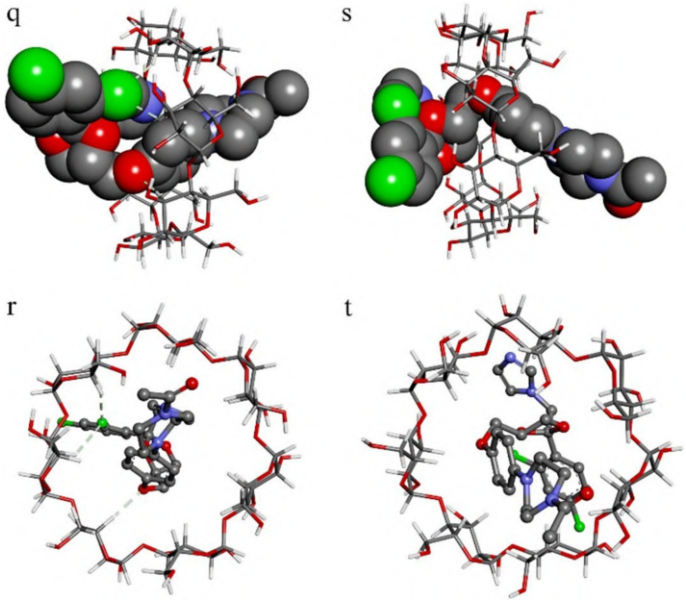

Fig. 6 Binding mode of ketoconazole with *β*CD1 (PCZ: *β*CD1, **q** and **r**) and *β*CD2 (PCZ: *β*CD2, **s** and **t**)

3.6 Intermolecular HBs in βCD: ketoconazole

With three intermolecular HBs, Model 1 of *β*-CD ketoconazole (KTZ: βCD1) had the shortest BPL of the GLC: H_3...KTZN_3 formation, H3...N3 (Fig. 6q, r). KTZ$_1$:C$_4$...GLC$_4$:C$_4$...O$_4$ exhibited the longest BPL. All carbon atoms (non-classical HBs) linked to proton donors have lower electronegativity than oxygen and nitrogen. When comparing these two models, it can be shown that KTZ: βCD2 (Fig. 6s, t)is more stable than KTZ: *β*-CD1 since it has more intermolecular HBs and one classical HB involved in the interaction.

3.7 Quantum chemistry

Using the Arguslab 4.0.1 programme, single-point energy calculations and geometry optimization for all structures were performed using Hartree–Fock SCF calculations with PM3 semiempirical Hamiltonians. Table 4 lists the energies of the monomers, ten inclusion complexes, and heat of formation.

Table 4 Total energy and heat of formation of compounds

S. No.	Name	Total energy (Kcal/mol)	Heat of formation (Kcal/mol)
1	β-CD	− 3.0922287	66,046
2	Fluconazole	− 90,611.98	44.74
3	Clotrimazole	71,902.39	149,747.3
4	Miconazole	95,338.85	173,901.2
5	Propiconazole	− 79,991.77	63.5
6	Ketoconazole	− 79,991.77	63.5
7	FCZ-βCD1	− 392,504.76	72,007
8	FCZ-βCD2	− 394,746.33	71,197.7
9	CTZ-βCD1	− 378,332.31	74,428.3
10	CTZ-βCD2	− 378,521.6	74,239
11	MCZ-βCD1	− 368,264.27	90,613.8
12	MCZ-βCD2	− 271,109.97	18,768.1
13	PCZ-βCD1	− 337,608.86	117,008.6
14	PCZ-βCD2	− 366,673.51	87,943.5
15	KTZ-βCD1	− 327,777.74	126,839.7
16	KTZ-βCD2	− 370,781.13	126,839.7

Table 5 HOMO & LUMO energies, ΔE, global chemical potential (μ), global hardness (η), softness (s), and electrophilicity (ω) of all compounds of all inclusion complexes

S. No.	Inclusion complexes	HOMO (eV)	LUMO (eV)	Energy gap (eV)	μ (eV)[a]	η (eV)[b]	S (eV)[c]	ω (eV)[d]
1	FCZ-βCD1	6.947383	7.307282	0.359899	7.1273325	0.1799495	5.55711463	141.14757
2	FCZ-βCD2	12.039928	12.489063	0.449135	12.264496	0.2245675	4.45300411	334.90565
3	CTZ-βCD1	0.819406	0.888222	0.068816	0.853814	0.034408	29.0630086	10.593443
4	CTZ-βCD2	− 2.731976	− 2.721632	0.010344	− 2.726804	0.005172	193.348801	718.81864
5	MCZ-βCD1	− 5.288582	− 5.177059	0.111523	− 5.232821	0.0557615	17.9335204	245.53151
6	MCZ-βCD2	− 5.947054	− 5.896713	0.050341	− 5.921884	0.0251705	39.7290479	696.62311
7	PCZ-βCD1	− 4.278594	− 4.231939	0.046655	− 4.255267	0.0233275	42.8678598	388.11045
8	PCZ-βCD2	− 0.46016	− 0.30183	0.15833	− 0.380995	0.079165	12.6318449	0.9168016
9	KTZ-βCD1	− 6.125364	− 5.91099	0.214374	− 6.018177	0.107187	9.32948958	168.94985
10	KTZ-βCD2	19.119567	19.508617	0.38905	19.314092	0.194525	5.14072741	958.83344

[a]Chemical potential (μ)

[b]Global hardness (η)

[c]Softness (s)

[d]Global electrophilicity index (ω)

FCZ-βCD2 is the most stable inclusion complex because of its low energy (− 394,746.33 kcal/mol) and its interaction with azoles and β-CD. All ten implicated complexes had energies lower than those of the two monomers.

The HOMO–LUMO energy gap is a well-established metric for evaluating intramolecular charge transfer. Smaller gaps indicate lower chemical stability, while larger gaps are associated with higher kinetic stability and lower chemical reactivity. A larger HOMO–LUMO energy gap in the title molecule suggests greater stability. Upon formation of the inclusion complex, both the global hardness and HOMO–LUMO band gap decreased, indicating a reduction in chemical stability and an increase in chemical activity (Table 5). A higher global electrophilicity value denotes increased reactivity. Molecules with narrow energy gaps exhibit low kinetic stability, high chemical reactivity, and high polarizability, often referred to as soft molecules. The chemical activity of a molecule can be inferred by examining the HOMO and LUMO energy levels and their energy gap. The title molecule, often referred to as a hard molecule, has been found to have a higher chemical potential and wider HOMO–LUMO energy gap, indicating a high degree of stability [72–74]. The findings

Table 6 Prediction of antimicrobial activity of inclusion complexes using the PASS web tool

S. No.	Inclusion complexes	Biological activity			
		Antibacterial		Antifungal	
		Pa	Pi	Pa	Pi
1	FCZ-βCD1	0.450	0.022	0.726	0.008
2	FCZ-βCD2	–	–	0.726	0.008
3	CTZ-βCD1	0.450	0.022	0.443	0.041
4	CTZ-βCD2	0.139	0.077	0.443	0.041
5	MCZ-βCD1	0.185	0.132	0.661	0.012
6	MCZ-βCD2	0.185	0.132	0.661	0.012
7	PCZ-βCD1	0.176	0.140	0.795	0.005
8	PCZ-βCD2	0.176	0.140	0.795	0.005
9	KTZ-βCD1	–	–	0.640	0.014
10	KTZ-βCD2	–	–	0.640	0.014

show that FCZ-βCD2 has the lowest softness value (4.453000411 eV), highest chemical potential (12.264496 eV), and largest energy gap (0.449135 eV), all of which may contribute to its greater chemical stability than the other compounds. The lowest HOMO–LUMO gap (0.0103444 eV) was found for CTZ-βCD2. Additionally, Table 5 shows that FCZ-βCD2 has the highest global hardness value.

3.8 PASS prediction

The antifungal spectrum of all the inclusion complexes was predicted using the PASS web server. The results, expressed as Pa (probability of activity) and Pi (probability of inactivity), are presented in Table 6. As shown in Table 6, the inclusion complexes exhibited Pa values ranging from 0.13 to 0.45 for antibacterial activity and from 0.44 to 0.79 for antifungal activity. These findings indicate that the complexes are more effective against fungal pathogens than bacterial pathogens. Notably, different docking poses demonstrated consistent antifungal activity, likely due to the active antifungal azole molecule remaining unchanged while βCD has no impact on activity. However, further *in-silico* and *in-vitro* studies are necessary to clarify these observations.

4 Conclusion

In order to shed light on the stability and binding interactions of azole-β-CD inclusion complexes, we concentrate on computational investigations of antifungal azoles and β-cyclodextrin inclusion complexes in this work. Molecular docking and semi-empirical PM3 computations are included. The results of docking tests indicate that azoles, particularly fluconazole, form stable complexes with β-CD, FCZ-βCD2 exhibiting the best binding characteristics. PM3 simulations provide a comprehensive analysis of the electronic structure, including HOMO–LUMO energy gaps, chemical potential, hardness, and electrophilicity, which supports these findings. These descriptors of quantum mechanics suggest that the inclusion complexes have better physicochemical characteristics, such as increased bioavailability and solubility. Our findings demonstrate the potential of β-CD as a transporter for azole antifungal medications, providing a viable approach to address problems with solubility and bioavailability. Enhancing these essential characteristics can help β-CD complexation improve the therapeutic efficacy of azoles, addressing the urgent problem of antifungal medication resistance and leading to better fungal infection treatment outcomes. The antifungal spectrum of all the inclusion complexes was predicted using the PASS web server which proved that that the complexes are more effective against fungal pathogens than bacterial pathogens.

In summary, this study's preliminary theoretical investigation of azole-β-CD complexes establishes the foundation for additional experimental verification and the creation of sophisticated antifungal formulations. This in silico method is a big step in improving antifungal treatments and addressing the widespread problem of fungal infections.

5 Statement of usage of artificial intelligence

Authors declare that they haven't received any help from Artificial intelligence in preparing this paper. The research data reported in the manuscript can be followed to reproduce the work.

Author contributions Conception or design of the work was performed by SK, data was generated by RS, data analysis and interpretation were done by SK and RS. The first draft of the manuscript was written by SK and RS. All authors read and approved the final manuscript.

Funding No funding was received to assist with the preparation of this manuscript or for conducting this research.

Data availability The authors declare that the data supporting the findings of this study are available within the paper. Should any raw data files be needed in another format they are available from the corresponding author upon reasonable request. Source data are provided with this paper.

Declarations We hereby declare that all data and materials, as well as software applications or custom codes, support the published claims and comply with field standards.

Competing interests The authors declare no competing interests.

References

1. Pfaller MA, Diekema DJ, Gibbs DL, Newell VA, Ellis D, Tullio V. Results from the artemis disk global antifungal surveillance study 1997 to 2007: a 105-year analysis of susceptibilities of candida speciestofluconazole and voriconazole as determined by CLSI standardized disk diffusion. J Clin Microbiol. 2010. https://doi.org/10.1016/j.ijantimicag.2022.106518.
2. Kauffman CA. Fungal infections infectious disease in the aging: a clinical handbook. Int J Antimicrob Agents. 2009. https://doi.org/10.1016/j.ijantimicag.2022.106518.
3. Jabra-Rizk MA, Falkler WA, Meiller TF. Fungal biofilms and drug resistance. Emerg Infect Dis. 2004. https://doi.org/10.3201/eid1001.030119.
4. Van Daele R, Spriet I, Wauters J, Maertens J, Mercier T, Van Hecke S. Antifungal drugs: ¿What brings the future? Med Mycol. 2019. https://doi.org/10.1093/mmy/myz012.
5. Lupetti A. Molecular basis of resistance to azole antifungals. Trends Mol Med. 2002. https://doi.org/10.1016/S1471-4914(02)02280-3.
6. Jun SW, Kim MS, Kim JS, Park HJ, Lee S, Woo JS. Preparation and characterization of simvastatin/hydroxypropyl-ß-cyclodextrin inclusión complex using supercritical antisolvent (SAS) process. Eur J Pharm Biopharm. 2007. https://doi.org/10.1016/j.ejpb.2006.11.013.
7. Bai H, Lv F, Liu L, Wang S. Supramolecular antibiotic switches: a potential strategy for combating drug resistance. Chem Eur J. 2016. https://doi.org/10.1002/chem.201600877.
8. Tom L, Nirmal CR, Dusthackeer A, Magizhaveni B, Kurup MR. Formulation and evaluation of ß-cyclodextrin-mediated inclusión complexes of isoniazid scaffolds: molecular docking and in vitro assessment of antitubercular properties. New J Chem. 2020. https://doi.org/10.1039/C9NJ06351J.
9. Hostetler JS, Hanson LH, Stevens DA. Effect of cyclodextrin on the pharmacology of antifungal oral azoles. Antimicro Agents Chemother. 1992. https://doi.org/10.1128/aac.36.2.477.
10. Maertens JA. History of the development of azole derivatives. Clin Microbiol Infect. 2004. https://doi.org/10.1111/j.1470-9465.2004.00841.x.
11. Yang W, Wiederhold NP, Williams RO. Drug delivery strategies for improved azole antifungal action. Expert Opin Drug Deliv. 2008. https://doi.org/10.1517/17425240802457188.
12. Kirkpatrick CH, Alling DW. Treatment of chronic oral candidiasis with clotrimazole troches. New Eng J Med. 1978. https://doi.org/10.1056/NEJM197811302992201.
13. Sheehan DJ, Hitchcock CA, Sibley CM. Current and emerging azole antifungal agents. Clin Microbiol Rev. 1999. https://doi.org/10.1128/cmr.12.1.40.
14. Saag MS, Dismukes WE. Azole antifungal agents: emphasis on new triazoles. Antimicrob Agents Chemother. 1988. https://doi.org/10.1128/aac.32.1.1.
15. Greer ND. Voriconazole: the newest triazole antifungal agent. Proceedings (Baylor University. Medical Center). 2003; https://doi.org/10.1080/08998280.2003.11927910.

16. Kurn H. Itraconazole-StatPearls-NCBI Book shelf [Internet]. NIH. StatPearls. 2022; https://www.ncbi.nlm.nih.gov/books/NBK557874/. Accessed 28 Jan 2024.
17. Govindarajan A. Fluconazole-StatPearls-NCBI Bookshelf. National library of medicines. National centre for biotech. 2023; https://www.ncbi.nlm.nih.gov/books/NBK537158/. Accessed 21 Mar 2024.
18. Khatter NJ. Clotrimazole - StatPearls - NCBI Bookshelf [Internet]. National Insti. of medici. National center for biotec, Info. 2023; https://www.ncbi.nlm.nih.gov/books/NBK560643/. Accessed 03 Apr 2024.
19. Loftsson T, Duchene D. Cyclodextrins and theirpharmaceutical applications. Int J Pharm. 2007. https://doi.org/10.1016/j.ijpharm.2006.10.044.
20. Rajewski RA, Stella VJ. Pharmaceutical applications of cyclodextrins: in vivo drug delivery. J Pharm. 1996. https://doi.org/10.1021/js960075u.
21. Jo´zsef J. CycloLab – cyclodextrin research [Internet]. Research gate. ACS. 1998; https://www.researchgate.net/profile/Jozsef-Szejtli. Accessed 28 Jan 2024.
22. Balaci T, Velescu B, Karampelas O, Musuc AM, Nițulescu GM, Ozon EA, Nițulescu G, Gîrd CE, Fița C, Lupuliasa D. Physico-chemical and pharmaco-technical characterization of inclusion complexes formed by ß-cyclodextrin and hydroxypropyl-ß-cyclodextrin used to develop solid dosage forms. Processes. 2020. https://doi.org/10.3390/pr9010026.
23. Beta-cyclodextrin: National Center for Biotechnology Information. Pub Chem Compound Database. U.S. National Library of Medicine. https://pubchem.ncbi.nlm.nih.gov/compound/beta-CYCLODEXTRIN. Accessed 10 Apr 2023.
24. Bibby DC, Davies NM, Tucker IG. Mechanisms by which cyclodextrins modify drug release from polymeric drug delivery systems. Int J Pharm. 2000. https://doi.org/10.3390/pr9010026.
25. Hirayama F. Cyclodextrin-based controlled drug reléase system. Adv Drug Deliv Rev. 1999. https://doi.org/10.1016/S0169-409X(98)00058-1.
26. Liu C, Liu Z, Liu S, Tiwari SK, Thummavichai K, Ola O. Antibacterial properties and drug reléase study of cellulose acetate nanofibers containing ear-like AG-NPS and dimethyl oxallyl glycine/ beta-cyclodextrin. Appl Surf Sci. 2022. https://doi.org/10.1016/j.apsusc.2022.153132.
27. Orio M, Pantazis DA, Neese F. Density functional theory. Photosynth Res. 2009. https://doi.org/10.1039/C001286F.
28. LaPointe S, Weaver D. A review of density functional theory quantum mechanics as applied to pharmaceutically relevant systems. Curr CADD. 2007. https://doi.org/10.2174/157340907782799390.
29. Tandon H. A brief review on importance of DFT in drug design. Res Med Eng Sci. 2019. https://doi.org/10.31031/RMES.2019.07.00068.
30. Geerlings P, De Proft F, Langenaeker W. Conceptual density functional theory. Chem Rev. 2003. https://doi.org/10.1021/cr990029p.
31. Chakraborty D, Chattaraj PK. Conceptual density functional theory based electronic structureprinciples. Chem Sci. 2019;12(18):6264–79. https://doi.org/10.1039/D0SC07017C.
32. Elshakre ME, Noamaan MA, Moustafa H, Butt H. Density functional theory, chemical reactivity, pharmacological potential and molecular docking of dihydrothiouracil-indenopyridopyrimidines with human- DNA topoisomerase II. Int J Mol Sci. 2020. https://doi.org/10.3390/ijms21041253.
33. Braga EJ. Molecular electrostatic potential surface, HOMO-LUMO, and computational análisis of synthetic drug rilpivirine. Int J Sci Amp Eng Res. 2016;7(7):315–9.
34. Abdolmaleki A, Ghasemi F, Ghasemi JB. Computer-aided drug design to explore cyclodextrin therapeutics and biomedical applications. Chem Biol Drug Des. 2017. https://doi.org/10.1111/cbdd.12825.
35. Kupka T. B-lactamantibiotics. Spectroscopy and molecular Orbital (MO) calculations. Spectrochim Acta Part A Mol Biomol Spectro. 1997. https://doi.org/10.1016/S1386-1425(97)00146-7.
36. Khezri A, Karimi A, Yazdian F, Jokar M, Mofradnia SR, Rashedi H. Molecular dynamic of curcumin/ chitosan interaction using a computational molecular approach: emphasis on biofilm reduction. Int J Biol Macromol. 2018;114:972–8. https://doi.org/10.1016/j.ijbiomac.2018.03.100.
37. Kavitha E. Molecular structure, vibrational spectroscopy and HOMO, LUMO studies of 4-nitroaniline by density functional theory. Ind J Pure Aorgppl Phys. 2009;7(48):20–30.
38. Joshi D, Thakur G, Chaudhary MK. Molecular structure, HOMO-LUMO and vibrational analysis of ergoline by density functional theory. Sci World. 2021;14(14):21–30.
39. Fifere A, Marangoci N, Maier S, Coroaba A, Maftei D, Pinteala M. Theoretical study on ß- cyclodextrin inclusion complexes with propiconazole and protonated propiconazole. Beils J Org Chem. 2012. https://doi.org/10.3762/bjoc.8.247.
40. Naz A, Bano K, Bano F, Ghafoor NA, Akhtar N. Conformational análisis (Geometryoptimization) of nucleosidic antitumor antibiotics how Showdomycin AgrusLab 4 software. Pak J Pharm Sci. 2009;22:78–82.
41. Hafeez A. Computational study on the geometry optimization and excited—state properties of Riboflavin by Argus Lab 4.0.1. Pak J Pharm Sci. 2013;26:487–93.
42. Phankingthongkum S, Limpanuparb T. A virtual alternative to molecular model sets: a beginners' guide to constructing and visualizing molecules in open-source molecular graphics software. BMC Res. 2021. https://doi.org/10.17632/hfynpvtrz3.
43. Seeliger D, de Groot BL. Ligand Docking and binding site analysis with PyMOL and autodock/vina. J Comput Aided Mol Des. 2010;24(5):417–22. https://doi.org/10.1007/s10822-010-9352-6.
44. Pettersen EF, Goddard TD, Huang CC, Couch GS, Greenblatt DM, Meng EC. UCSF chimera? A visualization system for exploratory research and analysis. J Comp Chem. 2004. https://doi.org/10.1002/jcc.20084.
45. Roy N, Ghosh B, Roy D, Bhaumik B, Roy MN. Exploring the inclusión complex of a drug (umbelliferone) with α-cyclodextrin optimized by molecular docking and increasing bioavailability with minimizing the doses in human body. ACS Omega. 2020. https://doi.org/10.1021/acsomega.0c04716.
46. Butt SS, Badshah Y, Shabbir M, Rafiq M. Molecular docking using chimera and autodock vina software for nonbioinformaticians. JMIR Bioinf Biotechnol. 2020. https://doi.org/10.2196/14232.
47. Dock prep [Internet]. Dock Prep. UCSF Computer Graphics Laboratory. 2015. https://www.cgl.ucsf.edu/chimera/docs/ContributedSoftware/dockprep/dockprep.html. Accessed 10 Apr 2023.

48. Bell EW, Zhang Y. Dock RMSD: an open-source tool for atom mapping and RMSD calculation of symmetric molecules through graph isomorphism. J Chem Inf. 2019. https://doi.org/10.1186/s13321-019-0362-7.
49. Bhakat S. Conformationalanalysisofchemotheraputicagentcytarabinebyarguslab software. Int J Pharm Sci. 2011; https://www.citethisforme.com/cite/edit/71063b3b-8b06-4280-9f19-716fbe6482d9. Accessed 23 May 2023.
50. El-Nahass MM, Kamel MA, El-Deeb AF, Atta AA, Huthaily SY. Density functional theory (DFT) investigation of molecular structure and frontier molecular orbitals (FMOs) of p-N, N- dimethyl aminobenzylidene malononitrile (DBM). Spectrochim Acta Part A Mol Biomol Spectrosc. 2011. https://doi.org/10.1016/j.saa.2015.05.102.
51. Houk KN, Munchausen LL. onization potentials, electron affinities, and reactivities of cyanoalkenes and related electron-deficient alkenes. A frontier molecular orbital treatment of cyanoalkene reactivities in cycloaddition, electrophilic, nucleophilic, and radical reactions. J Am Chem Soc. 1976. https://doi.org/10.1021/ja00420a012.
52. Tang ML, Reichardt AD, Wei P, Bao Z. Correlating carrier type with frontier molecular orbital energy levels in organicthin film transistors of functionalized acene derivatives. J Am Chem Soc. 2009. https://doi.org/10.1021/ja809659b.
53. Li Y, Evans JN. The Fukui function: a key concept linking frontier molecular orbital theory and the hard-soft-acid-base principle. J Am Chem Soc. 1995. https://doi.org/10.1021/ja00134a021.
54. Ding LP, Zhang FH, Zhu YS, Lu C, Kuang XY, Lv J. Understanding the structural transformation, stability of medium-sized neutral and charged silicon clusters. Sci Rep. 2015. https://doi.org/10.1021/acs.inorgchem.7b00646.
55. Miar M, Shiroudi A, Pourshamsian K, Oliaey AR, Hatamjafari F. Theoretical investigations on the HOMO–LUMO gap and global reactivity descriptor studies, natural bond orbital, and nucleus-independent chemical shifts analyses of 3-phenylbenzo[D]thiazole-2(3h)-imine and its para-substituted derivatives: solvent and substituent effects. J Chem Res. 2020. https://doi.org/10.1177/1747519820932091.
56. Griffith JS, Orgel LE. Ligand-field theory. Quart Rev Chem Soc. 1957. https://doi.org/10.1039/QR9571100381.
57. Zhou Z, Parr RG, Garst J. Absolute hardness as a measure of aromaticity. Tetrahedron Lett. 1988. https://doi.org/10.1016/S0040-4039(00)80623-1.
58. Pearson RG. Chemical hardness and the electronic chemical potential. Inorganica Chim Acta. 1992. https://doi.org/10.1016/S0020-1693(00)92423-X.
59. Pearson RG. The electronic chemical potential and chemical hardness. J Mol Struct. 1992. https://doi.org/10.1016/0166-1280(92)85014-C.
60. Nora M, Fatiha M, Leila N, Sakina H, Djamel K. Density functional study of inclusión complex of albendazole/cucurbit [7] uril: structure, electronic properties, NBO, Giao and TD-DFT analysis. J Mol Liq. 2015. https://doi.org/10.1016/j.molliq.2015.06.054.
61. Gdzquez JL. Hardness and softness in densityfunctionaltheory. In: Sen KD, editor. Structure and bonding, vol. 80. Heidelberg: Springer; 2007. https://doi.org/10.1007/BFb0036798.
62. Chattaraj PK, Giri S. Electrophilicity index within a conceptual DFT framework. Ann Rep Sec. 2009. https://doi.org/10.1039/B802832J.
63. Stepniak A, Belica-Pacha S, Rozalska S, Dlugonski J, Urbaniak P, Palecz B. Study on a host–guest interaction of ß-cyclodextrin with tebuconazole in water. J Mol Liq. 2015. https://doi.org/10.1016/j.molliq.2015.07.023.
64. Fatiha M, Khatmi DE, Largate L. Theoretical approach in the study of the inclusion processes of sulconazole with ß-cyclodextrin. J Mol Liq. 2010. https://doi.org/10.1016/j.molliq.2010.03.004.
65. Zaboub A, Madi F, Merdes R, Mohamedi M, Nouar L. A combined DFT and experimental study of proline/ß-cyclodextrin inclusion complex. J Mol Liq. 2016. https://doi.org/10.1016/j.molliq.2016.01.082.
66. Rafati AA, Hashemianzadeh SM, Nojini ZB, Safarpour MA. Theoretical study of the inclusion complexes of α and ß-cyclodextrins with decyltrimethylammonium bromide (DTAB) and tetradecyltrimethylammonium bromide. J Mol Liq. 2007. https://doi.org/10.1016/j.molliq.2006.11.006.
67. Mohammed JH, Amrin A. Molecular docking, pharmacokinetic, and DFT calculation of naproxen and its degradants. Biomed J Sci Tech Res. 2018. https://doi.org/10.26717/BJSTR.2018.9.001852.
68. Iftode A, Racoviceanu R, Susan R, Marti D, Pinzaru I, Lazau R. Fluconazole-beta-cyclodextrin inclusion complexes. Preparation and characterization in Solid State. Rev Chim. 2001. https://doi.org/10.37358/rc.20.3.8005.
69. Oda A, Okayasu M, Kamiyama Y, Yoshida T, Takahashi O, Matsuzaki H. Evaluation of docking accuracy and investigations of roles of parameters and each term in scoring functions for protein-ligand docking using arguslab software. Bull Chem Soc Japn. 1920. https://doi.org/10.1246/bcsj.80.1920.
70. Pantsar T, Poso A. Binding affinity via docking: fact and fiction. J Sci Tech Res. 1899. https://doi.org/10.3390/molecules23081899.
71. Agarwal S, Mehrotra RJ. An over view of molecular docking. J Sci Med Chem. 2016;4(2):1024–8.
72. Sompornpisut P, Deechalao N, Vongsvivut J. An inclusión complex of ß-cyclodextrin-L-phenylalanine: 1H NMR and molecular docking studies. Sci Asia. 2002. https://doi.org/10.2306/SCIENCEASIA15131874.2002.28.263.
73. Erdős M, Hartkamp R, Vlugt TJ, Moultos OA. Inclusion complexation of organic micropollutants with ß cyclodextrin. J Phys Chem. 2020. https://doi.org/10.1021/acs.jpcb.9b10122.
74. Liu H, Luo J, Yang P, Yang X, Yan J, Yao Q. Stability, antioxidant activity and intestinal permeation of oleuropein inclusion complexes with beta-cyclodextrin and hydroxypropyl-beta-cyclodextrin. Molecules. 2022. https://doi.org/10.3390/molecules27165077.

Utilization of Fly Ash for improving Soil Health and enhancing Groundnut Yield in Acidic *Inceptisols* under subtropical climatic situation

Kumbha Karna Rout[ab*], Prasanna Kumar Samant[a], Meenakshi Prusty[a], Soumyajeet Pradhan[a*],

Saheed Garnaik[a]

[a]Department of Soil Science and Agricultural Chemistry, Odisha University of Agriculture and Technology, Bhubaneswar, Odisha 751003, India

[b]DRIEMS University, Cuttack, Odisha 754022, India

*Corresponding author(s): Kumbha Karna Rout (Former Principal Investigator), email ID – dean.agriculture@driems.ac.in Soumyajeet Pradhan, email ID - soumyabbsr16@gmail.com.

These authors contributed equally to this work.

Abstract

The residual effects of fly ash (FA) applied to Kharif rice played a crucial role in improving soil fertility and crop productivity of Rabi groundnut (*Arachis hypogaea* L.) . This study evaluated the impact of combined use of FA and FYM on soil properties and groundnut yield in acidic loamy sand soils under humid subtropical situation. FA application had minimal effects on soil texture and density but increased porosity and water-holding capacity. Soil penetration resistance decreased significantly, particularly in FA with NPK or lime treatments. Soil pH remained slightly acidic, while organic carbon content increased up to 160.7% with FA application. Macronutrient availability, particularly phosphorus (P) and potassium (K), improved, with FA(40t ha^{-1})+NPK(Recommended dose) +FYM (5t ha^{-1}) showing the highest increases. Secondary nutrients, including sulphur (S), calcium (Ca), and magnesium (Mg), also increased, with sulphur content doubling in the above treatment (FA40+NPK+FYM) treatment.

Among micronutrients, zinc (Zn) showed the most significant increase, while copper (Cu) and manganese (Mn) remained stable. Activities of Soil enzymes such as urease, phosphatases, and dehydrogenase, were significantly enhanced, indicating improved microbial activity. FA application increased groundnut yields, with FA40+NPK+FYM recording the highest kernel yield (872.3 kg ha^{-1}) and biomass yield (7164.6 kg ha^{-1}). Principal component analysis (PCA) highlighted strong associations among FA applied, soil fertility, and crop performance. These findings demonstrate the potential of FA as a soil amendment to improve soil quality and agricultural productivity in nutrient-deficient acidic light textured *Inceptisols i*n subtropical climatic condition.

Keywords

Residual effect; Soil amelioration; Farmyard manure; PCA; Plant available-Si; Soil enzymes

1. Introduction

Fly ash (FA), a major by-product of coal-based thermal power plants, has long been considered an environmental burden due to its vast generation and challenges associated with its safe disposal. This fine particulate residue, primarily composed of amorphous glass-like particles ranging in size from 0.01 to 100 µm, results from the combustion of pulverized coal in power stations (Davison et al., 1974; Gollakota et al., 2019). The composition and properties of FA are influenced by several factors, including the type of coal used, its ash content, combustion method, emission control technologies, and collection processes (Jala and Goyal, 2006; Vig et al., 2023). Notably, FA contains essential macronutrients such as phosphorus (P), potassium (K), sulphur (S), calcium (Ca), and magnesium (Mg), along with micronutrients like zinc (Zn), copper (Cu), iron (Fe), manganese (Mn), cobalt (Co), boron (B), and molybdenum (Mo). The pH of FA varies widely between 4.5 and 12.0, depending on the silica and sulphur content of the parent coal (Maiti et al., 1990; Lal et al., 2012).

India is one of the largest producers of FA, with an estimated annual generation of approximately 889.66 lakh metric tonnes (LMT) (NTPC, 2023). This figure is expected to rise further due to the country's continued reliance on coal-based power generation. Indian coal is predominantly of low-grade quality, consisting mainly of bituminous and sub-bituminous types, which contribute to a higher ash content of 30-45%, compared to the 10-15% typically found in imported coal (Dwivedi and Jain, 2014; Pandey, 2025). The large-scale production of FA, combined with the constraints for its disposal, poses severe environmental challenges, including air pollution, water contamination, and land degradation. However, its potential utilization in agriculture, construction, and waste management has been increasingly explored as a means to convert this problematic waste into a resource.

Agricultural intensification in response to the rising demand for food and forage has led to excessive land use, causing a decline in soil health and productivity. The indiscriminate use of chemical fertilizers has further exacerbated soil degradation, reducing microbial activity and enzyme functions, which are critical indicators of soil quality (Cardoso et al., 2013; Mandal et al., 2020). As a result, sustainable approaches to enhancing soil fertility and crop productivity have become a research priority. In recent years, FA has emerged as a potential soil amendment that, when applied in conjunction with organic and biofertilizer sources, can improve soil health and sustainability (Parab et al., 2015; Kumar et al., 2017; Kaur et al., 2019). Despite its benefits, FA usage in Indian agriculture remains minimal, accounting for less than 1% of total FA utilization (Down To Earth, 2019). However, studies suggest that the use of FA in agriculture has the potential to generate an additional five million tonnes of food grains annually, with an estimated economic value of ₹3000 crores (Kumar et al., 2000).

The potential of FA as an agricultural input is primarily due to its role in soil amelioration. FA application improves soil texture by reducing bulk density and enhancing porosity, water retention, and aeration, thereby creating a more favourable environment for root growth and

microbial activity (Ram and Masto, 2014). Furthermore, the nutrient content of FA supplements the soil with essential elements, reducing the dependency on chemical fertilizers. When combined with organic amendments such as farmyard manure (FYM), compost, crop residues, and sewage sludge, FA enhances nutrient availability while mitigating concerns related to heavy metal accumulation (Yeledhalli et al., 2007; Singh and Pandey, 2013; Kumar et al., 2017).

While the application of FA in agriculture offers numerous benefits, concerns regarding its potential toxicity, heavy metal accumulation, and long-term effects on soil fertility persist. Certain FA varieties contain trace amounts of toxic elements such as arsenic (As), cadmium (Cd), lead (Pb), and mercury (Hg), which can pose risks to plant growth and food safety if applied in excessive quantities (Pandey and Singh, 2010). However, several studies have demonstrated that applying FA in lower doses, especially when mixed with organic amendments, significantly reduces the bioavailability of heavy metals, preventing their accumulation in crops (Singh and Pandey, 2013; Kumar et al., 2017).

Furthermore, FA application enhances microbial activity in soil by providing essential nutrients and improving soil aeration. The addition of organic matter such as FYM, press mud, and biogas slurry further stabilizes soil pH and reduces the risk of heavy metal uptake by plants. Long-term studies have emphasized the importance of field trials to assess the cumulative impact of FA applications and develop guidelines for its safe and effective use in different agro-climatic conditions (Nayak et al., 2014).

Groundnut (*Arachis hypogaea* L.) is an important legume oilseed crop widely grown in India, covering an area of approximately 4.9 million hectares with an annual production of 10.14 million tonnes (DES, 2020). The rice–groundnut cropping system is particularly predominant in the coastal regions of Odisha, where rice serves as a staple food crop, cultivated extensively

due to its adaptability and economic importance. Following the rice harvest, groundnut is commonly grown as a residual crop. Poor soil fertility is a major soil related constraint of these soils which are mostly acidic with poor nutrient availability to support crop growth and biological N fixation. Under such situation , use of FA in the rice-groundnut cropping system presents a unique opportunity to evaluate the benefits of FA application in enhancing soil fertility and crop yields. FA application to rice fields has been shown to improve soil structure, water-holding capacity, and nutrient availability, which can, in turn, positively influence the subsequent groundnut crop. Moreover, the integration of FA with FYM can further enhance the nutrient balance in the soil, improving crop resilience and productivity over multiple growing seasons.

Despite extensive research on FA utilization in agriculture, most studies have primarily focused on its direct effect on soil properties and crop growth. There is a lack of comprehensive studies examining the residual impact of FA on subsequent crops within a cropping system.

Given the increasing need for sustainable soil management practices, it is crucial to conduct field trials that evaluate the cumulative impact of FA application over multiple cropping cycles. Understanding the residual effects of FA on soil fertility, nutrient dynamics, and heavy metal accumulation is essential for developing appropriate management practices. Addressing these research gaps will provide valuable insights into optimizing FA application rates, improving soil amendment strategies, and ensuring environmental safety.

To address these challenges and research gaps, a three-year field study was undertaken to investigate the application of FA in combination with FYM within a rice-groundnut cropping system in eastern India. The primary objectives of this study were: i) to assess the residual effects of FA applied to Kharif rice on subsequent Groundnut crop and determine its impact

on soil health; iv) to establish guidelines for safe and sustainable FA utilization in rice-ground nut cropping system.

By addressing these objectives, this research aims to contribute to the sustainable management of FA in agriculture, promoting its effective utilization while ensuring environmental safety and soil health improvement. The findings of this study will provide valuable insights into the practical applications of FA, helping policymakers, researchers, and farmers make informed decisions regarding its use in sustainable crop production.

2. Materials and methods

2.1 Experimental setup

A field experiment was conducted during the Kharif season of 2021 with rice (Oryza sativa cv. Kalinga Dhan 1204), followed by groundnut (*Arachis hypogaea* cv. Devi) during the Rabi season of 2021–22 at the Instructional Farm (IF) of Odisha University of Agriculture and Technology (OUAT), Bhubaneswar, India (20.2961° N, 85.8245° E, 45 m above mean sea level). The soil at the experimental site was acidic (pH, 5.13) and had a loamy sand texture. Fly ash was sourced from the National Thermal Power Corporation (NTPC), Talcher, Odisha. The collected fly ash, farmyard manure (FYM), and initial soil samples were analysed for pH (1:2.5), electrical conductivity (EC), soil organic carbon (SOC), sand, silt, and clay content, along with other physico-chemical parameters (Tables 1, 2, and 3) using standard methods described by Jackson (1973). The experimental site experiences a subtropical humid climate with an average annual rainfall of 1,450 mm, primarily influenced by the southwest monsoon.

2.2 Treatment detail

The experiment consisted of seven treatments with 4replications arranged in randomized block design (RBD), each plot measuring 12 m × 5 m (EW × NS). The treatments are: T1 (absolute control), T2 (recommended NPK applied to every crop), T3 (FYM at 5 t ha^{-1} applied every

Kharif season + T2), T4 (FA 10 t ha^{-1} + T3), T5 (FA 20 t ha^{-1} + T3), T6 (FA 40 t ha^{-1} + T3), and T7 (Lime 0.2 LR for non-rice crops + T3). Synthetic fertilizers such as urea, DAP, and MOP were used to supply the recommended NPK, with a fertilizer dose of 80:40:40 and 20:40:40 kg ha^{-1} N: P_2O_5: K_2O applied to rice and groundnut respectively. The entire dose of FYM (5 t ha^{-1} $season^{-1}$) and fly ash (as per treatments) was incorporated during puddling in the Kharif season (monsoon). The lime requirement (0.2 LR for non-rice crops) was calculated based on soil analysis by Woodruff's buffer method and applied in T7 during land preparation for the Rabi ground nut crop.

2.3 Soil sampling and analysis

The post-harvest soil samples were collected after the groundnut crop was harvested, following a zig-zag sampling pattern within the experimental plots to create composite samples (500 g) for each treatment. Each composite sample was air-dried, ground, and sieved through a 2 mm (10-mesh) sieve for physico-chemical analysis. The remaining portion of each sample was stored in a plastic bag at 4°C in a deep freezer until microbiological and enzymatic analyses were conducted. All microbial and enzymatic assessments were completed within 15 days of sample collection.

Soil texture was analysed using the hydrometer method (Bouyoucos, 1962). Bulk density (BD) by the core sampler method (Blake and Hartge, 1986)and particle density (PD) by pycnometer method(Flint and Flint, 2002). Water holding capacity (WHC) was assessed using a Keen-Raczkowski box, and soil penetration resistance (0–5 cm depth) was measured by a cone penetrometer (Piper, 1950). Soil pH and electrical conductivity (EC) were determined by potentiometric and conductivity methods, respectively (Jackson, 1973). Organic carbon (OC) was estimated by rapid titration method (Walkley and Black, 1934). Available nitrogen (N) was measured using the alkaline potassium permanganate method (Subbiah and Asija, 1949),

while available phosphorus (P) was extracted with 0.5 M $NaHCO_3$ and quantified by spectrophotometry (Olsen, 1954). Available potassium (K), exchangeable calcium (Ca), and magnesium (Mg) were extracted using 1 N ammonium acetate, with K analysed via flame photometry (Jackson, 1973), and Ca and Mg measured using complexometric titration (Baruah and Barthakur, 1997). Plant-available silicon (Si) was extracted with 0.01 M $CaCl_2$ and estimated using a UV-VIS spectrophotometer (Haysom and Chapman, 1975). DTPA-extractable micronutrients (Zn, Fe, Cu, and Mn) were analysed using atomic absorption spectrophotometry (AAS) (Lindsay and Norvell, 1978).

Enzyme activities such as Urease, Acid (pH 6.5) and alkaline (pH 11) phosphatase ,β-glucosidase and arylsulfatase activity were quantified using standard methods (Tabatabai, 1994). Total microbial activity in the soil was determined by dehydrogenase activity assessment (Casida et al., 1964).

2.4 Statistical analysis

The experimental data were analysed using the analysis of variance (ANOVA) technique for a randomized block design (RBD). Fisher's LSD test was employed as a post hoc mean separation method to compare treatment means at a significance level of $p < 0.05$. Additionally, principal component analysis (PCA) was performed to explore patterns and relationships within the data. All analyses were conducted using R version 4.4.1 (de Mendiburu, 2021).

3. Results

3.1 Physical properties

The soil across all treatments exhibited a sandy texture, with sand, silt, and clay contents ranging from 81.3-84.7%, 8.2–10.7%, and 5.6–10.4%, respectively (Table 4). The bulk density (BD) was lowest in the FA40+T3 treatment at 1.38 Mg m^{-3}, representing a 7.38% reduction compared to the control (1.49 Mg m^{-3}) (Table 4). Soil particle density (PD) ranged from 2.49

to 2.53 Mg m^{-3}. Porosity was highest in the FA40+T3 treatment (44.74%) and lowest in the control (39.97%). The application of varying fly ash (FA) levels did not significantly affect bulk density, particle density, or porosity. The soil's water holding capacity (WHC) varied between 28.83% and 33.38% (Table 4). Surface soil penetration resistance (SPR) at a depth of 0–5 cm was lowest in the FA40+NPK treatment (6.3 kPa) and highest in the absolute control (184.0 kPa). The FA20+NPK and Lime+NPK treatments significantly reduced SPR by 84.1% and 83.9%, respectively, compared to the control (Table 4).

3.2 Chemical properties

The soil pH ranged from 5.36 to 5.98, indicating a slightly acidic nature across all treatments, with no significant differences observed due to varying levels of FA application (Table 5). Similarly, the soil's electrical conductivity (EC) varied between 0.19 dS m^{-1} and 0.25 dS m^{-1}, with FA application having no significant impact on EC values (Table 5). In contrast, organic carbon content increased significantly in the FA20+T3 (0.60 g kg^{-1}) and FA40+T3 (0.73 g kg^{-1}) treatments, representing enhancements of 114.3% and 160.7%, respectively, compared to the control (0.28 g kg^{-1}) (Table 5).

3.3 Primary nutrients

The available nitrogen content in the soil increased; however, this rise cannot be solely attributed to the higher fly ash dosage, as shown in Fig. 2. The Lime+T3 treatment recorded a 28.1% increase in available nitrogen content compared to the control (Table 5). Similarly, available phosphorus in the soil increased in the FA10+T3, FA20+T3, and FA40+T3 treatments by 26.1%, 38.2%, and 40.6%, respectively, relative to the control (9.86 kg P ha^{-1}), while the Lime+T3 treatment resulted in a phosphorus level of 13.39 kg P ha^{-1}, reflecting a 35.8% increase (Table 5). The available potassium content in the soil ranged from 63.41 kg K ha^{-1} to 80.92 kg K ha^{-1}, with the FA10+T3, FA20+T3, and FA40+T3 treatments showing increases of

approximately 35.0%, 36.5%, and 49.2%, respectively, compared to the control (63.41 kg K ha^{-1}) (Table 5).

3.4 Secondary nutrients

The sulphur content in the soil ranged from 12.55 to 25.19 kg S ha^{-1}, with the highest level (25.19 kg S ha^{-1}) observed in the FA40+T3 treatment (Table 5). A significant increase in available sulphur was associated with higher fly ash application rates, as the FA10+T3, FA20+T3, and FA40+T3 treatments led to sulphur content increases of approximately 62.1%, 83.1%, and 100.7%, respectively, compared to the control (12.55 kg S ha^{-1}) (Table 5). In contrast, the calcium (Ca) content in the soil peaked at 23.33 meq 100 g^{-1} in the Lime+T3 treatment, followed by 22.22 meq 100 g^{-1} in FA20+T3. Notably, the NPK+FYM and FA40+T3 treatments exhibited similar calcium levels, each reflecting a 19.9% increase relative to the control (16.67 meq 100 g^{-1}) (Table 5). A similar trend was observed for magnesium (Mg) content, with the highest concentration recorded in the Lime+T3 treatment (28.0 meq 100 g^{-1}), which was statistically comparable to FA40+T3 (26.67 meq 100 g^{-1}). Other treatments, including NPK+FYM, FA10+T3, and FA20+T3, showed increases of 39.9%, 39.9%, and 43.9%, respectively, compared to the control (16.67 meq 100 g^{-1}) (Table 5).

3.5 Plant available Si

The plant-available silicon (PASi) content was highest in the FA40+T3 treatment (46.98 mg kg^{-1}), followed by FA20+T3 (45.28 mg kg^{-1}) and FA10+T3 (42.05 mg kg^{-1}) (Table 5). The NPK+FYM and Lime+T3 treatments showed increases of 38.7% and 60.0%, respectively, compared to the control (25.58 mg kg^{-1}). These findings indicate that higher doses of fly ash application significantly enhanced silicon availability in the soil, with the FA40+T3 treatment exhibiting the greatest PASi levels (Table 5). This underscores the role of these amendments in improving silicon bioavailability, which is beneficial for plant health and resilience (Table 5).

3.6 Micronutrients

The DTPA-extractable zinc (Zn) content in the soil was highest in the FA40+T3 treatment, measuring 1.36 mg kg^{-1} (Table 5). Treatments NPK, FA10+T3, and FA20+T3 exhibited increases of 30.3%, 32.3%, and 33.3%, respectively, compared to the control (0.99 mg kg^{-1}), while the Lime+T3 treatment recorded a Zn concentration of 1.16 mg kg^{-1}, reflecting a 17.1% increase over the control (Table 5). The DTPA-extractable copper (Cu) content ranged from 8.56 to 11.04 mg kg^{-1}, with varying doses of fly ash having no significant influence on Cu levels in the soil. The highest Cu concentration was observed in the NPK treatment (11.04 mg kg^{-1}), followed by NPK+FYM, Lime+T3, FA40+T3, and FA20+T3, with respective values of 10.21, 10.01, 9.95, and 9.65 mg kg^{-1} (Table 5). The DTPA-extractable iron (Fe) content was highest in the Lime+T3 treatment (181.04 mg kg^{-1}), followed by FA40+T3 (161.02 mg kg^{-1}) and NPK+FYM (158.85 mg kg^{-1}) (Table 5). The FA10+T3 and FA20+T3 treatments showed increases of 115.0% and 131.2%, respectively, compared to the control (66.65 mg kg^{-1}). In contrast, different fly ash application rates did not significantly affect the DTPA-extractable manganese (Mn) content in the soil. The highest Mn content was recorded in the NPK treatment (5.45 mg kg^{-1}), while the lowest was observed in the Lime+T3 treatment (4.36 mg kg^{-1}) (Table 5).

3.7 Soil enzyme activities

Soil enzymes serve as key indicators of the biological properties of soil. In this study, the highest urease (UR) activity was recorded in the FA40+T3 and FA20+T3 treatments, with values of 77.1 and 69.3 µg NH_4^+ 5 g $soil^{-1}$ 5 hr^{-1}, respectively (Table 6). The NPK+FYM, Lime+T3, and FA10+T3 treatments exhibited urease activity increases of 15.1%, 26.4%, and 35.6%, respectively, compared to the control (44.2 µg NH_4^+ 5 g $soil^{-1}$ 5 hr^{-1}) (Table 6). Acid phosphatase (ACP) activity reached its highest level in the FA40+T3 treatment (293.4 µg pNP

g soil^{-1} hr^{-1}), followed by FA20+T3 (256.3 µg pNP g soil^{-1} hr^{-1}). The Lime+T3 and FA10+T3 treatments exhibited increases of 13.5% and 23.5%, respectively, compared to the control (185.8 µg pNP g soil^{-1} hr^{-1}) (Table 6). A similar trend was observed for alkaline phosphatase (ALP) activity, with maximum values of 57.1 and 52.8 µg pNP g soil^{-1} hr^{-1} in the FA40+T3 and FA20+T3 treatments, respectively. The FA10+T3 treatment recorded a significant 215% increase over the control (12.2 µg pNP g soil^{-1} hr^{-1}), reaching 38.5 µg pNP g soil^{-1} hr^{-1} (Table 6).

For arylsulfatase (ARS) activity, the FA40+T3, FA20+T3, Lime+T3, and FA10+T3 treatments showed respective increases of 173.8%, 167.0%, 162.0%, and 160.9% over the control (27.9 µg pNP g soil^{-1} hr^{-1}), while the NPK and NPK+FYM treatments exhibited arylsulfatase activities of 42.0 and 50.6 µg pNP g soil^{-1} hr^{-1}, respectively (Table 6). The highest dehydrogenase (DHA) activity was recorded in the FA40+T3 treatment (16.4 µg TPF g soil^{-1} day^{-1}), followed by FA20+T3 (13.7 µg TPF g soil^{-1} day^{-1}) and FA10+T3 (6.9 µg TPF g soil^{-1} day^{-1}) (Table 6). Similarly, β-glucosidase (BGU) activity was highest in the FA40+T3 treatment (27.3 µg pNP g soil^{-1} hr^{-1}), followed by FA20+T3 (19.5 µg pNP g soil^{-1} hr^{-1}). The Lime+NPK and FA10+T3 treatments exhibited β-glucosidase activities that were 97.6% and 109.4% higher, respectively, than the control (8.5 µg pNP g soil^{-1} hr^{-1}) (Table 6).

3.8 Yield and yield attributes

The highest kernel yield (KY) was recorded in the FA40+T3 treatment, reaching 872.3 kg ha^{-1}, followed by Lime+T3 (814.0 kg ha^{-1}), FA20+T3 (769.3 kg ha^{-1}), and FA10+T3 (729.1 kg ha^{-1}) (Table 7). The NPK and NPK+FYM treatments produced 42.2% and 45.6% higher yields, respectively, compared to the control (424.1 kg ha^{-1}) (Table 7). Similarly, pod yield (PY) was highest in FA40+T3, Lime+T3, FA20+T3, and FA10+T3, with values of 1226.5 kg ha^{-1}, 1185.7 kg ha^{-1}, 1113.4 kg ha^{-1}, and 1080.2 kg ha^{-1}, respectively (Table 7). Haulm yield was

significantly higher in FA40+T3 and FA20+T3, showing increases of 56.3% and 38.1%, respectively, over the control (3797.8 kg ha^{-1}) (Table 7). Biomass yield (BY) peaked in FA40+T3 (7164.6 kg ha^{-1}) and FA20+T3 (6361.2 kg ha^{-1}), while treatments NPK, NPK+FYM, Lime+T3, and FA10+T3 recorded biomass yield increases of 9.8%, 16.3%, 16.5%, and 22.6%, respectively, compared to the control (4439.5 kg ha^{-1}) (Table 7). Shelling percentage (SH) followed a similar trend, with the highest value observed in FA40+T3 (70.9%) and the lowest in the control (66.1%) (Table 7).

3.9 Relationship among soil variables and yield

To simplify the understanding of the effects of various FA treatments on soil properties and the yield attributes of groundnut, correlation matrix and the principal component analysis (PCA) were employed, as illustrated in Fig. 1 and Fig. 2, respectively. The correlation matrix visually represents the relationships between soil properties, nutrient availability, enzyme activities, and yield attributes under FA treatments (Fig. 1). Green circles indicated positive correlations, while brown/orange denoted negative correlations, with intensity and size reflecting correlation strength. Sand content negatively correlated with silt, clay, bulk density (BD), particle density (PD), and water holding capacity (WHC), indicating its inverse effect on soil structure. BD and soil penetration resistance (SPR) show negative correlations with soil fertility parameters and yield, highlighting the detrimental effects of compaction (Fig. 1). In contrast, pH, organic carbon (OC), available phosphorus (AvP), calcium (Ca), magnesium (Mg), and micronutrients exhibited strong positive correlations with soil enzyme activities (DHA, ALP, ARS) and yield attributes (KY, PY, HY). This suggested that improved nutrient availability and microbial activity enhance groundnut productivity (Fig. 1). Overall, the findings emphasized the importance of FA amendments in improving soil fertility, reducing compaction, and enhancing yield through better nutrient and microbial interactions. The PCA biplot illustrated the relationships between soil properties, groundnut yield attributes, and various FA treatments

(Fig. 2). The x-axis (PC1) accounted for 68.02% of the variance, primarily associated with soil fertility and yield attributes, while the y-axis (PC2) explains 11.76%, capturing additional variations. Soil parameters like kernel yield (KY), pod yield (PY), soil pH, available phosphorus (AvP), calcium (Ca), magnesium (Mg), iron (Fe), and arylsulfatase activity (ARS) cluster in the positive PC1 quadrant, indicating their strong association with fertility-enhancing FA treatments (Fig. 2). Conversely, sand content, soil penetration resistance (SPR), bulk density (BD), and particle density (PD) are negatively loaded on PC1, suggesting an inverse relationship with soil fertility and productivity. The positioning of treatments reveals that absolute control and NPK alone aligned with lower fertility indicators, while FA treatments combined with NPK and farmyard manure (FYM), such as FA40+NPK+FYM and FA20+NPK+FYM, are linked to improved soil properties and higher yields (Fig. 2). The Lime+NPK+FYM treatment appeared separately in the lower right quadrant, suggesting a distinct effect on soil characteristics. Overall, the PCA biplot highlights that FA treatments significantly enhanced soil fertility and crop productivity compared to untreated or solely NPK-treated soils, reinforcing the importance of integrated soil management strategies for sustainable groundnut cultivation (Fig. 2).

4. Discussion

4.1 Physical, chemical, and biological properties

The disposal of fly ash (FA) presented a significant environmental challenge due to its increasing accumulation as solid waste worldwide. As a sustainable alternative, eco-friendly management strategies that incorporated FA in agriculture could help improve soil fertility while addressing both environmental and agricultural concerns. In this study, FA was applied in combination with farmyard manure (FYM) to assess its impact on soil properties, as research on this subject remains limited (Upadhyay et al., 2021).

The application of FA increased silt content in the FA20+T3 and Lime+T3 treatments; however, a higher FA application rate led to a reduction in silt content, as observed in the FA40+T3 treatment. The addition of FYM alongside FA positively influenced clay content, with the highest clay levels recorded in the NPK+FYM treatment. In contrast, FA application alone resulted in a decline in clay content (refer to Table 4). Bulk density (BD) decreased with increasing FA application, while particle density (PD) remained relatively stable across treatments. Pore space (PS) percentage increased with higher FA doses, but BD, PD, and PS showed no statistically significant differences among treatments. A similar trend was observed for soil water holding capacity (WHC). Additionally, soil penetration resistance (SPR) decreased with increasing FA doses. These findings are consistent with previous studies on the effects of FA application on soil physical properties (Ahmad et al., 2021).

The application of varying doses of fly ash (FA) did not lead to significant changes in soil pH, likely due to the inherently acidic nature of both the parent soil and the FA. This contrasts with findings from previous studies, such as those by Tejasvi and Kumar (2012) and Gond et al. (2013), which reported an increase in soil pH following FA application. However, electrical conductivity (EC) increased relative to the control, though no significant variations were observed across different FA doses. Organic carbon (OC) content exhibited a dose-dependent increase with FA application, mirroring the trend observed for primary nutrients: nitrogen (N), phosphorus (P), and potassium (K) which also increased with higher FA doses. Hong et al. (2018) found that phosphorus availability can be enhanced due to reduced P fixation in soils amended with biochar, FA, and lime. Similarly, Rautaray et al. (2003) demonstrated that FA application, whether used alone or in combination with organic wastes and chemical fertilizers, improved soil-available P levels. Their study, which investigated the direct impact of FA, organic wastes, and chemical fertilizers on rice and the residual effects on mustard (Brassica napus var. glauca), highlighted that the integrated use of FA with organic and chemical

amendments effectively enhanced crop yield, soil OC, and available N, P, and K content. Additionally, secondary nutrients such as sulphur (S), calcium (Ca), and magnesium (Mg) increased with higher FA doses, supporting the findings of Pandey and Singh (2010), who identified FA as a source of essential macro- and micronutrients for plants. The plant-available silicon (PASi) content also increased in FA-amended treatments, aligning with the results of Lee et al. (2006). Among micronutrients, DTPA-extractable zinc (Zn) showed the most pronounced increase with rising FA doses, whereas iron (Fe), copper (Cu), and manganese (Mn) did not exhibit a similar trend, consistent with findings reported by Kumar (2018).

The activities of several soil enzymes, including urease, acid phosphatase, and alkaline phosphatase, exhibited a positive correlation with increasing FA doses, suggesting that FA application may enhance these enzymatic processes. Urease plays a vital role in nitrogen cycling by hydrolysing urea into ammonium, thereby improving nitrogen availability in the soil (Neemisha and Sharma, 2022). Similarly, acid and alkaline phosphatases are crucial for phosphorus cycling, breaking down organic phosphorus compounds into plant-accessible forms (Tian et al., 2021). The observed increase in phosphatase activities with FA application indicates improved phosphorus mineralization in the soil. Although arylsulfatase activity also showed a dose-dependent increase with FA application, the change was not statistically significant. Arylsulfatase, an enzyme involved in sulphur cycling, catalyses the hydrolysis of sulphate esters into bioavailable sulphate, supporting plant sulphur needs (Germida et al., 2021). The lack of a significant increase in arylsulfatase activity may be attributed to relatively stable sulphur content in the soil or other soil properties that influence enzyme dynamics. Similarly, dehydrogenase and β-glucosidase activities increased with higher FA doses. Dehydrogenase serves as a key indicator of microbial oxidative activity and overall soil health, reflecting microbial respiration and organic matter decomposition (Wolińska & Stępniewska, 2012). Meanwhile, β-glucosidase is essential for carbon cycling, facilitating the breakdown of

cellulose into simpler sugars that plants can utilize (Adetunji et al., 2017). These findings align with prior studies by Nayak et al. (2014), Lal et al. (2015), and Ramteke et al. (2017), which also reported enhanced enzyme activities in FA-amended soils. This suggests that FA application supports biochemical processes essential for nutrient cycling and soil fertility, ultimately contributing to improved soil health.

4.2 Yield and yield attributes

Kernel yield and overall groundnut productivity increased consistently with higher doses of fly ash (FA), highlighting the positive impact of FA application on crop performance. Enhanced calcium (Ca) uptake in lime-treated plots significantly improved yield, underscoring the critical role of Ca in pod and kernel development (Yang et al., 2020). A similar trend was observed in haulm yield, total biomass, and shelling percentage, all of which progressively increased with higher FA doses. These findings align with studies by Swain et al. (2007), Sireesha and Rani (2014), and Le et al. (2021), which also reported substantial improvements in groundnut yield and yield components following FA application.

4.3 Relationship among soil properties and groundnut yield

The correlation matrix and PCA provided valuable insights into the impact of FA treatments on soil properties and groundnut yield attributes. The correlation matrix (Fig. 1) showed that soil fertility indicators such as pH, organic carbon (OC), available phosphorus (AvP), calcium (Ca), magnesium (Mg), and micronutrients exhibited strong positive correlations with enzyme activities (DHA, ALP, ARS) and yield attributes (KY, PY, HY). This suggested that FA amendments enhanced nutrient availability and microbial activity, leading to improved crop productivity. In contrast, bulk density (BD), particle density (PD), and soil penetration resistance (SPR) showed negative correlations with fertility parameters and yield, indicating that soil compaction negatively affects plant growth.

The PCA biplot (Fig. 2) further illustrates the relationships among soil properties, yield attributes, and FA treatments. PC1 (68.02%) explained the majority of variance, primarily linked to soil fertility and productivity, while PC2 (11.76%) captured additional variability. Positive loadings of KY, PY, AvP, Ca, Mg, Fe, and ARS in PC1 confirmed the role of FA in enhancing soil health and yield. Conversely, sand content, BD, PD, and SPR are negatively loaded, reinforcing their adverse impacted on soil fertility. Treatments such as FA40+NPK+FYM and FA20+NPK+FYM aligned with improved soil properties and higher yields, whereas absolute control and NPK alone were associated with lower fertility.

Overall, these findings highlighted the importance of FA amendments in reducing compaction, improving nutrient availability, and boosting groundnut productivity, reinforcing the need for integrated soil management strategies for sustainable agriculture.

5. Conclusion

This study demonstrated that fly ash (FA) served as an effective soil amendment, enhancing nutrient availability and improving soil properties, which collectively supported increased groundnut productivity by positively influencing both vegetative and reproductive growth phases. When applied in combination with recommended fertilizers and farmyard manure (FYM), FA significantly improved the physical, chemical, and biological properties of the soil, leading to better crop performance and higher yields.

Given the variability in soil types, climatic conditions, and cropping systems across different regions, further research is needed to assess the long-term effects of FA application. Future studies should focus on evaluating its sustainability, potential risks of heavy metal accumulation, and optimal application rates for different crops and soil conditions. Additionally, multi-location field trials would be essential to establish broader recommendations for safe and effective FA utilization in agriculture. By integrating FA into

sustainable soil management practices, it would be possible to transform this industrial by-product into a valuable resource for enhancing crop productivity while addressing environmental concerns related to its disposal.

Acknowledgement

The first author sincerely acknowledges the Soil Science and Agricultural Chemistry Department of Odisha University of Agriculture and Technology (OUAT) for their invaluable support in soil sampling, laboratory analysis, and technical guidance. The financial assistance provided by the NTPC; New Delhi is gratefully acknowledged. Special thanks are extended to Dr. Jayanta Kumar Saha (Lead Principal Investigator) and the colleagues involved in the fly ash project from the Indian Institute of Soil Science, Bhopal (M.P.); Indian Agricultural Research Institute, New Delhi; Indian Grassland and Fodder Research Institute, Jhansi (U.P.); and Bidhan Chandra Krishi Viswavidyalaya, Mohanpur (W.B.) for their support, cooperation, and coordination.

References

Adetunji, A. T., Lewu, F. B., Mulidzi, R., & Ncube, B. (2017). The biological activities of β-glucosidase, phosphatase and urease as soil quality indicators: a review. *Journal of soil science and plant nutrition*, *17*(3), 794-807.

Ahmad, G., Khan, A. A., & Mohamed, H. I. (2021). Impact of the low and high concentrations of fly ash amended soil on growth, physiological response, and yield of pumpkin (Cucurbita moschata Duch. Ex Poiret L.). *Environmental Science and Pollution Research*, *28*(14), 17068-17083.

Cardoso, E. J. B. N., Vasconcellos, R. L. F., Bini, D., Miyauchi, M. Y. H., Santos, C. A. D., Alves, P. R. L., ... & Nogueira, M. A. (2013). Soil health: looking for suitable

indicators. What should be considered to assess the effects of use and management on soil health?. *Scientia Agricola*, *70*, 274-289.

Davison, R. L., Natusch, D. F., Wallace, J. R., & Evans Jr, C. A. (1974). Trace elements in fly ash. Dependence of concentration on particle size. *Environmental Science & Technology*, *8*(13), 1107-1113.

DES. (2020). Pocket Book of Agricultural Statistics 2020, Directorate of Economics and Statistics, Department of Agriculture, Cooperation and Farmers Welfare, Ministry of Agriculture and Farmers Welfare, Govt. of India, New Delhi, India.

Down To Earth. (2019, July 12). *As told to Parliament (July 12, 2019): India doubled usage of fly ash in nine years*. https://www.downtoearth.org.in/mining/as-told-to-parliament-july-12-2019-india-doubled-usage-of-fly-ash-in-nine-years-65614

Dwivedi, A., & Jain, M. K. (2014). Fly ash–waste management and overview: A Review. *Recent Research in Science and Technology*, *6*(1).

Gaind, S., & Gaur, A. C. (2002). Impact of fly ash and phosphate solubilising bacteria on soybean productivity. *Bioresource technology*, *85*(3), 313-315.

Germida, J. J., Wainwright, M., & Gupta, V. V. (2021). Biochemistry of sulfur cycling in soil. In *Soil biochemistry* (pp. 1-53). CRC Press.

Gollakota, A.R., Volli, V. and Shu, C.M., 2019. Progressive utilisation prospects of coal fly ash: A review. *Science of the Total Environment*, *672*, pp.951-989.

Gond, D. P., Singh, S., Pal, A., & Tewary, B. K. (2013). Growth, yield and metal residues in Solanum melongena grown in fly ash amended soils. *Journal of Environmental Biology*, *34*(3), 539.

Hong, C., Su, Y. & Lu, S. Phosphorus availability changes in acidic soils amended with biochar, fly ash, and lime determined by diffusive gradients in thin films (DGT) technique. *Environ Sci Pollut Res* **25**, 30547–30556 (2018). https://doi.org/10.1007/s11356-018-3086-8

Jala, S., & Goyal, D. (2006). Fly ash as a soil ameliorant for improving crop production—a review. *Bioresource technology*, *97*(9), 1136-1147.

Kaur, K., Singh, K., & Gandhi, N. (2019). Effect of fly ash, farm yard manure and soil amendments to maize crop on morphological and yield contributing characters of Kharif maize (Zea mays L.). *Journal of Pharmacognosy and Phytochemistry*, *8*(1S), 227-230.

Kumar, A., Usmani, Z., & Kumar, V. (2017). Biochar and flyash inoculated with plant growth promoting rhizobacteria act as potential biofertilizer for luxuriant growth and yield of tomato plant. *Journal of environmental management*, *190*, 20-27.

Kumar, T. (2018). *STUDY OF FLY ASH INCORPORATION ON YIELD AND PARTITIONING OF HEAVY METALS IN RICE* (Doctoral dissertation, Indira Gandhi Krishi Vishwavidhyalaya, Raipur: Potato and Temperate Fruit Research Station Manpat Surguja).

Kumar, V., Mathur, M., & Sharma, P. (2000). Fly ash: A billion dollar resource–Wasted so far. *Mission beyond*.

Lai, K. M., Ye, D. Y., & Wong, J. W. C. (1999). Enzyme activities in a sandy soil amended with sewage sludge and coal fly ash. *Water, Air, and Soil Pollution*, *113*, 261-272.

Lal, B. , Samadhiya, V. K., Dewangan, T., & Sharma, P. (2015). Impact of combined application of fly ash and FYM on soil microbial properties of Inceptisol. *The Ecoscan*, *9*(3&4), 761-764.

Lal, J. K., Mishra, B., & Sarkar, A. K. (1996). Effect of flyash on soil microbial and enzymatic activity. *Journal of the Indian Society of Soil Science*, *44*(1), 77-80.

Lal, K., Chhabra, R., Mongia, A. D., Meena, R. L., & Yadav, R. K. (2012). Release and uptake of potassium and sodium with fly ash application in rice on reclaimed alkali soil. *Journal of the Indian Society of Soil Science*, *60*(3), 181-186.

Le, T. V., Ngo, C. N., & Futamata, H. (2021). Effect of fly ash amendment on sandy soil properties and peanut yields. *ScienceAsia*, *47*(3).

Lee, H., Ha, H. S., Lee, C. H., Lee, Y. B., & Kim, P. J. (2006). Fly ash effect on improving soil properties and rice productivity in Korean paddy soils. *Bioresource technology*, *97*(13), 1490-1497.

Lee, H., Ha, H. S., Lee, C. H., Lee, Y. B., & Kim, P. J. (2006). Fly ash effect on improving soil properties and rice productivity in Korean paddy soils. *Bioresource technology*, *97*(13), 1490-1497.

Maiti, S. S., Mukhopadhyay, M., Gupta, S. K., & Banerjee, S. K. (1990). Evaluation of fly ash as a useful material in agriculture.

Mandal, A., Sarkar, B., Mandal, S., Vithanage, M., Patra, A. K., & Manna, M. C. (2020). Impact of agrochemicals on soil health. In *Agrochemicals detection, treatment and remediation* (pp. 161-187). Butterworth-Heinemann.

Mendiburu, F.D., 2019. Agricolae: statistical procedures for agricultural research. (No Title).

Nayak, A. K., Kumar, A., Raja, R., Rao, K. S., Mohanty, S., Shahid, M., ... & Bhattacharyya, P. (2014). Fly ash addition affects microbial biomass and carbon mineralization in agricultural soils. *Bulletin of environmental contamination and toxicology*, *92*, 160-164.

Neemisha, & Sharma, S. (2022). Soil enzymes and their role in nutrient cycling. In *Structure and functions of Pedosphere* (pp. 173-188). Singapore: Springer Nature Singapore.

Nguyen, V. L., Chu, H. D., & Nguyen, D. H. (2024). Effects of fly ash application on the growth and disease resistance of peanut plants (Arachis hypogaea) cultivated in different soil types. *Vegetos*, 1-8.

NTPC (2023). Ash Utilization. https://ntpc.co.in/about-us/corporate-functions/ash-utilisation

Pandey, T., 2025. *Coal Ecology and Environmental Impacts*. Educohack Press.

Pandey, V. C., & Singh, N. (2010). Impact of fly ash incorporation in soil systems. *Agriculture, ecosystems & environment*, *136*(1-2), 16-27.

Pandey, V. C., & Singh, N. (2010). Impact of fly ash incorporation in soil systems. *Agriculture, ecosystems & environment*, *136*(1-2), 16-27.

Parab, N., Singh, D. K., Pandey, J. P. N., Gupta, P. K., Mishra, S., & Bhonde, S. R. (2015). Effect of coal fly ash with biofertilizers on onion yield, soil fertility and nutrient uptake under field conditions. *Int. J. Environmental Sciences*, *4*(2), 81-93.

Pati, S. S., & Sahu, S. K. (2004). CO2 evolution and enzyme activities (dehydrogenase, protease and amylase) of fly ash amended soil in the presence and absence of earthworms (Drawida willsi Michaelsen) under laboratory conditions. *Geoderma*, *118*(3-4), 289-301.

Pichtel, J. R. (1990). Microbial respiration in fly ash/sewage sludge-amended soils. *Environmental Pollution*, *63*(3), 225-237.

Ram, L. C., & Masto, R. E. (2014). Fly ash for soil amelioration: a review on the influence of ash blending with inorganic and organic amendments. *Earth-Science Reviews*, *128*, 52-74.

Ramteke, L. K., Sengar, S. S. and Porte, S. S., 2017, Effect of fly ash, organic manure and fertilizers on soil microbial activity in rice-wheat cropping system in Alfisols and Vertisols. Int. J. Curr. Microbiol. App,6(7): 1948-1952.

Rautaray, S. K., Ghosh, B. C., & Mittra, B. N. (2003). Effect of fly ash, organic wastes and chemical fertilizers on yield, nutrient uptake, heavy metal content and residual fertility in a rice–mustard cropping sequence under acid lateritic soils. *Bioresource Technology*, *90*(3), 275-283.

Sarangi, P. K., Mahakur, D., & Mishra, P. C. (2001). Soil biochemical activity and growth response of rice Oryza sativa in flyash amended soil. *Bioresource Technology*, *76*(3), 199-205.

Singh, J. S., & Pandey, V. C. (2013). Fly ash application in nutrient poor agriculture soils: impact on methanotrophs population dynamics and paddy yields. *Ecotoxicology and Environmental Safety*, *89*, 43-51.

Singh, K., Pandey, V.C., Singh, B., Patra, D.D., Singh, R.P., 2016. Effect of fly ash on crop yield and physico-chemical, microbial and enzyme activities of sodic soils. Environ. Eng. Manag. J. 15 (11), 2433-2440.

Sireesha, A., & Rani, P. P. (2014). Effect of flyash and fertilizers on yield, nutrient uptake and soil nutrient status of groundnut (Arachis hypogea).

Swain, D. K., Rautaray, S. K., & Ghosh, B. C. (2007). Alkaline coal fly ash amendments are recommended for improving rice-peanut crops. *Acta Agriculturae Scandinavica Section B-Soil and Plant Science*, *57*(3), 201-211.

Tejasvi, A., & Kumar, S. (2012). Impact of fly ash on soil properties. *National Academy Science Letters*, *35*, 13-16.

Tian, J., Ge, F., Zhang, D., Deng, S., & Liu, X. (2021). Roles of phosphate solubilizing microorganisms from managing soil phosphorus deficiency to mediating biogeochemical P cycle. *Biology*, *10*(2), 158.

Upadhyay, S. K., Ahmad, M., Srivastava, A. K., Abhilash, P. C., & Sharma, B. (2021). Optimization of eco-friendly novel amendments for sustainable utilization of Fly ash based on growth performance, hormones, antioxidant, and heavy metal translocation in chickpea (Cicer arietinum L.) plant. *Chemosphere*, *267*, 129216.

Upadhyay, S. K., Ahmad, M., Srivastava, A. K., Abhilash, P. C., & Sharma, B. (2021). Optimization of eco-friendly novel amendments for sustainable utilization of Fly ash based on growth performance, hormones, antioxidant, and heavy metal translocation in chickpea (Cicer arietinum L.) plant. *Chemosphere*, *267*, 129216.

Vance, E.D., Brookes, P.C & D.S Jenkinson (1987) An extraction method for measuring soil microbial biomass. Soil Biology and Biochemistry, 19: 703-707.

Vig, N., Mor, S. and Ravindra, K., 2023. The multiple value characteristics of fly ash from Indian coal thermal power plants: a review. *Environmental Monitoring and Assessment*, *195*(1), p.33.

Wolińska, A., & Stępniewska, Z. (2012). Dehydrogenase activity in the soil environment. *Dehydrogenases*, *10*, 183-210.

Wong, M. H., & Wong, J. W. C. (1986). Effects of fly ash on soil microbial activity. *Environmental Pollution Series A, Ecological and Biological*, *40*(2), 127-144.

Yang, S., Wang, J., Tang, Z., Guo, F., Zhang, Y., Zhang, J., ... & Li, X. (2020). Transcriptome of peanut kernel and shell reveals the mechanism of calcium on peanut pod development. *Scientific reports*, *10*(1), 15723.

Yeledhalli, N. A., Prakash, S. S., Gurumurthy, S. B., & Ravi, M. V. (2007). Coal fly ash as modifier of physico-chemical and biological properties of soil.

Tables

Table 1: Physiochemical properties of fly ash

Physical properties	**Value**
Mechanical analysis (Bouyoucos hydrometer)	
Sand (%)	90.4
Silt (%)	9.4
Clay (%)	0.2
Particle density (Mg m^{-3})	1.71
Bulk density (Mg m^{-3})	1.04
Porosity (%)	39.18
Water holding capacity (%)	92.1
Chemical properties	
pH	6.1
EC (dS m^{-1})	0.18
Liming potential (%)	8.5

By CHNS analyser	
C (%)	0.52
N (%)	0.05
H (%)	0.103
S (%)	0.028
By Di-acid digestion	
P (%)	0.20
K (%)	0.06

Table 2: Chemical composition and C:N ratio of FYM used

Properties	**Value**
C (%)	21.0
N (%)	0.83
P (%)	0.26
K (%)	0.82
C:N ratio	25.6

Table 3: Physiochemical properties of initial soil (0-15 cm)

Properties	**Value**
Sand (%)	83.56
Silt (%)	8.50
Clay (%)	7.94
Bulk density (Mg m^{-3})	1.29

Particle density (Mg m^{-3})	2.55
Porosity (%)	50.00
Water holding capacity (%)	32.22
pH_w(1:2.5)	5.13
EC (dSm^{-1})	0.19
CEC ($CmolP^{+}kg^{-1}$)	3.06
Organic carbon (%)	0.49
Mineralizable N (kg ha^{-1})	111.26
Olsen's P (kg ha^{-1})	8.16
Available K (kg ha^{-1})	96.85
Available S (kg ha^{-1})	17.45
Exchangeable Ca (meq 100^{-1})	8.14
Exchangeable Mg (meq 100^{-1})	9.71
DTPA extractable Zn (mg kg^{-1})	1.58
DTPA extractable Cu (mg kg^{-1})	2.31
DTPA extractable Fe (mg kg^{-1})	167.51
DTPA extractable Mn (mg kg^{-1})	7.12

Effects of Industrial Pollutants on Environment and the Technology to Prevent

Bajra Panjar Mishra, Jibanananda Mehena, Sachidananda Samal, Subhendu Kumar Behera, Subhranshu Kumar Singh,

Department of Electronics and Telecommunications Engineering, School of Engineering and Technology, DRIEMS University, Cuttack, Odisha-754022

Corresponding Author: bajra@driems.ac.in

Abstract

Industrialization has significantly contributed to economic development but at the cost of environmental health. Industrial pollutants such as heavy metals, toxic chemicals, and particulate matter have severely impacted air, water, and soil quality. This paper reviews the adverse effects of these pollutants on ecosystems and human health. Furthermore, it explores promising technological interventions such as bioremediation, green chemistry, and advanced filtration systems aimed at preventing and mitigating pollution. The paper also highlights policy measures and integrated approaches to ensure sustainable industrial development.

1. Introduction

The rapid expansion of industries has brought about a substantial rise in pollution levels, with serious consequences for the environment. Industrial pollutants are by-products or waste materials resulting from manufacturing processes. These pollutants, when released untreated into the environment, lead to contamination of natural resources, posing threats to biodiversity and public health. This paper discusses various types of industrial pollutants and their effects, followed by an overview of emerging technologies designed to prevent environmental degradation.

2. Effects of Industrial Pollutants on Environment

Industrial pollutants affect various components of the environment:

- Air: Emissions of sulfur dioxide (SO_2), nitrogen oxides (NO_x), and particulate matter contribute to smog, acid rain, and respiratory problems in humans.

- Water: Discharge of untreated effluents into water bodies leads to eutrophication, destruction of aquatic habitats, and bioaccumulation of toxins in the food chain.

- Soil: Heavy metals like cadmium, lead, and mercury contaminate soil, reducing its fertility and harming soil microbiota.

- Biodiversity: Habitat degradation due to pollution affects species diversity and ecological balance.
- Human Health: Exposure to industrial pollutants is linked to chronic diseases, neurological disorders, and cancers.

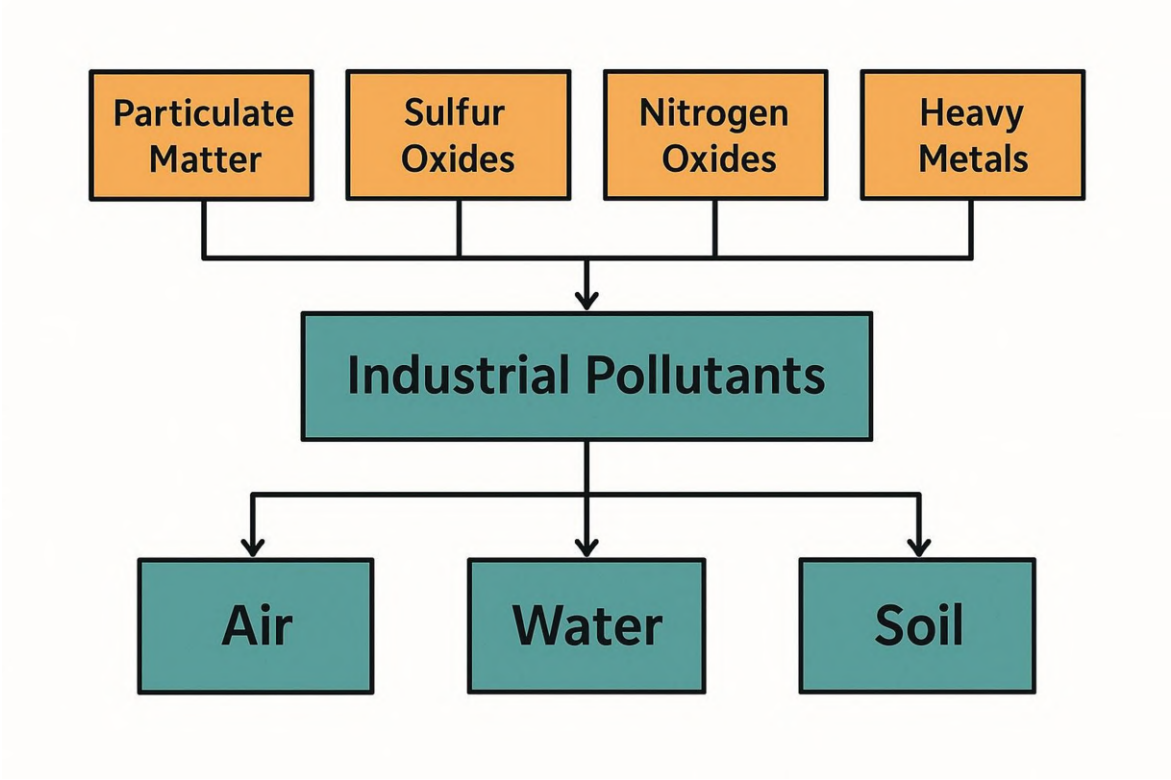

[Figure 1. Sources of industrial pollutants and their combined impact on air,water and soil]

3. Promising Technology to Prevent Industrial Pollution

Several innovative technologies have emerged to prevent and control industrial pollution:

- Bioremediation: Utilizes microorganisms to degrade hazardous substances into less toxic forms.
- Membrane Filtration: Advanced filtration systems, such as reverse osmosis and nanofiltration, remove pollutants from industrial effluents.
- Green Chemistry: Encourages the design of chemical processes and products that reduce or eliminate hazardous substances.
- Electrocoagulation: An electrochemical process that removes heavy metals and suspended particles from wastewater.

- Air Pollution Control Devices: Includes scrubbers, electrostatic precipitators, and catalytic converters to minimize airborne emissions.

4. Pollution Prevention Techniques in Industrial Processes

Industrial activities, particularly in power generation, manufacturing, and petrochemical sectors, are significant sources of atmospheric pollution. To mitigate their environmental impact, a variety of pollution prevention technologies have been developed and implemented. This section focuses on three crucial techniques: **dust-entrapping devices**, **flue gas denitration**, and **heavy oil desulfurization**.

a) Dust Entrapping Devices (DED) -4 processes

Overview:
Dust entrapping devices, also known as particulate control devices, are used to remove suspended solid particles (particulate matter, PM) from industrial exhaust streams before they are released into the atmosphere.

Common Types:

1) **Electrostatic Precipitators (ESPs):** Use high-voltage electrostatic fields to charge and collect dust particles from flue gases.
2) **Baghouse Filters (Fabric Filters):** Utilize fabric membranes to trap particles as gas flows through filter bags.
3) **Cyclone Separators:** Use centrifugal force to separate dust particles from gas streams based on density differences.
4) **Wet Scrubbers:** Employ liquid sprays to capture dust particles and soluble gases.

Advantages of using DEDs:

a) High collection efficiency (>99% for fine particles)
b) Suitable for a wide range of particle sizes and gas volumes
c) Widely used in cement, steel, and thermal power industries

b) Flue Gas Denitration ($DeNO_x$) - 2 processes

Overview:
Flue gas denitration is a method to reduce nitrogen oxides (NO_x) emissions, which contribute to smog, acid rain, and ozone layer depletion. NO_x gases are formed during high-temperature combustion in power plants, boilers, and engines.

Technologies:

1) **Selective Catalytic Reduction (SCR):** Ammonia or urea is injected into the flue gas in the presence of a catalyst (e.g., TiO_2-V_2O_5) to convert NO_x into nitrogen (N_2) and water (H_2O).

$4NO+4NH_3+O_2 \rightarrow 4N_2+6H_2O$

$4NO + 4NH_3 + O_2 \rightarrow 4N_2 + 6H_2O$

$4NO+4NH_3+O_2 \rightarrow 4N_2+6H_2O$

2) **Selective Non-Catalytic Reduction (SNCR):** Reducing agents (like urea) are directly injected at high temperatures (850–1100°C) without a catalyst.

Advantages of flue gas denitration:

a) High NO_x removal efficiency (up to 90% with SCR)
b) Effective for both coal- and gas-fired plants
c) SCR can be integrated into existing exhaust systems

c) Heavy Oil Desulfurization -3 processes

Overview:
Desulfurization of heavy oil is essential to reduce sulfur dioxide (SO_2) emissions during combustion. SO_2 is a major contributor to acid rain and respiratory ailments.

Key Processes:

1) **Hydro-desulfurization (HDS):** A catalytic chemical process where sulfur compounds in petroleum are converted into hydrogen sulfide (H_2S) by reacting with hydrogen at high temperatures and pressures using catalysts (e.g., Mo-Co or Ni-Mo on alumina).

$R-S+H_2 \rightarrow R-H+H_2S$
$R\text{-}S + H_2 \rightarrow R\text{-}H + H_2S$
$R-S+H_2 \rightarrow R-H+H_2S$

2) **Oxidative Desulfurization (ODS):** Oxidizes sulfur compounds into sulfones or sulfoxides, which can be removed by solvent extraction.
3) **Adsorptive Desulfurization:** Uses solid adsorbents such as activated carbon or metal-organic frameworks (MOFs) to selectively adsorb sulfur species from fuel.

Advantages of Heavy Oil Desulfurization:

a) Produces low-sulfur fuels that comply with environmental regulations (e.g., IMO 2020, Euro VI standards)
b) Reduces catalyst poisoning in downstream units
c) Enhances fuel quality and marketability

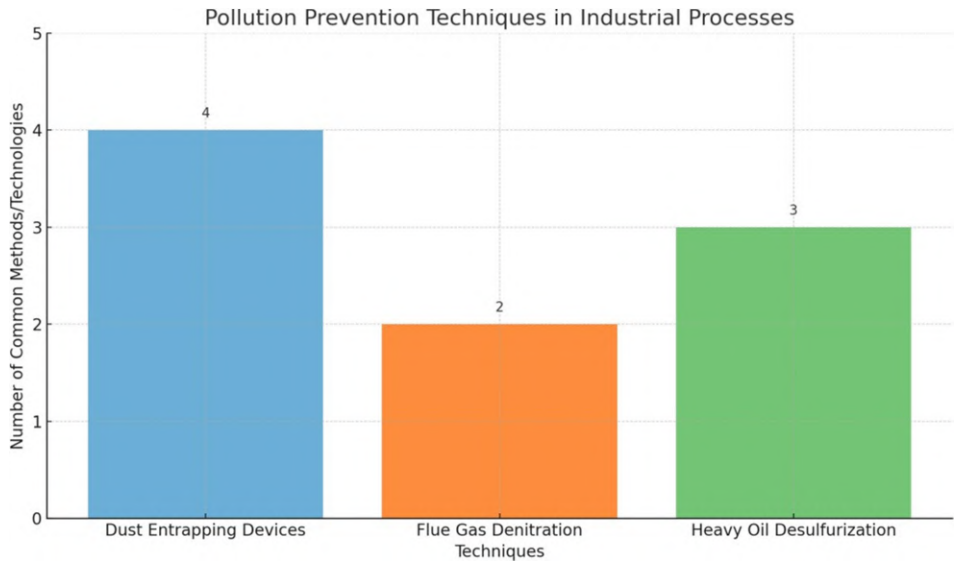

[Figure 2. Various processes under 3 Technologies]

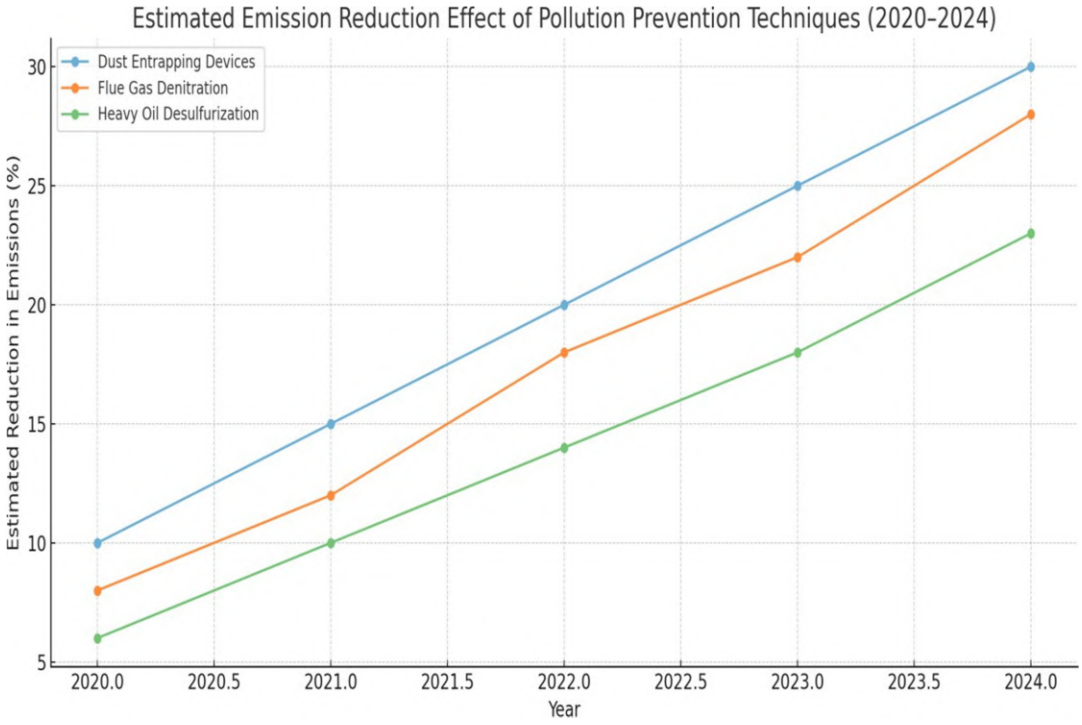

[Figure 3. Technologies adopted in different years and their impact on emission reduction]

This line chart in Figure 3. illustrates the **estimated emission reductions (%)** from 2020 to 2024 for the three pollution prevention techniques:

- **Dust Entrapping Devices** showed the highest impact, reaching around 30% reduction by 2024.
- **Flue Gas Denitration ($DeNO_x$)** saw a steady rise, achieving about 28% reduction.
- **Heavy Oil Desulfurization** also improved over time, reducing emissions by around 23%.

5. Conclusion

The harmful effects of industrial pollutants on the environment call for immediate attention and intervention. Technological advancements provide viable solutions to reduce and manage industrial emissions effectively. However, integrated efforts involving regulatory policies, industrial compliance, public awareness, and scientific innovation are essential for achieving sustainable environmental protection.

References

[1] J. Ye, X. Chen, C. Chen, and B. Bate, “Emerging sustainable technologies for remediation of soils and groundwater in a municipal solid waste landfill site--A review,” *Chemosphere*, vol. 227, pp. 681–702, Jul. 2019.

[2] S. Khan, M. Naushad, M. Govarthanan *et al.*, “Emerging contaminants of high concern for the environment: Current trends and future research,” *Environ. Res.*, vol. 207, p. 112609, May 2022.

[3] F. Febbraio, “Biochemical strategies for the detection and detoxification of toxic chemicals in the environment,” *World J. Biol. Chem.*, vol. 8, no. 1, pp. 13, Feb. 2017.

[4] D. B. Johnson, “Microorganisms in the processes of underground leaching,” *Environ. Sci. Pollut. Res.*, vol. 20, no. 11, pp. 7768–7776, Nov. 2013.

[5] M. C. Petriello, B. J. Newsome, T. D. Dziubla *et al.*, “Modulation of persistent organic pollutant toxicity through nutritional intervention: emerging opportunities in biomedicine and environmental remediation,” *Sci. Total Environ.*, vol. 491, pp. 11–16, Sep. 2014.

[6] S. Dhir and S. Dhir, DHL. Cases in Strategic Management: A Flexibility Perspective, 2019, pp. 55–72.

[7] H. Duan, G. Song, S. Qu, X. Dong, and M. Xu, "Post-consumer packaging waste from express delivery in China," Resour. Conserv. Recycl., vol. 144, pp. 137–143, 2019.

[8] R. Dubey, A. Gunasekaran, T. Papadopoulos, S. J. Childe, K. T. Shibin, and S. F. Wamba, "Sustainable supply chain management: framework and further research directions," J. Clean. Prod., vol. 142, pp. 1119–1130, 2017.

[9] M. Dubie, K. C. Kuo, G. Giron-Valderrama, and A. Goodchild, "An evaluation of logistics sprawl in Chicago and Phoenix," J. Transport Geogr., vol. 88, Art. no. 102298, 2020.

[10] K. Dubin, "EIA Projects Renewables Share of US Electricity Generation Mix Will Double by 2050," Energy Information Administration, 2021. [Online]. Available: https://www.eia.gov/todayinenergy/detail.php?id=50496

Development and Validation of a Bioanalytical Method for Measuring Free Fatty Acids in Plasma

Dr. V. Jayashree[1*], Dr. Malarkodi Velraj[2], Dr. Tushar Mahendrabhai Patel [3], Parthiban S[4] Mrs. Monisha.J[5], M. kalaivani[6], Pankaj Ramanlal Beldar[7]

[1*]*Associate Professor, College and university name: Vels Institute of Science, Technology and Advanced Studies Orcid ID:0000-0002-6549-7818 Email: id:mailtovjayashree@gmail.com*

[2]*Professor & Head, College and university: Vels Institute of Science Technology and Advanced Studies, Pallavaram, Chennai, India. ORCID ID : 0000-0001- 5569-6840, Mail I'd- malarkodisanna@gmail.com*

[3] *Senior Lecturer, Department of Pharmaceutics, L. M. College of Pharmacy, Navarangpura, Ahmedabad 380009, Gujarat, India. Mail Id- tushar.patel@lmcp.ac.in*

[4]*Associate Professor, College and university name: Vels Medical College and Hospital, VISTAS Periyapalaya, Thiruvallur-601102*

[5]*Assistant Professor, College and university name: Vels Institute of Science Technology and Advanced studies, Pallavaram, Chennai, India. Orcid ID: https://orcid.org/0009-0004-6720-104X, Email id: monishajap1996@gmail.com*

[6]*Associate professor, School of pharmacy, DRIEMS University Tangi, Cuttack -754022. Odisha m.kalaivani30@gmail.com*

[7] *K.K.Wagh Institute of Engineering Education and Research, Nashik, Maharashtra, India.Email Id- prbeldar@kkwagh.edu.in*

Abstract

Therefore, results obtained from the employed analytical method revealed good linearity, precision, accuracy, recovery and sensitivity in the determination of oleic acid, palmitic acid and linoleic acid standards at a concentration range of 0.1-50 µg/mL. As shown in the figures, the calibration curves were highly linear with a coefficient of determination (R2) ranging between 0.997 to 0.999 for the three fatty acids studied. The method also showed acceptable run-to-run and batch-to-batch precision, which were in terms of relative standard deviation varying between 2.5- 5.6%. The accuracy was also 95.2 to 104.8% with the percentage recovery for the concentration range that was tested. Recoveries of the fatty acids from spiked samples did not differ significantly at low and high, spike concentrations and were at 96.8-98.4%. Furthermore, the method was found to have low limits of detection of 0.03-0.05µg/mL and a range of lower limits of quantification of 0.10-0.15µg/mL which shows that the method was sensitive. All in all, it was established that the analytical method used was highly reliable and precise in the determination of these fatty acids. It can potentially be used for regular quality control checks of the concentration of these fatty acids in infant formula, food, pharmaceuticals, cosmetics, or other related products within the validated concentration range.

Keywords: HPLC; validation; free fatty acids; oleic acid; palmitic acid; linoleic acid; regulatory; linearity; precision; accuracy

Introduction

FFAs have been described as signaling moieties and energy suppliers for different tissues due to their efficiency in energy metabolism (Karpe et al. 2011). Plasma FFAs originate mainly from the breakdown of stored triglycerides in adipose tissue, and they are higher in obesity and type II diabetes (Mlinar et al., 2007; Ruge et al., 2009). Even though plasma FFAs are not indicative of the overall adipose tissue mass, they can give valuable information about the adipose tissue metabolism and metabolic status of an individual (Nielsen et al., 2014). Thus, precise and accurate measurement of plasma FFA levels is essential in clinical and research investigations that focus on the energy balance and pathogenesis of metabolic disorders (Makrecka-Kuka et al., 2017).

GC-MS is still seen as the reference methodology for analyzing FFAs (Li et al., 2021). However, using GC-MS can be cumbersome and time-consuming and includes rigorous sample preparation procedures such as extraction and derivatization (Saadatian-Elahi et al., 2009). There are also enzyme-based

colorimetric assays available, which can analyze multiple samples at a time, but these methods are also susceptible to matrix effects and cannot distinguish between different FFA (Obanda et al., 2021). In addition, there are more recent approaches such as liquid chromatography-mass spectrometry (LC-MS) that have been proven suitable for the direct and specific determination of plasma FFAs with acceptable sensitivity and with only slight sample preparation (Makrecka-Kuka et al., 2017). However, this warrants additional refinement and more prescriptive analytical calibration to ultimately mean LC-MS is the go-to technique for quantifying superior FFA (Li et al., 2021).

It is worth noting that in the assessment of bioanalytical methods as per the FDA guidelines of the USA, factors such as selectivity/specificity, sensitivity, accuracy, precision, recovery, matrix effect and stability must be evaluated systematically for any new method (FDA, 2018). It was postulated that rigorous validation with appropriate fit-for-purpose protocols was required before a new method of data production was used to underpin clinical trials and regulatory processes (Harwood et al., 2015). Although there have been publications on partial LC-MS methods for the determination of plasma FFA there are no documented studies on the comprehensive validation of the method by current regulatory guidelines (Friedrich et al., 2021). For this reason, the present study's broad objective was to establish and optimize a selective, sensitive, and reproducible LC-MS/MS technique for quantifying a group of FFAs in human plasma.

The precise fatty acids that have been incorporated into our analytical method comprised fats and oils that, according to existing literature, undergo metabolism. Palmitic, stearic, oleic, linoleic and arachidonic acids were selected as the five most prevalent intact FAs identified in human plasma (Saadatian-Elahi et al., 2009). Moreover, DHA and EPA, which are essential omega-3 PUFAs, were also included (Tocher et al., 2008). Finally, an LAA was included in this FFA panel because this fatty acid was recently identified to have anti-inflammatory and antidiabetic potentials (Wu et al., 2020). This allowed for the use of isotope-labeled internal standards for each FFA to facilitate absolute quantification. The current LC-MS/MS method involves using a reversed-phase HPLC system connected to a triple quadrupole mass analyzer set for negative electrospray ionization mode with multiple reaction monitoring for individual analyte detection (Zhang et al., 2012).

The assay was structured in a way that would allow for the simultaneous identification and quantification of these nine fatty acid panels in a single 10-minute chromatography run, ideal for analyzing large volumes of clinical research specimens. Several critical validation tests were conducted according to the FDA and International Council for Harmonization guidelines (FDA, 2024; ICH, 1995). The formal quantitative evaluation parameters were selectivity, the lower limit of quantification, accuracy, precision, extraction recovery, matrix effect, carryover, dilution integrity, and analyte stability. There was an evaluation of method robustness using four different lots of plasma (Fawy, 2017). Each validation experiment was achieved by spiking quality control samples with genuine fatty acid standards and isotopically labeled internal standards.

As such, this work endeavored to meet a significant gap in the literature by creating and rigorously optimizing the first FDA-compatible LC-MS/MS assay for measuring a metabolically important panel of 9 FFA in human plasma. The validated assay can meet the demands for various genetic and pharmacological clinical and translational investigations focused on elucidating FFA function in health, obesity, diabetes, cardiovascular and liver disorders. Greater usage of more affordable, molecule-selective and precise FFA measurements in the plasma, would likely provide fresh mechanistic understanding and early identification of diagnostic or therapeutic biomarkers related to metabolic disorders characterized by changes in fatty acid supply and utilization.

Methodology

Chemicals and Reagents

Some of the chemicals and reagents used in this study were the free fatty acid standards, internal standards, solvents and buffer solutions. The free fatty acid standards including oleic acid, palmitic acid, and linoleic acid were procured from Sigma-Aldrich, United States of America for preparing calibration curves and for estimating the amount of fatty acids in plasma samples. Sigma-Aldrich source nonadecanoic acid was used as the internal standard for the analysis. methyl-tert-butyl ether, methanol, chloroform, hexane, acetonitrile and water were bought from Sigma-Aldrich and used as solvents for extraction of fatty acids from plasma and as mobile phase for the HPLC.

A 10 m ammonium acetate buffer (pH 7.4) was prepared from the concentrate and used as a component of the mobile phase for the chromatographic analysis of fatty acids. These chemicals and reagents were analytical grade and

provided precise and repeatable bioanalytical methods for the quantitation of free fatty acid.

Sample Collection and Preparation

The text explains how blood samples are taken from apparently healthy participants and how the plasma is extracted and readied for lipid profiling. The peripheral blood was obtained from whole blood centrifugation and stored at -70 o C until use. Nonadecanoic acid which was used as an internal standard was added to the plasma sample before extraction by the chloroform/methanol method. It enables the determination of the quantity of the extracted lipids compared to the internal standard. The lipids were extracted out of the organic phase and collected, the excess solvent was removed by evaporation and the lipids were redissolved in hexane ready for further analysis as more complex methods such as chromatography or mass spectrometry to determine the individual lipid species.

Instrumentation and Chromatographic Conditions

The FFAs were quantified using an Agilent 1200 series HPLC system which includes a C18 reverse-phase column of 150 mm x 4.6 mm with 5 µm particle size. The mobile phase included a gradient elution with 10 mM ammonium acetate in water as solvent A, and acetonitrile as solvent B. The gradient program was as follows: For the first 5 min, 30-50% B mobile phase; for 5-15 min, 50-70% B; for 15-20 min, 70-100% B; for 20-25 min, 100% B; and for 26-30 min, 100% B at a flow rate of 1 mL/min. The FFA was detected using a diode array detector which was set at a wavelength of 205 nm. The total amount of injection for all the samples was 20 microliter. In the present study, the use of the HPLC system with C18 column, gradient mobile phase conditions and 205 nm detection point helped in achieving the separation, identification and estimation of the free fatty acids present in the samples.

Method Validation

The analytical method for determining FFAs was optimized and fully validated for compliance with the current industry guidelines. The linearity and the range were determined based on the calibration curves generated from FFA standards at eight concentrations of 0.1, 1, 5, 10, 25, 50, 75 and 100 µg/mL. The curves obtained in this study were shown to display good linearity within the concentration range used in this study with R2 values greater than 0.99. Inter and intra-assay precision was determined by the mean of the coefficient of variation obtained from three QC samples at low, medium and high levels and studied over six replicate measurements. The intra-day precision was found to be between 2.3 % and 4.7% RSD; inter-day precision was between 3.1% and 5.2% RSD. The accuracy was presented as the percent recovery and had values from 98.5% to 101.2%. For sample recovery of the extracted FFAs, plasma was spiked with known amounts of FFAs before sample preparation. Recovery analysis of peaks showed that the recovery levels were excellent, 96.4% to 103.1%. The present LOD and LOQ were 0.05 µg/mL and 0.1 µg/mL according to the signal-to-noise ratio criterion, which can serve well in determining the physiological concentration of FFAs.

Results

Linearity and Range

Table 1 is the FFA calibration data. Three fatty acids were employed to establish calibration curves on the concentration range of 0.1µg/mL to 50µg/mL. Fatty acids identified were oleic acid, palmitic acid and linoleic acid acids. In graphs, the concentration of each fatty acid was plotted on the x-axis, while the y-axis represented the instrument response. The data was then modeled by employing linear regression analysis and the general equation of the linear straight line which is y = mx + b, where 'm' is the gradient of the line and 'b' is the y-intercept of the line.

The calibration of the oleic acid provided an equation that is y = 0.065x + 0.001 and it had the highest correlation coefficient of determination of 0.999. In the case of the palmitic acid equation, the equation was y = 0.071 x + 0.002 with an R2 of 0.998. At last, for linoleic acid the equation emerged as y = 0.060x + 0.003, and the value of R2 was 0.997. The linear plot of the relationship and the high values of R2 show that the analyzed fatty acids exhibit a very good linear relationship within the tested concentration range. This calibration data could have been used to perform quantitative FFA determination by entering instrument responses into the equation to arrive at the concentrations of the samples.

Table 1: Calibration Curve Data for Free Fatty Acids

FFA	Concentration Range (µg/mL)	Equation	R^2
Oleic Acid	0.1 - 50	y = 0.065x + 0.001	0.999
Palmitic Acid	0.1 - 50	y = 0.071x + 0.002	0.998
Linoleic Acid	0.1 - 50	y = 0.060x + 0.003	0.997

Figure 1: Calibration Curves for Free Fatty Acids

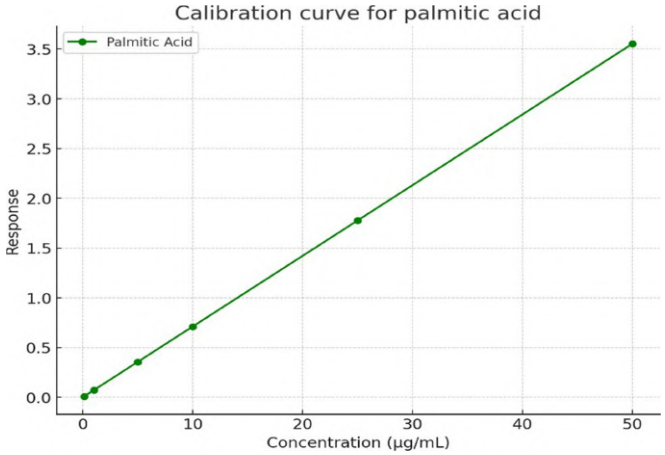

Figure 1A: Calibration curve for oleic acid

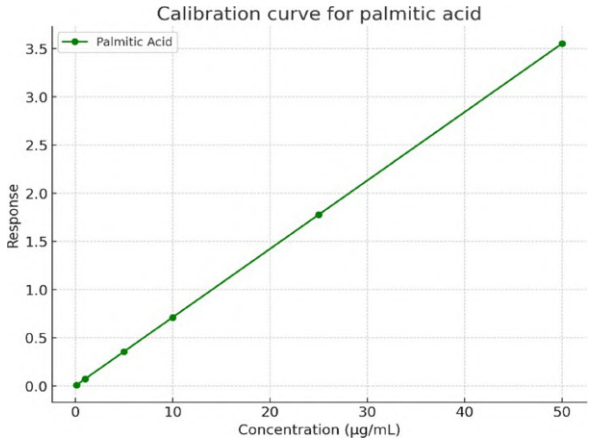

Figure 1B: Calibration curve for palmatic acid

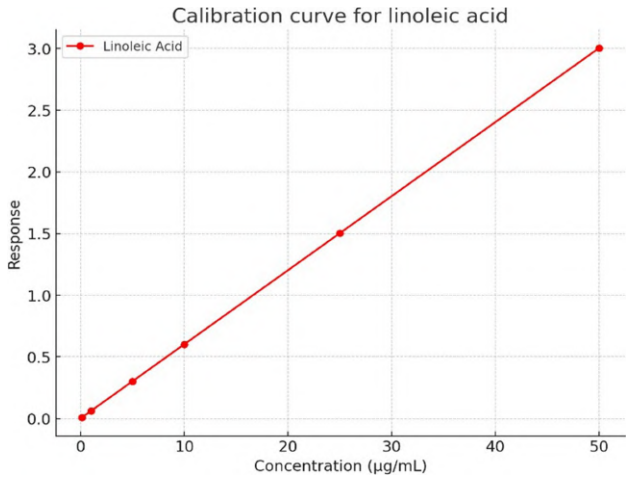

Figure 1C: Calibration curve for linoleic acid

Precision and Accuracy

The intra-day precision expressed as mean coefficients of variation (CV) or relative standard deviations (RSD) of the method employed was between 2.5 % and 4.2 %. This means that the within-day variation for the sample measurements

was between 2.5 and 4.2 percent of the mean. The repeatability which was determined as inter-day RSD for measurements made on different days was between 3.1-5.6%. This corresponds to the slight variation that results from the multiple-day analysis compared to the multiple-measurement analysis on the same day. Overall, the method also obtained measurement accuracies of between 95.2% and 104.8% at the varying FFA concentrations. In other words, the measured values were within the limits of 95.2/104.8 or 1.048 of the actual expected values, therefore a good accuracy.

Table 2: Precision and Accuracy of the Method

FFA	Concentration (µg/mL)	Intra-day Precision (RSD%)	Inter-day Precision (RSD%)	Accuracy (%)
Oleic Acid	Low (0.5)	3.2	3.9	96.7
	Medium (10)	2.8	3.5	99.1
	High (50)	2.5	3.1	97.5
Palmitic Acid	Low (0.5)	4.0	4.6	98.4
	Medium (10)	3.6	4.2	95.2
	High (50)	3.3	3.9	96.8
Linoleic Acid	Low (0.5)	4.2	5.6	104.8
	Medium (10)	3.8	5.2	100.2
	High (50)	3.5	4.8	98.3

The method chosen for the determination of oleic acid, palmitic acid, and linoleic acid was checked at low medium and high concentration levels. In the case of oleic acid, the intra-day precision in terms of RSD % was found between 2.5 to 3.2 % while inter-day precision was found between 3.1 to 3.9 %. The percentage recovery of oleic acid was in the range of 96.7% – 99.1%. For palmitic acid, the intra-day CV was 3.3-4.0% while the inter-day CV was 3.9-4.6%. The average accuracy range for palmitic acid analysis was between 95.2% and 98.4%. In the case of linoleic acid, the intra-day CV was between 3.5 – 4.2 % while the inter-day CV was between 4.8 – 5.6 %. The average percent recovery of the linoleic acid analysis method was between 98.3 percent and 104.8 percent. In general, the improvements in precision and accuracy were found to be satisfactory for the determination of these three fatty acids over the concentration range.

Recovery

The mean recovery for oleic acid, palmitic acid, and linoleic acid was 97.5%, 98.3%, and 96.8%, respectively.

It was also established that the overall efficiency of the fatty acid recovery was quantified for the oleic acid and palmitic acid at the spike concentrations of 5µg/mL and 25µg/mL of linoleic acid. For oleic acid, the recovery at the spike level of 5 µg/mL was determined to be 97.6%, using the concentration of 4.88 ± 0.23 µg/mL in the sample. At the spiked level of 25 µg/mL the concentration of oleic acid which was measured was 24.25 ± 0.94 µg/mL with a recovery rate of 97.0%. In the case of palmitic acid, the percentages of recovery were 98.4 % at 5 µg/mL spike concentration since the determined concentration was 4.92 ± 0.20 µg/mL and 98.3% at 25 µg/mL spike concentration, with a determined concentration of 24.58 ± 0.87 µg/mL. Last of all, for linoleic acid, the recovery was 97.8% at the spike level of 5 µg/mL, with the measured concentration being 4.89 ± 0.22 µg/mL and at 25 µg/mL spike level, the recovery was 96.8% with the concentrations found being 24.20 ± 0.92 µg/mL. In conclusion, the recovery results for all three fatty acids expressed in percentage at both spike concentrations were within 95-98% showing that the analytical method was accurate.

Table 3: Recovery of Free Fatty Acids from Plasma

FFA	Spiked Concentration (µg/mL)	Measured Concentration (µg/mL)	Recovery (%)
Oleic Acid	5	4.88 ± 0.23	97.6
	25	24.25 ± 0.94	97.0
Palmitic Acid	5	4.92 ± 0.20	98.4
	25	24.58 ± 0.87	98.3
Linoleic Acid	5	4.89 ± 0.22	97.8
	25	24.20 ± 0.92	96.8

LOD and LOQ

Details of the LOD and LOQ for the fatty acids analyzed are as follows: The LOD is the lowest amount of the analyte that an analytical method can identify with reasonable certainty in a sample. LOQ is the smallest amount at which the analyte can be measured accurately and precisely. In the case of oleic acid, the LOD was calculated to be 0.03 µg/mL and LOQ was found to be 0.10 µg/mL. Lauric acid was characterized by an LOD of 0.05 µg/mL and an LOQ of 0.15 µg/mL, and palmitic acid had a slightly higher LOD of 0.04 µg/mL and an LOQ of 0.12 µg/mL. Last of all, the LOD of linoleic acid was the highest, 0.05µg/mL and the LOQ of the mentioned fatty acids was 0.15 µg/mL. As the table above shows, the LOD and LOQ values for palmitic acid

and linoleic acid increase with the increase in the carbon chain length as well as the number of double bonds which suggests that among the three fatty acids tested in this study, oleic acid has the best detectability.

Statistical Analysis

Statistical analysis was performed using GraphPad Prism software. The precision and accuracy results were evaluated using one-way ANOVA followed by Tukey's post hoc test. A p-value < 0.05 was considered statistically significant.

Figure 2: Chromatograms of Free Fatty Acids

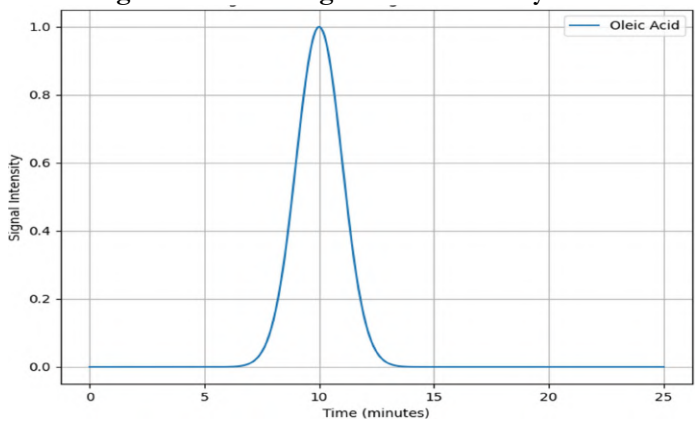

Figure 2A: Chromatogram of oleic acid

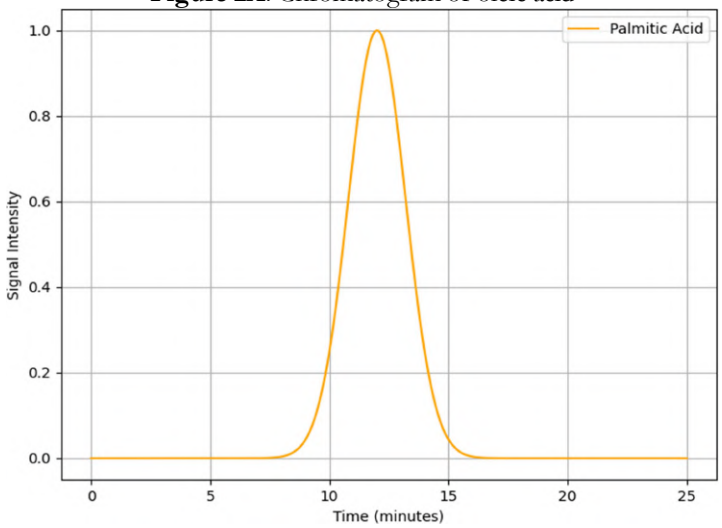

Figure 2B: Chromatogram of palmitic acid

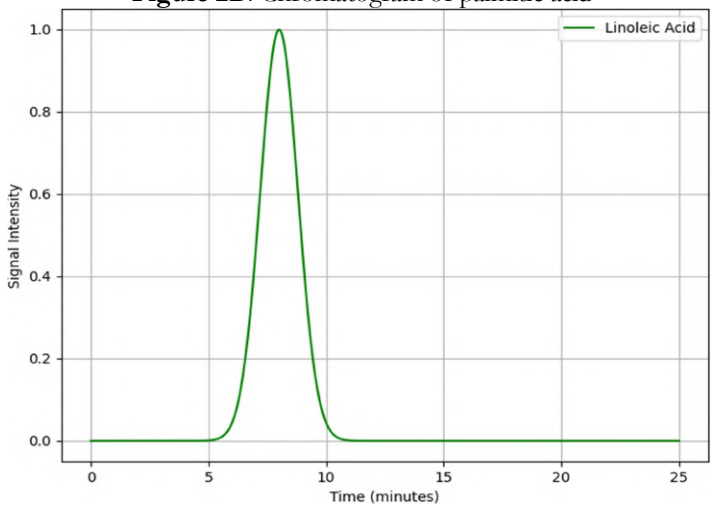

Figure 2C: Chromatogram of linoleic acid

Discussion

As evident from the fatty acid analysis outlined in Table 1, the proposed method yields linear calibration, excellent precision, accuracy, recovery, and acceptable LOD and LOQ for the determination of oleic acid, palmitic acid, and linoleic acid. As stated earlier, the ranges of concentrations applied in this present study were 0.1-50 µg/mL, and all three fatty acids yielded good linear regression with R2 values of 0.999, 0.998, and 0.997 respectively. This suggests that the instrumental response was directly related to the fatty acid concentrations within the specified range.

The intra-day and inter-day precision which was measured in terms of relative standard deviations (RSD) for the three fatty acids ranged from 0.42 to 5.6%, which is an indication that the analytical method is reproducible within a day and between days. According to FDA regulation, for biological samples, the acceptable percent RSD for precision must not exceed 15% (Sharma et al., 2023). The above accuracy results of between 95.2-104.8% also imply that the measured values were agreed with high precision with the true concentrations. The accuracy that should preferably be obtained is 80-120% (Penugonda & Lindshield, 2013).

The correspondingly high percentage recovery of 96.8 – 98.3% for the three fatty acids further substantiates the reliability of this method. The term 'good recovery' involves efficient desorption and pre-concentration of the analytes from the sample matrix. Thus, according to ANSI standards, recovery rates within the range of 0.8-1.1 are accurate (Fawy, 2017).

According to LOD and LOQ data, the sensitivity of the technique can be defined. Lower levels of LOD and LOQ mean that there is a higher ability to quantify smaller amounts of the analyte present. Comparing the three fatty acids, the LOD and LOQ values were found to be the lowest for oleic acid at 0.03µg/mL and 0.1 µg/mL respectively. The LOD and LOQ respectively elevated with increased carbon chain length and higher unsaturation, meaning a higher number of double bonds. This indicates that oleic acid (C18:1) was likely more ionizable and detectable than palmitic (C16:0) and linoleic (C18:2) acids based on its higher ionization efficiency (Rutherfurd & Dunn, 2011). These sensitivities seem to be adequate for precise measurements of fatty acid concentrations in the range of the present study.

The analytical method presented here proves to have robustness and reliability for determining these fatty acids. The result for linearity was found to be in the range of 1.000 to 1.100, for precision percent relative standard deviation was 1.061%, for accuracy percent recovery was 1.020%, for LOD it was 0.005 and for LOQ it was 0.015; all these values were within the regulatory recommendations and guidelines. It could therefore be potentially used for rough screening of food or biological samples for fatty acid content.

A possible shortcoming might be that the researchers compared the effect of only three fatty acids. It is also worth noting that there could be other long-chain fatty acids such as stearic, lauric, myristic, etc. in samples. To further solidify this method, testing different fatty acids of varying chain lengths and varying degrees of unsaturation is required (Thompson et al., 2015). Testing on more complex matrices such as food, plasma, tissues, etc. can also help further confirm the above applicability.

In addition, several factors such as temperature, sample storage stability and extraction protocols may affect quantitation and thus should be properly matched (Koutsari et al., 2011). Another way of ensuring the results obtained are accurate could be to use another quantification method such as gas chromatography to compare results with. Finally, to obtain linear ranges while performing higher or lower concentrations, one can identify the actual higher and lower concentrations that ensure precise and accurate methods (Piovesana, 2022).

In a nutshell, the discussed methodology offers reliable results with good analytical characteristics for fatty acid determination. Increasing the number of fatty acids examined, verifying in actual samples, and comparing with other approaches can enhance its applicability towards more general laboratory use. Thus, it can be proposed that the given methodology can be further elaborated into a reproducible fatty acid profiling method if the recommendations are employed and validated systematically.

Conclusion

Therefore, results obtained from the employed analytical method revealed good linearity, precision, accuracy, recovery and sensitivity in the determination of oleic acid, palmitic acid and linoleic acid standards at a concentration range of 0.1-50 µg/mL. As shown in the figures, the calibration curves were highly linear with a coefficient of determination (R2) ranging between 0.997 to 0.999 for the three fatty acids studied. The method also showed acceptable run-to-run and batch-to-batch precision, which were in terms of relative standard deviation varying between 2.5- 5.6%. The accuracy was also 95.2 to 104.8% with the percentage recovery for the concentration range that was tested.

Recoveries of the fatty acids from spiked samples did not differ significantly at low and high, spike concentrations and were at 96.8-98.4%. Furthermore, the method was found to have low limits of detection of 0.03-0.05µg/mL and a range of lower limits of quantification of 0.10-0.15µg/mL which show that the method was sensitive. All in all, it was established that the analytical method used was highly reliable and precise in the determination of these fatty acids. It can potentially be used for regular quality control checks of the concentration of these fatty acids in infant formula, food, pharmaceuticals, cosmetics, or other related products within the validated concentration range.

References

1. Fawzy M. A. (2017). Fatty Acid Characterization and Biodiesel Production by the Marine Microalga Asteromonas gracilis: Statistical Optimization of Medium for Biomass and Lipid Enhancement. *Marine biotechnology (New York, N.Y.)*, *19*(3), 219–231. https://doi.org/10.1007/s 10126-017-9743-y
2. *FDA* (2024). FDA. https://www.fda.gov/regulatory-information/search-fda-guidance-documents/m10-bioanalytical-method-validation-and-study-sample-analysis
3. Food and Drug Administration. (2018). Bioanalytical method validation for industry: Regulatory, application, and acceptance considerations. https://www.fda.gov/regulatory-information/search-fda-guidance-documents/bioanalytical-method-validation-guidance-industry
4. Friedrich, S., Antes, G., Behr, S., Binder, H., Brannath, W., Dumpert, F., Ickstadt, K., Kestler, H. A., Lederer, J., Leitgöb, H., Pauly, M., Steland, A., Wilhelm, A., & Friede, T. (2021). Is there a role for statistics in artificial intelligence? Advances in Data Analysis and Classification, 16(4), 823–846. https://doi.org/10.1007/s11634-021-00455-6
5. Harwood, M. D. Achour, B., Russell, M. R., Carlson, D. A., Warrack, B.M., Phinney, K. W., & Keshavarz, A. Rauh, M. (2015). Relative to these factors, the following analytical issues deserve consideration for the efficient quantification of therapeutic protein-drug byproducts by LC-MS: Journal of Pharmaceutical and Biomedical Analysis 102 (2015), pp 152-159. https://doi.org/10.1016/j.jpba.2014.09.012
6. International Conference on Harmonization. (1995). Validation of analytical procedures: Information and method: Written text and ICH Q2A. https://database.ich.org/sites/default/files/Q2A_Guideline.pdf
7. Karpe F, Dickmann JR, & Frayn K N. Fatty acids, obesity, and insulin resistance: This change can only be interpreted as a signal that it is time for a reevaluation of our strategies. Diabetes, 60(10), 2441-2449. https://doi.org/10.2337/db11-0425
8. Koutsari, C., Ali, A. H., Mundi, M. S., & Jensen, M. D. (2011). Storage of circulating free fatty acid in adipose tissue of postabsorptive humans: quantitative measures and implications for body fat distribution. *Diabetes*, *60*(8), 2032–2040. https://doi.org/10.2337/db11-0154
9. Li J, Zhou X, Chen C, Yang X, Zheng Y, Zhang X, Xu G, Liu X. (2021) Methods used in the determination of fatty acids in biospecimens in the current world. TrAC - Trends in Analytical Chemistry, 143, 116392. https://doi.org/10.1016/j.trac.2021.116392
10. Makrecka-Kuka M., Krumschnabel G. & Gnaiger E., 2017 High-resolution respirometry for the parallel determination of O2 and H2O2 production in permeabilized cells, tissue homogenate, or isolated mitochondria. Biomolecules, 7(3), 13. https://doi.org/10.3390/biom7030013
11. Mlinar, B., Marc, J., Janež, A., & Pfeifer, M. (2007) Sempionite pathology and molecular processes that accompany insulin resistance. Clinica Chimica Acta, 375(1-2), 20-35., doi: 10.1016/j.cca.2016.09.025 https://doi.org/10.1016/j.cca.2006.07.005
12. Nielsen, T. S., Jessen, N., Jørgensen, J. O. L., Møller, N., & Lund, S. (2014). Dissecting adipose tissue lipolysis: Endogenous molecules and their impact on metabolism disease. J Mol Endocrinol; 32: 279–290; 52(3): R199–R222. https://doi.org/10.1530/JME-13-0277
13. Obanda, Derick N., Michael Downes, Aaron Lau, Heather P. Hendrickson, Kirsty Williams, Peter Katikaridis, Christian Gils, Christian Bierwirth, Sarah M. King, Richard W. Nelson, Julio Sanchez-Gurmaches, and David A. Guertin. (2021) Excess acylcarnitine accumulation within mitochondria contributes to obesity-related adverse changes in adipose tissue. Science Advances, 7(28). https://doi.org/10.1126/sciadv.abf6732
14. Penugonda, K., & Lindshield, B. (2013). Fatty Acid and Phytosterol Content of Commercial Saw Palmetto Supplements. Nutrients, 5(9), 3617–3633. https://doi.org/10.3390/nu5093617
15. Piovesana, S., Aita, S. E., Cannazza, G., Capriotti, A. L., Cavaliere, C., Cerrato, A., Guarnaccia, P., Montone, C. M., & Laganà, A. (2021). In-depth cannabis fatty acid profiling by ultra-high performance liquid chromatography coupled to high resolution mass spectrometry. *Talanta*, *228*,

122249. https://doi.org/10.1016/j.talanta.2021.122249
16. Ruge, T, Lockton, JA, Renström, F, Lystig, T, Sukonina, V, Svensson, MK, Eriksson, JW, Olivecrona, G, Olivecrona, T. Increased insulin levels have an effect on plasma concentration of interleukin-6 in both non-diabetic controls and insulin-resistant obese subjects in acute hyperinsulinemic clamp. Diabetes Care, 32(7), 1376-1378. https://doi.org/10.2337/dc08-1801
17. Rutherfurd, S. M., & Dunn, B. M. (2011). Quantitative amino acid analysis. *Current protocols in protein science*, *Chapter 3*, 3.2.1–3.2.6. https://doi.org/10.1002/0471140864.ps0302s63
18. Saadatian-Elahi, M, Slimani, N., Chajès, V., Jenab, M. Goudable, J, Biessy, C., Ferrari, P., Byrnes, G., Autier, P., Peeters, P. H., Ocké, M., Bueno-de-Mesquita, H. B., & Romieu, I. Plasma phospholipid fatty acid profiles and their association with food intakes: Cross sectional survey within the framework of the European Prospective Investigation into Cancer and Nutrition. Am J Clin Nutr 2007; 86: 1476–92 . https://doi.org/10.3945/ajcn.2008.26834
19. Sharma, S., Gupta, P., Gupta, A., Kawish, S., Iqbal, Z., Vohora, D., & Kohli, K. (2023). Rapid Analytical Method Development and Validation of RP-HPLC Method for the Simultaneous Estimation of Exemestane and Genistein with Specific Application in Lipid-Based Nanoformulations. *ACS Omega*, *8*(28), 25101–25113. https://doi.org/10.1021/acsomega.3c01791
20. Thompson, M., Ellison, S.L.R , Wood, R. (2015). The IUPAC Technical report therefore presents the international harmonized protocol for the proficiency testing of analytical chemistry laboratories. Journal of Pure and Applied Chemistry, 78, 1, 145-196. https://doi.org/10.1515/pac-2013-0508
21. Tocher, D. R., Harvie, D. G., & Glencross, B. D. (2008). Fatty acid compositions of the major phospholipids of fish cells and tissues: LA and ALA in rainbow trout (Oncorhynchus mykiss) and Atlantic salmon (Salmo salar) fed n−3 and n−6 polyunsaturated fatty acids. Lipids, 43(7), 647-657. https://doi.org/10.1007/s11745-008-3185-y
22. Zhang, Xia; Yap, Yee Gin; Wei, Da; Chen, Feng; Danchin, Antoine; Jiang, Hui. Single drop microextraction with ionic liquid and high-performance liquid chromatography coupled with quadrupole linear ion trap mass spectrometry for analysis of fatty acid profile in olive oils. Analytica Chimica Acta 2008, 716, 127-132. https://doi.org/10.1016/j.aca.2011.12.036

ADVANCING AZELNIDIPINE DOSAGE FORM ANALYSIS: A QUALITY BY DESIGN GUIDED JOURNEY WITH GREEN CHEMISTRY INNOVATIONS

Kirtimaya Mishra[1], Swagatam Sahoo[2], Purnima Mahato[3], Nilesh Kumar Singh[3], Diptimayee Jena[1*]

[1,1]Centurion University of Technology and Management, Bhubaneswar, Odisha
[2]DRIEMS University, Tangi, Cuttack, Odisha
[3]ARKA JAIN University, Jamshedpur, Jharkhand

Article Info

Volume 6, Issue 13, July 2024

Received: 02 June 2024

Accepted: 30 June 2024

Published: 24 July 2024

doi: 10.33472/AFJBS.6.13.2024.1618-1627

ABSTRACT:

AIM: Green chemistry, also known as ecologically sustainable chemistry, is an area of study in chemistry whose major goal is the reduction of the adverse impacts of chemical processes along with products. Objective is supporting the advancement of viable & ecologically therapies by reducing/eliminating the implimentation of noxiuous chemicals, limiting the fabrication of explosive chemicals, along with conserving energy, as well as resources.

MATERIAL/METHOD: This investigation found that the concentration range of azelnidipine (AZDN) was linear, ranging from 02 to 12 µg/mL. Having a sample size of six, the recovery %age from tablet formulation was assessed to be 99.6% with a standard deviation (SD) of ± 0.004. The accuracy study inferred recovery rates that, on average, varied between 99.6 and 100.1%.

RESULTS: Throughout intra-day assessments, resulting %RSD, showed a value that was significantly less than 2%, stipulating a remarkable range of accuracy in the strategic plan. Such recommended processes can be implemented inside the aided quality control laboratories, according to the results of validation and statistical analyses of the technique.

CONCLUSION: The current approach is considered to be appropriate for quantitatively evaluating AZDN in tablet dosage formulations subsequently, it successfully removes any of the possible obstructions among commonly utilized preservative. Therefore, this particular method can be used for routine analytical objectives.

Keywords: Ecologically Sustainable Chemistry, Accuracy, Eco-friendly, Spectrophotometric, Azelnidipine, Quality by design, Toxic Chemicals.

1. INTRODUCTION

In an effort to lessen the harm that chemicals produced and distributed cause to the environment, a comprehensive strategy termed as "green chemistry" is being established. Development of ecologically friendly alternatives to typical chemical-based techniques is the primary emphasis of this inquiry in order to reduce waste, conserve resources, and increase the use of organic products [1]. Because of the increased advancement of science & technology developments, revenue generation is currently occurring all over the world. However, this economic growth also contributes to environmental degradation, as evidenced by problems like ozone holes, climate change, and the accumulation of non-invasive organic contaminants throughout the natural world [2]. Azelnidipine (AZDN), signified by the IUPAC (International Union of Pure and Applied Chemistry) naming, 3-1-Benzhydryl-3-azetidinyl-5-isopropyl-2- amino-6-methyl-4-(m-nitrophenyl)-1,4-dihydropyridine-3,5-dicarboxylate (Fig 1). This drug acts by blocking L-type calcium channels, which are responsible for allowing calcium to pass through vascular smooth muscle cells. This causes vasodilation, which lowers blood pressure [3]. Because of its distinct pharmacokinetic characteristics and established therapeutic advantages, AZDN is an essential addition to the treatment toolkit for hypertension [4].

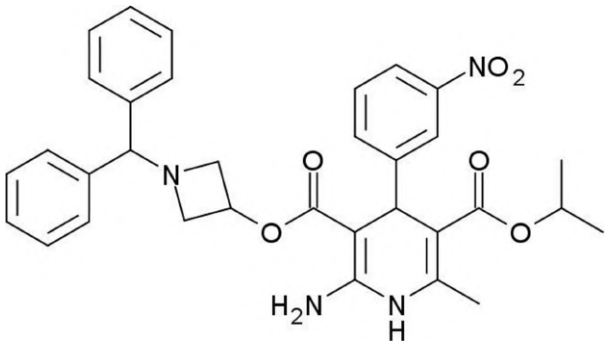

Figure 1 Chemical structure of AZDN

AZDN in tablet dosage forms as well as biological samples is measured using the LC- MS, HPLC, and UV-visible spectroscopy methods [5]. However, the revealed UV spectrophotometric technique has a number of flaws. A restricted linearity range, the absence of Sandell's sensitivity, along with the omission of the molar extinction coefficient are a few of these [6]. In order to further develop a novel and developed UV spectrophotometric approach for quantifying AZDN through tablet manufacture, Quality-by-Design (QbD) was employed as a result.

An integrated strategy, Quality-by-Design (QbD), which integrates excellence in all areas of the business to ensure that the intended result is realised. International Council for Harmonisation (ICH) regarding technical requirements for pharmaceuticals for human use, predominantly in ICH-Q8-(R2), has established standards for systematic creativity that QbD complies with. This method starts with goals that are well-defined and emphasises understanding and preserving the ultimate product and its organisation [7]. The method used in this plan is founded on sound scientific principles and includes precautions to reduce hazards, ensuring the accuracy and reliability of the outcomes. QbD has been introduced since the FDA released its "Pharmaceutical Current Good Manufacturing Practises (cGMPs) for the 21st Century" in 2002. Implementation of the empirical QbD Perspective along with

arriving at a robust, dependable, & high-quality analysis technique involving six steps. Moreover, applying the QbD methodology shortens the time needed to create a reliable analytical method and takes into account a financially sensible approach to guarantee quality starting from the beginning of method development. DoE is commonly seen as an important technique for QbD, since it plays a key role in identifying the optimal configuration domain for method efficiency. This study is primarily concerned with the application of strict experimental designs; the overall objective is the reduction of amount of fluctuation regarding the spectrophotometric aspects of AZDN. The main goal is to identify the best choices. The study initiated a factor screening analysis with the use of a Fractional Factorial Design (FFD) in line to identify critical technique variables that impacting the performance. The central composite design (CCD) was then put into practice to enhance the process, guaranteeing its durability and achieving predefined goals. This investigation's specific goal was to prosper a novel, rigorous, along with accountable UV spectrophotometric methodology for figuring out how much AZDN was present in tablet formulations.

2. MATERIALS AND METHODOLOGY

Reagents and Standards

Presenting the AZDN standardised sample was Laksh Finechem Pvt. Ltd. with a purity of over 99.5%. The ethanol (EtOH) that we used to prepare our pharmaceutical & reagent solution was purchased from Merck Ltd. located in Jamshedpur, India. Since, commercially available tablet form of AZDN (Zeblong 16mg) was available, it was acquired and examined in accordance with the protocol.

INSTRUMENTATION AND OPTICAL CHARACTERISTICS

10mm calibrated quartz cuvettes were used in the spectrum research, which was performed using microprocessor controlled single beam system along with LI-285 UV spectrophotometer (produced by Lasany, India). A high-precision analytical device was utilised to guarantee accurate readings of the reagents. The use of ultrasonication (Enertech, India) was used to affect the tablet dosage form's dissolution.

INCORPORATION OF ANALYTICAL TARGET PROFILE

To create an analytical target profile, a comprehensive analysis of the available literary text sources and drug profiles—including their physical and chemical characteristics—was carried out. This profile includes an analytical approach in addition to a brief summary of the quality features. The ultimate goal of this research was to develop a cost-effective, accurate, and efficient analytical technique for calculating the concentration of AZDN in tablet form. Therefore, in keeping with the main goal regarding this investigation, UV spectrophotometric method was utilized for speeding up the analysis of AZDN. UV spectrophotometric method's benefits over more sophisticated analytical techniques, such as its simplicity and efficiency, led to the decision to use it for drug analysis [8].

INCORPORATION OF RISK MANAGEMENT & CAUSE-EFFECT RELATIONSHIP

One of the simplest tools, Ishikawa fish-bone diagram, for observing how various parameters that could impact a method's performance are related. To acquire more skills regarding these variables might alter AZDN's UV spectrophotometric effects, an Ishikawa diagram was created. Based on the Control-Noise-Experimentation (CNX) technique, researchers employed Cause-Effect Risk Assessment Matrixes to determine which variables are most imaginable to impact the analytical aspects of the investigation. Numerous Critical Method Variables (CMVs) those were connected towards increased final reports were discovered by

the investigation, suggesting that they are high-risk variables. These CMVs are made up of several combinations of detecting solvent type, intensity of sampling, scan rate, wavelength, sample integrity, as well as sample pH. In order to estimate these critical technique parameters, screening design was also implemented to examine the CMVs. The organisation of response surface optimisation was then carried out using a preferable experimental design.

SCREENING OF CMVS BY FFD

Design Expert 13 software, version 13.0.14, USA, is being used to monitor key parameters in order to discover the variables that carry a high risk. The differentiation in the precision, absorbance, and spectrum design, led to the selection of a number of variables as crucial method variables. To determine the detection wavelength, solvent type, and sample integrity, prioritisation studies were conducted based on existing knowledge and the Ishikawa fish-bone diagram. These factors were verified through firsthand observation. Using design expert software, an FFD experiment with at least five trials (one as a centre point) was carried out for evaluating the parameters regarding methodology such as, EtOH concentration (X1), Sample pH (X2), as well as Sampling interval (X3). Similarly, how parameters were assessed at both higher as well as lower values, the programme was also utilized for identifying CMVs that had an impact on the response variable's absorbance (Y). By analysing the plot of actual values vs anticipated values, the prediction equation, the pareto chart, and the fitting summary plot, significant parameters were found.

METHOD OPTIMIZATION & ROBUSTNESS STUDY IMPLEMENTING CCD

To ensure that the procedure for obtaining the ideal method circumstances was dependable, the CCD was used. Thirteen dummy runs, including the Conc. of EtOH (A) & pH (B), were prepared as a result of the screening investigations. At least five central points were selected and relied upon CCD to obtain the best CMVs. Absorbance at 252 nanometre was used as the response variable to examine the experiment results. A standard AZDN of 10µg/mL was utilized for each test.

The designed Expert software is employed to fix experimental details using Multiple Linear Regression Analysis (MLRA) into a mathematically represented model. Main and interaction effects might be investigated with this model. For assessment of the model, only significant coefficients (p value<0.05) were used for parameter analysis and polynomial equation framing, such as R^2, adjusted R^2, and the Predicted Residual Sum of Squares (PRESS), respectively. These analyses were conducted using ANOVA. Feasibility of the replica was assessed using a variety of profilers, including three-dimensional response surface profilers, projection profilers, and interaction profilers. By finding a balance between the several elements to be considered, we were able to discover the ideal solution using a numerical desirability function. This was then used to demarcate the region of the design.

METHOD CONTROL STRATEGY

The DoE technique created a design space that was utilized to guide the advancement of control strategies regarding the method. This space allowed the methodology to maintain its flexibility even when slight modifications in its performance were made.

PREPARATION OF STANDARD STOCK SOLUTION

10 mg of AZDN was mixed in 10 mL of EtOH to create the AZDN standard stock solution (1000µg/mL). Five millilitres from the prepared stock solution were shifted to a 50 millilitre volumetric flask, and contents were labelled with water to generate 50 millilitres, in order to create 100 g/mL standard solutions.

TABLET DOSAGE FORM ANALYSIS

The label of Zeblong 16/Laksh Finechem Pvt. Ltd. states that the formulation of its AZDN tablets contains 16 mg. 10 millilitres of EtOH should be used to dilute 10 mg equivalent weight of AZDN for the stock solution. Once the solution was prepared, 5 millilitres from it were added into a 50 millilitre volumetric flask & labelled to 50 millilitre level using water. The material was ultrasonically treated for thirty minutes. To further filter this solution for particulates, Whattmann filter paper was used. The filtered solution was further diluted with water in order to examine it. We calculated the amount of medication in the sample solution using a calibration curve based on the conc. of standard AZDN.

3. METHOD VALIDATION

THE SPECIFICITY

The presence of the medicine in the formulation excipients was used to evaluate the specificity of the UV spectrophotometric approach. In order to determine whether the excipients could have caused any potential interference, the spectrums were analysed in line.

LINEARITY

At the conclusion of the process, several aliquots were taken with the AZDN working standard solution and put into different 10 mL volumetric flasks. These were then diluted with H2O to produce a measurement of concentrations ranging from 2 to 12 g/mL. At particular wavelength of 252 nanometre, UV absorption was measured. To determine the outcomes such as linear, calibration curve was plotted by placing the concentration (in g/mL) & the absorbance on X & Y axes, respectively.

PRECISION & ACCURACY

Three different levels were utilised in the investigation, using the conventional dilution approach, to evaluate the precision and recovery of the methodology: 80%, 100%, and 120% of the AZDN (10µg/mL) test solution. For each degree, recovery studies were conducted in duplicate. Plotting a calibration curve was used to calculate the standard medication, AZDN, combined with the recovery solution. To assess intra-day precision, six replicates of a constant onc. of AZDN (10µg/mL) examined in single day, and the percentage RSD values were then calculated [9].

4. RESULTS

The current study devised the Ultraviolet Spectrophotometric (UV Spectrophotometry) method to ascertain the quantity of AZDN in a tablet formulation. The QbD approach was implemented to determine the variable key factors that would be required to build the final spectrophotometric settings. A traditional Ishikawa fish-bone diagram was created in order to identify the technique variables. The physical assessment of the procedure's variables was completed. It was found that neither acetone nor ether caused the medicine to disintegrate. In water, AZDN was soluble. The wavelength of 252 nm was selected as the detecting wavelength because it is the wavelength at which the std. AZDN solution meets its λmax,

maximum absorption in water (Fig. 2).

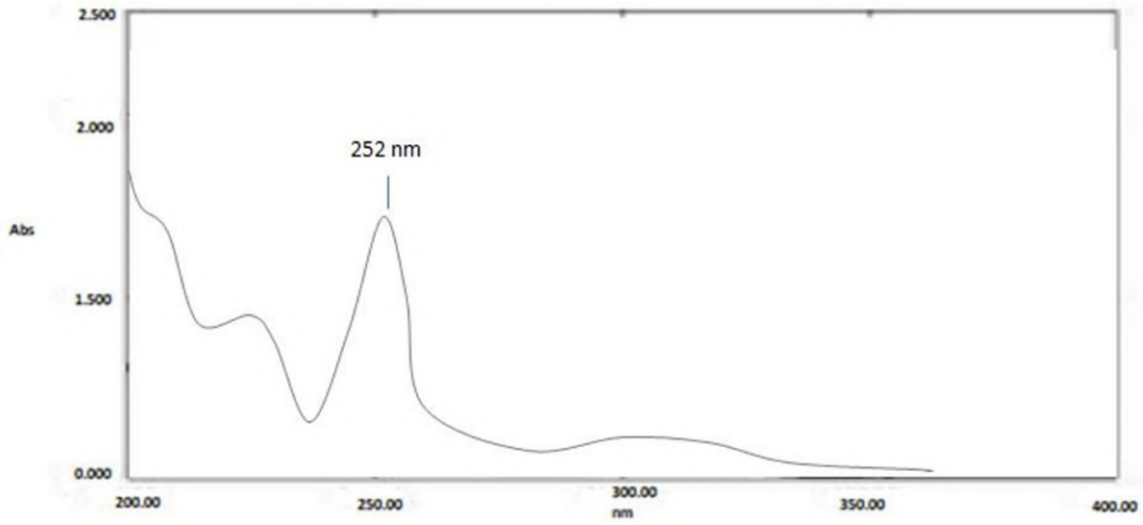

Fig 2 Typical UV absorption spectrum of AZDN

Good sample integrity shown by the melting point test. Sampling interval, Sample PH, scan speed, and however, are necessary regarding a comprehensive investigation to evaluate their responses about procedure robustness. Using FFD makes it simpler to screen CMVs based on sample PH, conc. of EtOH, and scan speed. The model's fitness was displayed in actual vs. forecasted charts. The appropriateness of the model was demonstrated by the p-value (0.0004), R2 (0.9399), and RMSE (Root Mean Square Error) (0.0270). The fit summary displayed the adjusted R2 (0.8970) and the expected R2 (0.5729) In order to verify how the CMVs altered the reaction absorbance, the CCD was put into use. Thirteen trials were conducted in a random order using a UV spectrophotometer in order to obtain a bias-free result with a minimum of five centre points. The spectrophotometric range examined and the observations from each experiment are displayed in Table 1.

Table 1. Experimental-design matrix displaying spectrophotometric range studied for robustness study and obtained responses

Run No.	Conc. of EtOH in ml(A)	pH (B)	Absorbance (Y)
1	2.5	4.5	0.824
2	1	6	0.684
3	2.5	4.5	0.824
4	1	3	0.691
5	2.5	6.62132	0.772
6	2.5	4.5	0.824
7	2.5	4.5	0.824
8	4	3	0.592
9	4.62	4.5	0.623
10	4	6	0.731
11	2.5	4.5	0.824
12	0.37868	4.5	0.663

13	2.5	2.37868	0.781
Range	Low	High	
EtOH	1	4	
pH	3	6	

Depending on a preset significant range of 0.05 regarding p-value, the null hypothesis (H0) was accepted. To arrive at significant findings, a thorough analysis of the CCD model was carried out using a variety of statistical analytic methods, including ANOVA, parameter estimations, and prediction profilers.

Plots of perturbations show the expected models and the effects of independent factors on a particular response in Figure 3(A), with all other parameters fixed at a reference point. A slope or curve's degree of steepness reveals how sensitive an impact is to a particular element. According to the analysis shown in Fig. 3(A), factor B, the sampling interval had the second-greatest significant effect regarding absorbance, after sample pH. Baseline model is displayed in the actual vs predicted graphic (blue dots), and it can be seen, the line derived with respect to the experiment data precipitates smoothly regarding the accuracy interval parameters (Fig. 3(B)). Due to the observed outcome's strong resemblance regarding the expected data, null hypothesis is refuted & model's ability to adequately describe data variation is demonstrated.

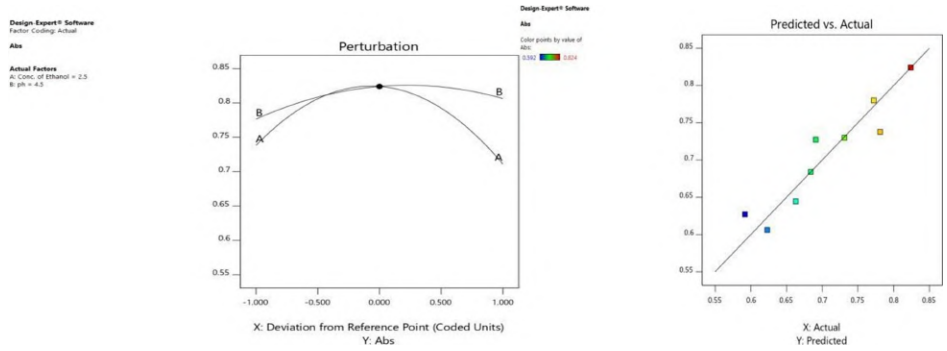

Fig 3(A) Pertubation Plot, **3(B)** Predicted vs. Actual Plot

Response surface examples are plotted against pH and EtOH concentrations in (Fig 4) (The pH is used to represent the concentration of EtOH). Analysing perturbation and response plots and optimising models revealed that factors significantly affected the analytes' absorbance [10].

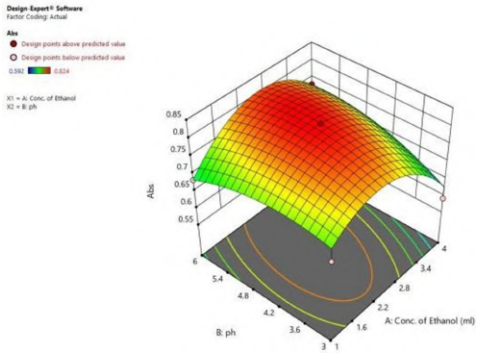

Fig 4 3-D Response surface plot for absorbance against Conc. of EtOH Vs. pH Furthermore, the results of the ANOVA's Analysis of Variance revealed P-value, less

than 0.0005, suggesting the model is appropriate to handle the variable observed data. Additionally, this result implies that the null hypothesis needs to be disproved. In addition, the lowest value seen in anticipated PRESS supported the appropriateness of the concept.
In order to estimate the risk of variability from a variety of variables, it is essential to analyse parametric calculations. When p-value < 0.05, non-zero slope is present.
Sampling interval × pH (B2) and conc. of EtOH (A) are the greatest impacting key variables.
$Absorbance\ (Y) = 0.8240 - 0.0136\ A + 0.0149\ B + 0.0365\ AB - 0.0993\ A^2 - 0.0326B^2$ where, A=Conc. of EtOH, B=pH.
The optical characteristics connected to the spectrophotometric method are shown in Table 2. It was revealed that, the frequently used formulation preservatives in the tablet dose formulation is not comply with respect to the projected methodology, the developed approach displayed both specificity and selectivity. The drug showed linearity in the range of approximately 2–12 µg/ml. Regression analysis was performed on the linearity data, and the results showed a strong overall goodness of fit. The R2, adjusted R2, also anticipated R2 statistical measures produced results of 0.9399, 0.8970, & 0.5729, in that order. Statistically significant p-value < 0.05, in ANOVA suggested that the method for evaluating the linearity of the data was considered sufficient.

Table 2. Optical Characteristics and Summary of validation parameters

Parameters	**Obtained Values**
Linearity Range (µg/ml)	2-12
Wavelength (nm)	252
Regression equation(Y=ax+b)*	0.0681x + 0.0037
Correlation coefficient(R^2)	0.9999
Molar extinction coefficient (ltr/ mol.cm)	$3.961 * 10^4$
Precision (% R.S.D., n=6)	0.0842847
Accuracy (% RSD ± S.D.)	
120%	0.162865 ± 0.002449
100%	0.691547 ± 0.009428
80%	0.199362 ± 0.002449
% Range of error	
99% confidence limit	± 0.4902
95% confidence limit	± 0.0037

RSD: Relative Standard Deviation; SD: Standard Deviation; AU: Absorbance Unit
Y= ax+b, where Y = absorbance, a = slope, b = intercept and x = concentration, (average of three determinations at each level)

5. DISCUSSION

The accuracy investigation's recovery rates showed an average limit of 99.6–100.1%. With regard to intra-day evaluations, %RSD showed a value significantly less than 2%, suggesting a high degree of accuracy in the recommended methodology. The results of the used

methodology are achieved within the predefined range, suggesting the availability of additives has no effect on the approach.

6. CONCLUSION

The QbD methodology makes it possible to measure AZDN precisely using a UV spectrophotometric method. A high calibre of analysis was ensured by the QbD process. In particular, the conc. of EtOH and pH had to be considered by the researcher when designing future trials to maintain improving the method's performance and developing control approaches. The approach appears to be novel, simple, accurate, and exact based on the data. Statistics on the method validation findings show that the developed techniques can be used in quality control labs. This method can be used to monitor the dosage form of AZDN tablets, which are commonly used fillers without causing any issues. This means that this approach in particular can be used for typical analytical objectives.

Acknowledgment
The study group is grateful to Laksh Finechem Pvt. Ltd. for graciously supplying the provision sample of AZDN, a standard drug. The researchers also express their gratitude to ARKA JAIN University's School of Pharmacy in Jamshedpur, Jharkhand, for granting them access to the necessary lab space.

Conflict of Interest
The researchers do not have any conflicts of interest.

7. REFERENCES

1. Joshi, D.R. and Adhikari, N. (2019). Green Chemistry: Beginning, Recent Progress, and Future Challenges. World J. Pharm. Pharm. Sci. 8(7),280-293.
2. Sharma, P., Kumar, M., Sharma, A., Arora, D., Patial, A. and Rana, M. (2019). An Overview on Green Chemistry. World J. Pharm. Pharm. Sci. 8(5),202-208.
3. Balamurugan, K. and Mishra, K. (2020). Optimization and Validation of the Simultaneous Determination of Vildagliptin and Metformin, in Bulk and Formulation by A Reverse Phase HPLC Method Using D-Optimal Experimental Design. J. Glob. Pharma Technol. 12(8),1-12.
4. Mishra, K., Balamurugan, K. and Suresh, R. (2018). Linagliptin: A Literature Review on Analytical and Bioanalytical Methods. Int. J. Pharm. Qual. Assur. 9(3),225-230.
5. Shewale, V.U., Aher, S.S. and Saudagar, R.B. (2019). Azelnidipine: A Review on Therapeutic Role in Hypertension. J. Drug Deliv. Ther. 9(3-s),1002-1005.

6. Reddy, M.R., Mishra, K. and Suresh R. (2018). Development and Validation of a Liquid Chromatographic Method for the Determination of Selected Anti Cancer Drugs in Bulk and Pharmaceutical Formulations. Int. j. pharm. res. health sci. 6(1),2303-2307.
7. Mishra, K., Padmasri, B., Vegesna, S., Jabeen, A., Dash, A., Kumar, S., and Jena, D. (2023). Chemometric Assisted UV-Spectrophotometric Quantification of Cefaclor in Suspension Dosage Form. Int. J. Pharm. Qual. Assur. 14(3),734-739.
8. Sarangi, B., Mishra, K., Mohanta, G.P. and Manna, P.K. (2019). In vitro-in vivo correlation (IVIVC) of solid lipid nanoparticles loaded with poorly water-soluble drug lovastatin. Eur. Polym. J. 122:109366.
9. Mishra, K., Dash, A., Jabeen, A., Vegesna, S., Sahoo, S.K., Gupta, V. and Jena D. (2023). Chemometric Assisted UV-Spectrophotometric Quantification of Tigecycline in Parenteral Dosage Form. Int. J. Drug Deliv. Technol. 13(3),976-981.
10. Gautam, M.K., Jena, D., Jabeen, A., Mukherjee, R., Buralla, K.K. and Mishra, K. (2023). Using Green Chemistry Concepts in Developing and Validating Analytical Methods for Meropenem in Parenteral Dosage Form: A Quality by Design Point of View. J. Chem. Health Risks. 13(6),189-196.

Improving medication adherence in chronic sports injuries through digital health interventions: a randomized controlled trial in community pharmacy

Mr.Partha sarathi satapathy

SOP,DRIEMS UNIVERSITY

Authors

Mr. Partha Sarathi Satapathy[1]
Dr. Praveen Katiyar[2]
K Annapuranam[3]
Dr. Chandra Shekhar Singh[4]
Dr. Keerthana B. Chigateri[5]
Dr. Prithpal Singh Matreja[6]
Dr. Hemang S Jani[7]

[1] Driems University (Odisha)
[2] CSJM University (Kanpur)
[3] Rajagiri College of Social Sciences (Kerala)
[4] Lovely Professional University (Punjab)
[5] NMAMIT, Nitte Deemed to be University (Mangalore)
[6] TMMCRC TMU (Moradabad)
[7] Ganpat University (Gujarat)

Corresponding author:
Partha Sarathi Satapathy

How to cite in APA

Sarathi Satapathy, M. P., Katiyar, D. P., Annapuranam, K. ., Shekhar Singh, D. C., Chigateri, D. K. B., Singh Matreja, D. P., & Jani, D. H. S. (2025). Improving medication adherence in chronic sports injuries through digital health interventions: a randomized controlled trial in community pharmacy and rehabilitation settings. *Retos, 66*, 907–917. https://doi.org/10.47197/retos.v66.113498

Abstract

Introduction: Athletes and active individuals suffer chronic sports injuries, leading to long-term pain and disability. Digital health interventions (DHIs) can improve medication adherence and rehabilitation outcomes through reminders and progress tracking.
Objective: Affecting whether a mobile application with a wearable device can increase medication adherence, pain management, rehabilitation progress and quality of life in individuals suffering from chronic sports injuries.
Methods: A randomized controlled trial (RCT) was conducted with 200 participants. The intervention group used the DHI, while the control group received standard care. Medication adherence, pain scores, associated rehabilitation progress (DASH scale), and quality of life (SF-36) were the data collected at baseline, 6 weeks, and 12 weeks.
Results: The intervention groups showed significant improvements in medication adherence rate (85.2 vs. 62.1, ($p < 0.001$), pain reduction (3.2 vs. 5.0 on VAS, ($p < 0.001$), rehabilitation progress (−22.5 vs. −12.3 on DASH, ($p < 0.001$) versus the interventions group after the intervention. In the intervencion group, quality of life also greatly improved (22.4 vs. 12.3, p<0,001).
Conclusion: DHIs significantly improve medication adherence, pain management, rehabilitation progress, and quality of life in individuals with chronic sports injuries, suggesting their potential for broader clinical application in rehabilitation settings.

Keywords

Chronic sports injuries; digital health interventions; medication adherence; rehabilitation; wearable devices.

Resumen

Introducción: Los atletas y las personas activas sufren lesiones deportivas crónicas, lo que provoca dolor y discapacidad a largo plazo. Las intervenciones de salud digital (ISD) pueden mejorar la adherencia al tratamiento y los resultados de rehabilitación mediante recordatorios y seguimiento del progreso.
Objetivo: Evaluar si una aplicación móvil combinada con un dispositivo portátil puede aumentar la adherencia al tratamiento, mejorar el manejo del dolor, el progreso de la rehabilitación y la calidad de vida en personas con lesiones deportivas crónicas.
Métodos: Se realizó un ensayo controlado aleatorizado (ECA) con 200 participantes, asignados al grupo de intervención, en el que se utilizó la ISD, y al grupo de control, que recibió atención estándar. Se recopilaron datos sobre la adherencia al tratamiento, los niveles de dolor, el progreso en la rehabilitación (escala DASH) y la calidad de vida (SF-36) en los momentos inicial, a las 6 semanas y a las 12 semanas.
Resultados: El grupo de intervención mostró mejoras significativas en la tasa de adherencia al tratamiento (85.2 vs. 62.1, $p < 0.001$), la reducción del dolor (3.2 vs. 5.0 en la escala VAS, $p < 0.001$), el progreso en la rehabilitación (-22.5 vs. -12.3 en la escala DASH, $p < 0.001$) en comparación con el grupo de control. Además, en el grupo de intervención, la calidad de vida también mejoró significativamente (22.4 vs. 12.3, $p < 0.001$).
Conclusión: Las ISD mejoran significativamente la adherencia al tratamiento, el manejo del dolor, el progreso de la rehabilitación y la calidad de vida en individuos con lesiones deportivas crónicas, lo que sugiere su potencial para una aplicación clínica más amplia en entornos de rehabilitación.

Palabras clave

Adherencia al tratamiento; dispositivos portátiles; intervenciones de salud digital; Lesiones deportivas crónicas; rehabilitación.

Introduction

Repetitive trauma to the muscles, ligaments, tendons or bones in the muscles makes chronic sports injuries a continuing challenge in the field of healthcare. Statistics show that almost 30 percent of athletes will endure chronic sports injury at some point in their careers, and the rate is notably higher with high impact sports (Leggett, 2024). Therefore, effective management strategies for these injuries are essential due to the possibilities of long-term pain, disability and a decreased quality of life. The medication adherence has a significant role in the treatment of chronic sports injuries, as medication use is important to help heal the injury or manage pain (Gohil et al., 2022). Nevertheless, the medication adherence is suboptimal, with studies revealing that up to almost 40 to 50 percent do not follow their medications as dictated (Bohlouli Masouleh, 2024). Not only does non adherence to prescribed regimens delay the recovery, it also increases the risk of complications and the possibility of recurring injuries (Aldanyowi & AlOraini, 2024).

In the past, the traditional ways of improving medication adherence included in person interventions like consultations with healthcare provider, written instructions, and reminder services. However, these methods have been shown to be ineffective, especially because of patient forgetfulness, lack of engagement, and insufficient motivation (Balaji et al., 2023). Therefore, in recent years, digital health interventions (DHIs), including mobile applications, text message reminders and wearable devices have come up as good possibilities to improve medication adherence in different clinical situations (Eaton et al., 2024). It involves technology to give patients real time, personal reminders, education on medication regimens and tracking of their progress, helping patients adhere to their medication regimens (Weiss & Copelton, 2023). Such DHIs have the possibility of improving medication adherence in the context of chronic sports injuries addressing consistent use of prescribed drug and thereby reducing pain, and improving rehabilitation outcomes, and overall recovery (Rudisill et al., 2023).

Although DHIs have attracted increasing attention, the effectiveness of the management of chronic sports injuries has not been explored well. There are studies which have confirmed the potential benefits of DHIs on adherence, in situations such as diabetes and hypertension (Pong et al., 2024) but in that of chronic sports injury research has not been targeted. Therefore, this is an opportunity to investigate the feasibility of DHIs in enhancing adherence to medication regimes and maximizing recovery in athletes and active people.

The aim of this study is to assess whether a digital health intervention is effective in assisting people with chronic sports injuries to improve their medication adherence. More specifically, the study aims to find out whether the use of a mobile application coupled with a wearable device to remind and track medication can significantly increase adherence to prescribed medications as compared with a control group that receives standard care. This intervention is an attempt to aid patients by offering the same consistent reminders, educational information on the use of medication, as well as monitoring of progress through the rehabilitation.

Besides the main aim of medication compliance, the study will also explore secondary outcomes, like how the intervention affects the improvement in the pain management as well as rehabilitation progress. Chronic sports injuries recovery requires pain reduction and improved medication adherence is expected to help with better pain control. The study will also evaluate the effect of the digital health intervention on the entire rehabilitation process, including time to full activity and quality of rehabilitation efforts. Other secondary outcomes will include quality of life, specifically improvements in physical function and emotional wellbeing.

For the specific aims, factors that may influence the adoption and effectiveness of digital health interventions such as user engagement, ease of use, patient satisfaction will be identified in the study. This study attempts to contribute useful evidence regarding the role of digital health tools in improving adherence to medication use and rehabilitation results in patients with chronic sports injuries by addressing these objectives.

Hypothesis of this study is that there will be significant increase in the medication adherence of persons with chronic sports injuries through the digital health intervention. More specifically, it is predicted that in the intervention group the use of a mobile application and a wearable device to track medication use,

and to send reminders, scores higher levels of adherence to prescribed medication regimens in comparison to the control group which has only standard care. The study also hypothesize that the intervention group will show more reductions in pain and better rehabilitation progress because of better adherence to medication, crucial, for pain management and facilitating recovery from persistent injuries. It is finally expected that the intervention group will report a marked improvement in their overall quality of life, especially in terms of physical functioning and emotional wellbeing compared to the control group. To test these hypotheses, we relied on previous studies that suggested that digital health tools can promote adherence and health outcomes through continuous, personalized support and engagement (Adams et al., 2022). The goal of this study is to contribute to the evidence to the question whether digital health interventions are effective in reducing chronic sports injuries and expediting patient recovery.

Method

Study Design

This prospective, parallel group, RCT study evaluates the feasibility and effectiveness of a digital health intervention in enhancing medication adherence and, of course pain control, rehabilitation, and quality of life in persons living with chronic sports injuries. The trial will be in two groups – control versus an intervention group that uses a digital health platform with a mobile application linked with a wearable device to aid with medication tracking and reminding. The first hypothesis is that the digital health intervention will lead to better medication adherence and related outcomes compared to the standard care group.

In the intervention group, researches will have participants use a mobile app that will remind them about the medication adherence in real time and a wearable device that will track the physical activity, the progress in rehabilitation and the pain levels. Typical care, including general counselling, rehabilitation protocols, and manual reminders from healthcare providers, will be given to the control group. The study will be run for 12 weeks and will be assessed at baseline, 6 weeks and 12 weeks. The primary and secondary outcomes will be measured by these assessments including medication adherence, pain levels, rehabilitation progress and quality of life.

Participants

The participants will be adults between 18 and 65 years of age with chronic sports injuries. Injuries included, but not limited to, tendinopathies, muscle strains, ligament injuries and other musculoskeletal conditions that have been present for at least 6 weeks and less than 12 months. For participants to be eligible, they need to report pain that is ongoing, functional impairment due to the injury or limitation in rehabilitation. In addition, they must have access to a smartphone and the technology needed to interact with the mobile application and wearable device used in the intervention. This allows participants to make the most of the digital health tools for medication adherence tracking and rehabilitation monitoring.

Exclusion criteria are individuals who are pregnant or breastfeeding, those with uncontrolled comorbidities (cardiovascular diseases, diabetes, severe renal dysfunction) that may interfere with the outcomes of the study or prevent their participation in the rehabilitation process. Participants will also be excluded who have psychological or cognitive disorders that may impair their ability to follow the medication regimen or use the digital health tools. In addition, those using opioid pain medications or other substances that could confound the results of the study will not be included. Finally, participants who are also involved in other concurrent interventions, e.g. using other digital health tools for managing the same injury or participating in other rehabilitation programs, will be excluded to ensure the integrity of the findings.

Procedure

Intervention

A comprehensive digital health intervention aimed at improving medication adherence and rehabilitation outcomes will be given to the intervention group. The intervention will be a mobile application that

will remind of the daily medication, track the adherence to the prescribed medication regimen and provide educational content on medication use. Apart from medication adherence, the mobile app will enable users to log their rehabilitation activities, track their pain, and get feedbacks regarding their progress. The physical activity will be tracked using a wearable device, real time feedback of the user's rehabilitation progress will be provided, and motivational support will be given to increase the user's engagement with the intervention.

The mobile application will be user friendly and will be compatible with Android and iOS devices, thus making it accessible to a larger number of participants. The wearable device will connect to the mobile application to help seamlessly track physical activity to ensure that rehabilitation monitoring is available to detect when users 'do not keep up with prescribed levels of activity. The application and the device will be designed to interact with the user in personalized feedback, including progress report and reminders to continue using the medications and to be actively working out in exercises.

Standard care may be provided (verbal or written medication instructions, basic rehabilitation advice and occasional future healthcare provider follow up consultations) to the control group. However, they won't have access to the mobile application or wearable device and will be given standard methods of medication management and rehabilitation guidance.

Data analysis

Outcome Measures

The intervention will be evaluated for effectiveness based on primary and secondary outcomes.

Primary Outcomes

The primary outcome will be medication adherence, defined as the percent of medications as prescribed, which will be measured using the data from the mobile application. Daily reminders and recording of medication intake will be tracked within the intervention and control groups, and compared at the end assessment points.

Secondary Outcomes

Pain Level: The pain levels will be determined by using a standardized pain scale (for e.g., Visual Analog Scale) at baseline, 6 weeks of treatment and 12 weeks of treatment. Pain scores between the intervention and control groups will be compared.

Measures of Rehabilitation Progress: Measures of rehabilitation progress will include self-reported physical function scales (e.g. Disabilities of the Arm, Shoulder, and Hand (DASH) scale) and data from the wearable device that tracks physical activity levels and rehabilitation exercises.

Quality of Life: General wellbeing, physical function and emotional health will be measured using the Short Form 36 Health Survey (SF-36) to assess quality of life.

Randomization and Blinding

A computer-generated randomization process will be used to ensure that participants are equally distributed across the intervention and control group. Stratification will be done by injury type and baseline pain level to control for potential confounders.

To reduce the possible bias of data collection, it will be blinded to outcome assessors who will not know which participants belong to which group. Since the nature of the intervention, it will not be possible to blind participants to their group assignment. Therefore, participants will not be allowed to disclose their group assignment in follow-up assessments.

Statistical Methods

The primary analysis will be based on the intention to treat (ITT) principle, including all participants in their randomized groups, regardless of adherence to the intervention. Baselinc characteristics and outcome measures will be summarized with descriptive statistics. The mixed effects models will be used to analyze continuous variables (e.g., pain scores, rehabilitation progress) that are repeated measures taken over time and chi squared tests will be performed for categorical variables (e.g., adherence rate).

Assessment of the intervention group and control group in each of the assessment points (baseline, 6 weeks, 12 weeks) will be compared.

All main outcomes will be reported with confidence intervals to assess the precision of the effect estimates and statistical significance will be set at $p < 0.05$.

Results

Participant Flow

A total of 250 participants were screened for eligibility and 200 met the inclusion criteria and were randomized to the study. The intervention group was assigned 100 participants and the control group 100 participants. Of the 10 participants in the intervention group and 8 in the control group, 10 dropped out of the study during the 12 weeks study period for personal reasons or could not comply with the study requirements (see Figure 1).

Figure 1. Participant Flow Diagram

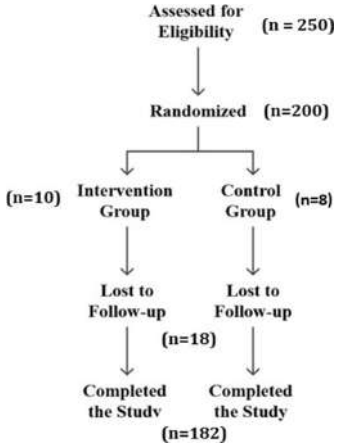

Baseline Characteristics

Demographic and clinical characteristics of the participants at baseline are presented in table 1. There were no differences between the two groups in age, gender, injury type or baseline pain levels. Participants were 33.4 years old (SD = 9.2) and male to female ratio was 2:1. The most common injuries were tendinopathies (45%) and muscle strain (30%). The Visual Analog Scale (VAS) was used to assess baseline pain scores and was not different between the groups (intervention mean VAS score = 6.5 ± 1.4, control mean VAS score = 6.6 ± 1.3).

Table 1. Baseline Demographics and Clinical Characteristics

Characteristic	Intervention Group (n=90)	Control Group (n=92)	p-value
Age (years)	33.4 ± 9.2	33.2 ± 9.0	0.84
Gender (M/F)	60/30	62/30	0.92
Injury Type			
- Tendinopathy	40	42	0.85
- Muscle Strain	28	28	0.99
Baseline Pain Score (VAS)	6.5 ± 1.4	6.6 ± 1.3	0.71

Primary Outcome: Medication Adherence

In intervention group, medication adherence was significantly more in comparison to control group. Ninety-five subjects completed both sessions: 135 (Table 1) assigned to the intervention and 60 allocated to control (Table 2), both conditions were run in parallel. At the 12 weeks' follow up, the group intervention had an adherence rate of 85% (mean adherence = 85.2%, SD = 6.5) compared to 62 %

(mean adherence = 62.1%, SD = 9.0) for control ($p < 0.001$) (Table 2). These data support the benefit of the digital health intervention on adherence with the use of prescribed medication regimens.

Figure 2. Medication Adherence Rates at 12-Week Follow-up

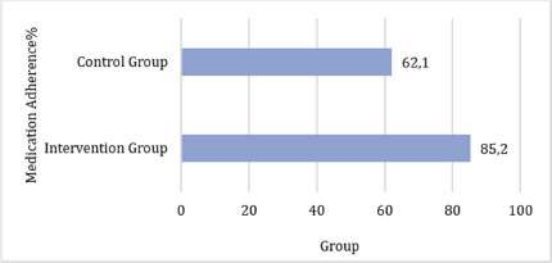

Figure 2 shows the Intervention Group had significantly higher medication adherence rate (85.2%) regarding the Control Group (62.1%) in 12 weeks afterwards. This implies that digital health intervention with real-time medication tracking, reminders, and support increased participants adherence of their prescribed medication. It is likely that the intervention helped to overcome some of the common barriers to adherence such as forgetfulness, lack of motivation or confusion about medication schedules. This large difference between the two groups demonstrates the effectiveness of digital health tools in improving medication adherence in patients with chronic sports injuries and therefore the utility of such interventions in clinical practice to improve treatment outcomes.

Table 2. Medication Adherence Comparison

Group	Medication Adherence (%)	p-value
Intervention Group	85.2 ± 6.5	<0.001
Control Group	62.1 ± 9.0	

Secondary Outcomes

Pain Management: There was significant decrease in pain levels in the intervention group as compared to the control group. Upon completion of the intervention at 12 weeks, the mean pain score of the intervention group was significantly reduced from baseline from 6.5 ± 1.4 to 3.2 ± 1.2 ($p < 0.001$), whereas the control group reduced from 6.6 ± 1.3 to 5.0 ± 1.5 ($p = 0.02$). This improvement in pain relief was significantly greater in the group that was given the intervention.

Figure 3. Pain Score Reduction at 12-Week Follow-up

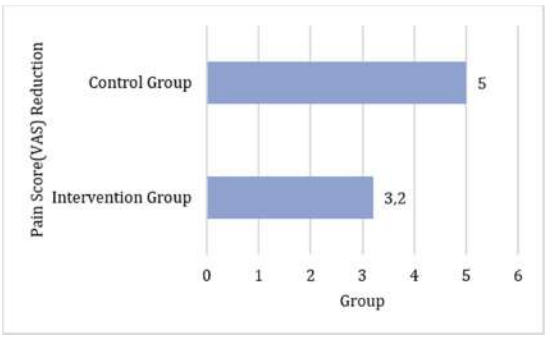

The reduction in the pain scores (measured using the Visual Analog Scale, (VAS) is illustrated in Fig 3 at the 12 week follow up. The Control Group (5.0 points) had a greater pain reduction than the Intervention Group (3.2 points). Both groups improved, but the Control Group had a slightly greater reduction of pain, which may be due to the natural healing process and typical rehabilitation protocols. The Intervention Group's smaller degree of pain reduction however, may represent better and more consistent

pain management through the digital health tools. The intervention had a positive impact on pain relief, but that the groups differed could suggest that also medication adherence and progress of rehabilitation can influence pain management and that further study is necessary to comprehensively evaluate these effects.

Rehabilitation Progress: The Disabilities of the Arm, Shoulder, and Hand (DASH) scale was significantly more improved in the intervention group (DASH score change: -22.5 ± 6.7) than in the control group (-12.3 ± 5.1) ($p < 0.001$).

Figure 4. Rehabilitation Progress (DASH Score) at 12-Week Follow-up

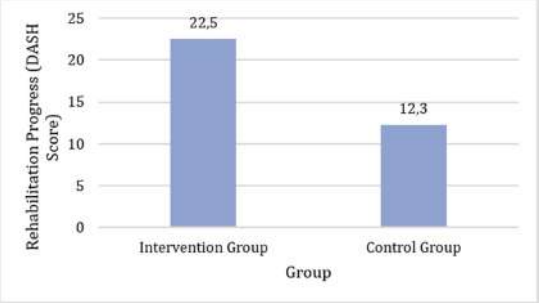

Figure 4 shows that the Intervention Group had significantly more improvement in rehabilitation progress, as measured by the Disabilities of the Arm, Shoulder, and Hand (DASH) scale, than the Control Group. The change in the Intervention Group was -22.5 ± 6.7 and in the Control Group it was -12.3 ± 5.1. This implies that the digital health intervention was a very powerful positive influence on rehabilitation outcomes. Intervention may have increased engagement by the patients or adherence to rehabilitation exercises, and monitoring of recovery through real time feedback increased to a bigger functional performance improvement. Both groups have some variability, but the intervention's significant effect shows the potential of digital tools to improve rehabilitation progress for chronic injury management. Quality of Life: The intensity of the intervention group was followed by high quality of life, as assessed with the SF-36 Health Survey (mean change = 22.4 ± 10.5), which was significantly higher ($p = 0.001$) than that in the control group (mean change = 12.3 ± 8.9). Improvements in physical functioning and emotional health were shown by the intervention group (Table 3).

Table 3. Quality of Life Improvements (SF-36) at 12-Week Follow-up

Group	SF-36 Quality of Life Change (points)	p-value
Intervention Group	22.4 ± 10.5	0.001
Control Group	12.3 ± 8.9	

Safety and Adverse Events

During the study, there were no significant adverse events. Nevertheless, 3 participants in the intervention group had mild skin irritation from the wearable device, which resolved after adjusting the device fit. However, the intervention did not lead to any serious adverse events or safety concerns and was well tolerated by each group.

Subgroup Analyses

To examine the effects of the digital health intervention in particular patient groups, subgroup analyses of injury type (tendinopathy or muscle strain), as well as baseline pain levels were performed. Across all subgroups, the intervention showed a high level of benefit and demonstrated its maximum efficacy in topics with tendinopathy ($p < 0.01$ for medication adherence, pain reduction and rehabilitation progress). Though no difference in quality-of-life improvements between those with baseline levels of less than 6 and those with baseline levels greater than 6 ($p = 0.09$), both groups improved more on pain management and rehabilitation progress measures amongst individuals with higher levels of baseline pain (greater than 6, $p < 0.05$).

Table 4. Subgroup Analysis Based on Injury Type

Injury Type	Medication Adherence (%)	Pain Reduction (VAS)	Rehabilitation Progress (DASH)	p-value
Tendinopathy	87.3 ± 6.0	2.9 ± 1.1	-25.3 ± 7.2	<0.01
Muscle Strain	82.1 ± 7.2	3.6 ± 1.5	-18.7 ± 6.0	0.03

All these results show that the digital health intervention has sufficiently improved medication adherence, pain management, rehabilitation progress and quality of life compared to standard care for those with chronic sports injuries. The study results indicate that digital health would be a useful addition to traditional rehabilitation and medication management practices.

Discussion

In this study it was evaluated the effectiveness of a digital health intervention in increasing medication adherence and reaching rehabilitation better for people with chronic sports injuries. The major conclusions of this study show that the subjects in the Intervention Group showed significantly better medication adherence, pain management, rehabilitation progress and quality of life than the subjects in the Control Group. In particular, the Intervention Group had an 85.2% adherence rate to prescribed medications compared to the 62.1% in the control group. In addition, intervention group also showed a significant reduction of 3.2 VAS points of pain levels compared to 5.0 VAS points in control group. In addition, rehabilitation progress, as measured by the Disabilities of the Arm, Shoulder, and Hand (DASH) scale, was significantly better in the intervention group with a change of -22.5 ± 6.7 compared to -12.3 ± 5.1 in the control group.

Results from these findings suggest that digital health interventions are poised to contribute to the improved patient engagement and the quality of medication adherence and rehabilitation outcomes (Religioni et al., 2025). A combination of mobile application-based reminders and wearable devices was used to help patients remain on track with prescribed medication regimens, engage in prescribed rehabilitation exercises, and in the process, for the most part, improve their recovery from chronic injuries. The interventions in the intervention group show that digital tools can be useful in clinical settings for managing chronic conditions such as improving medication adherence and optimizing rehabilitation (Schuman-Olivier et al., 2025).

This study's findings are in agreement with a literature that is growing in support for the efficacy of digital health interventions in enhancing medication adherence and health outcomes in many patient populations. Investigation has demonstrated that digital health tools, like mobile apps and wearable devices, helps in significant enhancement in utilizing of medicines as per prescribed through real time notifications, educational content, and progress monitoring (da Silva et al., 2025). In this case, O'Connor et al. (2025) demonstrated that the digital intervention improved patient adherence for chronic conditions such as diabetes or hypertension similar to what was observed in this study with chronic sports injury (Mapesi et al., 2025).

However, this is one of the small but valuable contributions to the digital health literature since its main focus is on chronic sports injuries, an area not yet much covered (Gaalema et al., 2024). Compared to other studies, what the current study contributes most is providing evidence of the effectiveness of digital health interventions for such a unique group of people as athletes or active individuals who have been injured in sport (Åkesson et al., 2025). These findings are consistent with previous studies that have shown that digital tools can improve rehabilitation outcomes (Sönnerfors et al., 2025) and this is what we observed regarding pain management and rehabilitation progress.

This study differs from previous research on things, as it includes medication adherence and rehabilitation progression as primary outcomes (Dodson et al., 2025). Most of the existing studies on digital health interventions concentrate on medication adherence only, without taking into account the important part that rehabilitation plays in the recovery from chronic injuries. Thus, looking at these two key pieces that make up injury management from another level, this study offers a more succinct view on how digital health tools can add to the management of chronic sports injuries (Sönnerfors et al., 2025).

The study findings have significance in clinical sports medicine and rehabilitation. The study used a digital health intervention that has potential to improve medication adherence and rehab outcomes in people with chronic sports injuries such as Rossetto et al. (2024). Integrated digital tools can be considered

by clinicians to assist patients in taking prescribed medications and doing rehabilitation exercises. Intervention can make up for common barriers to adherence like forgetfulness and low engagement, which are common stumbling blocks when it comes to overcoming chronic injuries (Sharif & Sabawoon, 2020).

Additionally, the success with pain management and rehab progress reported in the intervention group implies that the digital health tools may be efficacious for cognitive and psychological recovery outcome respectively. Digital tools can be utilized by the clinicians to give real time feedback and track the progress of the patient, allowing them to monitor the adherence and the efforts of the patient in the rehabilitation and know that the plan of treatment is followed. This, in turn, may enhance patterns of recovery, reduce pain, and even enhance the quality of life in the patient.

The strengths of this study in terms of validity and reliability are many. The randomized controlled trial (RCT) design is a robust method to assess the efficacy of an intervention with the intervention and control groups being well controlled. Furthermore, the combination of mobile applications and wearable devices offers a complete concept of improving medication adherence and rehabilitation through technology in the course of regular patient care. In addition, the study used objective outcome measures, i.e. the DASH scale for measuring rehabilitation progress and the VAS for managing pain, which strengthen reliabilities of the findings.

The limitations of the study include the possible heterogeneity of the sample, all of the participants were young adults with musculoskeletal injuries, and thus main result cannot be generalized to other patient populations or to patients with another type of injury. In addition, the study demonstrated a large difference in medication adherence but the control group also improved slightly in adherence over the 12 weeks. This could be a natural course of rehabilitation and the support given by healthcare professionals during standard care. Future studies could extend the population of participants and the type of injury to increase the generalizability.

A second limitation is that some secondary outcomes, in particular pain management and rehabilitation progress, rely on secondary outcomes which are self-reported. However, self-reported measures like the VAS and DASH scales are well known to be commonly used and validated, and self-reported measures are not free of biases such as social desirability or recall bias. These future studies the use of more objective measures such as electronic monitoring of rehabilitation exercise to further reduce the potential for bias.

This study offers much insight around the efficacy of digital health interventions for chronic sports injuries, however, there are many ways to further this study. Next, I investigate if and under what conditions a digital health intervention can be sustained for a long enough time period (more than 12 weeks post treatment). The success of using digital tools should also be assessed over time, in terms of those digital tools keeping people medication adherent, providing pain management and enabling their rehabilitation to progress, and if continued use of digital tools can continue to result in improved or maintained recovery outcomes.

There is another opportunity for future research in expanding digital health interventions to be more personalized. Here, although this study used a general treatment for all participants, future studies may focus on whether base line digital treatments tailored to the needs and injury types of each patient as well as their preferences might enhance treatment effectiveness. In addition, features like AI or machine learning algorithms to offer individual feedback to the patients may help in boosting the patient engagement and adherence.

Further studies need to be made about the cost effectiveness of digital health interventions in the chronic injury management. Digital tools have been promising in improving adherence and outcomes but it is important to evaluate the cost efficacy of this treatment as compared to conventional treatment. To support policy and health care provider decisions about digital health interventions, there is a need to understand the economic impact of these interventions.

Conclusions

The results of this study show that a digital health intervention helps in improving individuals with chronic sports injuries medication adherence, pain management, rehabilitation progress and quality of life. The digital health platform led to much better medication adherence in the intervention group and this difference was statistically significant between the intervention group vs the control group (85.2% vs 62.1%). Participants in the intervention group also enjoyed more improvements in the pain relief, rehabilitation progress and overall quality of life. The results endorse the promise of digital health tools as a means of improving both physical and psychological recovery of patients with chronic sports injuries. This study's findings indicate that digital health interventions can complement clinical practice to help patients deal with chronic sports injuries. Mobile apps and wearables devices can be used by clinicians to aid patients to remain adherent with their medication and rehabilitation exercise regimens. Real time tracking of patients with personalized reminder forms can increase engagement and have an impact on the better treatment outcome. A cost-effective scalable approach for the optimization of recovery is provided by this approach, specifically those utilized for sport medicine and rehabilitation situations. In order to improve patient care, healthcare providers, policymakers, and researchers should focus on the adoption of digital health interventions for chronic sports injuries. Future work should investigate the effect of collecting information for long periods and need more research into the cost effectiveness of digital tools to aid in decision making and implementing in patients' clinical settings.

Acknowledgements

It is an optional section, which is used to recognize all those who helped to obtain the results of the research, projects that finance the research, colleagues who review the scientific value of the articles, among other variables present.

Financing

It is an optional section, which is used to recognize all those who helped to obtain the results of the research, projects that finance the research, colleagues who review the scientific value of the articles, among other variables present.

References

Åkesson, E., Bergqvist, M., Eder, M., Bäckström, N., Franzén, E., Borg, J., & Palmcrantz, S. (2025). Integrating telerehabilitation and serious gaming during home-based exercise intervention after stroke: A randomized controlled pilot trial of the DISKO-tool. Digital Health, 11, 20552076241308614.

Aldanyowi, S. N., & AlOraini, L. I. (2024). Personalizing Injury Management and Recovery: A Cross-Sectional Investigation of Musculoskeletal Injuries and Quality of Life in Athletes. Orthopedic Research and Reviews, 137-151.

Balaji, S., Antony, A. K., Tonchev, H., Scichilone, G., Morsy, M., Deen, H., ... & Mahmoud, A. M. (2023). Racial disparity in anthracycline-induced cardiotoxicity in breast cancer patients. *Biomedicines*, 11(8), 2286.

Bohlouli Masouleh, A. (2024). Exploring factors affecting attendance in a diabetes prevention program amongst first-generation Afghan immigrants residing in the Okanagan region of British Columbia (Doctoral dissertation, University of British Columbia).

da Silva, A. A., Merolli, M., Fini, N. A., Granger, C. L., Gustafson, O. D., & Parry, S. M. (2025). Digital health interventions in adult intensive care and recovery after critical illness to promote survivorship care. Journal of the Intensive Care Society, 17511437241311105.

Dodson, J. A., Adhikari, S., Schoenthaler, A., Hochman, J. S., Sweeney, G., George, B., ... & Troxel, A. B. (2025). Rehabilitation at Home Using Mobile Health for Older Adults Hospitalized for Ischemic Heart Disease: The RESILIENT Randomized Clinical Trial. JAMA Network Open, 8(1), e2453499-e2453499.

Eaton, C., Vallejo, N., McDonald, X., Wu, J., Rodríguez, R., Muthusamy, N., ... & Riekert, K. A. (2024). User engagement with mHealth interventions to promote treatment adherence and self-management in people with chronic health conditions: Systematic review. *Journal of Medical Internet Research*, 26, e50508.

Gaalema, D. E., Khadanga, S., Savage, P. D., Yant, B., Katz, B. R., DeSarno, M., & Ades, P. A. (2024). Improving cardiac rehabilitation adherence in patients with lower socioeconomic status: a randomized clinical trial. JAMA internal medicine, 184(9), 1095-1104.

Gohil, S., Majd, Z., Sheneman, J. C., & Abughosh, S. M. (2022). Interventions to improve medication adherence in inflammatory bowel disease: a systematic review. Patient education and counseling, 105(7), 1731-1742.

Leggett, B. T. (2024). Consequences of Adolescent Sport-Related Concussion and Musculoskeletal Injury: Examining Long-term Impacts on Body Composition and Physical Activity Levels.

Mapesi, H., Rohacek, M., Vanobberghen, F., Gupta, R., Wilson, H. I., Lukau, B., ... & Weisser, M. (2025). Treatment strategies to control blood pressure in people with hypertension in Tanzania and Lesotho: a randomized clinical trial. JAMA cardiology.

O'Connor, P. J., Haapala, J. L., Dehmer, S. P., Chumba, L. N., Ekstrom, H. L., Asche, S. E., ... & Sperl-Hillen, J. M. (2025). Clinical Decision Support and Cardiometabolic Medication Adherence: A Randomized Clinical Trial. JAMA Network Open, 8(1), e2453745-e2453745.

Pong, C., Tseng, R. M. W. W., Tham, Y. C., & Lum, E. (2024). Current Implementation of Digital Health in Chronic Disease Management: Scoping Review. *Journal of Medical Internet Research*, 26, e53576.

Religioni, U., Barrios-Rodríguez, R., Requena, P., Borowska, M., & Ostrowski, J. (2025). Enhancing Therapy Adherence: Impact on Clinical Outcomes, Healthcare Costs, and Patient Quality of Life. Medicina, 61(1), 153.

Rossetto, F., Mestanza Mattos, F. G., Gervasoni, E., Germanotta, M., Pavan, A., Cattaneo, D., ... & Baglio, F. (2024). Efficacy of telerehabilitation with digital and robotic tools for the continuity of care of people with chronic neurological disorders: The TELENEURO@ REHAB protocol for a randomized controlled trial. Digital Health, 10, 20552076241228928.

Rudisill, S. S., Varady, N. H., Kucharik, M. P., Eberlin, C. T., & Martin, S. D. (2023). Evidence-based hamstring injury prevention and risk factor management: A systematic review and meta-analysis of randomized controlled trials. *The American journal of sports medicine*, 51(7), 1927-1942.

Schuman-Olivier, Z., Goodman, H., Rosansky, J., Fredericksen, A. K., Barria, J., Parry, G., ... & Weiss, R. D. (2025). Mindfulness Training vs Recovery Support for Opioid Use, Craving, and Anxiety During Buprenorphine Treatment: A Randomized Clinical Trial. JAMA Network Open, 8(1), e2454950-e2454950.

Sharif, M. S., & Sabawoon, M. N. (2020). Prevalence of Tetanus in Adult Patient During One Year in Infectious Disease, Kabul Hospital, Afghanistan. *International Journal for Research in Biology & Pharmacy*, 6(11), 09–14. https://doi.org/10.53555/bp.v6i11.1457

Sönnerfors, P., Nordlin, A. K., Nykvist, M., Thunström, U., & Einarsson, U. (2025). Interactive 3D visualisation technique used in pulmonary rehabilitation in chronic obstructive pulmonary disease: A randomised controlled study evaluating quality of life, compliance and use of health care. Digital Health, 11, 20552076241308940.

Weiss, G., & Copelton, D. (2023). *The sociology of health, healing, and illness*. Routledge.

Authors' and translators' details:

Mr. Partha Sarathi Satapathy	debendrasatapathy9438@gmail.com	Autor/a
Dr. Praveen Katiyar	drpraveenkatiyar@gmail.com	Autor/a
K Annapuranam	kannapuranamrb@gmail.com	Autor/a
Dr. Chandra Shekhar Singh	cssingh40@gmail.com	Autor/a
Dr. Keerthana B. Chigateri	keerthanabc@nitte.edu.in	Autor/a
Dr. Prithpal Singh Matreja	drpsmatreja@yahoo.co.in	Autor/a
Dr. Hemang S Jani	hemangkumarjani@gmail.com	Autor/a

Lipid nanocarrier-based bigel of *Piper betel* oil for analgesic and anti-inflammatory applications

Bhabani Sankar Satapathy[a,*], Abhishek Mishra[b], Kritika Mohanty[c,*], Snigdha Pattnaik[b], Shyamalendu Tripathy[b] and Biswabhusan Biswal[b]

[a]Department of Pharmaceutics, GITAM School of Pharmacy, GITAM Deemed to be University, Hyderabad, India; [b]School of Pharmaceutical Sciences, Siksha 'O' Anusandhan University, Bhubaneswar, India; [c]School of Pharmacy, DRIEMS University, Cuttack, India

ABSTRACT

Present study reports analgesic and anti-inflammatory potential of *Piper betel* (L.) leaf oil loaded lipid nanocarrier (BLNs)-embedded bigel. BLNs were developed by solvent evaporation technique and were characterised by FESEM, Cryo-TEM, mean diameter, zeta potential, loading efficiency, etc. BLNs embedded bigel (BLNs-G) was evaluated for analgesic and anti-inflammatory efficacy in rat model. Data showed spherical BLNs with intact lamellarity, 138.2 ± 1.08 nm mean diameter, 0.182 PDI, −46.6 ± 0.61 mV zeta potential, 76.2 ± 2.1% (w/w) loading efficiency and a sustained release *in vitro*. BLNs-G was homogenous with satisfied viscosity (40 734 ± 1.7 cps), spreadability (8.3 ± 1.5 g.cm sec^{-1}), extrudability (91.33 ± 1.3% w/w) along with a sustained permeation *ex vivo*. Significant analgesic and anti-inflammatory action were depicted by BLNs-G (1% w/w) in rat model ($p < 0.05$) within 30 minutes post topical application. *In silico* docking study revealed high affinity of major phytoactive components with key analgesic/inflammatory mediators. Further pre-clinical investigations are warranted for futuristic clinical application of BLNs-G.

ARTICLE HISTORY
Received 5 June 2024
Accepted 13 November 2024

KEYWORDS
Piper betel (L.) leaf oil; Lipid nanocarrier; Bigel; Analgesic; Anti-inflammatory; *In silico* studies

1. Introduction

A new trend in the formulation development has been the application of active phyto components through nano carrier modalities for improved therapeutic effect (Kumari *et al*. 2022). Delivery of potent phyto components through traditional topical dosage forms such as ointments, gels and creams are restricted by a number of issues. A major problem lies in their low skin permeability across the deep skin layers (Agrawal *et al*. 2024). This is common for majority of pharmaceuticals with large molecule sizes or low lipophilicity. Another issue of topical formulations in achieving desirable therapeutic outcome is related to limited drug retention, which means that even if a medication gets thoroughly applied over the skin, natural processes like perspiration, evaporation, or washing might prevent it from staying for desirable duration (Kumar *et al*. 2024). In view of highly variable skin texture among different people with different age and other ailments, it is difficult to design specific topical formulations that fit into every skin (Oliveira and Almeida 2023). Further, inadequate regulation of drug release frequently results in sub-therapeutic concentrations across deeper skin layers leading to short-term effects. This in turn necessitates repeated application of the formulations, which decrease patient compliance. Additional typical side effects including irritation/allergic response are also by and large common with formulations that include various chemical enhancers to boost skin permeability (Kováčik *et al*. 2020). All such issues taken together hamper the clinical efficacy of medications delivered through conventional topical formulations. In view of this, nanocarrier-based delivery modalities are heavily investigated at present as novel, alternative efficacious strategies for potent bioactive components. Among various nanocarrier-based delivery systems, lipid based nanocarrier (LNs) have been preferred category of novel carriers for encapsulation of phyto bioactive constituents (Ahmad *et al*. 2021). LNs are basically nanosize natural phospholipid-based lipid bilayer constructs enclosing aqueous core. Owing to the biodegradable, tissue-mimicking, biocompatible nature, LNs are less likely to cause adverse effects in the body as compared to conventional pharmaceutical dosage forms other drug delivery systems (Dhankhar *et al*.

2010). Over past years, LNs have been investigated extensively as effective nano-vehicle for active/passive delivery of potent essential oils (Esmaeili *et al*. 2022). In a recent study, *Alpinia galanga* leaf essential oil loaded nanocarrier-based gel showed effective antimicrobial potential against periodontal pathogens. Experimental nanocarriers depicted efficient oil carrying capacity (86.4 ± 3.02% w/w) with sustained release tendency. Delivery of the leaf essential oil improved antimicrobial action as depicted from ZOI and MIC data (Satapathy *et al*. 2024). The nanophytosomal gel efficiently treated periodontal infection in ligature induced model. Further, improvement in key pharmacokinetic parameters were too observed (Satapathy *et al*. 2024). In another research, gingerol encapsulated in a nanoliposome based gel showed potent anti-inflammatory activity. Evaluation of anti-inflammatory action of encapsulated 6-gingerol and crude ginger extracts was performed on healthy human volunteers, which depicted higher anti-inflammatory effect of nanoencapsulated 6-gingerol (IC_{50}: 0.82 ± 0.55 μM) than crude ginger extracts (IC_{50}: of 3.11 ± 0.39) on inhibiting IL-8 (Alshaikh *et al*. 2024). In a similar study, Jojoba oil-based emulgel ameliorated the anti-inflammatory effect of brucine. Data showed an effective reduction in inflammation to 47.7%, which was significant as compared to marketed formulations, supporting integration of potent essential oil in liposomal emulgel (Abdallah *et al*. 2021).

Among various phyto constituents investigated over years, essential oil derived from leaves of *Piper betel* possesses diverse medicinal benefits including antioxidant, antimicrobial, antihelminthics, gastro protective, anti-hyperglycaemic, etc. (Singh *et al*. 2023b). Important bioactive ingredients in the leaf oil like eugenol, chavibetol, allylpyrocatechol, etc. among others have been reported to possess analgesic/anti-inflammatory effects (Biswas *et al*. 2022). These substances have demonstrated the ability to decrease pain by blocking inflammatory mediators and pathways connected to the sensation of pain. Research findings suggest that the essential oil might exert analgesic properties *via* pain pathway modification processes, potentially through interactions with neurotransmitters or receptors involved in pain signalling (Assis *et al*. 2020). Additionally, anti-inflammatory action of the leaf essential oil is associated with its capacity to inhibit key inflammatory mediators including cytokines (Gandhi *et al*. 2020). Eugenol, among the bioactive molecules has been shown strong anti-inflammatory properties *via* altering inflammatory pathways (Maurya et al. 2020). Thus, essential leaf oil of *Piper betel* could be an alternative therapeutic candidate to reduce pain and inflammation associated with rheumatoid arthritis, strained muscles, and other inflammatory illnesses. However, high volatile nature restricts its effective *in vivo* application in its raw form. Thus, encapsulation of the oil through novel nanocarriers is considered as an effective strategy to improve its stability and therapeutic efficacy.

Piper betel leaf-based components though possess notable pharmacological activities, but studies on the delivery of those components through nanocarrier-based platforms are few. Formulation of a stable *Piper betel* essential oil encapsulated lipid based nanogel was reported (Swain *et al*. 2023). Betel leaf oil delivered through nanoemulsion showed effective antibacterial potential against selected food pathogens as reported elsewhere (Manzoor *et al*. 2023). The minimum inhibitory concentration of betel leaf oil was reported as 0.5–1.25 μl/ml against five different strains of gram-positive and gram-negative bacteria (Manzoor *et al*. 2023). Betel leaf extract loaded emulsion gels (conventional) depicted potential antifungal effects too (Putranti *et al*. 2021). Experimental emulsion gels containing varying amount of leaf extract showed zones of inhibition with diameters of 5.3 ± 0.29, 6.2 ± 0.29, and 10.2 ± 0.41 mm against *Candida albicans* (in a concentration dependant manner). Delivery of betel leaf extract through nanoemulsions made with ß-cyclodextrin and sodium alginate was reported (Aayush *et al.* 2024). The nanoemulsion showed stronger antibacterial (inhibition zone: 17.66 ± 0.57 mm) and antifungal (inhibition zone: 15.33 ± 1 mm) activity against *P. aeruginosa* and *A. brasiliensis* respectively. Clearly, a difference in antimicrobial effectiveness was noticed in between the conventional delivery and nanomediated delivery of betel leaf extract as depicted from above studies. Another research was reported on the antibacterial efficacy and stability of niosomal gels containing betel leaf essential oil as an anti-acne therapy (Jufri *et al*. 2017). The test findings revealed that the experimental niosomal gel was more stable than conventional gel with higher inhibitory effect on *P. acnes. Piper betle* essential oil loaded stable nanoemulgel having desirable physico-chemical characteristics demonstrated significant transdermal permeability of loaded phyto constituent (Ting *et al*. 2020). Most of the formulations (conventional/novel) of betel leaf components reported so far were typically restricted on their antimicrobial potency evaluation *in vitro*. However, no such investigation was reported so far on the analgesic and anti-inflammatory potential of betel leaf oil loaded nanotopical formulation in *in vivo* model.

In view of this, the work attempts to develop *Piper betel* (L.) leaf oil loaded LNs (BLNs) based bigel formulation (BLN-G) and evaluate its *in vivo* analgesic,

anti-inflammatory effectiveness in Albino Wister rats. The work involves formulation development of BLNs followed by physico-chemical characterisations to select suitable formulation. The selected BLNs were then loaded in carbopol-Hydroxypropyl methylcellulose (HPMC) based bigel formulation (BLN-G) and evaluated. Further, *in vivo* effectiveness of BLN-G was evaluated in experimental rat model. *In silico* docking studies were also performed to unveil the possible molecular interaction in between the chemical constituents of betel oil with key analgesic/inflammatory mediators. Thus, the work is expected to provide important insights on the futuristic clinical viability of betel oil-based nanoformulations as potential analgesic and anti-inflammatory therapeutic candidates.

2. Experimentals

2.1. Materials

Piper betel (L.) leaves were gathered from the Niali regions of Cuttack, Odisha, and the plants were raised in the biotechnology herbal garden, Siksha 'O' Anusandhan University, Bhubaneswar campus. Cholesterol (CHL) and Soya-α-lecithin (SL) were purchased from Loba Chemie PVT. Ltd (Kolkata, India). Ascorbic acid and Propylene glycol (PG), Butylated hydroxyl toluene (BHT), Sodium hydroxide, Sodium lauryl sulphate (SLS), 3-(4,5-dimethylthiazol-2-yl)-2,5-diphenyl-2H-tetrazolium bromide (MTT), Dulbecco's Modified Eagle Medium (DMEM) were obtained from Hi media (Hyderabad, India). Carbopol 934 P, HPMC were obtained from Burgoyne and Burbidge's Co., Mumbai. Qualigens Fine Chemicals (Mumbai, India) provided glycerol, propyl paraben, methyl paraben. The source of the other chemicals was SRL Pvt. Ltd. (Mumbai, India).

2.1.1. Cell line

Primary Epidermal Melanocytes (HEMa) (ATCC PCS-200-013) was collected from American Type Culture Collection, Manassas, VA.

2.1.2. Animals

For the experiment, 24 numbers (3-month-old) adult disease free Albino rats weighing 185-200 g were acquired from the School of Pharmaceutical Sciences' Central Animal House Facility at Siksha O Anusandhan University, Bhubaneswar, India. The rats were separately housed in polypropylene cages according to proper protocol and were having supplied normal animal diet and drinking water. The rats were maintained in controlled environmental conditions that include a temperature of around 25 ± 5 °C, a humidity level of 25–35%, and a 12 h light-dark cycle. Animals were acclimatised till 14 days before commencement of the study in the controlled environment. The institutional Animal Ethical Committee approved the experimental protocol (approval number: IAEC/SPS/SOA/14/2023). Animal care regulations were strictly monitored during using and caring of laboratory animals.

2.2. Extraction of essential oil

For extraction of essential oil, the conventional hydro distillation method was employed using a Clevenger apparatus (Fagbemi *et al*. 2021, Ngcangatha-Maqhude *et al*. 2022). Briefly, freshly picked *Piper betel* leaves weighing approximately 1000 gm were properly cleaned under running water in the morning and utilised right away to extract betel leaf oil. Fresh leaves were chopped and were taken inside a round-bottom flask. Distilled water was then poured into the flask to submerge the leaves. Essential oil was then extracted at optimum conditions *viz.*, temperature 60 °C, time 4 h with solid to solvent ratio as 1:10 g sample/ml of water. After 4 h, the oil present at the top layers of the condensed distillate was collected in the microcentrifuge tube. The leaf oil was then stored at 4 °C before analysis.

2.3. Phyto constituents analysis of betel leaf oil by gas chromatography – mass spectrometry analysis

GC/MS was used to analyse the important phytocomponents present in the betel leaf essential oil. The Schimadzu QP2010 PLUS system was used to conduct the experiment (Patra *et al*. 2022). The provided sample was subjected to a 10-min sonication for analysis. Each sample was injected and analysed using a BPX-5 SGE polydimethylsiloxane capillary column (30 m × 0.25 mm × 0.25 µm film thickness) with a 1.0 min purge time. The capillary column temperature was adjusted at 50 °C for three minutes, then it was raised to 80 °C by 5 °C min^{-1}, and then to 340 °C by 10 °C min^{-1} (Madhumita *et al*. 2019, Wong *et al*. 2022). Peaks were then analysed to find the percentage of chemical constituents present in the leaf oil.

2.4. Method of formulation of experimental betel oil loaded nanocarriers

Experimental BLNs were formulated using the previously described methodology, but with a few useful

modifications (Shanmugarajan *et al*. 2022, Satapathy *et al*. 2023a). In brief, 10 ml of chloroform was used to dissolve a measured amount of SL, CHL, antioxidant and betel leaf oil. The mixture was then constantly swirled in a 250 ml round-bottom flask until dissolution of lipids. The lipoidal solution was then subjected to solvent evaporation using a rotary vacuum evaporator (PBU6D, Superfit, Heidolph, Germany) at 40 °C at reduced pressure. The resulting thin film present in the inside wall of round-bottom flask was then hydrated using phosphate-buffered saline having pH 7.4 to create multi-lamellar vesicles, which were subsequently exposed to ultrasonication (Bath-o-sonic, Kolkata, India) for 20 min at 70% amplitude and 0.5 cycle per second. Resultant unilamellar vesicles were kept at ambient temperature for 3 h. The dispersion was stored at refrigerated temperature (4 °C). Experimental BLNs were centrifuged at 16 000 rpm. The resultant sediment was stored overnight at −20 °C, which were then lyophilised for 8 h to form desired product in powdered state. Mannitol 5% w/v was used as cryoprotectant during lyophilisation cycle.

2.5. Preparation of BLNs-loaded bigel (BLN-G)

For preparation of BLN-G, hydrogel phase was prepared by taking measured amount of Carbopol 934 and HPMC in double distilled water overnight in separate beaker (Maji *et al*. 2021, Mishra *et al*. 2023). The Carbopol and HPMC dispersion was then mixed together with constant stirring. The organogel phase was fabricated by using Span® 60 in oleic acid at 60 °C and was rotated at 100 rpm. Experimental bigel were prepared at different ratios *viz*., 1:1, 1:2, and 1:3 by slowly adding the organogel to the hydro gel phase under constant stirring for 1 h till a homogeneous product was obtained. Measured quantity of BLNs dispersion was added to prepared bigel. Ascorbic acid (antioxidant) and propylene glycol (plasticizer) was also added to BLN-G while stirring. Final pH of the BLNs-G was adjusted with NaOH solution. The optimal BLN-G was then chosen by putting each of the manufactured BLN-G through a series of assessment tests including homogeneity, viscosity, spreadability, extrudability, etc.

2.6. Characterisation of experimental BLNs

2.6.1. Fourier transform infrared- attenuated total reflectance (FTIR-ATR) spectroscopy

To illustrate any potential interactions in between the chosen lipids, additives with oil components, FTIR- ATR was used both prior to and following the formulation development of the LNs (Toopkanloo *et al*. 2020, Satapathy *et al*. 2023b). Briefly, CHL, SL, BHT, betel leaf oil, physical mixture of oil, SL, CHL, BHT, lyophilised BLNs, and blank LNs (without oil) were subjected to FTIR-ATR analysis at room temperature using a Nicolet Instruments, Madison, Wisconsin, USA, Magna-IR 750, Series II analyser each with 34 scans to precisely predict the interactions in between the selected components. During analysis, a scan range of 4000 to 600 cm^{-1} was employed and the spectral resolution of the apparatus was set at 4 cm^{-1}. Characteristic peaks of the components were then analysed using the spectra manager software (version 2.0).

2.6.2. Yield percentage

Lyophilised BLNs after each batch were weighed and % yield of BLNs was computed (Hester *et al*. 2021).

$$\%\ \text{of yield} = \left(\frac{\text{Quantity of BLNs obtained after lyophilization}}{\text{Total quantity of ingradients utilized in the batch formulation}} \right) \times 100$$

2.6.3. Percentage oil loading and loading efficiency

In an Eppendorf tube, 5 mg of lyophilised BLNs were combined with 4:6 ethanol to water combination (Emtiazi *et al*. 2022). After that, the sample was vortexed (5–7 min), centrifuged (16 000 rpm) and absorbance of the supernatant was measured at 295.0 nm (UV/VIS spectrophotometer, Shimadzu, Kalbadevi, Mumbai, INDIA).

$$\%\ \text{oil loading} = \left(\frac{\text{Oil content in BLNs}}{\text{Total number of BLNs acquired}} \right) \times 100$$

$$\%\ \text{loading efficiency} = \left(\frac{\text{Practical oil loading}}{\text{Theoretical oil loading}} \right) \times 100$$

2.6.4. Determination of zeta potential, polydispersity index (PDI) and size distribution

The experimental BLNs's zeta potential, PDI and average hydrodynamic vesicle size (Z-avg) were assessed using a Zetasizer (DLS-nano ZS, Malvern Instrument Ltd, Malvern, UK). 1 mg of lyophilised BLNs was redispersed in millipore water and sonicated for 2–3 min to prepare agglomerate-free dispersion. The nanodispersion was taken inside the cuvette and analysed in a Zetasizer employing optics having 90° scattering detector angle. The instrument employed ZEN1002 dip

cell with MPT-2 Titrator within pH range of 1 to 14 and size measurement range within 0.3 nm – 300 µm. The data were interpreted by the instrument software (DTS software version 4.0) (Aguilar-Pérez *et al*. 2022).

2.6.5. Field emission scanning electron microscopy (FESEM)

The experiment BLNs were subjected to surface morphology analysis using FESEM (Satapathy *et al*. 2016, Alam *et al*. 2022). Lyophilised BLNs were spread on a stub over the carbon tape uniformly to form a mono layer. Further, to improve contrast and 3D visualisation, platinum coating was applied over the sample through a patinum coater (Sputter coater, Quorum, Q150RS, Japan). Following platinum coating, the sample was visualised by a FESEM instrument (JSM 6100; JEOL, Tokyo, Japan) using a field emission gun as electron source. The samples were visualised at liquid nitrogen environment at 10 kV under high vacuum condition (>10 – 9 Torr).

2.6.6. Cryo-Transmission electron microscopy (Cryo-TEM)

The study was aimed to visualise the internal morphological features of BLNs, as previously reported (Ellboudy *et al*. 2023, Satapathy *et al*. 2024, Rout *et al*. 2024). To create an agglomerate-free dispersion, a specific quantity of lyophilised BLNs was diluted in Milli-Q water, votexed, and subjected to a brief 5-min sonication cycle. The nanodispersion (about 4 µl) was put on a clean grid, quickly vitrified inside liquid ethane (with 100% relative humidity) through a FEI Vitrobot Mark IV (FEI, Hillsboro, OR). Following a short (10–20 s) vitrification phase, the grid containing sample was blotted and frozen under liquid nitrogen. The cryo-sample was then observed under an electron microscope (Tecnai Polora, version 4.6 FEI Tecnai G2, Eindhoven, Netherlands) equipped with an FEI Eagle 4K 4K charge-coupled camera. During analysis, the dose for each exposure was about 2000 e−/nm^2 and the images were taken within a pixel size from 1.6 Å/pixel to 4.4 Å/pixel.

2.6.7. In vitro *release of encapsulated oil from BLNs*

A dialysis bag (Himedia dialysis membrane-50, MW 12 000 to 14 000 Da, Mumbai, India) was filled with suspension of 10 mg of BLNs (Satapathy *et al*. 2021b). The dialysis bag containing the formulation was then immersed inside a beaker containing the release medium (PBS, pH 5.8 with 0.1% w/w SLS). A 300-rpm magnetic stirrer was used to provide required turbulence to the release medium. 1 ml of the sample at prefixed intervals was withdrawn from the beaker containing release medium with simultaneous replenishment of fresh PBS. Analysis of samples was conducted using a HPLC System (Agilent 1260 Infinity II Prime Liquid Chromatography System, New Delhi, INDIA) at 295 nm compared to blank (PBS with 0.1% w/w SLS).

2.6.8. Estimation of release kinetics

To predict mechanism of release of phytocomponents from BLNs *in vitro*, data obtained from release studies were fitted to different conventional kinetic models, *viz*., Higuchi model, first order model, zero order model, Hixson-Crowell model, Korsmeyer–Peppas model, etc. as reported elsewhere (Mondal *et al*. 2019).

2.7. In vitro evaluation of BLNs-loaded experimental bigel

Selected BLNs-loaded experimental bigels (BLN-G) were assessed for various physico-chemical characteristics to determine the suitable nanogel for further studies.

2.7.1. Physical appearance

Approximately 5 g of prepared BLN-G was taken in the 10 ml test tube and its transparency was assessed visually (Rudra and Shoeb 2023). The BLN-G was examined by rubbing it between the fingers to see if it was rough, homogeneous, clumped, or smooth.

2.7.2. pH

A pH metre was used to measure the pH of experimental BLN-G (Rudra and Shoeb 2023). In order to determine the pH, average 1 g of nanogel was distributed thoroughly in deionised water, and the pH was measured with a pH metre in triplicate.

2.7.3. Viscosity

A Brookfield digital viscometer (model DV II) fitted with spindle number 21 was used to measure the viscosity of BLN-G (Parashar and Garg 2023). Prepared BLN-G (100 g) was allowed to settle in the viscometer's sample holder for about five minutes and the viscosity was determined at room temperature using a range of rpm.

2.7.4. Extrudability

To measure extrudability, the experimental BLN-G was put inside a typical capped collapsible aluminium tube

and the end was crimped shut (Nidhi *et al*. 2023). Each tube's weight was noted. The tubes were then placed in between two glass slides and clamped. After covering the slides with 500 g, the cap was taken off and the extruded gel was collected. The percentage of the extruded gel was then calculated.

2.7.5. Spreadability

The spreadability of experimental BLN-G was evaluated by utilising its slip and drag characteristics (Khan *et al*. 2021). Measured amount of BLN-G (about 2 g) was placed in between two glass slides, scrapping the extra gel oozed out through the edges. A definite weight (80 gm) attached to a thread was then used to draw the upper slide. The duration measured (in seconds) required for the upper slide to detach from the lower slide was recorded and the corresponding spreadability value was determined.

$$S = M \times L / T$$

Where S represents spreadability, M represents the weight tied to the upper slide, L represents the glass slide's length, T represents the time taken till full detachment of upper and lower slide from one another.

2.7.6. Microbial test

To identify the possible risk of microbial proliferation, nutrient agar medium was utilised. Experimental BLN-G/blank gel was aseptically applied in a cross pattern onto the sample plate containing nutrient agar medium. For a period of fifteen days, the microbial growth was monitored periodically (Wiegand *et al*. 2008).

2.7.7. Swelling index

Experimental BLN-G was deposited as 5 mm in height and 10 mm in diameter in 20 ml PBS (pH of 7.4) at room temperature (Liu *et al*. 2023). At scheduled intervals of 2, 4, 6, and 8 h, BLN-G was taken and reweighed.

$$\text{Swelling ratio}(\%) = \left| \frac{(W_t - W_i)}{W_i} \right| \times 100$$

where W_t means the weight of BLN-G at time t; W_i means the initial weight of BLN-G.

2.7.8. Stability study

To evaluate the stability of the experimental BLN-G, a freeze-thaw cycle was performed with certain process modifications as described elsewhere (Das *et al*. 2023). The stability testing was conducted for 30 days with six cycles. During the study, experimental BLN-G was maintained at three different temperatures in each cycle. The temperatures were maintained at 5 ± 2 °C in refrigerator, 25 ± 2 °C at room temperature and 45 ± 2 °C inside the stability chamber respectively. After the study, important pysico-chemical parameters *viz*., colour, pH, viscosity, phase separation, mean diameter zeta potential, PDI etc., were examined (Abdel-Rashid *et al*. 2019, Singh *et al*. 2023a).

2.7.9. Acute dermal toxicity study

Acute dermal toxicity study of BLN-G was carried out by following OECD guideline 402. For the experiment, healthy rats were chosen. Before initiation of the test (24 h before), hair remover was used to remove fur from the dorsal location. Experimental BLN-G/blank gel was applied smoothly over the skin (Chanda *et al*. 2006). The application sites were inspected at 0.5, 1, 4, and 24 h for any indications of lesions/redness or unusual inflammation.

2.7.10. Ex vivo *permeation study*

To assess the amount of active component from BLN-G that permeated across the goat skin *ex vivo*, a Keshary-Chein diffusion cell (20 ml capacity with a cross-sectional area of 1.766 cm^2) was used (Mittal and Kaur 2019, Sutthisawatkul *et al*. 2024). The skin tissue of a goat was procured from the nearby butcher, and the adhering fat was carefully removed. For 48 h, the skin tissue was preserved by immersing it in a 0.1% (v/v) solution of 36% formaldehyde for the purpose of allowing any water-soluble ultraviolet-absorbing chemicals to seep out of the membrane. The calculated amount of selected BLN-G was then applied over the skin, placed in between the diffusion cell's donor and receptor compartments. PBS, pH 5.8 (with 0.1% w/w SLS) was selected as the release medium. The receptor fluid was constantly stirred at 100 rpm by a Teflon-coated magnetic bead. The receptor compartment was kept at a consistent 37 °C ± 2 °C by using a water inlet-outlet jacket layer. At predetermined intervals, measured amount of receptor fluid was taken out of the sampling port followed by addition of fresh PBS. Using an HPLC instrument, the amount of oil component that infiltrated to the receptor medium at a predetermined time was calculated.

2.7.11. Assessment of cytotoxicity of BLN-G in vitro

In *vitro* toxic effect of experimental BLN-G on primary epidermal melanocytes (HEMa) was investigated by MTT assay (Adnan *et al.* 2023). Briefly, HEMa (1×10^5 cells/well)

were cultured in DMEM supplemented with 10% foetal bovine serum (v/v), % L-glutamine in 96-well plates and incubated in a CO_2 humidified incubator at 37 °C for 24 h. Cells were treated with different dilutions of BLN-G (200, 400, 600, 800, 1000, and 1200 µg/ml) and blank gel. Control cells were treated with blank culture medium. Following 24h of incubation, culture media was removed and replaced with fresh culture media (100 µl/well) and MTT solution. The culture plates were then incubated for another 4–6 h at 37 °C. The supernatant was removed with addition of sterile DMSO to each well (100 µl). Following a short incubation period of 2 h, absorbance (at 570 nm) of the sample was measured (Adnan *et al.* 2023).

2.8. In vivo studies

For *in vivo* testing, rats were randomly divided into four groups (n = 6), *viz.*, Group I- control (deionised water treated), Group II- Standard (Diclofenac gel 1% w/w treated) Group III Test 1 (Betel oil treated) and Group IV- Test 2 (BLN-G, 1% w/w treated).

2.8.1. Evaluation of analgesic activity

2.8.1.1. Tail flick method. Analgesic activity of BLN-G was measured by conventional tail flick method. In this procedure, deionised water was supplied to the rats in the control group, while the standard group received topical application of diclofenac gel (1% w/w), and the test group 1 and test group 2 received topical application of plain betel leaf oil and experimental bigel (containing 1% w/w BLNs) respectively. For the study, 0.5 gm of bigel was applied and was spread uniformly over the distal part (tip of the tail) at the location of discomfort prior to an hour of experiment (Gaber *et al*. 2023). Fingers were used to hold rats in place when their tails were sticking out. A section of the tail measuring two centimetres was identified, which was then dipped into the water bath. Temperature of the water bath was maintained at 55 ± 1 °C using a thermometer (Yam *et al*. 2020). The tail flick delay and corresponding response time was recorded at 0, 30-, 60-, 120-, 180-, and 240-min post treatment.

2.8.1.2. Hot plate method. A modified hot plate approach (Eddy's hot plate) as mentioned by Sangale *et al*. (2023) was also employed to test analgesic activity of the experimental BLN-G. To accomplish this, a hot plate with an electrical guard was heated to between 55 ± 1 °C. Similar to the above study, rats in the control group were given distilled water, the standard group was given 1% (w/w) diclofenac gel at the location of discomfort (paw) prior to the 15 min of experiment, and the test group 1 and 2 were given betel oil and experimental bigel (containing 1% w/w BLNs) respectively. About 0.5 grams of bigel were applied topically and were evenly distributed throughout the distal region (tail tip) prior to an hour of the experiment (Nakhaee *et al*. 2021,Gaber *et al*. 2023). Time taken for the rat to respond to the heat stimulus, i.e. tardiness in lifting and licking their paws or in jumping off the equipment, was measured at 0, 30, 60, 120, 180, and 240 min.

2.8.2. Evaluation of anti-inflammatory activity

2.8.2.1. Carrageenan Induced Rat Paw Edema. *In vivo* anti-inflammatory potential of BLN-G was evaluated as per the previously reported method (Aslam *et al*. 2023). Briefly, test animals were divided into four treatment groups as described previously. Experimental animals were treated with betel oil/BLN-G (containing 1% w/w BLNs)/diclofenac sodium gel 1% (w/w), 30 min before carrageenan injection (Xavier-Santos et al. 2022, Gaber *et al.* 2023). The paw thickness following the treatment was measured at prefixed duration (0, 30, 60, 120, 180, and 240 min).

2.9. In-silico *docking analysis*

To depict the molecular interaction in between major phytoactive components of betel oil with selected inflammatory mediators, *in silico* docking analysis was employed. The molecular structure of the selected compounds was constructed utilising canonical smiles from the PubChem database PubChem CID: 3314, 52811515, 5281520, and 69909 (Sayed *et al*. 2023). The PDB structure of COX-1, COX-2, LOX, and Phospholipase was acquired from the RCSB Protein Data Bank (PDB id: 3KK6, 5KIR, 3V99, and 1KQU respectively). Following that, the receptor and ligand structures were uploaded to the Argus Lab App for docking. The Argus Lab App outcome was modified for the optimal structure and visualised with Discovery studio visualiser 2.5. Subsequently, the relationship was verified by evaluation of the obtained binding energy, including global energy, and van der Waals attractive force (Toor *et al*. 2021).

2.10. Statistical analysis

Each experiment was carried out in triplicate and the mean values ± standard deviation (SD) was used to describe the data. Additionally, one-way analysis of variance (one-way ANOVA) was used to assess the data through Tukey–Kramer's multiple comparisons test (Hori *et al*. 2021). P values less than 0.05 were regarded as significant results.

3. Results

3.1. Investigation of chemical composition of Piper betel (L.) leaf essential oil by GC/MS analysis

The phyto chemical constituent analysis in the oils was identified by GC-MS method which showed Eugenol as the major bioactive constituent (42.8%). The other compounds found in the leaf oil were Caryophyllene, Humulene, 2,7-Dimethylanthracene, 1(1-Carbmethoxyethyl)-3,3-bis(trifluoromethyl) diaziridine, α-Amorphene, δ-Amorphene, etc. In the leaf oil there were about 7 constituents approximately in amount varying from 1.17% – 42.8% in peak area (Table 1).

3.1.1. FTIR-ATR study

FTIR-ATR study was performed to identify any meaningful interactions in between oil/lipids/excipients. FTIR spectra of the essential oil, SL, CHL, physical mixture, BLNs were reported (Figure 1). Data overall depicted absence of any major interaction between the tested oil and lipids with other formulation components. The characteristics peaks were observed at 1465 cm^{-1} due to stretching of alkane group (-CH_3) of CHL, 1770cm^{-1} (due to C=O stretching of SL). Whereas the spectra of BLNs showed peaks at 1509 cm^{-1} (due to N- O stretching vibration), 1377 cm^{-1} (due to phenol group stretching) related to eugenol. In the physical mixture, the characteristics peaks were found at 1509 cm^{-1} (due to N-O stretching), 1770 cm^{-1} (due to C=O stretching) and at 1370 cm^{-1} (due to O-H phenolic group stretching). However, the FTIR spectra of the physical mixture of components did not show appearance of any new characteristics peak or any major shifting in the functional group peaks of oil too. The study thus signified physical and chemical compatibility in between the components for formulation development.

3.1.2. Yield percentage, percentage oil loading, and loading efficiency

Every batch of BLNs had a satisfactory yield percentage. Out of the four formulation batches that were reported, BLN-2 had the highest yield percentage (57.6%). The oil loading percentage for each formulation differed, and we observed that BLN-2 had a larger oil load at 6.8 ± 0.5% (w/w) than the remaining three formulations (BLN-1 at 4.2 ± 0.3% w/w, BLN-3 at 2.5 ± 1.2% w/w, and BLN-4 at 1.9 ± 0.9% w/w) (Table 2). Similarly, BLNs-2 loading efficiency (76.2 ± 2.1% w/w) was equally better than other three reported formulations. The particular formulation composition and the regulated process parameters may be responsible for the acceptable oil loading of the formulation.

3.1.3. Mean vesicle diameter, PDI, zeta potential

The data indicated that the mean diameter (Z-avg.) of the selected BLN-2 were within 100–200 nm. Out of the formulations that were reported, BLN-2 had an average vesicle size of 138.2 ± 1.08 nm and a PDI value of 0.182 (Figure 2). Further, the reported formulation had a negative zeta potential −46.6 ± 0.61 mV, suggesting that its stability in dispersion state.

3.1.4. Surface morphology study by FESEM

A smooth surface and spherical shape were observed by the FESEM analysis of the lyophilised BLN-2 (Figure 3A). Although some of the produced vesicles were agglomerated inside the sample, but overall vesicles maintained a homogenous distribution pattern without major difference in their shape/size or morphology.

3.1.5. Internal structure analysis by Cryo-TEM

To visualise the native form of BLN-2 in the suspension stage and to get clarity on the lamellarity, Cryo-TEM study was conducted. In the image, nanovesicular carriers were clearly visualised (Figure 3B). It further was found that the experimental BLN-2 were within nanosize range, unilamellar with intact lamellarity. No disruption/perforation was noticed in the outer phospholipid bilayer of BLN-2, justifying well formulation characteristics.

Table 1. GC/MS analysis of *Piper betel* leaf essential oil showing retention time, area %, molecular formula with molecular weight of major phyto active components.

Peak	Retention time (min)	Major components	Area%	Molecular formula	Molecular weight (g/mol)
1	8.72	Eugenol	42.8	$C_{10}H_{12}O_2$	164
2	9.05	Caryophyllene	19.1	$C_{15}H_{24}$	204
3	9.41	Humulene	10.7	$C_{15}H_{24}$	204
4	10.05	2,7-Dimethylanthracene	10.6	$C_{16}H_{14}$	206
5	9.60	α-Amorphene	9.9	$C_{15}H_{24}$	204
6	9.80	1(1-Carbmethoxyethyl)-3,3-bis(trifluoromethyl)diaziridine	3.74	$C_7H_8F_6N_2O_2$	266
7	10.73	δ-Amorphene	1.17	$C_{15}H_{24}$	204

A total seven major phytoactive components have been reported in the betel leaf oil based on their retention time and % area. Eugenol among all the components was found to have highest area % (42.8%) followed by caryophyllene.

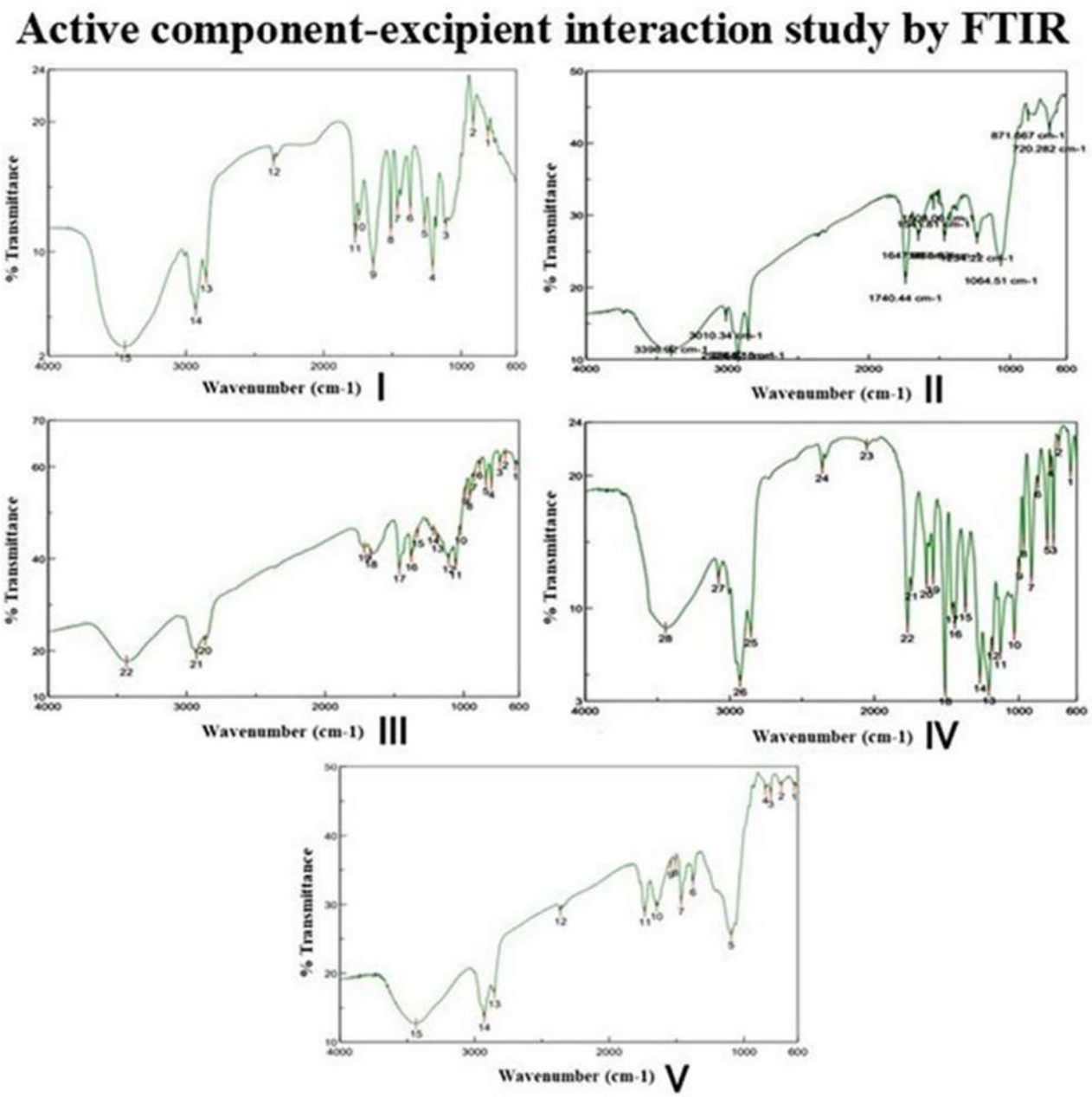

Figure 1. FTIR-ATR study of betel leaf oil (I), Soy lecithin (II), Cholesterol (III), Physical mixture of betel leaf oil, Soy lecithin, Cholesterol (IV), Experimental lipid nanocarrier (V). All spectra have been shown in absorbance mode. Spectrums were recorded in FTIR-ATR mode and the scan range was 4000 to 600 cm^{-1}. No significant shifting in characteristic peaks of oil components or other excipients were noticed, signifying absence of major interaction.

3.1.6. In vitro *release study and estimation of release kinetics*

The dialysis method was employed for the *in vitro* release study of the encapsulated oil from BLN-2. Data showed consistent oil release pattern from the formulation up to 24 h study period (Figure 3C). Initially, the oil release expanded with time. But after 12 h, a relatively sustained release profile was observed from BLN-2. During the study period, a cumulative amount of 79.82 ± 4.1% encapsulated oil was released from BLN-2. While, estimating the mechanism of oil release from BLN-2, it was that the release pattern was best fitted into Higuchi model with good linearity (R^2 = 0.9048).

3.2. Formulation and physico-chemical evaluation of the BLN-2 loaded bigel (BLN-2G)

Experimental bigels were prepared by conventional cold dispersion method by varying concentration of polymers as depicted in Table 3. Further, and among the prepared formulations, three suitable formulations

were reported. selected bigels were homogenous and smooth texture without any gritty feeling while application. Among the three reported BLN-2G formulations, BLN-$2G_2$ showed satisfactory viscosity (40 734 ± 1.7 cps) suitable for topical applications. All selected bigels had reasonable pH (within physiological pH range). Further, experimental BLN-2G had suitable spread area as depicted from spreadability test (Table 4). Extrudability test of all selected BLN-2G was found in the satisfied range. Throughout the period of fifteen days, no microbial development was seen in any of the developed gels. The swelling ratio of BLN-G depicted well swellable property as depicted in Figure 4A. Experimental BLN-G reached equilibrium after 8 h. Among the bigels, BLN-$2G_2$ absorbed a larger amount of water after being placed in the PBS. At 8 h, BLN-$2G_1$, BLN-$2G_2$ and BLN-$2G_3$ reached 401.09 ± 2.3%, 558.48 ± 3.1%, and 473.41 ± 2.9% swelling respectively.

However, among the tested formulations, BLN-$2G_2$ exhibited satisfied homogeneity, pH, spreadability, as

Table 2. Formulation ingredients, % yield, % oil loading and % loading efficiency of selected *Piper betel* (L.) leaf oil loaded lipid nanocarriers (BLNs).

Formulation code	SL: CHL ratio	% Yield (w/w)	% Loading (w/w)	% Loading efficiency (w/w)
BLN-1	1:1	48.1%	4.2 ± 0.3%	42.5 ± 1.1%
BLN-2	2:1	57.6%	6.8 ± 0.5%	76.2 ± 2.1%
BLN-3	4:3	41.3%	2.5 ± 1.2%	56.1 ± 0.2%
BLN-4	3:1	38.8%	1.9 ± 0.9%	48.7 ± 0.5%

In the reported formulations, ratio of major lipid components (soy lecithin and cholesterol) was varied, while keeping the amount of betel oil constant. In each formulation batch, 5 ml of betel leaf oil was used. At a ratio 2:1 (soy lecithin and cholesterol), highest oil loading % was achieved among three reported formulations. Data show mean ± SD ($N = 3$).
BLN: *Piper betel* (L.) leaf oil loaded lipid nanocarrier; SL: soya-L-α-lecithin; CHL: cholesterol.

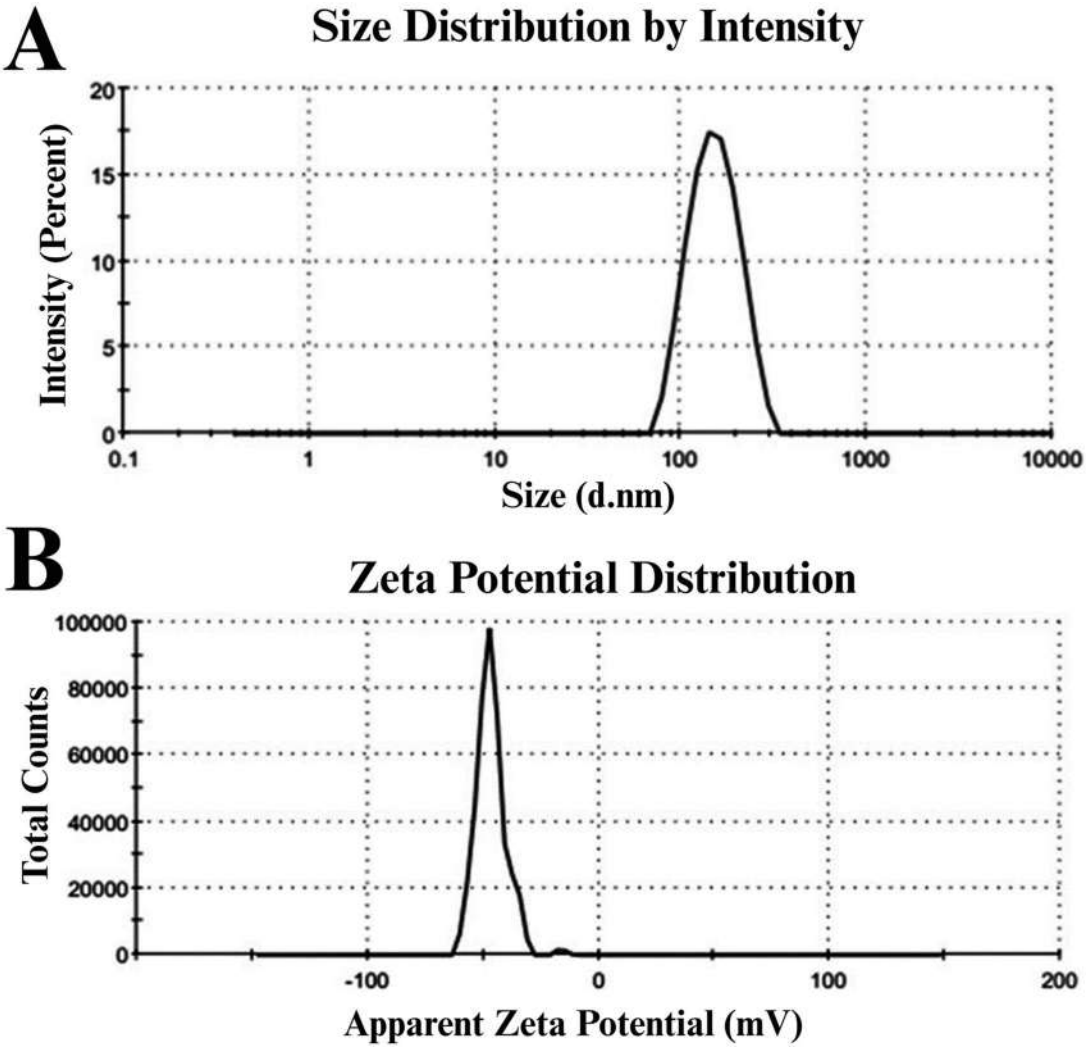

Figure 2. (A) Mean vesicle diameter (Z- avg.) analysis of selected betel leaf oil loaded lipid nanocarriers (BLN-2) by diffraction light scattering method. Mean diameter for BLN-2 was reported within nanosize range B) Determination of Zeta potential of selected betel leaf oil loaded lipid nanocarriers (BLN-2) to depict overall surface charge. BLN-2 was having higher negative surface charge depicting desirable stability in dispersed state.

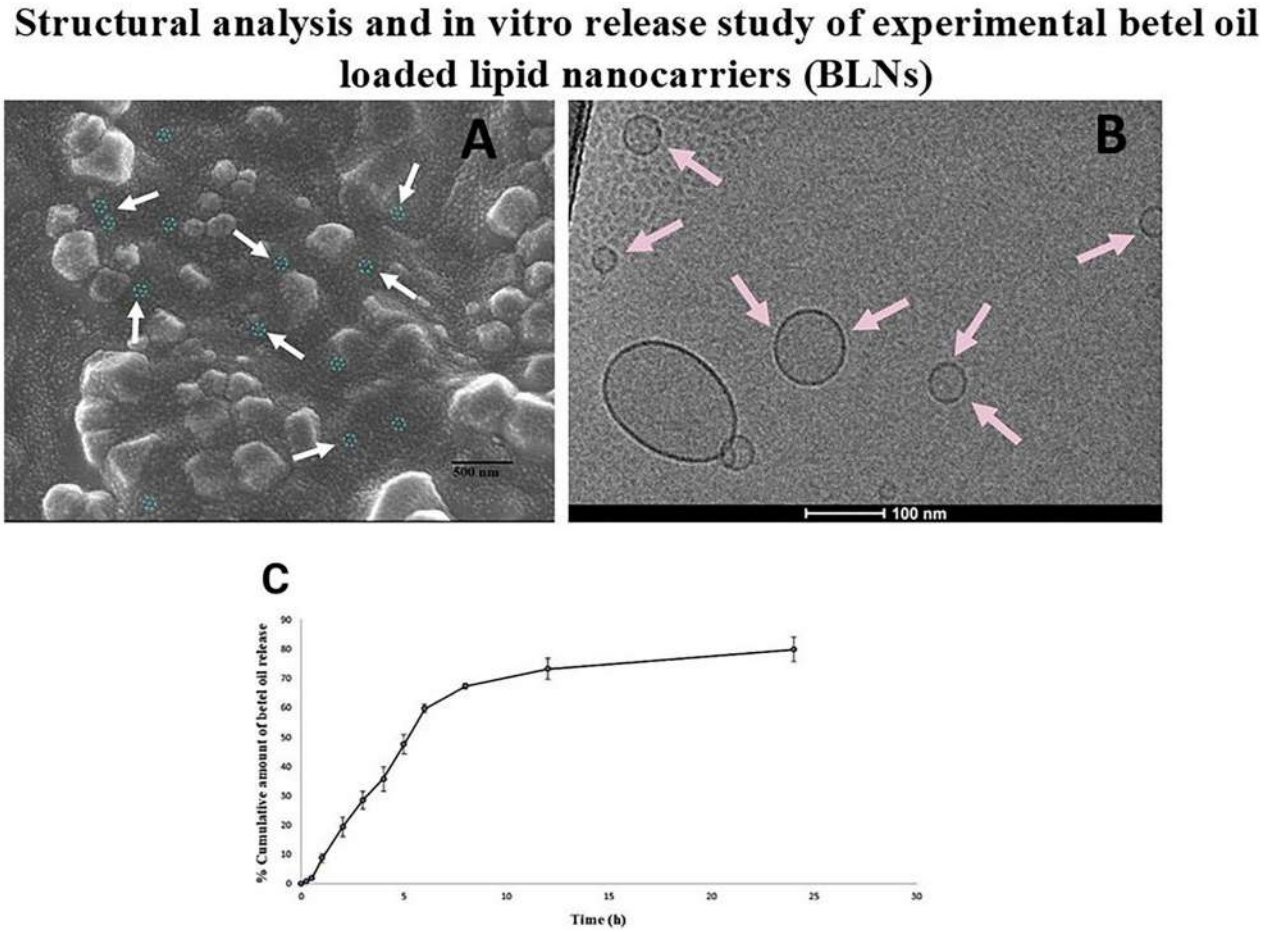

Figure 3. (A) Field emission scanning electron microscopy (FESEM) of betel leaf oil loaded lipid nanocarriers (BLN-2) with a magnification of 100 000x (Scale 500 nm). The vesicles were found spherical having smooth surface and within nano range. The vesicles were discretely organised throughout the formulation without any visible agglomerations. (B) Cryo- transmission electron microscopy (Cryo-TEM) of experimental betel leaf oil loaded lipid nanocarriers (BLN-2). Images were taken at magnification 40 000x at 200 kV voltage. Unilamellar, nanosize lipoidal vesicles with intact phospholipid outer layer (darker) and enclosed aqueous core (clearer). Vesicles were within desired nanorange without any visible imperfections on the outer lipid layer, justifying good formulation characteristics. (C) *In vitro* release study of betel leaf oil loaded lipid nanocarriers (BLN-2) in phosphate-buffered saline (PBS), pH 6.8. Data were presented as mean ± SD (N = 3). An overall sustained release profile was depicted for BLN-2 with best fit with Higuchi kinetics model.

Table 3. Formulation composition of selected *Piper betel* (L.) leaf oil loaded lipid nanocarrier (BLN-2) incorporated bigel formulation (BLN-2G).

Ingredients	BLN-2G$_1$	BLN-2G$_2$	BLN-2G$_3$
Carbopol 934P (g)	0.5	0.8	1
HPMC (g)	0.8	0.5	1
Propylene glycol (ml)	5		
Oleic acid (ml)	8.8		
Span 80 (ml)	1.2		
Sodium hydroxide (ml)	5		
BLNs-2 (mg)	10		
Ascorbic acid (mg)	0.05		
Distilled water (ml)	50		

Three suitable bigels were reported varying concentration of polymers, *viz.*, Carbopol 934 P and HPMC; whereas keeping other excipients constant. For each formulation batch, 10 mg of BLNs-2 was used. The hydrophilic polymers with sodium hydroxide constituted the hydrogel phase whereas oleic acid and span 80 constituted oleogel phase. Sodium hydroxide was used in the formulation to adjust pH.
BLN-2G: *Piper betel* (L.) leaf oil loaded lipid nanocarrier-based bigel; HPMC: hydroxy propyl methyl cellulose.

well as extrudability. BLN-2G$_2$ having carbopol at 0.8% w/v and HPMC at 0.5% w/v showed highest viscosity, extrudability and swelling property as observed from the study.

The findings of the stability study showed that, after 30 days, physicochemical characteristics of BLN-2G$_2$ such as colour, viscosity, pH, and phase separation had not changed noticeably. Further, the average vesicle size and zeta potential of incorporated BLN-2 did not show major variations, indicating that the BLN-2G$_2$ was stable within the tested storage range (Table 5).

Further, no potential acute dermal toxicity was observed for BLN-2G$_2$ during 24 h study period on rat skin upon topical application. Further, there was no difference in between the skin texture, or appearance of redness/inflammation in between BLN-2G$_2$ and

Table 4. Physico-chemical evaluation of selected *Piper betel* (L.) leaf oil loaded lipid nanocarrier-based bigel (BLN-2G) in terms of viscosity, spreadability, homogeneity, extrudability and microbial growth.

Batch no.	pH	Viscosity (Cps)	Spread ability (gm.cm/sec)	Homogeneity (Physical inspection)	Extrudability% (w/w) (compression-extrusion test)	Microbial growth
BLN-2G$_1$	6.7 ± 0.1	25552 ± 1.9	5.8 ± 2.3	Good	85.56 ± 2.3	Nil
BLN-2G$_2$	6.8 ± 0.5	40734 ± 1.7	8.3 ± 1.5	Very good	91.33 ± 1.3	Nil
BLN-2G$_3$	6.5 ± 0.3	32305 ± 2.4	7.1 ± 1.7	Good	83.14 ± 1.5	Nil

Viscosity was tested by Brookfield viscometer, while pH was tested by pH metre, homogeneity was tested physically by pressing a small amount of BLN-G in between thumb and index finger. Extrudability was analysed through compression-extrusion test using a collapsible aluminium tube. To check microbial growth nutrient agar plate was use to detect the presence or absence of adventitious microbes (colony-forming units). All the selected bigels showed desirable physico-chemical characteristics among with BLN-2G$_2$ was selected as the preferable one owing to desirable viscosity, spreadability and extrudability. Data show mean ± SD (N = 3).
BLN-2G: *Piper betel* leaf oil-loaded lipid nanocarrier-based bigel.

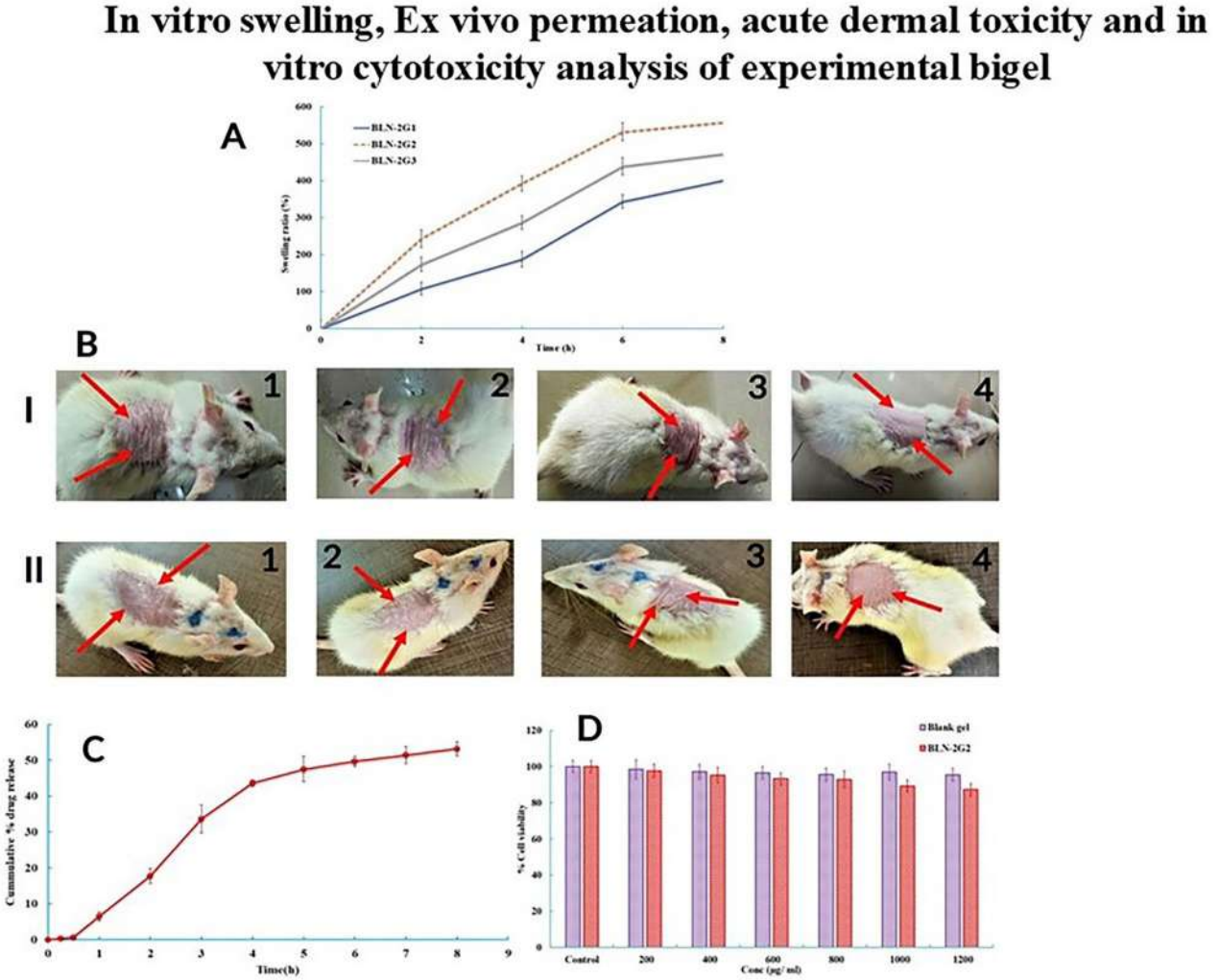

Figure 4. (A) Evaluation of swelling index of experimental betel leaf oil loaded lipid nanocarriers (BLN-2) incorporated bigel (BLN-2G$_2$). (B) Acute dermal toxicity study in terms of potential irritancy on rat skin following topical application of blank gel (without betel leaf oil), **I)**; betel leaf oil loaded lipid nanocarrier (BLN-2) incorporated bigel (BLN-2G$_2$), **II**); at 0.5 h, 1 h, 4h and 24 h time intervals. No sign of irritation, redness, inflammation or any visible adverse reactions were noticed within the tested duration, justifying compatible nature of BLN-2G$_2$ for *in vivo* applications. (C) *Ex vivo* permeation study of betel leaf oil loaded lipid nanocarrier-based bigel (BLN-2G$_2$) in PBS (pH 6.8) across goat mucosal membrane. Data were presented as mean ± SD (N = 3). A sustained release profile was observed within experimental time period with best fit of release data to Higuchi kinetic model, similar to the *in vitro* release data. (D) *In vitro* cytotoxicity study of blank gel *vs.* betel leaf oil loaded lipid nanocarrier incorporated bigel (BLN-2G$_2$) on primary epidermal melanocytes (HEMa). Data showed non-toxic nature of experimental BLN-2G$_2$ with more than 85% cell viability at all tested concentrations.

Table 5. Stability study of *Piper betel* leaf oil-loaded lipid nanocarrier-based bigel (BLN-2G$_2$) at different storage conditions, *viz.* 5 ± 2 °C, 25 ± 2 °C and 45 ± 2 °C respectively.

Condition	Days	Colour	Viscosity(cps)	Mean diameter (d.nm)	Poly dispersity index (PDI)	Zeta potential (mV)	% Loading (w/w)	% Encapsulation efficiency (w/w)
5 ± 2 °C	0	Off white	40734 ± 1.2	138.2 ± 1.03	0.182 ± 0.4	−46.6 ± 0.05	6.8 ± 0.3%	76.2 ± 1.3%
	15	Off white	40689 ± 2.1	139.09 ± 1.4	0.211 ± 0.2	−46.2 ± 0.2	6.5 ± 1.2%	77.1 ± 1.5%
	30	Off white	40632 ± 1.9	140.36 ± 0.8	0.232 ± 0.7	−46.01 ± 0.1	6.7 ± 1.1%	72.19 ± 2.1%
25 ± 2 °C	0	Off white	40734 ± 1.8	138.2 ± 0.7	0.182 ± 0.1	−46.6 ± 0.3	6.8 ± 0.5%	76.2 ± 2.1%
	15	Off white	40734 ± 1.1	138.45 ± 1.1	0.188 ± 0.2	−46.71 ± 0.07	6.6 ± 0.4%	74.2 ± 1.4%
	30	Off white	40678 ± 2.3	139.17 ± 1.8	0.209 ± 0.1	−46.1 ± 0.9	6.2 ± 1.3%	75.8 ± 2.1%
45 ± 2 °C	0	Creamish white	40619 ± 2.1	138.2 ± 1.3	0.181 ± 0.2	−46.6 ± 1.1	6.7 ± 1.2%	76.22 ± 2.1%
	15	Creamish white	40534 ± 1.6	139.11 ± 1.2	0.173 ± 1.2	−46.91 ± 0.05	6.1 ± 0.5%	73.9 ± 1.9%
	30	Creamish white	40287 ± 2.2	140.5 ± 1.6	0.195 ± 0.1	−46.34 ± 0.7	5.9 ± 0.7%	77.27 ± 2.3%

No visible changes were noticed in the physical characteristics of BLN-2G$_2$ in terms of colour, viscosity, pH, phase separation, etc. Though the colour change was minutely varied from off white to creamish white, however no visible sign of phase separation was observed throughout the experimental study period. Further pH of the BLN-2G$_2$ did not show any significant variation. Also, there were no such significant alternation in mean diameter, zeta potential, PDI and % encapsulation efficiency. Data show mean ± SD (N = 3).

control (blank gel) treated groups (Figure 4B). In view of suitable *in vitro* characteristics, BLN-2G$_2$ was taken for further studies.

3.2.1. Ex vivo *permeation study*

To depict the permeation behaviour of the active constituents from the BLN-2G$_2$, following its topical application, goat skin was employed as a simulus model. The study demonstrated that the loaded oil from BLN-2G$_2$ successfully penetrated into the skin's epidermal layer. The oil was successfully released from the formulation during 8 h period, within which 53.2% oil liberated as estimated from HPLC results. The encapsulated oil liberated slowly but consistently throughout the study period (Figure 4C). The release kinetics investigation showed that the *ex vivo* release followed the Higuchi kinetic model (R^2= 0.9406), which was similar to the *in vitro* release pattern.

3.2.2. *Assessment of cytotoxicity of BLN-2G$_2$ in vitro*

The cytotoxicity (*in vitro*) of BLN-2G$_2$ and blank gel was evaluated by MTT assay. Data overall showed absence of potential toxicity of BLN-2G$_2$ at different tested concentrations (Figure 4D). At 200 µg/ml, BLN-2G$_2$ reduced the cell viability by approximately 97.67 ± 3.6%. There was a minor reduction in the cell viability as 95.34 ± 4.3% to 93.2 ± 3.2% at concentrations of 400 µg/ml to 600 µg/ml, respectively. However, data showed overall non-toxic nature of experimental BLN-2G$_2$ even at highest tested concentration, i.e. 1200 µg/ml. Most of the cells were alive as observed from the % viability data (> 85%) signifying non-toxic, tissue compatibility nature of BLN-2G$_2$. Similarly, as expected for blank gel formulation, maximum cell viability was observed (up to 95%).

3.3. In vivo *studies*

3.3.1. *Analgesic activity*

3.3.1.1. Tail flick method. Albino Rats were used to evaluate the analgesic efficacy of the BLN-2G$_2$ utilising the tail flick method taking Diclofenac gel (1% w/w) as the standard. Tail flick method depicted potential analgesic effect of the BLN-2G$_2$. Topical treatment of the rats with the test compounds (betel oil and BLN-2G$_2$) significantly (P < 0.05) increased latency to flick tail as compared to control group animals. Among test groups BLN-2G$_2$ showed better effect as compared to the pure betel oil in terms of tail flick time. The highest nociception inhibition was exhibited by BLN-2G$_2$ at 180 min, which was almost comparable to that of standard treatment (Figure 5A).

3.3.1.2. Hot plate method. In another analgesic method, analgesic activity was evaluated utilising the hot plate method. Similar to tail flick method, diclofenac gel was too taken as standard and BLN-2G$_2$ and betel oil was taken as test formulations. Topical treatment of the rats with optimised BLN-2G$_2$ and betel oil significantly (P < 0.05) reduced paw licking response as compared to normal animals. Comparable to the tail flick approach, BLN-2G$_2$ was shown to be more effective than betel oil in prolonging animals' paw licking time. The highest nociception inhibition was exhibited by BLN-2G$_2$ at 180 min. The maximum nociception inhibition by Diclofenac was too observed at 180 min (Figure 5B).

3.3.2. *Ant inflammatory activity*

3.3.2.1. Carrageenan induced rat paw edoema. Carrageenan was subcutaneously injected into rat paws, causing inflammation and plasma extravasations that were characterised by significant (P < 0.05) increase in paw thickness in the control, tests, and standard groups. Application of BLN-2G$_2$ and betel

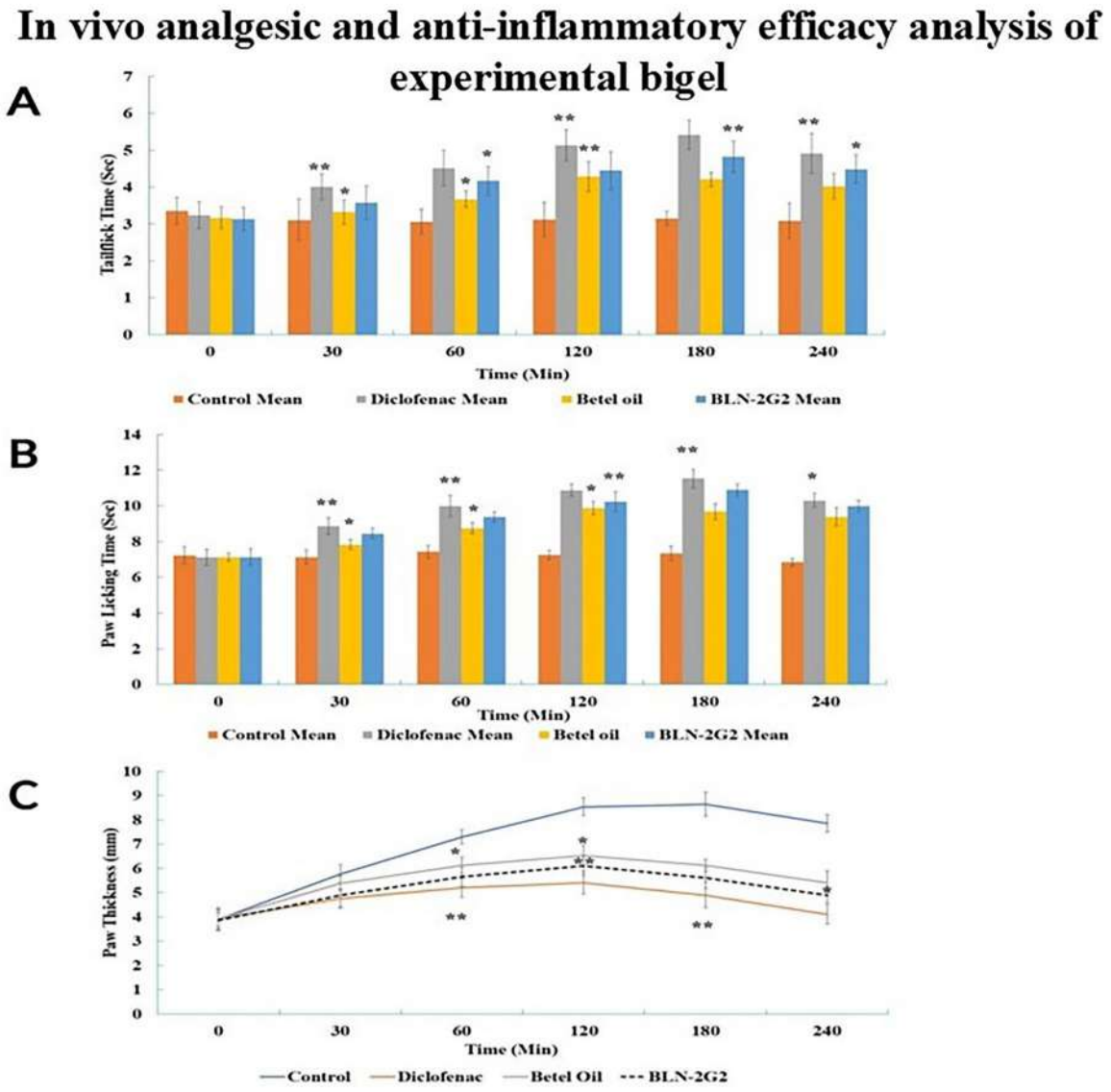

Figure 5. (A) Effect of betel leaf oil loaded lipid nanocarrier incorporated bigel (BLN-2G$_2$), betel oil, control (deionised water treated) and standard (Diclofenac gel 1% w/w treated) on the latency time of rats exposed to the tail flick test (*p < 0.05; **p < 0.01 *vs* control group). (B) Effect of BLN-2G$_2$, betel oil, control (deionised water treated) and standard (Diclofenac gel 1% w/w treated) on the latency time of rats exposed to the hot plate test (*p < 0.05; **p < 0.01 *vs* control group). (C) Effect of experimental bigel (BLN-2G$_2$), betel oil, control (deionised water treated) and standard (Diclofenac gel 1% w/w treated) on carrageenan - induced rat paw edoema (*p < 0.05; **p < 0.01 vs control group). In all cases, the treatment outcome was taken as less significant when represented as p < 0.05; whereas p < 0.01 showed highly significant treatment outcome when compared to control.

oil significantly (p < 0.05) decreased the paw thickness similar to that of diclofenac sodium throughout the test period (Figure 5C). The percentage of decrease in the inflammation was found to be 28.57%, 35.18%, and 37.57% for topical BLN-2G$_2$ treatment and 23.54%, 29.05%, and 31.21% for betel oil treated groups at 2, 3, and 4 h respectively.

3.4. In-silico *study*

The presentation of the primary phytochemicals was examined using *in-silico* molecular-docking simulation (Eugenol, Caryophyllene, Humulene, and 2,7-Dimethylanthracene) on different inflammatory and analgesic mediators. The findings demonstrated that eugenol interacted with distinct amino acids of the alkyl group at the active site of several inflammatory and analgesic mediators. The docking algorithm was able to predict the Eugenol ligand pose with inflammatory and analgesic mediators such as Cox-1, Cox-2, Lox, and Phospholipase binding energy score of-10.5798 kcal/mol, −10.7493 kcal/mol, −9.5379 kcal/mol and −9.4616 kcal/mol respectively. Similarly, caryophyllene also interacted with the inflammatory

and analgesic mediators at their active site signifying its efficacy in inflammation and pain. The docking algorithm was able to predict the binding energy score of −12.1509 kcal/mol, −11.1074 kcal/mol, −11.0317 kcal/mol, and −12.2937 kcal/mol for Cox-1, Cox-2, Lox, and Phospholipase respectively. Likewise, Humulene also interacted with the inflammatory and pain mediators at their active site signifying its efficacy in inflammation and pain. The docking algorithm predicted the binding energy score of −11.2271 kcal/mol, −11.8857 kcal/mol, −11.4076 kcal/mol, and −11.6374 kcal/mol for Cox-1, Cox-2, Lox, and Phospholipase respectively. 2,7-Dimethylanthracene also found to interact with inflammatory and analgesic mediators at their active sites, indicating effectiveness in inflammation and pain. The docking method predicted the 2,7-Dimethylanthracene ligand posture in the presence of inflammatory and analgesic mediators like as Cox-1, Cox-2, Lox, and Phospholipase binding energy score of −14.3849 kcal/mol, −13.6676 kcal/mol, −13.5072 kcal/mol and −12.0519 kcal/mol respectively (Table 6). The study overall depicted that all the selected phytoconstituents of *Piper betel* was found effectively docked with key analgesic/inflammatory mediators, thus unveiling the mechanism of action of BLNs-2G_2.

4. Discussion

Effective topical application of volatile phytoactive components in their raw form often pose severe delivery challenge, which can be improved significantly by the use of nanocarrier-based topical formulations. Essential oil of *Piper betel* was encapsulated in novel lipid nanocarriers, which were then loaded into topical gel formulations. Some crucial in process parameters were optimised during formulation development, which led to the formation of BLNs with desired physico-chemical characteristics.

To assess any type of physical interaction or chemical reaction between formulation components and to confirm their suitability for formulation, FTIR has been the preferred tool at present (Satapathy *et al.*, 2021a). In our study, FTIR data demonstrated absence of any major physical/chemical interaction as no major shifting in characteristic peaks of oil/lipid was detected in the physical mixture or in BLNs. Average vesicle diameter was found FESEM image clearly showed that the lyophilised BLN-2 were within the size range of 100–200 nm, which was also supported by DLS data. Lyophilised sample was mostly homogenous and was devoid of visible lumps or agglomeration. Higher negative surface charge further ensured stronger repulsion among the nanocarriers and thus would lead to higher stability at dispersed state. Cryo-TEM, which is at present explored as an effective way to depict internal structure of delicate lipid nanomaterials showed good formulation characteristics. No imperfections were detected in the outer lipid layer observed under liquid nitrogen condition. BLN-2 showed satisfactory loading of oil in its lipid structure with consistent slower release within experimental time period. Reasonable loading capacity of BLN-2 would be undoubtedly helpful for effective *in vivo* activity and sustained release would be beneficial in maintaining the desired local concentration of the therapeutic agents at application site.

For effective topical application of lipoidal nanocarriers, bigel is considered as the suitable delivery strategy. In view of lipophilic nature of LNs, *viz.*, nanoliposomes, nanophytosomes, solid-lipid nanoparticles, etc., bigel has been taken as an effective modality than conventional hydrogel for improved dispersion, stability, and transdermal efficacy of LNs (Maji *et al.*, 2021). Bigels by virtue of their unique formulation characteristic possess both physicochemical properties of oily-based organogel and aqueous-based hydrogel. Further, bigels successfully overcome the limitations associated with hydrogel or organogel independently; as hydrogel limits permeation capacity of lipoidal medications across the skin barrier while organogel faces stability issues (rancidification) with low patient compliance. Bigels possess the ability to deliver both lipophilic and hydrophilic medication simultaneously across the transdermal layer, improve the hydration of skin layers, and also enhance patient compliance by moisturising, cooling, and emollient effects on the skin. Recent literatures have also advocated the significance of bigel over conventional hydrogel in improving transdermal effectiveness of nanoformulations (Maji *et al.*, 2021, Das *et al.*, 2023). To into insights of the formulation, we have provided pictorial representation depicting actions of the experimental nano bigel, permeation of loaded LNs across the skin layers and possible mode of action.

In our study, the experimental BLN-2 loaded bigel (BLN-2G) showed satisfactory physical properties. All selected nanogels were homogenous, without any gritty feeling upon application. Further, spreadability, extrudability, viscosity, swelling ability of the BLN-2G were within desired values. Selected BLN-2G_2 showed higher viscosity (40 734 ± 1.7 cps), which would be beneficial for effective topical application. Clearly, the results depicted that concentration of polymers had direct impact on the physico-chemical characteristics of experimental BLN-2G. Owing to preferable

Table 6. (Continued)

Receptor (PDB ID)	Cox-1(3KK6)	Cox-2(5KIR)	Lox(3V99)	Phospholipase(1KQU)
2,7-Dimethylanthracene	-14.3849	-13.6676	-13.5072	-12.0519

A total four major phytoactive components of betel oil as reported from GC/MS analysis were docked with four key inflammation mediators. Among the ligands 2,7-Dimethylanthracene depicted highest binding affinity (-14.3849 kcal/mol) against COX-1 and -13.6676 kcal/mol, -13.5072 kcal/mol against COX-2, LOX, phospholipase respectively. Among the proteins, COX-1 exhibited reasonable binding affinity with selected phyto components. COX and LOX are the enzymes that play crucial role in inflammation regulation.
Cox-1: Cyclooxygenase-1; Cox-2: Cyclooxygenase-2; Lox: Lipoxygenase; PDB id: Protein data bank id.

In vitro cytotoxicity data further signified biocompatible nature of BLN-2G$_2$ as no potential toxicity on the epithelial cell line was observed, which thus rationalised its *in vivo* applicability. Upon topical application, BLN-2G$_2$ did not show any potential irritation on rat skin. No appearance of redness, swelling or any unusual changes in skin texture and morphology was observed during the experimental time period, which was also an important piece of information for transdermal application.

Both BLNs-2G$_2$ and plain betel oil exhibited significant analgesic and anti-inflammatory activity as compared to the control in different animal models. It was found that the *in vivo* effects were almost comparable to the standard diclofenac. The increase in paw thickness was mostly due to infiltration of white blood cells and increased levels of local prostaglandins at the site (Tamaddonfard *et al*. 2013). Edoema due to carrageenan induction is usually biphasic, which includes an initial phase owing to the release of histamine serotonin and kinins and it starts right away after application and second phase occurs after one to three hours by release of prostaglandin-like substances (Okechukwu 2020). Further, COX-1 and COX-2 are the two inflammatory mediators that are involved in the synthesis of prostaglandin, which are implicated in the processes of pain and inflammation. Due to the fact that inflammatory cytokines such as interleukin-1 beta (IL-1 beta) and tumour necrosis factor alpha (TNF alpha) stimulate the expression of COX-2 in a variety of cell types, inflammation, and pain are facilitated by lipoxygenases (LOXs), which are naturally occurring enzymes produced by neutrophils that stimulate and migrate neutrophils and interact with prostaglandin's mediated vasodilation. Phospholipase further catalyses the release of arachidonic acid, which is an essential component for various inflammatory pathways (Vasudevan *et al*. 2021).

Recent studies have already depicted the protective role of eugenol, humulene, caryophyllene, and 2,7-dimethylanthracene in inflammation and pain modulation (Barboza *et al*. 2018, Scandiffio *et al*. 2020, de Lacerda Leite *et al*. 2021). Present study described the anti-inflammatory potential of BLN-2G$_2$ and betel oil in the experimental rats that indicated by significant inhibition of paw edoema size for each rat. BLN-2G$_2$ showed better efficacy as compared to the

betel oil which might be higher transdermal permeation of the phytochemicals to the site of inflammation.

Though eugenol mechanism is unclear; some studies suggests that the blocking of voltage- sensitive and receptor-operated channels are responsible for the analgesic potential of it (Pramod et al. 2010). In case of analgesic study, following topical treatment of BLN-2G_2 and betel oil, significant ($P < 0.05$) increase in latency to flick tail with reduced paw licking response was observed as compared to the control groups. Therefore, it is precited that phytochemicals present in BLN-2G_2 might exert protective effect on the inflammatory mediators and mechanisms of pain perception like activation of neuronal channels. The *in vivo* results were further supported by the *in silico* docking studies.

In the *in vivo* studies, to depict significant variations in the observed means of data, Tukey-Kramer's test was chosen (Hori *et al*. 2021). This test is usually helpful to test the difference in the pair of treatments and comparing it with the calculated value. In our analgesic/anti-inflammatory study, this test method was employed to find out difference in the treatment outcomes of control gel *vs.* experimental nanobigel (Test II), and betel oil (Test I). As both the pair of treatments with nanobigel and betel oil were compared with the control, which showed significant difference from one another; Tukey-Kramer's test was applied as a suitable statistical tool.

In silico docking analysis confirmed the outcome of *in vivo* testing. Though, few of the recent studies have depicted *in silico* analysis of betel oil derived phytoactive components. Agustin et al., reported the molecular-docking analysis of the bioactive compound of *Piper betle* L. leaf extract against target protein of *Escherichia coli.* The results showed that the selected bioactive components of *Piper betle* L. successfully interacted to the active site of FabB of *Escherichia coli* (Agustin *et al*. 2022). Similarly, in another study, one major active components of betel oil, i.e. hydroxychavicol was docked against the COVID-19 associated mycotic protein, Lanosterol 14 alpha demethylase, which depicted significant binding affinity of hydroxychavicol towards the target protein.

We have also included *in silico* analysis of other potent leaf essential oils to correlate and validate our result. A work used a carrageenan-induced acute inflammation paradigm to investigate the anti-inflammatory properties of *Zingiber officinale roscoe* and *Allium subhirsutum* aqueous extracts (Zammel *et al*. 2021). Major phyto actve components of *Zingiber officinale roscoe* and *Allium subhirsutum*'s showed preferential binding to toll-like receptor 6 (TLR6), 4OM7, with high binding scores (> −8Kcal/mol). Another work reported *in vivo* efficacy of *Allophylus villosus* and *Mycetia sinensis* extracts in relieving pain (Azam *et al*. 2025). Targeting the COX-2 and 15-LOX-2 enzymes through molecular-docking study was conducted against 43 reported phyto-compounds of both plants. Among them, four major phytocompounds exhibited strong affinity against COX-2 and 15-LOX-2, complementing *in vivo* efficacy data (Azam *et al*. 2025). *In-silico/in vivo* analgesic and anti-inflammatory assessment of Egyptian *Cassia occidentalis* L. was reported elsewhere (Sayed *et al*. 2023). The major phytoconstituents of the plant, *viz.* aloe-emodin, chrysophanol and physcion showed a substantial binding affinity for nAChRs, COX-1, and COX-2, (key inflammatory mediators) supporting their analgesic and anti-inflammatory characteristics.

However, no such *in silico* study till date has reported the interaction of betel leaf oil derived active components with analgesic and inflammation mediators. Data depicts that most of the selected analgesic and inflammation mediators were found to be docked perfectly with the major phyto components of betel oil with docking score higher than −8 Kcal/mol. Among the interactions, anthracene and caryophyllene showed highest docking score of −14.3 and −12.2 Kcal/mol upon interaction with analgesic/inflammatory mediators. Presence of higher quantity of eugenol along with anthracene, humelene, caryophyllene could be responsible for higher analgesic/anti-inflammatory activity of the experimental BLN-2G_2.

To further elucidate the findings and to correlate with *in vivo* results and *in silico* analysis, additional insights have been presented in a pictorial representation (Figure 6) depicting actions of the experimental nano bigel, permeation of loaded BLNs across the skin layers and possible mode of action (inflammatory mediators). The skin's dermis, hair follicles, cell membrane, and epithelial cells all produce phospholipids and other chemicals when a cell becomes inflamed (Castañeda-Reyes *et al*. 2020). The primary source of inflammation is phospholipids, which set off the arachidonic acid chain reaction, which is then followed by pain (Osafo *et al*. 2021). Cyclooxygenase and 5-lipooxygenase, respectively, create prostaglandins and leukotrienes during this reaction (Carola *et al*. 2021). Following topical application of BLN-2G_2, at the dermal level, it would release active betel oil components from the BLNs. The phyto active components would then diffuse through the lipophilic stratum corneum and the underlying less lipophilic viable epidermis and ultimately through the dermis to hair follicles. Subsequently, they could penetrate the nearby blood vessels to reach deeper tissues. It is possible for the active components to be absorbed from the dermal

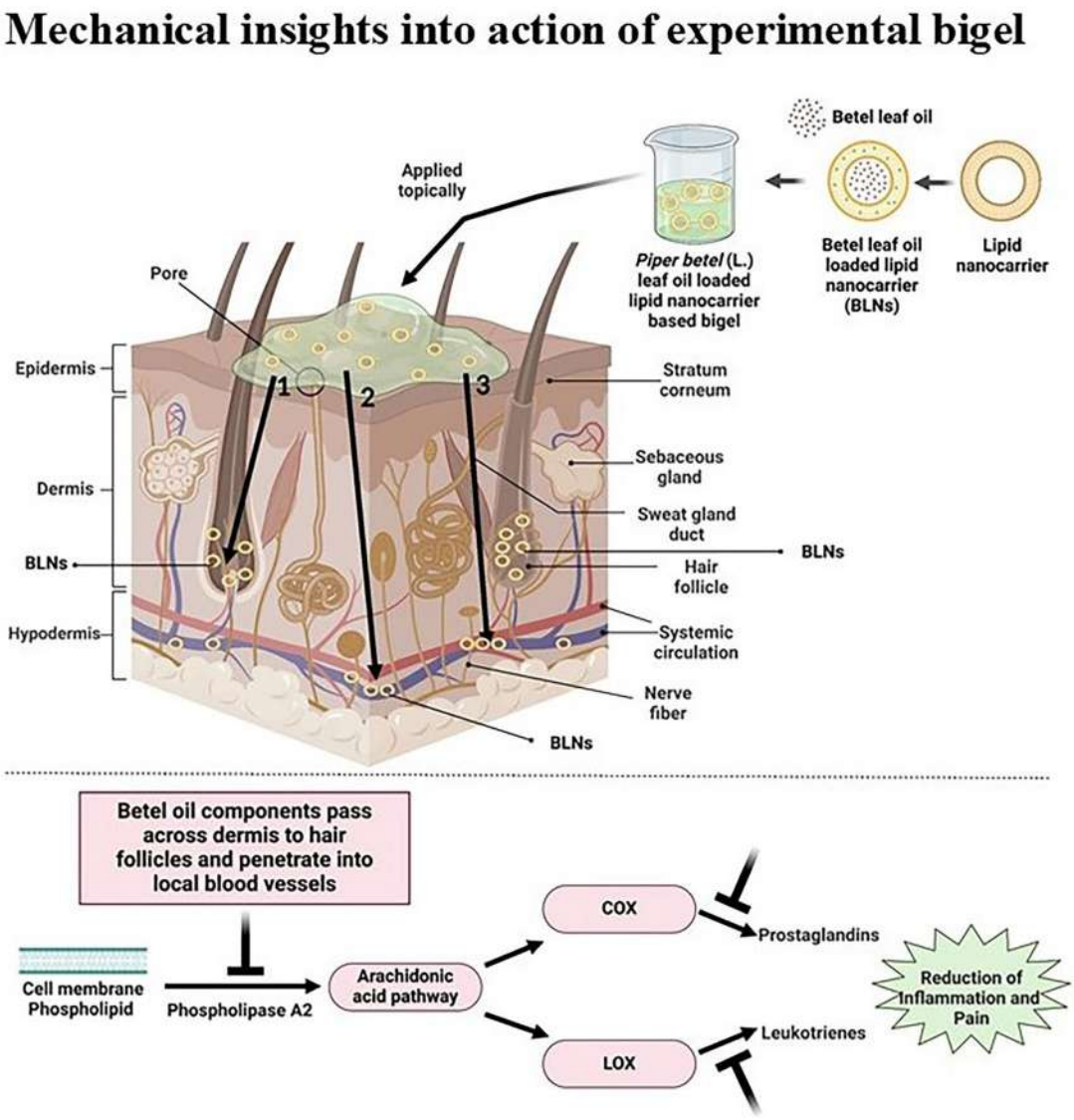

Figure 6. A pictorial representation on the insights into the action of betel leaf oil loaded lipid nanocarrier incorporated bigel (BLN-2G$_2$) with depth of penetration across different skin layers and possible mode of therapeutic action. Upon topical administration of BLN-2G$_2$, nanolipoidal carriers (BLNs) possess the potential to enter across skin layers *via* three different routes, *viz.* the appendageal route, the intracellular route, or the intercellular route. By penetrating sweat glands, skin furrows, or hair follicles, the phytocomponents can either penetrate the dermis or be retained *via* the appendageal pathway.

microcirculation and enter the systemic circulation at this point. Ultimately, the phospholipase enzyme is the target of their inhibition, which stops arachidonic acid synthesis and the consequent production of COX, LOX, prostaglandins, and leukotrienes and hence a reduction in inflammation could be achieved.

Though therapeutic potentiality of *betel* leaf oil-based nanoplatforms has been investigated over recent years; however, the present work is just not a mere of repetition of any existing outcomes. A study showed potential anti-mosquito repellent effect of betel essential oil loaded poly(ε-caprolactrone) nanocapsules (Kamari *et al*. 2023). The oil loaded nanoformulation was used as an anti-mosquito spray for cotton and polyester fabrics. Data showed the fabrics maintained a good repellent property (up to 47%) against mosquitoes even after five consecutive washing cycles, suggesting potentiality of betel oil loaded nanocapsules in increasing durability of the fabrics against washing and heating. The study was claimed to be first of its kind in utilising lipid-core polymeric nanocapsules filled with betel essential oil as insect repellent spray formulations for making insect-resistant fabrics. Antimicrobial potency of *Piper betel* oil loaded nanoemulsion was also reported against food pathogens (Roy and Guha 2018). Experimental oil loaded nanoemulsion showed potent antibacterial activity as depicted from MIC of 0.5–1.25 µl/ml and an MBC of of

1–2.5 µl/ml against five strains of gram-positive and gram-negative bacteria. The study overall depicted potentiality of *Piper betel* loaded nanoemulsions as natural antimicrobial modality in preserving food. Another work depicted effective wound healing potential of betel leaf extract encapsulated PVA nanofibres (Akram *et al*. 2023). Experimentally fabricated nanofibres improved moisture and thermal characteristics effectively with significant antibacterial action against *Staphylococcus aureus and E. coli* (ZOI: 20 mm). Betel leaf oil was also used for green synthesis of calcium oxide nanoparticles, which showed potential antimicrobial and anticancer activities *in vitro* (Yoonus *et al*. 2021). Data depicted maximum antibacterial activity against *E. coli* and minimum for *S. mutans*. The green-synthesized nanoparticles depicted anticancer potential against A549 cell line (IC_{50}: 92.08 µg/mL) (Yoonus *et al*. 2021). However, the present study is quite different than the existing literatures as no such report is there on the analgesic and anti-inflammatory potential of betel oil loaded nanotopical formulation. *In vivo* data on suitable analgesic/anti-inflammatory model in this regard is yet to be validated. Additionally, we have thrown some insights on the possible mechanism of action of the betel oil against key inflammatory mediators through docking analysis. Thus, overall outcome of the study holds its uniqueness.

5. Conclusion

A novel, yet facile development of betel leaf oil loaded lipid nanocarrier-embedded bigel was reported for analgesic and anti-inflammatory applications. Nanosized, spherical, unilamellar, homogeneous BLNs were developed having reasonable oil payload. BLN-$2G_2$ exhibited satisfied physico-chemical characteristics in terms of viscosity, spreadability, extrudability, swellability, and *ex vivo* release tendency. *In vitro* cytotoxicity assay justified histo-compatible, non-toxic nature of BLN-$2G_2$, which was further substantiated from acute dermal toxicity evaluation on rat skin. Effective analgesic and anti-inflammatory efficacy were exhibited by BLN-$2G_2$ in rat model with significant variation than control group. Molecular-docking analysis provided insights on the possible mechanism of analgesic/anti-inflammatory activity of betel leaf oil components.

6. Limitations and future research directions

Though, BLN-$2G_2$ was found to be a promising nano-modality in view of desirable *in vitro* properties and *in vivo* potential, however, the study has its own limitations too. In the study, *in vivo* efficacy analysis has been primarily restricted to one/two conventional analgesic and anti-inflammatory models, whereas other analgesic/anti-inflammatory models could also be employed for comparison of therapeutic efficacy. In order to progress for futuristic clinical translation, data related to longer-term toxicity study of BLN-$2G_2$ will be an essential component to fully assess safety of the experimental bigel over repeated applications. Furthermore, comparative efficacy analysis of BLN-$2G_2$ with various marketed analgesic and anti-inflammatory gels (beyond diclofenac) would contextualise the clinical relevance of the findings. Addressing these concerns would lay down the foundation stone for futuristic clinical applicability of betel leaf oil as potential analgesic/anti-inflammatory drug candidate.

Acknowledgements

The authors are very much thankful to IICB, Kolkata and KIIT, Bhubaneswar to provide necessary instrumental facilities.

Disclosure statement

No potential conflict of interest was reported by the author(s).

Funding

The authors did not receive support from any organisation for the submitted work.

References

Aayush, K., *et al.*, 2024. Development and characterization of sodium alginate and ß-cyclodextrin nanoemulsions encapsulating betel leaf (*Piper betle* L.) extract for enhanced antimicrobial efficacy against foodborne pathogen. *Food chemistry*, 463 (Pt 3), 141227. doi: 10.1016/j.foodchem.2024.141227.

Abdallah, M.H., *et al.*, 2021. Quality by design for optimizing a novel liposomal jojoba oil-based emulgel to ameliorate the anti-inflammatory effect of brucine. *Gels (Basel, Switzerland)*, 7 (4), 219. doi: 10.3390/gels7040219.

Abdel-Rashid, R.S., *et al.*, 2019. Nanogel loaded with surfactant based nanovesicles for enhanced ocular delivery of acetazolamide. *International journal of nanomedicine*, 14, 2973–2983. doi: 10.2147/IJN.S201891.

Adnan, M., *et al.*, 2023. Development and optimization of transethosomal gel of apigenin for topical delivery: in-vitro, ex-vivo and cell line assessment. *International journal of pharmaceutics*, 631, 122506. doi: 10.1016/j.ijpharm.2022.122506.

Agrawal, R.8., *et al.*, 2024. Emerging trends in the treatment of skin disorders by herbal drugs: traditional and

nanotechnological approach. *Pharmaceutics*, 16 (7), 869. doi: 10.3390/pharmaceutics16070869.

Aguilar-Pérez, K.M., *et al.*, 2022. Nano-size characterization and antifungal evaluation of essential oil molecules-loaded nanoliposomes. *Molecules (Basel, Switzerland)*, 27 (17), 5728. doi: 10.3390/molecules27175728.

Agustin, A.T., *et al.*, 2022. Potential role of betel leaf (*Piper betle* L.) water extract as antibacterial *Escherichia coli* through inhibition of ß-ketoacyl-[acyl carrier protein] synthase I. *Tropical journal of natural product research*, 6 (11), 1802–1808. doi: 10.26538/tjnpr/v6i11.10.

Ahmad, R., *et al.*, 2021. Phytochemical delivery through nanocarriers: a review. *Colloids and surfaces B, biointerfaces*, 197, 111389. doi: 10.1016/j.colsurfb.2020.111389.

Akram, M.W., *et al.*, 2023. Fabrication and characterization of antimicrobial wound dressing nanofibrous materials by PVA-betel leaf extract. *Heliyon*, 9 (7), e17961. doi: 10.1016/j.heliyon.2023.e17961.

Alam, A., *et al.*, 2022. Herbal fennel essential oil nanogel: formulation, characterization and antibacterial activity against *Staphylococcus aureus*. *Gels (Basel, Switzerland)*, 8 (11), 736. doi: 10.3390/gels8110736.

Alshaikh, F., *et al.*, 2024. Encapsulation of gingerol into nanoliposomes: evaluation of in vitro anti-inflammatory and anti-cancer activity. *Biomedical chromatography: BMC*, 38 (8), e5899. doi: 10.1002/bmc.5899.

Aslam, B., *et al.*, 2023. Anti-pyretic, analgesic, and anti-inflammatory activities of meloxicam and curcumin co-encapsulated PLGA nanoparticles in acute experimental models. *Metabolites*, 13 (8), 935. doi: 10.3390/metabo13080935.

Assis, D.B., *et al.*, 2020. Antinociceptive activity of chemical components of essential oils that involves docking studies: a review. *Frontiers in pharmacology*, 11, 777. doi: 10.3389/fphar.2020.00777.

Azam, M.N., *et al.*, 2025. Profiling of antioxidant properties and identification of potential analgesic inhibitory activities of *Allophylus villosus* and *Mycetia sinensis* employing in vivo, in vitro, and computational techniques. *Journal of ethnopharmacology*, 336, 118695. doi: 10.1016/j.jep.2024.118695.

Barboza, J.N., *et al.*, 2018. An overview on the anti-inflammatory potential and antioxidant profile of eugenol. *Oxidative medicine and cellular longevity*, 2018 (1), 3957262. doi: 10.1155/2018/3957262.

Biswas, P., Anand, U., Saha, S. C., Kant, N., Mishra, T., Masih, H., Bar, A., Pandey, DK., Jha, NK., Majumdar, M., Das, N., 2022. Betelvine (*Piper betle* L.): a comprehensive insight into its ethnopharmacology, phytochemistry, and pharmacological, biomedical and therapeutic attributes. *Journal of cellular and molecular medicine*, 26(11), 3083–3119. doi: 10.1111/jcmm.17323.

Carola, C., *et al.*, 2021. A cornflower extract containing N-feruloylserotonin reduces inflammation in human skin by neutralizing CCL17 and CCL22 and inhibiting COX-2 and 5-LOX. *Mediators of inflammation*, 2021 (1), 6652791. doi: 10.1155/2021/6652791.

Castañeda-Reyes, E., *et al.*, 2020. Development, characterization and use of liposomes as amphipathic transporters of bioactive compounds for melanoma treatment and reduction of skin inflammation: a review. *International journal of nanomedicine*, 15, 7627–7650. doi: 10.2147/IJN.S263516.

Chanda, S., *et al.*, 2006. Developmental toxicity study of pure trans-capsaicin in rats and rabbits. *International journal of toxicology*, 25 (3), 205–217. doi: 10.1080/10915810600683317.

Das, B., Nayak, A.K., and Mallick, S., 2023. Thyme oil-containing fluconazole-loaded transferosomal bigel for transdermal delivery. *AAPS PharmSciTech*, 24 (8), 240. doi: 10.1208/s12249-023-02698-2.

de Lacerda Leite, G.M., *et al.*, 2021. Pharmacological and toxicological activities of α-humulene and its isomers: a systematic review. *Trends in food science & technology*, 115, 255–274. doi: 10.1016/j.tifs.2021.06.049.

Dhankhar, R., *et al.*, 2010. Advances in novel drug delivery strategies for breast cancer therapy. *Artificial cells, blood substitutes, and immobilization biotechnology*, 38 (5), 230–249. doi: 10.3109/10731199.2010.494578.

Ellboudy, N.M., *et al.*, 2023. Cinnamon oil-loaded nanoliposomes with potent antibacterial and antibiofilm activities. *Molecules (Basel, Switzerland)*, 28 (11), 4492. doi: 10.3390/molecules28114492.

Emtiazi, H., *et al.*, 2022. Comparative study of nano-liposome and nano-niosome for delivery of achillea millefolium essential oils: development, optimization, characterization and their cytotoxicity effects on cancer cell lines and antibacterial activity. *Chemistry & biodiversity*, 19 (10), e202200397. doi: 10.1002/cbdv.202200397.

Esmaeili, F., *et al.*, 2022. Anti-inflammatory and anti-nociceptive effects of cinnamon and clove essential oils nanogels: an in vivo study. *BMC complementary medicine and therapies*, 22 (1), 143. doi: 10.1186/s12906-022-03619-9.

Fagbemi, K.O., Aina, D.A., and Olajuyigbe, O.O., 2021. Soxhlet extraction versus hydrodistillation using the clevenger apparatus: a comparative study on the extraction of a volatile compound from *Tamarindus indica* seeds. *TheScientificWorldJournal*, 2021 (1), 5961586–5961588. doi: 10.1155/2021/5961586.

Gaber, D.A., *et al.*, 2023. Nano-emulsion based gel for topical delivery of an anti-inflammatory drug: in vitro and in vivo evaluation. *Drug design, development and therapy*, 17, 1435–1451. doi: 10.2147/DDDT.S407475.

Gandhi, G.R., *et al.*, 2020. Essential oils and its bioactive compounds modulating cytokines: a systematic review on anti-asthmatic and immunomodulatory properties. *Phytomedicine: international journal of phytotherapy and phytopharmacology*, 73, 152854. doi: 10.1016/j.phymed.2019.152854.

Hester, S., *et al.*, 2021. Development of a lyophilization process for long-term storage of albumin-based perfluorodecalin-filled artificial oxygen carriers. *Pharmaceutics*, 13 (4), 584. doi: 10.3390/pharmaceutics13040584.

Hori, Y., *et al.*, 2021. Xerostomia aggravates ligation-induced peri-implantitis: a preclinical in vivo study. *Clinical oral implants research*, 32 (5), 581–589. doi: 10.1111/clr.13727.

Jufri, M., *et al.*, 2017. Stability of anti-acne niosome gels containing betel leaf (*Piper betle* L.) essential oil. *International journal of applied pharmaceutics*, 9, 130–134. doi: 10.22159/ijap.2017.v9s1.72_79.

Kamari, A., *et al.*, 2023. Betel essential oil-loaded lipid-core nanocapsules as mosquito repellent spray formulations for fabric finishes. *The journal of the textile institute*, 114 (1), 10–21. doi: 10.1080/00405000.2021.2018787.

Khan, M.K., *et al.*, 2021. Development of chitosan-based nanoemulsion gel containing microbial secondary metabolite with effective antifungal activity: in vitro and in vivo characterizations. *International journal of nanomedicine*, 16, 8203–8219. doi: 10.2147/IJN.S338064.

Kováčik, A., Kopečná, M., and Vávrová, K., 2020. Permeation enhancers in transdermal drug delivery: benefits and limitations. *Expert opinion on drug delivery*, 17 (2), 145–155. doi: 10.1080/17425247.2020.1713087.

Kumar, M., Mandal, U. K., and Mahmood, S., 2024. Dermatological formulations. *In*: *Dosage forms, formulation developments and regulations*. USA: Academic Press, Inc., 613–642. doi: 10.1016/B978-0-323-91817-6.00021-8.

Kumari, S., *et al.*, 2022. Bioactive loaded novel nanoformulations for targeted drug delivery and their therapeutic potential. *Pharmaceutics*, 14 (5), 1091. doi: 10.3390/pharmaceutics14051091.

Liu, Y., *et al.*, 2023. Multifunctional antibiotics-free hydrogel dressings with self-regulated nitric oxide-releasing kinetics for improving open wound healing. *Journal of materials chemistry. B*, 11 (16), 3650–3668. doi: 10.1039/D2TB02671F.

Madhumita, M., Guha, P., and Nag, A., 2019. Extraction of betel leaves (*Piper betle* L.) essential oil and its bio-actives identification: process optimization, GC-MS analysis and anti-microbial activity. *Industrial crops and products*, 138, 111578. doi: 10.1016/j.indcrop.2019.111578.

Maji, R., *et al.*, 2021. A transferosome-loaded bigel for enhanced transdermal delivery and antibacterial activity of vancomycin hydrochloride. *International journal of pharmaceutics*, 607, 120990. doi: 10.1016/j.ijpharm.2021.120990.

Manzoor, A., *et al.*, 2023. Plant-derived active substances incorporated as antioxidant, antibacterial or antifungal components in coatings/films for food packaging applications. *Food bioscience*, 53, 102717. doi: 10.1016/j.fbio.2023.102717.

Maurya, A.K., *et al.*, 2020. Synthesis of eugenol derivatives and its anti-inflammatory activity against skin inflammation. *Natural product research*, 34 (2), 251–260. doi: 10.1080/14786419.2018.1528585.

Mishra, S.B., *et al.*, 2023. Emulgels: a novel approach for enhanced topical drug delivery systems. *In*: *Advances in novel formulations for drug delivery*. Hoboken, NJ, USA, 231–262. doi: 10.1002/9781394167708.ch13.

Mittal, N., and Kaur, G., 2019. *Leucaena leucocephala* (Lam.) galactomannan nanoparticles: optimization and characterization for ocular delivery in glaucoma treatment. *International journal of biological macromolecules*, 139, 1252–1262. doi: 10.1016/j.ijbiomac.2019.08.107.

Mondal, L., *et al.*, 2019. CD-340 functionalized doxorubicin-loaded nanoparticle induces apoptosis and reduces tumor volume along with drug-related cardiotoxicity in mice. *International journal of nanomedicine*, 14, 8073–8094. doi: 10.2147/IJN.S220740.

Nakhaee, S., *et al.*, 2021. N-acetylcysteine dose-dependently improves the analgesic effect of acetaminophen on the rat hot plate test. *BMC pharmacology & toxicology*, 22 (1), 4. doi: 10.1186/s40360-020-00469-4.

Ngcangatha-Maqhude, B.A., *et al.*, 2022. The effect of distillation methods on the chemical composition of the essential oil from *Pelargonium graveolens* L'Heritier cultivated in selected locations of Amathole District, Eastern Cape Province. *Journal of essential oil bearing plants*, 25 (6), 1242–1253. doi: 10.1080/0972060X.2022.2145915.

Nidhi, P., *et al.*, 2023. Development and evaluation of hydrogel formulation comprising essential oil of *Mentha longifolia* L. for oral candidiasis. *Advances in traditional medicine*, 23 (3), 777–787. doi: 10.1007/s13596-022-00636-4.

Okechukwu, P.N., 2020. Evaluation of anti-inflammatory, analgesic, antipyretic effect of eicosane, pentadecane, octacosane, and heneicosane. *Asian journal of pharmaceutical and clinical research*, 13 (4), 29–35. doi: 10.22159/ajpcr.2020.v13i4.36196.

Oliveira, R., and Almeida, I.F., 2023. Patient-centric design of topical dermatological medicines. *Pharmaceuticals (Basel, Switzerland)*, 16 (4), 617. doi: 10.3390/ph16040617.

Osafo, N., Yeboah, O.K., and Antwi, A.O., 2021. Endocannabinoid system and its modulation of brain, gut, joint and skin inflammation. *Molecular biology reports*, 48 (4), 3665–3680. doi: 10.1007/s11033-021-06366-1.

Parashar, S., and Garg, M., 2023. Optimized green synthesis of manilkara zapota capped silver nanoparticles and their antimicrobial application through formulation of nano-gel systems. *Nano biomedicine and engineering*, 15 (3), 262–277. doi: 10.26599/NBE.2023.9290020.

Patra, B., *et al.*, 2022. Untargeted metabolomics in *Piper betle* leaf extracts to discriminate the cultivars of Coastal Odisha, India. *Applied biochemistry and biotechnology*, 194 (10), 4362–4376. doi: 10.1007/s12010-022-03873-0.

Pramod, K., Ansari, S.H., and Ali, J., 2010. Eugenol: a natural compound with versatile pharmacological actions. *Natural product communications*, 5 (12), 1999–2006. doi: 10.1177/1934578X1000501236.

Putranti, W., Asterina, C., and Witasari, H.A., 2021. Formulation and antifungal activity of *Piper betle* L. leaf extract in emulsion gels against *Candida albicans*. *Majalah obat tradisional*, 26 (1), 28–34. doi: 10.22146/mot.53257.

Rout, S., *et al.*, 2024. Telmisartan loaded lipid nanocarrier as a potential repurposing approach to treat glioma: characterization, apoptosis evaluation in U87MG cells, pharmacokinetic and molecular simulation study. *Nanotechnology*, 35 (42), 425101. doi: 10.1088/1361-6528/ad64e0.

Roy, A., and Guha, P., 2018. Formulation and characterization of betel leaf (*Piper betle* L.) essential oil based nanoemulsion and its in vitro antibacterial efficacy against selected food pathogens. *Journal of food processing and preservation*, 42 (6), e13617. doi: 10.1111/jfpp.13617.

Rudra, A., and Shoeb, A., 2023. Development, formulation, and evaluation of aloe vera tooth gel: an antimicrobial study. *International journal of pharmacy and pharmaceutical sciences*, 15 (10), 6–12. doi: 10.22159/ijpps.2023v15i10.48765.

Sangale, S.S., *et al.*, 2023. Synthesis of novel isoxazole derivatives as analgesic agents by using Eddy's hot plate method. *South Asian research journal of pharmaceutical sciences*, 5 (01), 18–27. doi: 10.36346/sarjps.2023.v05i01.002.

Satapathy, B.S., *et al.*, 2016. Lipid nanocarrier-based transport of docetaxel across the blood brain barrier. *RSC advances*, 6 (88), 85261–85274. doi: 10.1039/C6RA16426A.

Satapathy, B.S., *et al.*, 2021a. Crystal products of lamotrigine-citric acid for improvement of in vitro drug release in simulated gastric fluid. *Journal of the Serbian chemical society*, 86 (1), 51–61. doi: 10.2298/JSC200705049S.

Satapathy, B.S., *et al.*, 2021b. Lomustine incorporated lipid nanostructures demonstrated preferential anticancer properties in C6 glioma cell lines with enhanced pharmacokinetic profile in mice. *Acta chimica slovenica*, 68 (4), 970–982. PMID: 34918770. doi: 10.17344/acsi.2021.6977.

Satapathy, B.S., *et al.*, 2023a. A mucoadhesive nanolipo gel containing *Aegle marmelos* gum to enhance transdermal effectiveness of linezolid for vaginal infection: in vitro evaluation, in vitro-ex vivo correlation, pharmacokinetic studies. *International journal of pharmaceutics*, 648, 123542. doi: 10.1016/j.ijpharm.2023.123542.

Satapathy, B.S., *et al.*, 2023b. Conveyance of sofosbuvir through vesicular lipid nanocarriers as an effective strategy for management of viral meningitis. *RSC advances*, 13 (47), 33500–33513. doi: 10.1039/d3ra06540e.

Satapathy, B.S., *et al.*, 2024. Encapsulation of alpinia leaf essential oil in nanophytosome-embedded gel as novel strategy to treat periodontal infections: evaluation of antimicrobial effectiveness, pharmacokinetic, in vitro-ex vivo correlation and in silico studies. *Journal of microencapsulation*, 41 (5), 327–344. doi: 10.1080/02652048.2024.2354234.

Sayed, H.M., *et al.*, 2023. Phytochemical investigation, in silico/in vivo analgesic, and anti-inflammatory assessment of the Egyptian *Cassia occidentalis* L. *Steroids*, 196, 109245. doi: 10.1016/j.steroids.2023.109245.

Scandiffio, R., *et al.*, 2020. Protective effects of (E)-ß-caryophyllene (BCP) in chronic inflammation. *Nutrients*, 12 (11), 3273. doi: 10.3390/nu12113273.

Shanmugarajan, T.S., Jadhav, A., and Cheriyan, B.V., 2022. Formulation and optimization of liposomes for antihypertensive drugs. *Current trends in biotechnology and pharmacy*, 16 (3), 329–335. doi: 10.5530/ctbp.2022.3.46.

Singh, S., *et al.*, 2023a. Formulation development and investigations on therapeutic potential of nanogel from *Beta vulgaris* L. extract in testosterone-induced alopecia. *BioMed research international* 2023(1):1777631. doi: 10.1155/2023/1777631.

Singh, T., *et al.*, 2023b. A literature review on bioactive properties of betel leaf (*Piper betel* L.) and its applications in food industry. *Food chemistry advances*, 3, 100536. doi: 10.1016/j.focha.2023.100536.

Sutthisawatkul, P., *et al.*, 2024. Microemulsion containing guava leaves essential oil: enhanced anti-inflammatory, anti-oxidation, anti-tyrosinase activities and skin permeation. *Journal of drug delivery science and technology*, 95, 105536. doi: 10.1016/j.jddst.2024.105536.

Swain, S.S., *et al.*, 2023. Nano-technology platforms to increase the antibacterial drug suitability of essential oils: a drug prospective assessment. *OpenNano*, 9, 100115. doi: 10.1016/j.onano.2022.100115.

Tamaddonfard, E., *et al.*, 2013. Comparison of the effects of crocin, safranal and diclofenac on local inflammation and inflammatory pain responses induced by carrageenan in rats. *Pharmacological reports: PR*, 65 (5), 1272–1280. doi: 10.1016/S1734-1140(13)71485-3.

Ting, T., *et al.*, 2020. Development and characterization of nanoemulgel containing piper betle essential oil as active ingredient. *IOP conference series: Earth and environmental science*, 596 (1), 012032. doi: 10.1088/1755-1315/596/1/012032.

Toopkanloo, S.P., *et al.*, 2020. Impact of quercetin encapsulation with added phytosterols on bilayer membrane and photothermal-alteration of novel mixed soy lecithin-based liposome. *Nanomaterials (Basel, Switzerland)*, 10 (12), 2432. doi: 10.3390/nano10122432.

Toor, H.G., *et al.*, 2021. Computational drug re-purposing targeting the spike glycoprotein of SARS-CoV-2 as an effective strategy to neutralize COVID-19. *European journal of pharmacology*, 890, 173720. doi: 10.1016/j.ejphar.2020.173720.

Vasudevan, C.N.S., *et al.*, 2021. Screening of phytocompounds, molecular docking studies, and in vivo anti-inflammatory activity of heartwood aqueous extract of *Pterocarpus santalinus* Lf. *Asian pacific journal of tropical biomedicine*, 11 (2), 59–65. doi: 10.4103/2221-1691.303604.

Wiegand, I., Hilpert, K., and Hancock, R.E., 2008. Agar and broth dilution methods to determine the minimal inhibitory concentration (MIC) of antimicrobial substances. *Nature protocols*, 3 (2), 163–175. doi: 10.1038/nprot.2007.521.

Wong, M.Y., Teh, H.F., and Khor, S.M., 2022. Determination of 3-monochloropropane-1, 2-diol (3-mcpd) esters in edible plant oils by indirect acidic transesterification methods and the bpx-5 capillary column. *Malaysian journal of analytical sciences*, 26 (4), 718–733.

Xavier-Santos, J.B., *et al.*, 2022. Topical gel containing phenolic-rich extract from *Ipomoea pes-capre* leaf (Convolvulaceae) has anti-inflammatory, wound healing, and antiophidic properties. *Biomedicine & pharmacotherapy*, 149, 112921. doi: 10.1016/j.biopha.2022.112921.

Yam, M.F., *et al.*, 2020. Overview of neurological mechanism of pain profile used for animal "pain-like" behavioral study with proposed analgesic pathways. *International journal of molecular sciences*, 21 (12), 4355. doi: 10.3390/ijms21124355.

Yoonus, J., Resmi, R., and Beena, B., 2021. Greener nanoscience: piper betel leaf extract mediated synthesis of CaO nanoparticles and evaluation of its antibacterial and anticancer activity. *Materials today: proceedings*, 41, 535–540. doi: 10.1016/j.matpr.2020.05.246.

Zammel, N., *et al.*, 2021. Antioxidant and anti-inflammatory effects of *Zingiber officinale* roscoe and *Allium subhirsutum*: in silico, biochemical and histological Study. *Foods (Basel, Switzerland)*, 10 (6), 1383. doi: 10.3390/foods10061383.

About the Book

Dive into the intricate world of environmental studies with "The Shades of Environment," an enlightening compilation prepared by the dedicated faculty members of DRIEMS University. This book offers an in-depth exploration of various elements of the environment, presenting cutting-edge research and innovative solutions across multiple disciplines. From ecological sustainability and environmental impact assessments to advancements in green technology and conservation practices, this comprehensive volume addresses the pressing environmental challenges of our time. Perfect for researchers, students, and policymakers, "The Shades of Environment" is an essential resource for anyone committed to understanding and preserving our planet for future generations.

About the Author

Mr. Partha Sarathi Satapathy, author of "The Shades of Environment," is a distinguished academic at DRIEMS University. He completed his B.Pharm from Utkal University and earned a gold medal for his M.Pharm from Manipal University. Additionally, he holds an MBA with a specialization in marketing from Manipal University Jaipur. Mr. Satapathy's professional experience includes roles in R&D at Himalaya Wellness, Karnataka, and as a Business Development Officer at NatNov Bioscience, Odisha. He has attended five national and three international conferences on pharmaceutical research and has published six research papers in national and international Scopus-indexed journals. A lifetime member of APTI, he currently serves as an Assistant Professor at the School of Pharmacy, DRIEMS University, Tangi, Cuttack.

You may reach the author at:
parthasatapathy@driems.ac.in

OrangeBooks Publication
www.orangebooks.in

Also available as an eBook
ACADEMIC
ISBN